Passivation Layers of Ultra-Advanced High Strength Steels and High Strength Steels

Prifysgol Abertawe
Swansea University

REBECCA DEWFALL

SUPERVISOR: DR MARK COLEMAN

Materials and Manufacturing Academy
Faculty of Science and Engineering

Submitted to Swansea University in fulfilment of the requirements for the Degree of:

Engineering Doctorate

April 2024

Declaration

Declarations

This work has not previously been accepted in substance for any degree and is not being concurrently submitted in candidature for any degree.
Signed: Rebecca Dewfall
Date: Wednesday 1st May, 2024

This thesis is the result of my own investigations, except where otherwise stated. Other sources are acknowledged by footnotes giving explicit references. A bibliography is appended.
Signed: Rebecca Dewfall
Date: Wednesday 1st May, 2024

I hereby give consent for my thesis, if accepted, to be available for electronic sharing
Signed: Rebecca Dewfall
Date: Wednesday 1st May, 2024

The University's ethical procedures have been followed and, where appropriate, that ethical approval has been granted.
Signed: Rebecca Dewfall
Date: Wednesday 1st May, 2024

Signed: Rebecca Dewfall
Date: Wednesday 1st May, 2024

Acknowledgements

The success of this project has largely been due to the help and support of others. I would deeply like to thank those around me for their encouragement and energy to persevere, especially when it felt like the finish line would never be in sight!
I am deeply indebted to my supervisors Dr. Mark Coleman, Dr. Fiona Robinson and Dr. Didier Farrugia. They were thrust with me after numerous supervisor changes but I could not of asked for better mentors. They have provided endless advice and endured countless questions from myself, not only helping to further develop this project but for helping me to flourish.
I am extremely grateful to my fellow doctorate friends for keeping me company during the never ending hours of sample preparation.
Finally I would like to express my never ending gratitude to my partner for keeping me fed during my endless hours of late evening writing.

Abstract

The fundamental ambition of this thesis is to assess the effects of chemical composition, temperature and elapsed time reaction on scale formation. The control of oxidation rates and oxide morphology are focal points of interest along with the evolution and formation mechanisms of scale morphology with time and temperature.
An approach using rapid alloy prototyping (RAP) was selected to help discern the effects of common alloying elements Mn, Si and Mo, on overall scale formation using a wt% comparable to that seen in high strength industrial grades. RAP was successfully used to investigate the formation of oxides associated with Mn, Si and Mo in isolation. The oxide thickness was shown to vary significantly depending on the alloying additions. A minimum fundamental addition of 1wt.% Si was requisite in order to produce a complete passivation layer.
Industrial steel grades were investigated to predict the oxidation rates, scale formation and blister regimes that may form within the hot-strip mill. New and previously unidentified blister formation mechanisms were discovered. Blister upon cooling was discovered during air cooling and observed on a number of samples. Unique and new phenomena such as blister crown splitting and secondary blister were identified on DP800 due to the presence of a conglomerated spinel phase and hematite in the outer oxide.
Plant trials were conducted with differing coiling temperatures after hot rolling to determine the effect on internal oxidation. It was discovered that coiling temperature had a significant impact on the depth of internal oxidation after hot rolling, with a strong negative correlation associated between temperature and depth of the internal oxidation zone. The recommended coiling temperature has been implemented in the United Kingdom, Netherlands and India, eliminating issues surrounding cleanliness after hot-band annealing.
Analysis was conducted using; TGA, EBSD, EDS, WDS, FIB and FEG-SEM imaging.

Contents

List of Figures

List of Tables

1 Introduction

Oxide scale is an inevitable by-product of the high temperatures used during rolling in the hot-strip mill (HSM). During rolling, slabs are stationed in the reheat furnace for 2-5hrs to increase their internal energy to soften the slab before rolling. The slab is passed through pairs of rolls to reduce its thickness, producing a strip steel with the desired thickness and surface finish for the final product.

An initial primary scale will form during the reheating of the slab at 1200-1250°C; growing to 2-3mm in thickness [1]. The temperature distribution along the furnace is regulated by a zone temperature control system. The oxidation reaction is an exothermic reaction and helps to reduce the energy input into the furnace and is therefore somewhat beneficial. Once the slab is reheated, its then descaled, and a secondary scale starts to form during the rolling process. The temperature of rolling of the preheated ingot should be as great as possible to reduce flow stress, allowing for heavy deformation steps and the most efficient processing route [2]. Nonetheless the effects of the rolling temperature must be considered to ensure there is not an excessive growth of secondary and tertiary scale.

Secondary scale is less than 100μm but grows at a brisk rate. Secondary scale is relatively easy to remove using less energy and a lower descaling force in comparison to primary scale [3].

Tertiary scale is formed after the finishing strip mill descaler at temperatures less than 1000°C. Tertiary scale is of the utmost importance because of the severity of defects it creates. Tertiary scale is at risk of fracture and blistering during rolling in the finishing mill. During rolling it frequently becomes embedded into the underlying strip, creating a defect known as rolled in scale. This thesis aims to investigate tertiary scale and the fundamental formation mechanisms of the defects created.

The oxide scales formed on steel during rolling are composed primarily of 3 iron oxides [4]; wustite, magnetite and hematite. Commonly, wustite will form 95 % of the scale, magnetite 4% and hematite 1%; if left at room temperature however wustite can transform to magnetite and these ratios will be subject to change. The inner layer of scale (wustite) is where the greatest oxygen deficiency is present and will contain a high number of defects producing a highly porous structure [4]. Larger voids are found in the outer layer of hematite and these tend to array along the oxide grain boundaries [5]; hematite is the hardest and most brittle phase. The effects of pores on the development of oxide scale is controversial and not well understood [4]. Literature thus far has been highly focused on the phase ratios of iron oxide with little attention to the characterisation and misorientation of the grain boundary, grain size and shape related features [6].

Thermodynamics determines what reaction will occur, and kinetics determines the rate of reaction. The common alloying elements used in ultra-advanced high strength steels

and high strength steels such as Si and Mn will produce complex and intricate oxides. The reactant product will be unique for each steel grade and composed of a multitude of phases. The advanced steel grades are premium products designed for specialist use and products. The oxides formed are extremely detrimental and hard to process. Poor surface quality due to oxidation can result in a loss of customer satisfaction, customer litigation, material loss, cutbacks and high processing costs. Thus, its of great importance to minimise scale and improve passivation. The effects of alloying elements on oxidation rate, kinetics and related microstructure are not well understood and will be investigated.

The fundamental ambition of this thesis is therefore to assess the effects of chemical composition, temperature and elapsed time reaction on scale formation of ultra-advanced high strength steels and high strength steels. The control of oxidation rates and oxide morphology are focal points of interest along with the evolution and formation mechanisms of scale morphology with time and temperature.

2 Literature Review

In this chapter a comprehensive overview of relevant topics is presented. The iron-carbon system and common alloying elements are first discussed in section 2.1; to provide essential background knowledge pertinent to the industrial steel grades examined. Prominent topics relevant to composition, temperature and time reaction on scale formation are discussed in oxidation; section 2.2.

2.1 Steel

2.1.1 The Iron-Carbon system

A phase diagram is used to represent the limits of stability of phases within a chemical system at equilibrium. A phase diagram can predict the solid-state reactions in an equilibrium heat treatment and the final phase composition; allowing tight control of the properties [7]. A phase in a thermodynamics system is a domain of chemical uniformity that is physically and often mechanically distinct. The simple Fe-C binary metastable phase diagram is integral into understanding the fundamentals behind steels and influences even the most complex of alloying systems. The metastable Fe-C phase diagram is shown in figure 1 and is more applicable for practical applications than that of the Fe- graphite phase diagram, due to the low wt% of C used in the bulk of modern steels [7].

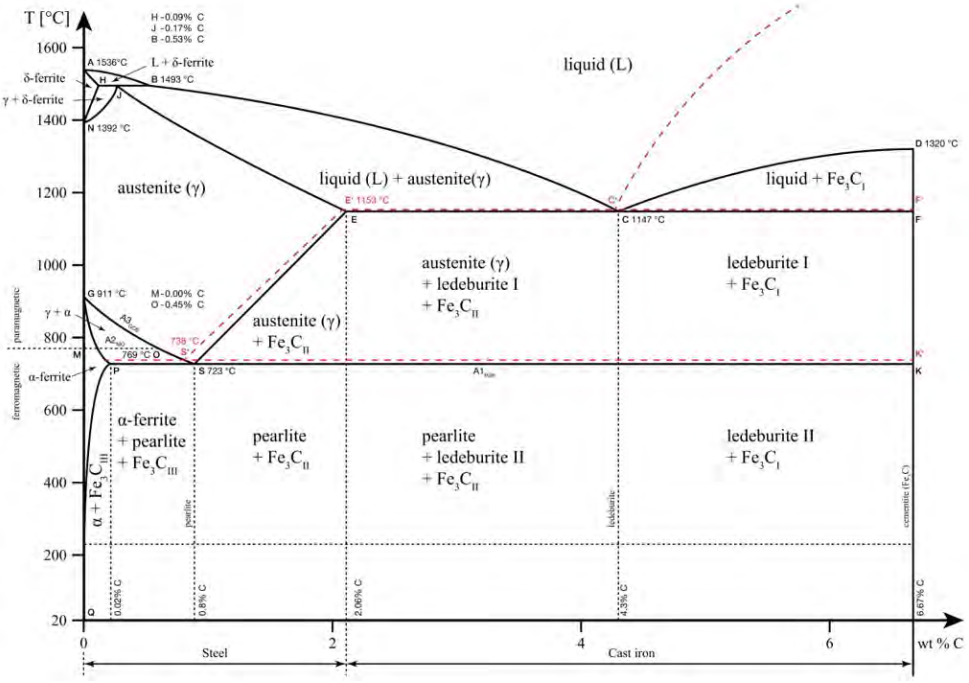

Figure 1: Fe-C Phase digram [7]

Several decisive temperatures, or critical points, exist in the metastable Fe-C phase diagram: the A1 temperature at 723°C, the A3 temperature at 910°C and the A4 temperature at 1394°C [8]. At 727°C upon equilibrium cooling, a critical eutectoid reaction occurs, transforming any remaining austenite into ferrite and cementite. At

0.022-0.76wt% C the reaction will be hypo-eutectoid with pro-eutectoid ferrite and above 0.76wt% C the reaction will be hyper-eutectoid with pro-eutectoid cementite. At 0.76wt% C the reaction forms a lamellar structure of the 2 phases.
The A3 temperature of pure iron is 910°C, but upon the addition of C the temperature will be progressively lowered [8]. The A4 temperature, unlike the A3 temperature, raises with the addition of C expanding the gamma field.

2.1.2 Alloying Elements

To quantify the effects of alloying elements on steel, ternary phase diagrams would need to be assessed over a range of temperatures. This can become complex and tiresome as ternary phase diagrams are more complex than that of a binary phase diagram with reactions occurring on a locus not an invariant. A more straightforward approach would be to assess the effect of alloying elements on the Fe-C phase diagram by appraising how it interacts with the γ phase field.
Alloying elements can influence the equilibrium phase diagram in two ways either by expanding the gamma field, encouraging the formation of austenite over a wider compositional limit or by contracting it and encouraging the formation of ferrite over a wider compositional limit [9] [8]. This can be split into four classes open field, closed field, expanded field and contracted field [9].

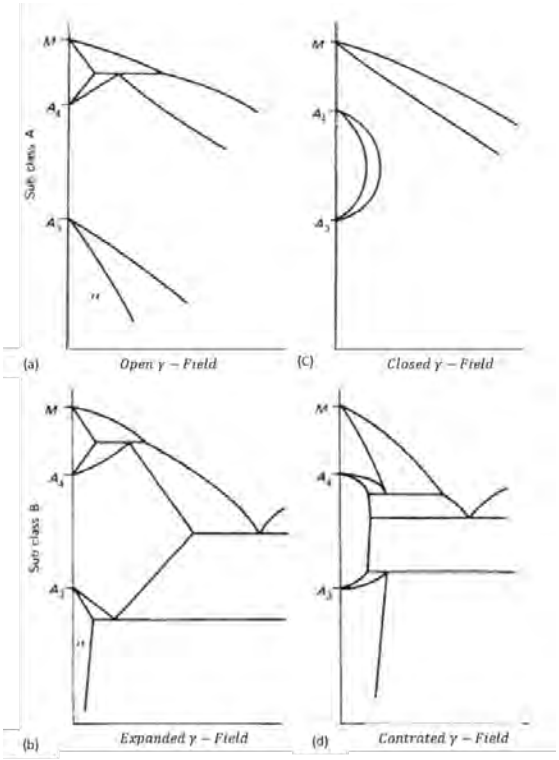

Figure 2: Gamma Field [8]

Open Field Elements within this group have the ability to depress the austenite transformation temperature, creating a stabilising effect. When added in sufficient concen-

tration, they can completely eliminate the bcc- iron phase down to room temperature.

Manganese Mn is a strongly austenite stabilising element due to its FCC crystal lattice and the rothery hume principal, making it a highly useful element in the formulation of austenitic steels. Mn has the ability to stabilise austenitic steels and is largely used in the 200 steel austenitic series; in concentrations of 4%Wt to 15.5%wt Mn [9]. When added in sufficient concentration of up to 15%wt, Mn can depress the transformation temperature of $\gamma \Rightarrow \alpha$ down to room temperature [10], producing an austenitic steel. Increasing the concentration of Mn increases the A3 temperature and decreases the A1 temperature, opening the gamma field [10].
Mn is not a strongly carbide forming element and is considered one of the best elements at retaining C. It can be added to steel in large quantities compared to that of an element such as Ti, which cannot be added in greater quantities than 0.3 wt% due to its carbide forming properties .
Mn has a strong affinity for S and prevents the detrimental formation of iron sulphide [10]. MnS is a primary idiomorphic crystal with a high melting point of 1610°C and is thus not affected by any heat treatments the steel may undergo. Iron sulphide has a low melting temperature and may rupture during rolling [11] [8]. MnS precipitates along ferritic grain boundaries introducing a stress concentration and potentially causing issues with void formation [8]. Mn improves the machinability of steel by forming MnS reducing the brittleness of S.
Mn increases hardenability, abrasion resistance and tensile strength of steel but reduces ductility [11]. If added at too high a concentration however, alongside high C, embrittlement can set in.
Mn is one of the most commonly used elements in U-AHSS and HSS and will undergo selective oxidation [12]. When exposed to oxygen Mn will react to form MnO [13]. If the oxide forms a continuous layer the it will act as a protective layer, shielding the underlying steel and preventing further oxidation. Nonetheless MnO will commonly form during annealing of U-AHSS and HSS prior to galvanising. Its selective oxidation is of concern due to the MnO at the surface deterioration the wettability between the underlying steel and the molten Zn [12]. The oxidation of Mn steels will be examined throughout this thesis.

Expanded Field Within the expanded field the γ formation range is expanded, but the formation is cut off by compound formations such as Fe_3C [11]. C and N are the key influential alloying elements within this group [11].

Carbon C composition in steel varies massively depending on the grade of steel. In austenitic, ferritic and duplex steels the carbon content is kept deliberately low (0.005-0.003 wt%) in order to retain the desired mechanical properties. In martensitic steels C is added in quantities of 0.15-0.2 wt% to increase hardness and strength of the metal at the loss of ductility [11] [8].

C has a sufficiently small atomic radius of 0.91A [11] in comparison to that of iron making it an interstitial solute. C will fit in the interstitial sites present in the FCC and BCC structures however some distortion will still take place. Within the BCC structure the C will not occupy the larger tetrahedral holes due to the large strains. The C atom would have 4 nearest iron atom neighbours which would be displaced, creating a large strain within the structure. The octahedral sites are more favourably placed because there are only 2 neighbouring iron atoms which will be distorted by the interstitial C atom, making octahedral sites the more accommodating interstitial site [8]. Increasing the C concentration decreases ductility and increases hardness and strength.

Closed Field Elements within the closed field group restrict the formation of gamma, causing the gamma field to constrict. The formation of bcc ferrite is encouraged.

Silicon Si is a strong ferrite stabiliser and at high levels with low C the gamma loop will close entirely. If the C content is greater than 0.05 wt% it will not close [8].
Si when added in specific concentrations produces many unique and specialist steel grades. Electrical steels are a highly popular, but difficult steel to manufacture and contain between 0.5% and 5.0%wt Si.
Its common for silicon steels to undergo heat treatments to a produce a grain orientated Si steel with a favourable crystallographic texture for ease of magnetisation [11]. Non-oriented electrical steels are a sub-group of electrical steels where the individual crystals are randomly oriented. Non-oriented electrical steels produce broadly isotropic magnetic properties making them excellent candidates for rotating machinery such as electrical motors and generators [14].
The addition of silicon increases the electrical resistivity of a material resulting in the reduction of induced eddy currents and power losses. Higher quantities of Si will decrease magnetic anisotropy; lowering magnetic hysteresis losses and resulting in more beneficial isotropic magnetic properties [15].
Si additions will increase the resistivity of an electrical steel because the resistivity of pure iron at room temperature is $9.71E^{-8}\Omega$m, while Si has a resistivity of 0.1-60Ωm. An addition of 3 wt% Si will increase the resistivity of an electrical steel fourfold [16] [17].
Si is a substitutional solute in steel and retards the diffusion of C through the crystal lattice [18]. When Si is added to steels the hardness and strength of the steel can be greatly improved, this is due to the substitutional Si atom having a larger atomic radius than that of the Fe atom it has replaced. The distortion of the lattice creates strain energy hindering the flow of plastic deformation [18]. It also creates a strong covalent bond with the Fe atom further strengthening the steel. Nonetheless, high additions of Si will promote the formation of long-range ordered phases which in-turn will promote the embrittlement of steel. Thus, electrical steels are extraordinarily brittle and impractical to cold roll [11]. Electrical steels require processing for favourable grain size, texture and orientation whilst taking into consideration their extreme brittleness.
Si is well known to significantly impact the oxidation behaviour of steel [19] [20].

Silicon will enhance the formation of protective oxide layers on the surface of steel when exposed to oxidative environments and high temperatures. Selective oxidation can form SiO_2 however Si will also frequently form fayalite, a complex spinel phase with the composition Fe_2SiO_4. Fayalite may act as a protective oxide however it can negatively impact the processing of the steel due to inclusions and its strong adherence to the steel surface below [21]. The oxidation of electrical steels will be examined throughout this thesis.

Aluminium Metallic Aluminium is one of the most commonly used alloying additions [2]. Its a popular alloying element within the automotive industry; providing a high weight to strength ratio and serves many integral purposes [2]. During the liquid metal stage, aluminium is used as a deoxidiser, removing excess oxygen from the melt to improve porosity in the solidified steel [22]. The formation of Al2O3 is an exothermic reaction, helping to reduce energy input needed to keep the steel at temperature before casting. The formation of Al2O3 promotes the formation of ferrite pancake grains.
Al is one of the most effective elements in the control of grain growth [22]. Elements such as V, Ti and Zr are also used for grain refinement, but they readily form carbides. These three elements adversely affect hardenability because the carbides formed are stable and difficult to dissolve in austenite prior to quenching [2].
One of the key benefits provided by Al is its ability to tie up excess N. The hard stable AlN precipitates increases the hardness of the steel, improving the mechanical properties of the steel. The removal of N from solution promotes high toughness and provides grain refinement [22]. AlN can either exhibit a hexagonal structure in stable form at room temperature, or a metastable cubic structure. In normalised and heat-treated steels AlN is used for grain refinement. AlN is a classic example of grain boundary pinning by small particles of a second phase [22].
Al may also be added to electrical steels to improve the resistivity of the material, however the impact is not as great as that of Si [23].

Contracted Field Elements within the contracted field encourage the formation of ferrite, restricting the formation of austenite, but the range of formation is cut short by compound formation. Boron is a key element within this field [8].
Figure 3 provides a summary of the effects from alloying elements on steel [23] [22] [16] [17].

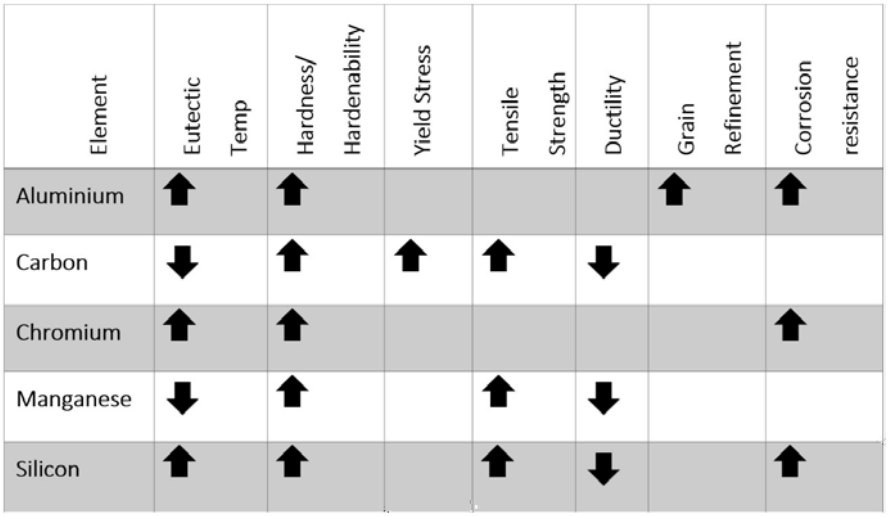

Figure 3: Alloying elements and a summary of influences

2.2 Oxidation

The phenomena of oxidation at high temperature is inevitable and toilsome to govern. Under most conditions pure metals and alloys are thermodynamically unstable. The atoms at surface of the respective base metal have fewer respective neighbours than those within the bulk of the metal matrix [6]. The atoms at the surface of the metal are thence highly reactive and will react to produce a more thermodynamically stable product. Depending on the composition of the base metal and reaction conditions, an oxide, sulphide, carbide or nitride is commonly formed [7]. Reaction rates increase rapidly with temperature due to an increase in the average kinetic energy of particles, increasing collision rates. High temperature in this instance is 500°C and above. Resistance at high temperature and the formation of protective layers therefore becomes imperative in order to minimise oxidation. Oxide scales can arise during the hot rolling of a product through a reaction of elements in the material with the atmosphere. The protective action of these scales depends on several factors. Oxidation lifetime can be formally defined as the time-to-breakaway [18]. Figure 4 provides a summary of the effects of temperature on oxidation.

2.2.1 Thermodynamic Considerations of Oxidation

In order to obtain an understanding of high temperature oxidation reactions, an understanding is needed to determine whether a metal or any alloying components, may react with a given component of a gas phase [19]. The rationalisation of the observed products is often complex, involving the reaction of multicomponent alloys. Further complications arise from the additions of liquids or solid deposits which can produce additional reaction products [19]. Equilibrium thermodynamics is essential in ascertaining whether a reaction is feasible, whether evaporation or condensation of a species is possible and the conditions under which this may occur. [19] The second law of thermodynamics, Gibbs free energy, is shown in equation (1). Here Gibbs free energy is a

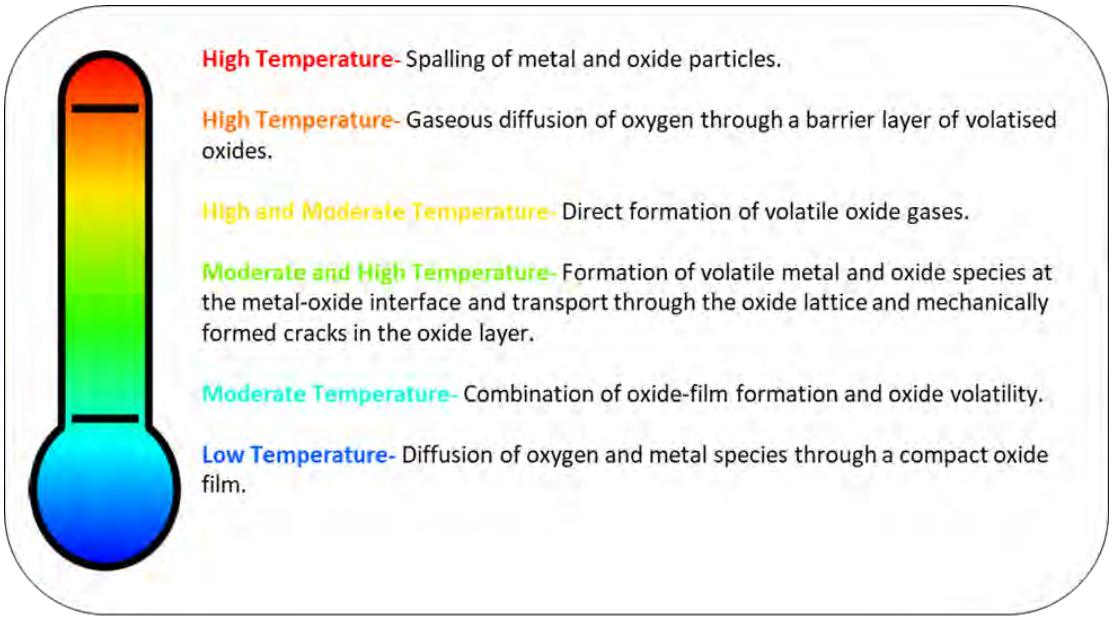

Figure 4: Summary of oxidation phenomena [6] [18] [19]

thermodynamic quantity equal to enthalpy minus the product of entropy and absolute temperature. Temperature and pressure must be kept constant.

$$\Delta \mathrm{G} = \Delta \mathrm{H} - T\Delta \mathrm{S} \tag{1}$$

ΔH is the change of enthalpy of a system; its a measure of the energy liberated during the reaction. If the value is negative, energy is emitted during the reaction; if the value is positive, energy is required for the reaction to occur [19] [18]
ΔS is the change of entropy of a system; its a measure of the change in the possibilities for disorder products compared to the reactants. If an ordered state such as a solid were to transform into a liquid, a somewhat less ordered state, the entropy would be positive. The greater the degree of disorder, the more favourable the reaction. This is due to the laws of thermodynamics; the greater the degree of disorder, the greater the number of possible locations and arrangements of the molecules [19].
During oxidation, gas molecules are adsorbed onto the surface of the respective metal. The adsorption results in a loss of a degree of freedom; thus, adsorption results in a decrease in entropy (disorder). A simultaneous decrease in both entropy and the free energy of a system also implies a decrease of enthalpy [19] [18].

$\Delta \mathrm{G} < 0$ A spontaneous reaction will occur
$\Delta \mathrm{G} = 0$ The system is in equililbrium
$\Delta \mathrm{G} > 0$ The reaction is thermodynamically impossible

2.2.2 Kinetics of Reaction

To identify the reaction mechanisms and to determine the rate-limiting process of a reaction, its important to understand the kinetics of reaction. Thermodynamics ascertains the direction of a reaction, whereas kinetics ascertains the rate of a chemical reaction. During oxidation, the simplest oxidation reactions will obey linear, parabolic or logarithmic models; however these represent limiting and ideal cases [24]. Whilst under real life applications it is common to encounter deviations from these ideal models, requiring a combination or use of intermediate rate equations. This will be discussed in the following sections.

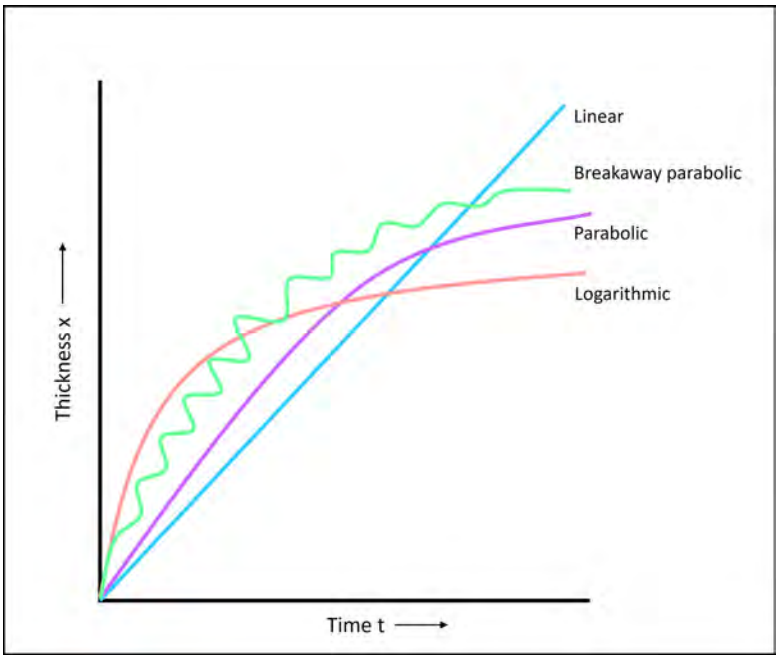

Figure 5: Kinetics of reaction; rate of oxidation

2.2.3 Rate of Oxidation

For oxidation to proceed its necessary for ionic and electronic transport processes to advance through the growing oxide layer. The growing oxide layer is accompanied by ionising phase-boundary reactions and the formation of a new oxide at a site dependent upon whether cations or anions are transported through the oxide layer [19]. Simplifying this model Wagner [25] [19] developed his acclaimed theory for the oxidation of high temperature metals. The Wagner theory of oxidation describes oxidation behaviour where diffusions of ions is the rate determining step under highly idealised conditions [19] Before proceeding with the derivation of Wagner's theory a simplified treatment may first be used to emphasise the important features of diffusion-controlled oxidation [19].

Simplified diffusion-controlled oxidation If its assumed that [19];

1. Cationic transport across the growing oxide layer underpins the rate of oxidation and,

2. Thermodynamic equililbrium has been established at each interface [19];

Then the outward flux will be equal and opposite to the inward flux; where the inward flux of cation defects may be represented by vacancies. Thus, the outward flux, $j_{M^{2+}}$, can be expressed as [19]

$$j_{M^{2+}} = -j_{v_m} = D_{v_m} \frac{c_{v_m}^{''} - c_{v_m}^{'}}{x} \tag{2}$$

Where;
x= oxide thickness D_{v_m}= diffusion coefficient for cation vacancies,
$c_{v_m}^{''}$ = vacancy concentration at scale-metal interface,
$c_{v_m}^{'}$ = vacancy concentration at scale-gas interface,
The value of $c_{v_m}^{''} - c_{v_m}^{'}$ is a constant due to thermodynamic equilibrium. Thus, the rate of oxide thickening can be given by [19];

$$\frac{dx}{dt} = \frac{k'}{x} \tag{3}$$

Where,

$$k' = D_{v_m} V_{ox} (c_{v_m}^{''} - c_{v_m}^{'}) \tag{4}$$

and,
V_{ox}= molar volume of the oxide
Using equation(3), the parabolic law can be derived through integration; noting that $x = 0$ at $t = 0$,

$$x^2 = 2k't \tag{5}$$

The cation-vacancy concentration of the oxide can be related to the oxygen partial pressure of a system via [19],

$$c_{v_m} = const.p_{O_2}^{\frac{1}{n}} \tag{6}$$

Considering both equation(5) and (6), the variation of parabolic rate constant with oxygen partial pressure can be predicted [19],

$$k'\alpha(p_{O_2}^{''}) \tag{7}$$

Wagner theory of oxidation For the Wagner theory of oxidation to hold valid, a list of assumptions must be met [19] [6] [26];

1. The oxide layer is a compact, perfectly adherent scale
2. The migration of ions or electrons is the rate-controlling process
3. Thermodynamic equilibrium is established at both metal-scale and scale-gas interfaces
4. The oxide scale shows only small deviation from stoichiometry and, hence, the ionic fluxes are independent of position within the scale

5. Thermodynamic equilibrium is established locally throughout the scale
6. The scale is thick in comparison to the distances over which space charge effects (electrical double layer) occur
7. Oxygen solubility in the metal may be neglected

An independent activity gradient is established for both the metal and non-metal across the scale. Consequently, metal ions and oxide ions will tend to migrate in opposing directions across the scale. The migration of charged ions sets up an electric field across the scale, transporting electrons across the scale from metal to atmosphere. Due to the conservation of charge, the relative migration rates of cations, anions and electrons are, accordingly, balanced and no net charge transfers will occur across the oxide layer as a result of ion migration [19]. Functioning as charged particles, the ions will respond to both chemical and electrical-potential gradients; providing the net driving force for ion migration.

A particle, i, carrying a charge, Z_i, in a position where the chemical-potential gradient may be given by $\frac{\partial \mu_i}{\partial x}$ and the electrical-potential gradient $\frac{\partial \phi}{\partial x}$, is acted on by a force given by [19],

$$\frac{1}{N_A}(\frac{\partial \mu_i}{\partial x} + Z_i F \frac{\partial \phi}{\partial x}) J particle^{-1} cm^{-1} \tag{8}$$

Where,

N_A = Avogadro's number,

F = Faraday's constant

The application of force to a particle i creates a drift velocity, $v_i(cms^{-1})$, proportional to that of the acting force [19]. The particle mobility,B_i, is defined as the average drift velocity per unit force, particle $cm^2 J^{-1} s^{-1}$. A negative sign will arise in the equation because the drift velocity takes place in the positive direction for negative potential gradients. The flux of particles may therefore be obtained as [19],

$$j_i = C_i v_i = -\frac{C_i B_i}{N_A}(\frac{\partial \mu_i}{\partial x} + Z_i F \frac{\partial \phi}{\partial x}) \tag{9}$$

Where,

C_i = the concentration of $i(molcm^{-3})$

The mobility of a particle, i, may be related to the conductivity, K_i, and the self-diffusion coefficient, D_i, by comparing the flux of particles [eq] for limiting cases of zero electrical-potential gradient and zero chemical-potential gradient to Ficks first law and Ohms law respectively [19],

$$J \alpha \frac{dc}{dx} \tag{10}$$

$$I = \frac{V}{R} \tag{11}$$

The relationship may then be used to surmise partial conductivity [19],

$$k_B T B_i = D_i = \frac{RT\kappa_i}{C_i(Z_i F)^2} \tag{12}$$

Where,
k_B = Botlzmann constant
The mobility B_i, in equation (12) for partial conductivity may be superseded using the relationship derived in equation (8), to produce a new relationship describing the flux of cations, anions or electrons through the oxide layer [19],

$$j_i = -\frac{\kappa_i}{Z_i^2 F^2}(\frac{\partial \mu_i}{\partial x} + Z_i F \frac{\partial \phi}{\partial x}) \tag{13}$$

Due to the vastly differing mobilities; electrons, cations and anions would move at different rates through the oxide, setting up electric fields tending to oppose the independence of the species.
The three species migrate at rates that are defined by the fundamental need to maintain electroneutrality throughout the scale, such that there is no net charge across the oxide scale. Neutrality can conceivably be achieved, due to the very high mobility of electrons and or electronic defects. The Wagner theory of oxidation originally involved cations, anions and electrons. The bulk of oxides show exceptionally high electronic mobility, whereas the mobilities of anions and cations is generally far lower by many orders of magnitude. Its therefore logical to simplify the relationship ignoring the migration of the slower-moving ionic species. In the common event that both cations and electrons are the mobile species within an oxide or sulphide species, corresponding fluxes may be derived; where Z_c and Z_e are the charges on cations and electrons respectively [19].

$$j_c = -\frac{\kappa_c}{Z_c^2 F^2}(\frac{\partial \mu_c}{\partial x} + Z_c F \frac{\partial \phi}{\partial x}) \tag{14}$$

$$j_e = -\frac{\kappa_e}{Z_e^2 F^2}(\frac{\partial \mu_e}{\partial x} + Z_e F \frac{\partial \phi}{\partial x}) \tag{15}$$

The requirement for electro-neutrality is given by [19],

$$Z_c j_c + Z_e j_e = 0 \tag{16}$$

Further rearrangement and substitution of equation (14) and (15), $\frac{\partial \phi}{\partial x}$ is eliminated and $Z_e = -1$, the flux of cations becomes [19],

$$j_c = -\frac{\kappa_c \kappa_e}{Z_c^2 F^2(\kappa_c + \kappa_e)}(\frac{\partial \mu_c}{\partial x} + Z_c \frac{\partial \mu_e}{\partial x}) \tag{17}$$

The ionisation of a metal is represented by $M = M^{z_c} + Z_c e$, and thus at equilibrium [19],

$$\mu_m = \mu_c + Z_c \mu_e \tag{18}$$

Therefore,

$$j_c = -\frac{\kappa_c \kappa_e}{Z_c^2 F^2 (\kappa_c + \kappa_e)} \frac{\partial \mu_M}{\partial x}, \tag{19}$$

Where, κ_c, κ_e and $\frac{\partial \mu_M}{\partial x}$ are instantaneous values at that location. Due to the likelihood of these values changing, its necessary to integrate equation (19) [19].
j_c will therefore be defined in terms of scale thickness, x, and the measurable metal chemical potentials at the metal-scale interface, $\mu_M^{'}$, and the scale-gas interface, $\mu_M^{''}$,

$$j_c \int_0^x dx = -\frac{1}{Z_c^2 F^2} \int_{\mu_M^{'}}^{\mu_M^{''}} \frac{\kappa_c \kappa_e}{\kappa_c + \kappa_e} d\mu_M \tag{20}$$

Then,

$$j_c = -\frac{1}{Z_c^2 F^2 x} \int_{\mu_M^{'}}^{\mu_M^{''}} \frac{\kappa_c \kappa_e}{\kappa_c + \kappa_e} d\mu_M \text{mol cm}^{-2} s^{-1} \tag{21}$$

Similarly for the flux of electrons [19],

$$j_e = -\frac{1}{Z_c^2 F^2 x} \int_{\mu_M^{'}}^{\mu_M^{''}} \frac{\kappa_c \kappa_e}{\kappa_c + \kappa_e} d\mu_M \text{mol cm}^{-2} s^{-1} \tag{22}$$

Additionally, if the metal concentration within the oxide is $C_M$mol cm^{-3}, then flux may further be expressed as [19],

$$j_c = C_M \frac{dx}{dt} \tag{23}$$

$$j_e = C_M \frac{dx}{dt} \tag{24}$$

2.2.4 Linear Rate Law

Kinetic behaviour determines the variation, in the rate of oxidation as a function of time. Kinetic behaviour may be expressed by logarithmic, parabolic or linear behaviour, creating the three kinetics laws respectively [4].
The linear rate law describes the rate of oxidation being directly proportional to time,

$$x = k_1 t \tag{25}$$

Where,
k_1 = the linear rate constant
The result is instantaneous oxidation when a metal comes into contact with oxygen [19]. The linear rate law can commonly be observed under conditions where a phase-boundary process is the rate-determining step for the reaction.
Principally, diffusion through the scale is unlikely to be rate limiting in the initial stages of oxidation; i.e. when the scale is thin [19]. Therefore, the reactions occurring at the metal-scale interface can be considered fast, i.e., ionisation of metal with a cation conductor, or, ionisation of a metal with anion conducting scales [19]. Scrutiny can

therefore be accordingly diverted to the scale-gas interface.

Adsorption Adsorption can be classified into two categories known as either, physiosorption or chemisorption. This classification will be based on the interaction between the adsorbate molecules and the adsorption surface and the resulting bond [27]. Chemisorption in oxidation is a process that occurs between the scale atoms and a gas species; thereby making it extremely important when dealing with reactions at the scale-gas interface. Chemisorption requires a high activation energy for the reaction to occur. During the process of chemisorption, the reactant gas molecules will approach an active site at the scale surface whereby they will become adsorbed onto the surface. The result obtained is a monolayer of the adsorbate attached to the surface of the adsorbent [27]. Active sites are categorised by their high surface energy, commonly due to surface defects such as kinks or a mismatch of orientations [28]. The chemical bond formed between the adsorbate and adsorbent is far stronger than that of the weak van der waals bonds formed during physiosorption [27]. Particle size, initial concentration and temperature will affect the rate of chemisorption.
The adsorbate, (in this case oxygen), strongly attracts electrons from within the oxide lattice. The removal of electrons from the scale causes a deviation in the concentration of electron defects at the scale-gas interface. This process can be represented as in equation [19],

$$\frac{1}{2}O_2(g) \rightarrow \frac{1}{2}O_2(ad) \rightarrow O(ad) \rightarrow^{e^-} O^-(chem) \rightarrow^{e^-} O^{2-}(latt) \tag{26}$$

Where, oxygen is the active oxidising species in the gas phase [19]. In the case of high temperature these reactions do lead to constant rate kinetics and can therefore be assumed to be rapid surface reactions.
In high temperature oxidation, indication of linear law may signify a catastrophic reaction due to the cracking of the oxide scale, scale delamination or spallation. This exposes a fresh surface of metal promptly increasing oxide formation [24].

Transition to Parabolic Oxidation As discussed, any initial scale developed is very thin, allowing for the rapid diffusion of species through the scale. A virtual equilibrium is established with constant-rate kinetics at the scale-gas interface; denoting the initial stages of oxidation. This stage will occur for a period of time depending on the conditions under which the reaction ensues. Nonetheless, as the reaction proceeds a constant flux must be maintained. The flux of iron diffusing through the oxide is inversely proportional to the oxide thickness. As the oxide thickens, the metal activity gradient must fall but, it cannot fall below the value in equilibrium with the atmosphere [29]. Thus, there must be a reduction in the metal activity gradient across the scale and, accordingly an attrition in ionic flux and reaction rate. At this point the diffusion of iron ions must become the rate-controlling step and the rate falls with time according to a parabolic rate law [29].

2.2.5 Parabolic Rate Law

Parabolic law predicts the rate of oxide formation is inversely related to time. The oxide thickness is measured as the reaction parameter [19]. Thus, as time increases, the rate of scale formation decreases. Metals whom follow parabolic law are beneficial due to the increased path for the ionic diffusion of metal or oxygen [24]. As scale growth continues, diffusing species must travel further and thus, they take longer to reach the interface. Rate of oxide formation following parabolic kinetics may be written as [19]:

$$\frac{dx}{dt} \propto 1 \text{ or } \frac{dx}{dt} = \frac{k^{'}}{x} \tag{27}$$

Integration of equation (27) then gives the measurement of scale thickness(x) [19],

$$x = k^{'} t^{-1/2} \tag{28}$$

Where,

$k^{'}$ = the scaling constant $cm^2 s^{-1}$

The measurement of mass increase, (m), with time is given by [19],

$$(\frac{m}{A})^2 = k^{''} t \tag{29}$$

Where,

A is the area of reaction,

$k^{''}$ is the parabolic rate constant $g^2 cm^{-4} s^{-1}$

The measurement of metal surface recession, is given by [19],

$$l^2 = 2k_c t \tag{30}$$

Where,

k_c is the corrosion constant defined by measuring the thickness of consumed metal $cm^{-2} s^{-1}$

The rate and duration of oxidation employing parabolic law is highly dependent upon factors such as specimen geometry and scale mechanical properties. Geometry plays a critical role because as the reaction proceeds, the metal core gets smaller and hence, the area of metal-scale interface grows smaller. Thus when the reaction rate is expressed in terms such as mass gain per unit area, taking only the initial surface area will incur small but significant errors.

2.2.6 Transport Mechanisms

The mechanism of oxidation may be simplified by dividing it into two stages. Firstly, oxidation will proceed at a linear rate, followed by a parabolic rate of oxidation [30]. Secondly, diffusion-controlled oxidation of ionic species through the newly formed oxide layer [30].

Initial oxidation is often far lower than expected or predicted. The discrepancy may be due to adsorbed structures, that will then form mutual phase domains. The adsorbed atoms can also cause appreciable displacement of the substrate atoms, forcing the lattice to adopt a new configuration [31]. In this instance the oxide is reconstructed to form a new pseudo-oxide [31]. Due to the ionic nature of metal oxides, the transport of species through the product cannot practicably be neutral. Several mechanisms may be considered to explain the transport of ions through ionic solids, involving stoichiometric and non-stoichiometric crystals.

2.2.7 Stoichiometric

Highly stoichiometric compounds correspond to an exact and fixed composition with a small integer ratio among the atomic components [31]. The concept is related to Dalton's law of multiple proportions [32]. The atoms occupy precise crystal lattice points where neither impurities nor defects can exist [31]. Non-stoichiometry epitomises a deviation from the well-defined stoichiometry, through the introduction of point defects such as vacancies and impurities upon forming a solid solution. The excellent uniformity and high efficiency of stoichiometric compounds makes them an excellent choice for electronic and optic devices due to the perfect ordering of atoms [31].
The defect structure is uncertain for a large majority of oxide compounds due to the requirement of further understanding of issues relating to the crystal structure. The issue of understanding is related to; coordination sites for metal cations, ionic-covalent bonding states, oxygen to oxygen interactions, degree of oxidation, effect of the size ratio of metal to oxygen on crystal deformation, defect interactions, population of point defects and their configurations associated with ordering and disordering, and solid solution ranges [31].
The balance between ionic and covalent bonding depends on an individual oxide. The variable energy states associated with defect generation make predicting the bond length, lattice size and mode of deformation challenging. Oxides may show deviations from stoichiometry; depending on the oxygen pressure, the transition metals form numerous non-stoichiometric oxide phases with ions of differing valences resulting in varying metal ion to oxygen ratio [31].
Simple consideration of the presence of interstitial impurities and oxygen vacancies is not sufficient in confirming the defect structure of an oxide. A non-stoichiometric oxide may have highly ordered defects at high concentrations in order to lower the free energy of the compound. Resulting interactions may also create clusters of point defects. This has been proposed for Fe vacancies in the wustite phase where a superlattice can form. Thus, its imperative to be aware of and to consider the quantity of impurities or vacancies [31]. In a highly stoichiometric ionic compound, the predominant point defects are Schottky and Frenkel defects [33].

Schottky Point defects are the simplest of defects that can be found within a crystal phase [33]. They do not possess lattice structure in any dimension and are thus defects of zero dimensionality [34]. Ionic mobility is demonstrated due to the existence of ionic vacancies. For electro-neutrality to be preserved, an equal number of vacancies on cationic and anionic sub-lattices must be presupposed [19]. Since vacancies exist on both sub-lattices, its expected that both anion and cations will be mobile within the structure. This is known as a Schottky defect [19].

Frenkel Frenkel defects may be explained in the case were the anion lattice is ideal and that only cations are mobile. The cation lattice contains cation vacancies and interstitials in equal concentrations in order to maintain electroneutrality across the crystal. The cation can thus travel across both interstitial and vacancy sites [19].
Nonetheless neither the Frenkel nor Schottky transport mechanism can explain the mechanism by which electrons may migrate [19]. In order for the oxidation reaction to proceed neutral atoms must migrate or both ions and electrons must migrate [19]. If migration is dominated by cations, scale formation develops at the scale-gas interface. In the case of anion migration dominating, scale formation develops at the metal-scale interface [19]. To ascertain how simultaneous migration of ions and electrons occurs during the formation of oxides, its necessary to assume that the oxide is a non-stoichiometric compound [19].

2.2.8 Non-stoichiometry

As previously discussed, non-stoichiometry implies that the metal to non-metal atom ratio is not derived by a chemical formula. In a non-stoichiometry compound, a cation or anion may exhibit variable valency on its sub-lattice. There is an increased likelihood of a metal or a cation exhibiting variable valency [19]. Non-stoichiometric ionic compounds may be classified as a semiconductor and thus may show negative or positive behaviour as an n-type or p-type respectively.

Negative (n-type) semiconductors An n-type semiconductor is characterised by negative carriers. Negative carriers may arise, when there is an excess of metal or a deficit of non-metal. The electrical conductivity is reliant upon the concentration of conduction-band electrons. Thus, the measurement of electrical conductivity as a function of oxygen partial pressure serves to define the rate law and indicate the predominant defect [19].
In a non-metal deficit or a metal excess material, the negative carriers may be formed due to the discharge and subsequent evaporation of an oxygen ion. The electrons from the evaporated oxygen ion then enter the conduction band and a vacancy is created on the anion lattice. The process can be represented as seen below [19],

$$O_O = V_{\ddot{o}} + 2e^{'} + \frac{1}{2}O_2 \tag{31}$$

The vacant oxygen-ion site is surrounded by positive ions and the result is an area with a large positive charge. The large positive charge acts as an energy trough which draws in surrounding negative free electrons. Therefore, the vacancy and free electrons can be associated according to [19],

$$V_{\ddot{o}} + e^{'} \rightarrow V_{\dot{o}} \tag{32}$$

$$V_{\dot{o}} + e^{'} \rightarrow V_{o} \tag{33}$$

Thus, there is a high possibility of doubly a charged, singly charged and neutral charged vacancies existing. The relationship between the concentration of anion vacancies, conduction-band electrons and the dependence of electrical conductivity, with regards to oxygen partial pressure, may be derived as shown;
Doubly charged,

$$\kappa \propto C_{e'} \propto p_{O_2}^{-\frac{1}{6}} \tag{34}$$

Singly charged,

$$\kappa \propto C_{e'} \propto p_{O_2}^{-\frac{1}{4}} \tag{35}$$

Neutral (independent of pO_2)

$$\kappa \propto C_{e'} \tag{36}$$

The power of the oxygen partial pressure is negative in the case of n-type semiconductors.

Positive (p-type) semiconductors A p-type semiconductor is characterised by positive carriers. Positive carriers may arise when there is a deficit of metal or an excess of non-metal. Semi-conduction in a p-type semiconductor arises from the formation of vacancies on the cation lattice with electron holes, giving rise to conduction. The formula may be written as $M_{(1-\delta)}O$, with δ, varying widely.
The ability of an electron hole to materialise lies within a metal ions capacity to emanate in multiple valence states. The closer neighbouring valence states are in terms of ionisation energy, the easier its to induce a cation vacancy through the p-type formation mechanism. In the case of a cation with energetically close valence states, its relatively simple for an electron to transfer from a 2+ ion to a 3+ ion, thus reversing the charge on the two ions. The 3+ site is then seen to offer a low-energy position for an electron, designated as an 'electron hole' [35].
The formation of a metal-deficit p-type semi-conductor with cation vacancies and positive holes is shown in the process below [19];

$$Adsorption : \frac{1}{2}O_2(g) = O(ad) \tag{37}$$

$$Chemisorption : O(ad) = O^{-}(chem) + h\cdot \tag{38}$$

$$Ionization : O^{-}(chem) = O_o + V + h \tag{39}$$

Overall,

$$\frac{1}{2}O_2 = O_o + 2h\cdot + V'' \tag{40}$$

If its assumed that Henry's law is obeyed and that the overall reaction is the only guiding mechanism by which defects form [19] [36],

$$C_h^2 C_{V''} = K_{15} p_{O_2}^{\frac{1}{2}} \tag{41}$$

Stoichiometry for electrical neutrality,

$$C_h = 2C_{V''} \tag{42}$$

Then,

$$C_h = const.p_{O^2}^{-\frac{1}{6}} \tag{43}$$

Electrical conductivity is expected to vary proportionally to the electron-hole concentration. Nonetheless a further possibility, is that a cation vacancy may bond with an electron hole. In this case the formation of vacancies and electron holes, upon oxidation is represented as [36] [19]:

$$\frac{1}{2}O_2 = O_O + h\cdot + V' \tag{44}$$

Where,

C_h is related to pO_2 as shown below,

$$C_h = const.p_{O^2}^{-\frac{1}{4}} \tag{45}$$

The concentration of doubly charged vacancies will increase according to $p_{O^2}^{-\frac{1}{6}}$ and singly charged vacancies will increase according to $p_{O^2}^{-\frac{1}{4}}$. Thus, doubly charged vacancies will correspondingly dominate at low oxygen partial pressures and singly charged vacancies will respectively will dominate at high oxygen partial pressures.

Intrinsic semiconductors Intrinsic semiconductors are a subsidiary of the semiconductor classification. Although they exhibit close stoichiometry, they show high electrical conductivity independent of oxygen partial pressure. This behaviour is common

when the concentration of electronic defects exceeds that of ionic defects [20]. Equilibrium of electronic defects is established upon the production of a 'quasi-free' electron and an electron hole, when an electron is excited from a valence band to a conduction band [20].

$$Null = h \cdot + e^{'} \tag{46}$$

It should be noted that very few oxides are classified as intrinsic semiconductors [19].

Non-planar growth Initial oxidation mostly treats ideal cases and situations such as adsorption, nucleation and film formation on different crystal faces on single crystals. Further, oxide films have been assumed to have an even thickness and to be plane parallel [35].
Metals are predominantly polycrystalline and in turn the grains will have different orientations. Hence, the film thickness will vary from one grain to another [35]. As an oxide grows and develops into a scale, non-planar growth may develop.
Non-planar growths refer to features that are not confined within a single plane and thus, they have a three-dimensional quality.
This may involve whiskers, columnar crystals, blades and platelets [35].
An oxide whisker is a single-crystalline oxide which possesses a high aspect ratio morphology [37]. Growth of oxide whiskers is anisotropic and one directional. There are multiple growth mechanisms which have been suggested for whiskers such as catalysts [38] [39], fast ion diffusion through defects [26] [40], stress [41] and chlorine atmospheres [37].
Numerous studies have shown that whiskers consist of the higher valence oxide in a multi-layered scale such as Fe_2O_3 in the oxidation of iron [35].
It was reported that whiskers of a single crystal of Fe_2O_3 grew out of the oxide surface, preferentially from a Fe_3O_4 grain boundary. The planar interface has been proposed to serve as a short-circuit diffusion path, providing rapid internal diffusion of Fe [42]. Whiskers have also been shown to contain hollow cores [35]. These easy diffusion paths facilitate rapid metal ion transport to the tip of the whisker and thus accounts for growth observed at the tip [35]. The overall reaction rate is thought to be governed by growth of a base film or scale.
In addition to whiskers, iron may exhibit other non-planar features such as an iron oxide pyramids and pits. The growth mechanism for pyramids and pits is akin to that of whisker formation. At intermediate temperatures lattice diffusion becomes a more paramount transport mechanism and broadens the growth pattern of the whisker to yield pyramidal crystals [35]. At high temperatures lattice diffusion is the predominant transport process. Screw dislocations with high tension serve to form growth pits. Growth pits may only form when the availability of the oxidant at the surface is the rate-determining process [35].

2.2.9 Oxide Growth

When considering the oxidation of a complex alloying system such as steel, its impossible to find an idealised situation that conforms to a single mode of rate control. The following section will first consider the oxidation of a pure metal in order to simplify the rate controlling steps.

2.2.10 Oxidation of a Pure Metal

Upon exposure to an oxidising atmosphere, a metal will experience an initial rapid reaction. If the parabolic law is considered, the scale thickness must initially be extrapolated to zero and an infinite rate is predicted [19]. The preliminary stage of oxidation, nonetheless, is not infinite and thus, the initial stages of oxidation must be governed by a process other than ionic transport through thin oxide scales [19].
Firstly, consider the processing of gas molecules on the oxide surface [19]:

$$O_2(g) \rightarrow O_2(ad) \rightarrow 2O(ad) = 2O^-(chem) + 2h\cdot \rightarrow 2O^{2-}(latt) + 4h\cdot \qquad (47)$$

Where, adsorption, dissociation, chemisorption and ionisation of oxygen would occur respectively, a constant reaction rate would be established [19]. Notwithstanding, these processes are so swift that the reaction rate is rarely observed. Commonly an oxide is almost immediately of sufficient thickness for ionic diffusion through the scale to be the governing step. At this point, a parabolic rate law is found to hold for a period whose duration depends upon factors such as scale mechanical properties and specimen geometry [12].
Specimen geometry is imperative because, as a reaction proceeds, the metal core decreases and so the area of metal-scale interface gets smaller. This becomes critical when a reaction rate is expressed as mass gain per unit area, because taking the initial surface area of the metal specimen to be constant can lead to considerable errors [12].
It has been shown that unless corrections are made for the reduction of the scale-metal interface, the rate of reaction will fall below that of the predicted on the basis of the parabolic rate law on the basis that the scale maintains contact with the metal [43].
At the oxidation reaction proceeds stresses are generated within the scale. In a system where cations are mobile, growth stresses will arise as metal atoms diffuse outwards at the metal-scale interface. The scale must relax during outward diffusion of the cations in order to maintain contact with the metal. In the instance the scale does not relax, voids will form at the metal-scale interface. On a planar interface relaxation may occur readily. Nonetheless, on edges and corners, relaxation is not possible because forces are restraining movement in the required two or three directions [19].
The geometry of the scale is stabilised at these non-planar interface and resists relaxation. Thus, in order to maintain contact with the metal, the scale must undergo creep maintained at a rate determined by the rate of metal removal. The adhesion between scale and metal is the maximum force exerted to cause scale creep whilst maintaining

contact. Hence, unless scaling rate is low or the scale is quite plastic contact will be lost as the reaction proceeds and the structural integrity of the scale will fail. As scale continues to thicken, contact will be lost in any real situation involving corners [19]. As contact between the scale and metal is lost, the area across which cations can be supplied is decreased and the cations have a longer diffusion distance. An increased diffusion distance ultimately results in a reaction rate decline.
Upon loss of contact between the scale and metal; oxygen activity rises correspondingly with a decrease of metal activity. As oxygen activity rises, the oxygen partial pressure in equilibrium with the oxide inner surface rises and oxygen is adsorbed into the pore, diffusing across the pore and forming a new oxide on the fresh metal surface. Thus, a porous zone of scale is developed between the outer layer of compact scale and the metal. The outward diffusion of cations is maintained through the porous scale with oxide scale dissociating faster at grain boundaries than grain surfaces [12].
The above highlights the dangers of extrapolating data from small physical sample sizes to produce predictive models for larger pieces or pieces with different geometries.

2.2.11 Internal Oxidation

Internal oxidation occurs when oxygen diffuses into an alloy and causes sub-surface precipitation of the oxides of one or more alloying elements [35]. When inward diffusion of oxygen ions in the alloys exceeds that of the outward diffusion of cations, oxidation will take place internally in the alloy matrix [35]. Internal oxidation may result in a rapid decline of physical properties within a material and unlike some external oxides, will provide no protective action [44]. The process continues unhindered until a critical mole fraction of oxide in the alloy is reached obstructing further oxygen diffusion into the matrix [35].

The necessary prerequisites for internal oxidation are as follows [12];

1. $\Delta G^{\circ}(BO_{\upsilon})$, the free formation of solute metal oxide $< \Delta G^{\circ}$, the free formation of the base metal oxide. Thus ΔG° for solute metal oxide must be more negative than that of the base metal oxide.

2. ΔG for the reaction, $B + \upsilon O = BO_{\upsilon}$. Therefore, the base metal must have a sufficient solubility and diffusivity for oxygen to establish the minimum required activity of oxygen at the reaction front.

3. Solute concentration of the alloy must be lower than the transition

4. Surface layer must allow for the dissolution of oxygen into the alloy at the start of oxidation.

Internal oxidation proceeds in the following manner. Oxygen arbitrates into the base metal through the external surface, or at the alloy-scale interface; if an external scale

is already present. The oxygen may then diffuse inward through the metal matrix establishing a reaction front. The critical activity product of $a_B a_O^v$ (the nucleation of precipitates), is established at this front through inward diffusion of oxygen and outward diffusion of solute. Nucleation of an oxide precipitate will procced and the precipitate will grow until the reaction front drives forward and the supply of solute B is depleted at the location. Subsequent precipitate growth occurs by Ostwald ripening. The mechanism of internal corrosion however is dependent on local concentrations and diffusivities of the oxygen and solute [44].

Ostwald ripening is the process of dissolution of small precipitates and deposition on the larger precipitates. The driving force is the difference in solubility between the small and large precipitates. Smaller precipitates have a higher radius of curvature and are thus more soluble than that of larger precipitates with a lower radius of curvature [45]. Ostwald ripening in this instance may be characterised by a constant volume rate; diffusion-controlled ripening [46] [22].

The growth of internal oxidation zones is assumed to approximately follow parabolic kinetics. The composition and structure of the internal oxide evolves as the reaction proceeds and thus, the oxidation rate kinetics often deviate from simple rate equations [35]. Oxygen will dissolve in the alloy phase and the oxide will constitute the least noble alloying component. The presumed process is governed by lattice diffusion of reactants in the metal matrix. The study of internal oxidation is complex and quantitative descriptions are arduous [35].

2.2.12 Kinetics of Internal Oxidation

The kinetics of internal oxidation may be derived for a planar specimen employing the quasi-steady state approximation. The quasi-steady approximation necessitates the assumption that the arbitrated oxygen concentration varies linearly across the zone of internal oxidation. Due to the linear variation, oxygen flux through the internal oxidation zone (IOZ) can be given by Fick's first law [19],

$$J = \frac{dm}{dt} = D_O \frac{N_O^{(S)}}{X V_m} (molcm^{-2}s^{-1}) \tag{48}$$

Where,

$N_O^{(S)}$ is the oxygen solubility in A $(atom\ fraction)$

V_m is the molar volume of solvent metal or alloy $(cm^3 mol^{-1})$

D_O is diffusivity of oxygen in A $(cm^3 s^{-1})$

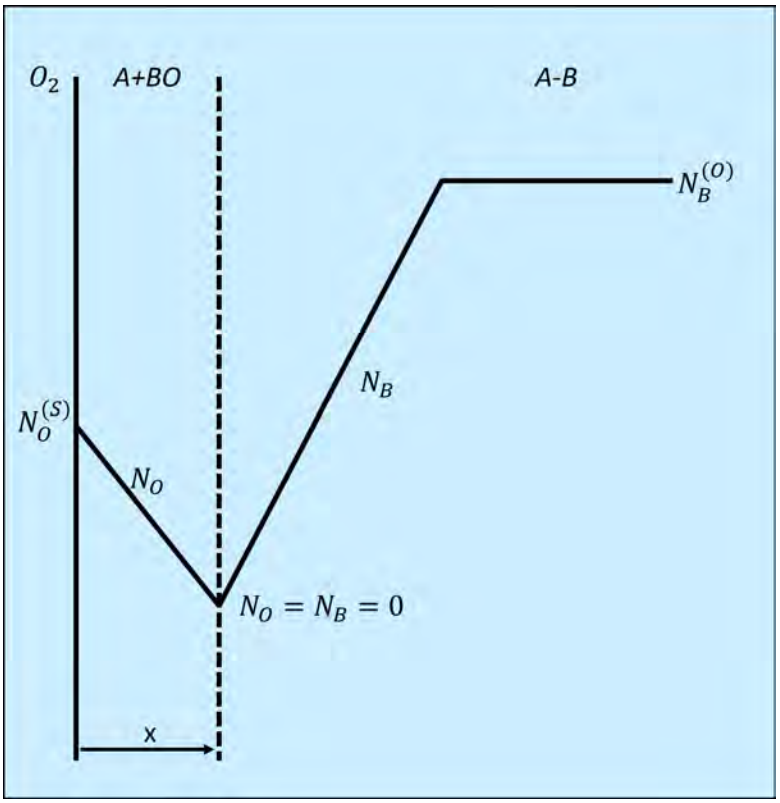

Figure 6: Concentration profiles

If counter-diffusion of solute B is assumed to be negligible, the amount of oxygen accumulated within the IOZ per unit area of reaction front is given by [19],

$$m = \frac{N_B^{(O)} \upsilon X}{V_m} (molcm^{-2}) \tag{49}$$

Where,

$N_B^{(O)}$ is the initial solute concentration

Flux may then be given by

$$\frac{dm}{dt} = \frac{N_B^{(O)} \upsilon}{V_m} \frac{dX}{dt} \tag{50}$$

Equating and rearranging equations (49) and (50),

$$XdX = \frac{N_O^{(S)} D_O}{\upsilon N_B^{(O)}} dt \tag{51}$$

Whereby upon integration, the penetration depth of the IOZ may then be found,

$$X = \left[\frac{2N_O^{(S)} D_O}{\upsilon N_B^{(O)}} t \right]^{\frac{1}{2}} \tag{52}$$

Where the penetration depth has a parabolic time dependence,

$$X \propto t^{\frac{1}{2}} \tag{53}$$

Nonetheless this is often an oversimplification as the solubility of the product is rarely 0. Furthermore, diffusion through the IOZ may not be assumed to be set equal to bulk diffusion through the substrate lattice. Diffusion flux will be highly depend on the interfacial transport mechanisms which will vary depending on morphology and density of precipitates [44].

2.2.13 Precipitation

Precipitation of oxides with reactive solute metals is a phenomenon that occurs during internal oxidation [47]. The formation of precipitates may increase the number of crack initiation sites due to stresses generated upon its formation. At the outset, oxide precipitates form as unstrained particles and further develop into regions of highly strained precipitates during a morphological transformation [48] [49]. During precipitation growth dislocations and stacking faults may form around the precipitate due to mismatch in lattice orientations. [50]. An increased strain energy within the alloy matrix will thereby lead to embrittlement of the surface layer and deterioration of strength and creep resistance [44]. Nonetheless, precipitation hardening may also occur if the precipitates are finely distributed through the alloy matrix. Thus the importance of the solubility product of internal oxides is integral in order to prevent the degradation of the material and control of final properties [44] [30].
In order to understand the solubility product of oxides in a non-ideal solution the thermodynamics of reaction must first be understood. Consider the oxidation of a pure metal, $\propto$ phase, at a constant temperature and pressure [19],

$$nB^{\propto}(s) + \frac{\upsilon}{2}O_2(g) = B_nO_\upsilon(s) \tag{54}$$

With the standard free energy change of reaction [19],

$$\Delta G^0_{B_nO_\upsilon} = G^0_{B_nO_\upsilon} - nG^{0,\propto}_B - \frac{\upsilon}{2}G^0_{O_2} \tag{55}$$

Where,

$G^0_{B_nO_\upsilon}$ is the molar free energy of the oxide product,
$G^{0,\propto}_B$ is the molar free energy of the pure metal,
$G^0_{O_2}$ is the molar free energy of oxygen,
$\Delta G^0_{B_nO_\upsilon}$ is take as a linear function of temperature.

Deeming the oxidised metal as a solute element in a multi-component alloy A-B-M, where A represents a solvent more noble than B, and M is not involved in the reaction. B may then act as a β phase producing an internal precipitate,

$$n\underline{B}^{\beta} + v\underline{O} = B_nO_v \tag{56}$$

with the underscore signifying a solid solute.
The standard free energy of change will then equal [19],

$$\Delta G_{B_nO_v} = \mu_{B_nO_v} - n\mu_B^{\beta} - v\mu_O^{\beta} \tag{57}$$

Where,

$\mu_{B_nO_v}$ is the chemical potential of the oxide precipitate,
μ_B^{β} is the solute element of B,
μ_O^{β} is the solute element of O.

The chemical potentials may be found respectively,

$$\mu_{B_nO_v} = G^0_{B_nO_v} + RT \ln a_{B_nO_v} \tag{58}$$

$$\mu_B^{\beta} = G_B^{0,\beta} + RT \ln a_B^{\beta} \tag{59}$$

$$\mu_O^{\beta} = G_O^0 + RT \ln a_O \tag{60}$$

Where,

$a_{B_nO_v}$ is the activity of the oxide precipitate,
a_B^{β} is the activity of the solute element B,
a_O is the activity of the element O

The molar free energy of oxygen, $G_O^0 = \frac{1}{2}G_(O_2)^0$, and activity of oxygen, a_O, can be expressed in terms of oxygen partial pressure $p_(O_2)$ in atm,

$$a_O = (p_{O_2})^{\frac{1}{2}} \tag{61}$$

Leading to the chemical potential of solute oxygen, μ_O^{β},

$$\mu_O^{\beta} = \frac{1}{2}G^0_{O_2} + \frac{1}{2}RT \ln p_{O_2} \tag{62}$$

Substituting the chemical potentials from equations (58), (59) and (60) into the standard free energy equation, equation (57), yields,

$$\Delta G_{B_nO_v} = G_{B_nO_v} - nG_B^{0,\beta} - \frac{v}{2}G^0_{O_2} + RT \ln \frac{a_{B_nO_v}}{(a_B^{\beta})^n (p_{O_2})^{\frac{v}{2}}} \tag{63}$$

At equililbrium, the free energy of reaction is zero hence [19],

$$\frac{a_{B_nO_v}}{(a_B^{\beta})^n (p_{O_2})^{\frac{v}{2}}} = exp\left[\frac{\Delta G^0_{B_nO_v} + n(G_B^{0,\alpha} - G_B^{0,\beta})}{RT}\right] \tag{64}$$

If the oxide precipitate, B_nO_v, is considered as a pure stoichiometric compound, the activity of element B is related to concentration through,

$$a_B^\beta = \gamma_B^\beta N_B \tag{65}$$

Where,

N_B is the mole fraction of element B,

γ_B^β is the activity coefficient of B in regard to the specified standard state in β phase.

The mole fraction of solute oxygen, N_O, may be related to the partial pressure according to,

$$\gamma_O N_O = (p_{O_2}^{\frac{1}{2}}) \tag{66}$$

Thus the free energy of reaction at equilibrium may now be expressed as [19],

$$\frac{1}{(\gamma_B^\beta N_B)^n(\gamma_O N_O)^v} = exp\left[-\frac{\Delta G^0_{B_nO_v} + n(G_B^{0,\alpha} - G_B^{0,\beta})}{RT}\right] \tag{67}$$

Considering the solubility product of the oxide precipitate,

$$K_{sp(B_nO_v)} = (N_B)^n(N_O)^v \tag{68}$$

The free energy of reaction may be described as,

$$K_{sp(B_nO_v)} = \frac{1}{(\gamma_B^\beta N_B)^n(\gamma_O N_O)^v} exp\left[-\frac{\Delta G^0_{B_nO_v} + n(G_B^{0,\alpha} - G_B^{0,\beta})}{RT}\right] \tag{69}$$

At definitive temperature, the exponential becomes a constant independent of the alloy composition. The solubility product may also be considered a constant at specific temperatures, implying that the solution obeys Henry's law and both the activity coefficient γ_B^β and γ_O are constant. However, γ_B^β and γ_O are both functions of alloy composition. Thus, the effect of non-ideal behaviour on a solution of the solubility product, B_nO_v, is reliant on γ_B^β and γ_O composition dependence [19].

Precipitate in a dilute solution In a dilute solution, the activity coefficient of solute element B and O are expressed as a function of alloy composition in alloy (A-B-M) [19],

$$\ln \gamma_B^\beta = \ln \gamma_B^{0,\beta} + \varepsilon_B^B N_B + \varepsilon_B^M N_M + \varepsilon_B^O N_O \tag{70}$$

and

$$\ln \gamma_O = \ln \gamma_O^0 + \varepsilon_O^O N_O + \varepsilon_O^B N_B + \varepsilon_O^M N_M \tag{71}$$

Where [19],

ε_j^i and ε_i^i are the first-order iteration parameters governed by B and O.

$\ln \gamma_B^{0,\beta}$ and $\ln \gamma_O^0$ are the activity coefficients of solute B and O at infinite dilution

respectively.
At oxygen concentrations below 10^{-4}, $\varepsilon_B^O N_O$ and $\varepsilon_O^O N_O$ may be neglected.
Hence,

$$\ln \gamma_B^\beta = \ln \gamma_B^{0,\beta} + \varepsilon_B^B N_B + \varepsilon_B^M N_M \tag{72}$$

and

$$\ln \gamma_O = \ln \gamma_O^0 + \varepsilon_O^B N_B + \varepsilon_O^M N_M \tag{73}$$

Thus, solute interactions of oxide precipitates must be governed by the interaction parameters ε_B^M and ε_O^M.
To quantify the impact of alloying element M, on the solubility product, a parameter $\propto$ is introduced. The parameter $\propto$ is a ratio between the solubility product with and without alloying element M [19].

$$\propto = \frac{K_{sp(B_nO_\upsilon)A-B-M}}{K_{sp(B_nO_\upsilon)A-B}} = exp[-(n\varepsilon_B^M + \upsilon\varepsilon_O^M)N_M] \tag{74}$$

The closer value of $\propto$ to 1, the lower the impact of element M on the solubility. At 1, M will have no consequence on B_nO_υ. At $\propto < 1$, M will reduce the solubility product, enhancing precipitation of B_nO_υ in the alloy. When $\propto > 1$ M increases solubility thus, suppressing the precipitation of B_nO_υ [19].

Magnetite precipitation Under certain cooling regimes, oxide scale of commercial strip steels will thermodynamically decompose via a eutectoid reaction into iron and magnetite [50]. It has been shown that magnetite tends to precipitate during thermodynamic decomposition within the oxygen-rich area at the magnetite-wustite interface. It has also been shown that magnetite may precipitate at the wustite substrate interface of adherent oxide scales; this phenomenon produces a 'magnetite seam' [51]. The magnetite seam may be observed with a heavily serrated edge and rounded pores, implying that a row of continuous crystals have grown from the wustite-iron interface [50], shown in figure7. Nonetheless the formation of magnetite at an iron-wustite interface is thermodynamically highly improbable due to the higher stability of iron-rich wustite over oxygen-rich regions [50].
Thus, to explain this phenomenon, the formation mechanism of magnetite precipitates may be discussed. Regularly, the precipitation of magnetite occurs in epitaxy with wustite as a consequence of oxygen penetration beneath the oxide or due to localised decomposition of wustite [50]. Further mechanisms may include impurities, oxidation at an interface by de-cohesion, stress-induced nucleation or nucleation due to the presence of carbon [50] [52].
The region just below the surface of a steel will be enriched in micro alloying elements. The strain generated may lower the stability of the wustite phase, decomposing the wustite phase more readily and acting as a nucleation site for the magnetite precipitates [52].

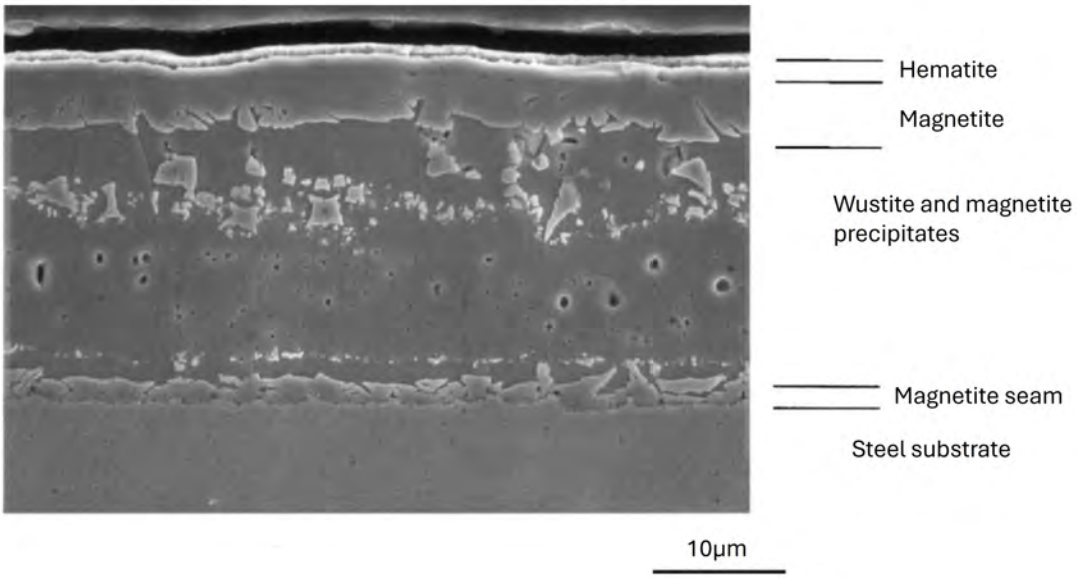

Figure 7: Typical structure of an iron oxide, showing a thin outer hematite layer, an intermediate magnetite layer, a thick inner wustite layer with magnetite precipitates and a magnetite seam at the scale-steel interface [53].

Precipitate morphology Many of the consequences of an IOZ are intimately related to the morphology of oxide precipitates. Precipitate morphology may influence mechanical and magnetic properties of an alloy. When considering the morphology of precipitates size, shape and distribution should be discussed.
Oxide particle size is determined by [26] [19],

1. The rate of nucleation as the internal oxidation front passes
2. The Ostwald ripening phenomena

Time will play a key factor in determining the size of precipitates. A precipitate will grow through the arrival of oxygen and solute at its surface. The longer the period of growth, the larger the precipitate. Nonetheless the longer the period of growth of a precipitate, the greater the depletion of solute within the surrounding area before the next nucleation event. Due to this phenomenon, factors which favour high nucleation rates will decrease precipitate size and those which favour high growth rates will increase precipitate size [54].
If nucleation is governed by the velocity of an oxidation front (aka., the rate at which a critical supersaturation front may be built) and growth is limited by time available for growth of a precipitate, size is therefore inversely proportional to the front velocity,

$$r \propto \frac{1}{\overrightarrow{v}} \tag{75}$$

Considering a planar specimen and the differentiated equation for flux, the velocity of a planar specimen may be given as [36],

$$\overrightarrow{v} = \frac{dX}{dt} = \frac{N_O^{(S)} D_O}{\upsilon N_B^{(O)}} \frac{1}{X} \tag{76}$$

Increasing temperature may have a negligible effect on nucleation rate however it has a greater effect on growth rate so that particle size increases with increasing temperature of internal oxidation [36]. As the penetration front increases, the velocity will markedly decrease, whereby the surrounding area will become so depleted of solute that no further nucleation will prevail. The decreased velocity of the supersaturated front results in the growth of elongated or needle-like oxide precipitates. Additionally, elongated precipitate formation is promoted by inward interfacial diffusion of oxygen along metal-oxide interfaces.

Nucleation is also greatly influenced by the particle-matrix interfacial free energy. Considering the classical free energy formation of a nucleus with radius r, neglecting strain [19],

$$\Delta G = 4\pi r^2\sigma + \frac{4}{3}\pi r^3 \Delta G_V \tag{77}$$

Where [19],

σ is the specific interfacial free energy,

ΔG_V is the free-energy change per unit volume of precipitate formation,

Nuclei with radius greater than r^* will be prone to spontaneous growth. Differentiating at point r^* yields,

$$\frac{d\Delta G}{dr} = 8\pi r^*\sigma + 4\pi r^{*2}\Delta G_V = 0 \tag{78}$$

Further solving for r^*,

$$r^* \frac{-2\sigma}{\Delta G_V} \tag{79}$$

The critical free energy of formation may then be calculated through simplification and substitution of r^*,

$$\Delta G^* = \frac{16}{3}\pi \frac{\sigma^3}{\Delta G_V^2} \tag{80}$$

Using the ΔG^* the absolute reaction-rate theory may be described as,

$$J = \omega C_O exp\left(-\frac{\Delta G^*}{RT}\right) \tag{81}$$

Where,

C_O is the concentration of reactant molecules,

ω is the frequency at which atoms are added to the critical nucleus.

The nucleation rate is therefore proportional to the exponential, $\exp\left(-\frac{\Delta G^*}{RT}\right)$, which is dependent on σ^3. Thus, particle size will increase with increasing σ. The influence of σ is also present in the coarsening of the particles where interfacial free energy is the driving force.

Lastly, the relative stability of the internal oxide, ΔG°, influences formation. The increased stability lowers ΔG_V, resulting in higher nucleation rates and smaller particles [36].

The size of internal oxide precipitates may therefore be determined by several fac-

tors [36] [19].

To influence the formation of a larger precipitate:

1. A deeper front penetration, X
2. High solute concentrations, $N_B^{(O)}$
3. Lower pO_2
4. Higher temperatures, T
5. Higher particle-matrix interfacial free energies,
6. Low oxide precipitate stability

Transition to External Oxidation Internal oxidation is sustained until a critical value of mole fraction in the alloy is reached [47]. The point at which the initial solute concentration reaches the critical value, the penetration velocity of the internal oxidation zone will fall below the minimal threshold needed to sustain it. The outward diffusion of solute is sufficient to produce an outer layer, halting internal oxidation [19].

2.2.14 Formation of External Scales

The formation of external scales is an extraordinarily broad subject area, making an exhaustive literature review on the subject impractical. Thus, this section aims to complete a short but detailed overview of the topic.
The composition of external scale formation will be dependent on that of the alloy's composition. Atmosphere will further influence scale composition, nonetheless, in order to avoid convolution only regular atmosphere will be regarded here.
External oxidation is commonly accompanied, simultaneously by internal oxidation [6]. As previously discussed, the transition from internal oxidation to external oxidation is dependent on a critical volume fraction of internal oxide precipitates. Above this critical volume fraction the oxide will transition to external oxidation.
In a simple binary alloy containing A-B, were B is the less noble element, oxides AO and BO will form. After an initial reaction period the following cases may be considered [19].

- If the binary alloy composition is near that of pure A, AO will form almost exclusively
- If a high concentration of B is present, BO will form almost exclusively.
- In the instance of an intermediate composition, both AO and BO will form.

In the latter case that both AO and BO form, a variety of alternative situations may arise depending on the properties of AO and BO [19],

- If the 2 oxides are completely miscible, they will form an oxide solid solution
- If the oxides are immiscible, they will separate
- If it lowers the energy of the system, the oxides may react to form another oxide product such as ABO_2

The complexity of the situation further increases with ternary and multi-phase systems. The least noble element may be selectively oxidised at high concentrations. Nonetheless the number of possible reactions increases exponentially when this element is present at lower concentrations. Thermodynamic software may aid in the prediction of behaviour of such complex systems however its not always entirely accurate and thus cannot be fully relied on [19].

2.2.15 Oxide Adherence

Regulating the adherence of an oxide layer to the underlying steel substrate is pivotal for in determining the final use and ultimate quality of a steel product. In many instances oxide adherence is essential for ensuring long-term performance and durability of a steel product [55]. Adherent oxide layers can as a barrier protecting the underlying steel substrate [56]. Protection from corrosion of Fe-Cr alloys is attributed to the formation of a dense adherent chromia layer. Selective oxidation of alloying elements such as Cr, Si, Al, Mn can produce adherent and protective oxide layers [55]. Nonetheless in other instances adherent oxide layers can be extremely detrimental, creating surface defects and decreasing the wettability of the steel surface for final coatings.

The adherence of the oxide to the underlying steel substrate is maintained by plastic readjustment of the oxide scale [6]. Oxide morphology, including its thickness, roughness and microstructure, will significantly influence the adherence of an oxide layer. A well-developed oxide layer with a dense and uniform structure will adhere strongly to a substrate compared to a porous or unevenly formed oxide [53]. Wustite and magnetite demonstrate notable plasticity and maintain strong adhesion to steel, primarily because of their chemical compatibility and robust inter-facial bonding with Fe. Nonetheless, voids and cavities often develop via vacancy condensation within the oxide, leading to potential failure. When the oxide/metal interface experiences critical vacancy supersaturation, void formation can occur, followed by potential further condensation, ultimately jeopardising the oxide's integrity [56].

The geometry of a specimen significantly affects the adherence of an oxide layer. Failure of the oxide layer commonly occurs at corners or edges due to the geometric limitations imposed by the three-dimensional structure of the scale. Stress concentrations localise at corners and edges due to deformation constraints. Plastic flow is hindered, and stress distribution is disrupted, creating a high stress gradient [57]. Elevated stresses adversely affect both the mechanical integrity of the oxide and its adhesion.

Thermal stresses and growth stresses will also negatively impact oxide adherence. Thermal stresses are caused by the differential expansion and contraction between the

oxide layer and underlying substrate [57]. The difference in thermal coefficients creates mismatched lattice strains at the interface, leading to the accumulation of internal stresses. Consequently, voids, gaps, or discontinuities may form at the oxide-substrate interface, ultimately causing the detachment of the oxide from the substrate [58]. Additionally, as the oxide layer expands, internal stresses and void formation may further compromise its integrity and adherence to the substrate.

2.2.16 Oxide Defects

Oxidation can give rise to a myriad of issues and defects throughout the manufacturing stages of steel, encompassing casting, rolling, forging, heat treatment, and final product coating. These defects, stemming from oxides on steel surfaces, can profoundly impact material performance, reliability, and service life. From surface imperfections to internal structural weaknesses, the consequences of oxide-related defects reverberate across the entire lifecycle of steel products, affecting their mechanical properties, dimensional accuracy, and overall quality. Comprehensive understanding of oxide defects is imperative for effectively managing and mitigating oxidation-induced issues, which are pivotal for maintaining the integrity and durability of steel components.

Inclusions Oxide inclusions are the incorporation of an oxide particle or cluster that is embedded within a metal matrix. Inclusions can vary widely in terms of their size, shape, and chemical composition, and they are typically formed during the production or processing of steel [36]. They can originate from various sources, including impurities present in the raw materials used for steel making, degradation of refractory materials used in furnaces or ladles during metal processing, or oxidation reactions occurring during high-temperature processing stages [59]. In addition to acting as stress concentration points within the metal matrix, oxide inclusions can also influence other properties of the steel. For example, they can affect the mechanical properties, machinability, and corrosion resistance of the metal [59]. Moreover, the presence of oxide inclusions can impact the cleanliness and homogeneity of the steel, which are critical factors in determining its overall quality and performance.

Internal Oxidation Internal oxide precipitates are formed when oxygen diffuses into an alloy, causing selective oxidation of one or more alloying elements [35]. While the formation of internal oxide layers is discussed in 2.2.12, their impact on steel performance remains unexplored. These internal oxide precipitates or layers disrupt the continuity of the steel matrix, compromising its structural integrity [60]. Stress concentration occurs notably at the interfaces between the oxide and the surrounding metal, further exacerbated by the relative brittleness of the oxide layers compared to the surrounding matrix. These stress concentrations heighten the susceptibility to deformation, fracture, and fatigue failure within the steel matrix. Additionally, internal oxide layers can induce inter-granular fracture by weakening the bond between adjacent

grains, facilitating crack propagation along grain boundaries [60]. Moreover, the process of internal oxidation results in sub-surface depletion of alloying elements, leading to disparities in the mechanical properties of the steel matrix.

Blister Blister is a defect attributed to a localised loss of adhesion between the oxide and underlying substrate. High temperatures will result in the swelling of surface scale producing a bubble like feature [61]. Blisters can subsequently become embedded in the steel substrate during hot rolling in the finishing mill. This defect, known as rolled-in scale, poses significant challenges in various industries, leading to machinery wear, decreased customer satisfaction, inferior surface finish, material loss, and reduced profits. Despite its prevalence, many aspects of blister formation remain poorly understood [62]. Therefore, this thesis aims to investigate blister formation mechanisms to enhance comprehension of compositional effects.

2.2.17 Methods of Investigation

The study of high-temperature oxidation takes many forms, often with a predominant focus on understanding the kinetics of oxidation. Beyond kinetics, investigations are also conducted to explore oxidation mechanisms, aiming to clarify the nature of the oxidation process.

Kinetics Thermogravimetric analysis (TGA) is a valuable technique that is often employed in oxidation studies to ascertain the kinetics of reaction [63]. During TGA, the mass of a sample is continuously recorded against a specified time-temperature programme. TGA is used to characterise materials that experience mass gain/loss related to oxidation, decomposition, and dehydration [63]. As oxidation occurs, the sample undergoes a chemical reaction resulting in weight changes. The rate and extent of mass changes can be used to calculate several important parameters. The rate of oxidation can be determined by analysing the gradient of the mass loss curve. Onset temperature can be deduced using TGA data, which is the temperature at which the oxidation reaction expeditiously begins. Activation energy can be calculated using TGA data through the Arrhenius equation, which relates the reaction rate to temperature and activation energy [64]. Activation energy provides critical insights into the energy barrier required for oxidation. Furthermore, TGA data can be used to determine the reaction order of the oxidation process, which describes the dependence of the reaction rate on the concentration of reactants Burling.

Phase Identification In the past, conventional metallographic sample preparation and examination have been used to identify phases present in the oxide scale. Optical and scanning electron microscopy are typically used for identifying oxide phases, however these methods are not an accurate way to correctly identify oxide phases as it is not correlated to the crystal structure of the phases [6].

Electron Backscatter Diffraction (EBSD) is a powerful microscopy technique used to analyse the crystallographic structure and orientation of a materials microstructure [65]. EBSD involves directing a beam of highly focused electrons onto a sample surface, causing a number of the electrons to be scattered and backscattered. Some of the electrons will then be identified by a detector, which is typically composed of a phosphor screen and a charge coupled device camera. The electrons will produce Kikuchi patterns which are the electron diffraction patterns [66]. The patterns contain a large amount of information regarding the crystal structure of a phase such as d-spacing, lattice parameters and crystal planes [67].
In steel alloys EBSD can easily distinguish hematite from the other crystalline structures in the oxide phase due to its trigonal crystal structure. Nonetheless Fe(BCC), wustite and magnetite all have cubic structures. In such cases, the identification of these phases hinges upon disparities in their lattice parameters [6]. EBSD is a powerful and versatile tool enabling the identification of phases within oxidised materials by analysing crystallographic orientations, distinguishing between different phases like oxides, intermetallic compounds, and residual unoxidised material. EBSD also facilitates the characterisation of grain growth and morphological changes during oxidation, offering insights into mechanisms such as coalescence and coarsening. Additionally, it aids in texture analysis by revealing material anisotropy, which is crucial for understanding mechanical, thermal, and electrical behaviours of oxidised materials. EBSD's ability to identify phase boundaries and interfaces is essential for comprehending microstructural evolution and mechanical properties [65]. Nonetheless EBSD requires meticulous sample preparation and a conductive surface. Oxide samples are usually fragile and prone to degradation, making preparation for EBSD arduous and time consuming [6].
Energy-Dispersive X-ray Spectroscopy (EDS) and Wavelength-Dispersive X-ray Spectroscopy (WDS) are additional techniques that can be used in conjunction with EBSD to provide a comprehensive overview of the composition, structure and properties of an oxide. EDS detects X-rays emitted by a sample when it is bombarded by a focused beam of electrons [68]. The incoming beam can energize an electron within an inner shell, displacing it from its shell and generating an electron hole. Subsequently, an electron from an outer shell may occupy this vacancy, emitting an X-ray in the process. An energy dispersive spectrometer can measure the quantity and energy of these emitted X-rays from a sample, allowing for the determination of its elemental composition [68]. WDS also relies on the emission of X-rays however a crystal will diffract the wavelengths producing a diffraction pattern and the wavelength is then calculated using Braggs law. WDS typically offers a higher spectral resolution (5 eV) compared to EDS (over 100 eV) [69]. Nonetheless, WDS data collection is slower than EDS due to the sequential monitoring of individual elements in WDS, while EDS can simultaneously gather a spectrum of all elements present in the sample [69]. EDS is particularly useful for elemental mapping and surface analysis, while WDS excels in accurate quantitative analysis and resolving complex spectra in highly heterogeneous oxide samples.

Rapid Alloy Prototyping Rapid alloy prototyping (RAP) is a versatile technique employed to swiftly evaluate the properties and characteristics of various alloy systems by expeditiously generating and analysing a diverse range of alloy compositions. It encompasses a spectrum of methodologies and approaches that enable the efficient exploration of new and innovative alloys. By systematically varying alloy compositions and analysing resulting properties, RAP facilitates the rapid identification of correlations between composition, microstructure, and material properties [70]. In contrast to conventional trial-and-error methods, RAP significantly diminishes the time and expenses associated with material development. It furnishes researchers with crucial data and insights early in the materials development phase, empowering informed decision-making regarding further investigation or optimisation of alloy compositions [70].
Bulk RAP involves the fabrication of alloy compositions in bulk form, featuring gradient compositions or systematic variations in alloying elements. This technique enables the coverage of a broad spectrum of compositions in a single experiment. Combinatorial synthesis or high-throughput screening systems are commonly employed to produce bulk RAP samples [70].
Powder rapid alloy prototyping (RAP), involves the synthesis of alloy compositions in powder form, followed by compaction and additional processing. An advantage of powder RAP lies in its ability to precisely regulate processing conditions, including temperature, pressure, and atmosphere. This methodology offers flexibility in swiftly exploring a diverse spectrum of alloy compositions while presenting opportunities for customising microstructures and properties [71]. This thesis aims to explore the application of powder RAP oxide studies related to silicon (Si), manganese (Mn), and molybdenum (Mo), and their impact on oxidation rates and oxide morphology.

3 Objectives

Oxidation within hot-strip mills severely impacts the surface quality of strip products, resulting in numerous defects, cutbacks, customer rejections, and potential litigations. The tertiary scale, generated prior to the finishing mill, is particularly concerning due to the severity of defects it induces. This scale often fractures and becomes embedded during rolling, leading to rolled-in scale defects. In low-alloyed steels, tertiary scale typically comprises a multiphase, three-layered iron oxide structure. However, in advanced high-strength steels with additional alloying elements like Mn, Si, and Mo, oxide morphologies can vary, complicating the understanding of their effects on scale formation and adhesion. To address this complexity, a rapid alloy prototyping (RAP) approach is employed to assess the impact of common alloying elements on overall scale formation, as detailed in Chapter 5. Subsequently, investigations into pertinent industrial steel grades aim to comprehend oxidation rates and scale formation within the hot-strip mill, leading to predictions of temperature regimes and oxidation rates to optimise surface quality and throughput for hot rolling.

Blister formation, a prevalent issue stemming from tertiary scale, occurs due to oxide growth, resulting in surface scale swelling at elevated temperatures. Despite being a catastrophic defect, the mechanisms underlying blister formation remain poorly understood, motivating further investigation as outlined in Chapter 7. Furthermore, the final morphology and composition of external scale are influenced by coiling temperatures, while internal oxidation, suspected to exacerbate post-hot coiling, remains under-explored. To address these gaps, plant trials in Chapter 8 aim to elucidate the impact of coiling temperature on internal oxidation, crucial for strip steels' mechanical, magnetic properties, surface appearance, and processing characteristics. Through these endeavours, a comprehensive understanding of oxidation effects in hot-strip mills can be attained, paving the way for improved surface quality, productivity, and overall performance of steel products.

Aims

The fundamental ambition of this thesis is to assess the effects of chemical composition, temperature and elapsed time reaction on scale formation of ultra-advanced high strength steels and high strength steels. The control of oxidation rates and oxide morphology are focal points of interest along with the evolution and formation mechanisms of scale morphology with time and temperature.

The following objectives of each chapter are as follows:

Chapter 5 - Oxidation of Rapid Alloy Prototyping Samples Chapter 5 aims to determine the influence of Mn, Si and Mo on oxidation rates, morphology and oxide thickness. The effect of Si on passivation and the critical temperature of oxidation are of great importance. A principal goal is to determine the best RAP composition from an industrial standpoint.

Chapter 6 - Oxidation of Industrial Steels Chapter 6 aims to assess the effect of temperature on the rate of oxidation for 5 industrial steel grades. The steel grade with the lowest rate of oxidation is of great interest and how the rate of oxidation is effected by increasing temperature.

Chapter 7 - External Oxidation Blistering Chapter 7 aims to determine the formation mechanism of blister for 3 industrial steel grades. The effect of temperature and time on blister formation along with the severity of the blister are of utmost importance.

Chapter 8 - Industrial Optimisation of Internal Oxidation Chapter 8 aims to investigate the effect of coiling temperature on internal oxidation of an electrical steel. The depth of internal oxidation and the cleanliness after hot-band annealing are of greatest concern.

4 Materials and Experimental Methods

4.1 Materials

The materials utilised in this thesis encompass both new and innovative alloys, as well as several relevant industrial steel grades. RAP samples were fabricated and subjected to oxidation in Chapter 5. Meanwhile, industrial steel grades in their original state were employed in Chapters 6, 7, and 8.

4.1.1 Materials for Chapter 5

Figure 8 schematically characterises the experimental process route used to produce the RAP samples for this work. The 20g process route selected amalgamates powder selection, weighing and compaction to produce crucibles which are then melted to produce an ingot. The ingot was then further heat treated and rolled to produce the final desired product. A key limitation of the 20g process route is the inability to repeat oxidation examinations due to limited material availability. Each RAP sample takes approximately 1.5 hours to produce and will undoubtedly have slight variations making repeats difficult and time consuming. Thus, only one sample was oxidised and produced for each composition.

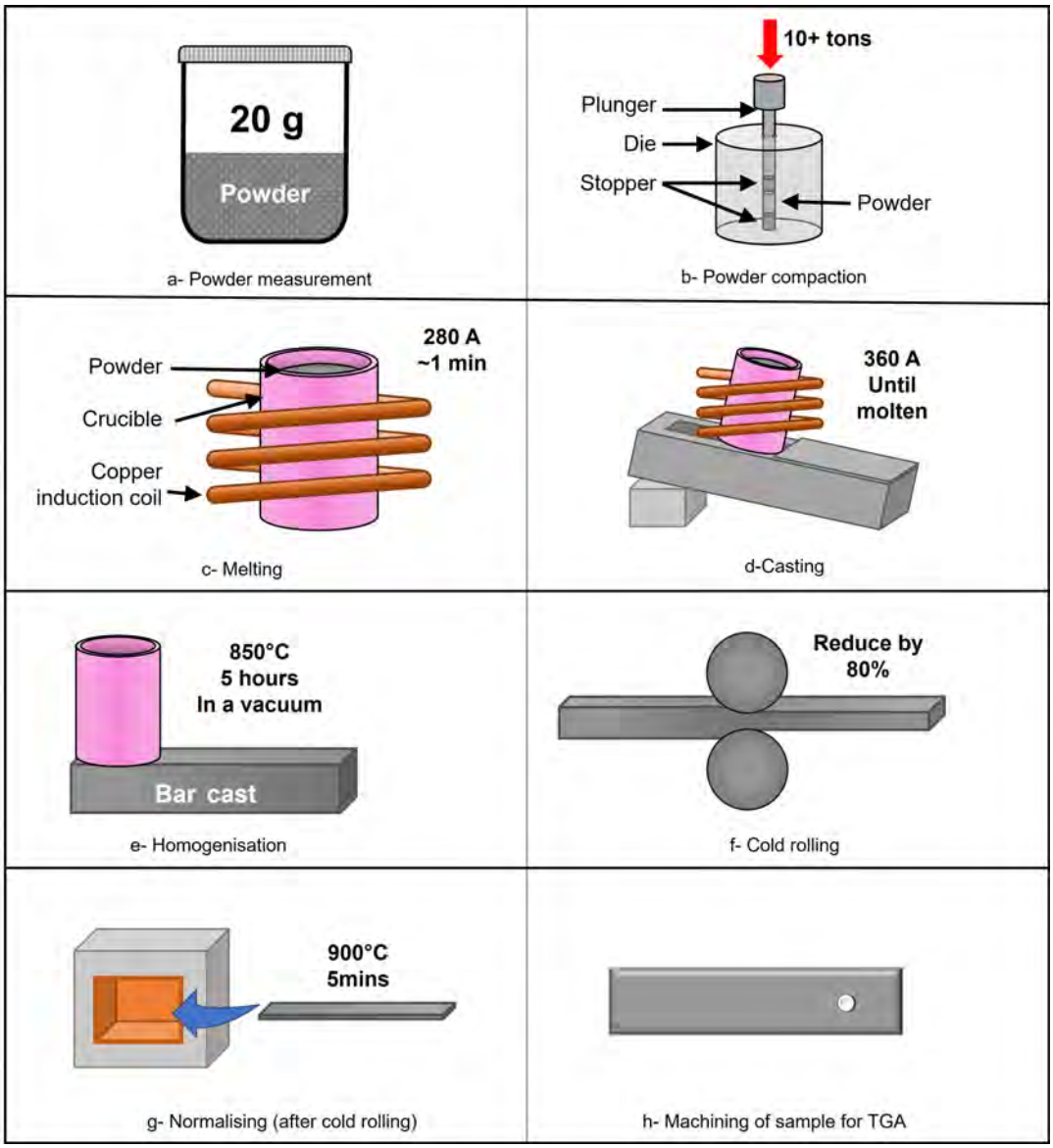

Figure 8: Process example for 20g RAP route

Weighing The elemental powders were weighed out on a high precision balance (OHAUS Pioneer PA214CM) and blended to 20g using a stoichiometric mix to produce the desired composition based upon wt %. With a precision of 1 mg on the balances, it was found that the composition error attributed to the weighing balance would be approximately 0.0067%, even for the lower 0.1 wt-% [72]. The error percentage for the target and measured mass of each sample produced is located in the appendix.

Element	Size (µm)	Purity (%)
Fe	450	99.000
C	75	99.997
Mn	150	99.500
Si	150	97.500
Mo	103	99.900

Table 1: Powder

Compaction The blended powders underwent dry compaction utilising a 25 kN Tinius-Olson compression testing rig, applying a force of 20 kN. This process resulted in the formation of a pellet measuring 12 mm in diameter and 20 mm in length. Dry compaction is a crucial step in rapid alloy prototyping, as it facilitates the consolidation of the powder mixture into a solid form, ensuring uniformity and integrity of the sample for subsequent processing and characterisation.

Casting The compacted pellets were carefully positioned within a 30 / 12 mm diameter alumina crucible. Induction heating was then employed within an argon atmosphere characterised by an exceptionally low oxygen content ranging from 1 to 10 ppm. This controlled environment ensured minimal oxidation during the melting process. Induction heating allowed for the rapid and uniform heating of the pellets, ensuring thorough melting and homogenisation of the alloy composition [72]. The molten alloy was subsequently cast into solid samples. Final composition of the sample is checked using OES.

Rolling After the casting process, the ingots undergo a crucial step of homogenisation within a vacuum furnace, where they are subjected to 24 hours of treatment at 1200°C. This extended duration ensures the uniform distribution of alloying elements and the elimination of any residual stresses or inhomogeneities within the ingots. Subsequently, the homogenised ingots are allowed to cool gradually within the furnace, promoting controlled solidification and minimising the risk of thermal stresses.
For further processing, the cooled ingots are subjected to rolling operations using a cold roller. Reduction to 80% of the original thickness is employed in this process, aiming to achieve a final thickness of approximately 2 mm. However, it should be noted that achieving a reduction to 2 mm thickness may not be feasible for all compositions due to variations in material properties, such as brittleness. In such cases, adjustments may be required in the rolling parameters to accommodate the specific characteristics of each alloy composition. This meticulous process ensures the production of uniform, high-quality samples suitable for subsequent characterisation and analysis in the context of rapid alloy prototyping.

4.1.2 Materials for Chapter 6

Chapter 6 delved into the kinetics of six distinct steel compositions, as detailed in Table 2. These compositions were obtained directly from Tata Steel Europe. The steel samples underwent casting and hot rolling at Port Talbot, Tata Steel Europe as per standard procedures and conditions. Samples were taken after hot rolling then cut and prepared for further investigation.

	C	Si	Mn	Al	Cr
Interstitial Free	0.004	0.019	0.1	0.004	-
Low Carbon	0.047	0.019	0.23	0.036	-
3812	0.15	0.1	0.86	0.036	0.028
S63	0.08	0.15	1.14	0.026	0.37
DP800 Hyperform	0.155	0.4	2.032	0.589	0.028
B32	0.003	3.2	0.2	0.9	-

Table 2: Compositions of steel grades received from Tata Steel Europe for chapter 6 (wt%)

4.1.3 Materials for Chapter 7

Chapter 7 examined the occurrence of blister formation on three distinct steel compositions, detailed in Table 3. These compositions were procured directly from Tata Steel Europe and underwent casting and hot rolling at Port Talbot, Tata Steel Europe, following standard procedures. Following hot rolling, samples were extracted, sectioned, and readied for further analysis.

	C	Si	Mn	Al	Cr
3812	0.150	0.100	0.860	0.036	0.028
DP800 Hyperform	0.155	0.440	2.032	0.589	0.028
B32	0.003	3.200	0.200	0.900	-

Table 3: Composition of steels grades investigated within this chapter as recieved from Tata Steel Europe (wt%)

4.1.4 Materials for Chapter 8

Chapter 8 explored the influence of coiling temperature on the development of internal oxide precipitates in the steel composition detailed in Table 4. This steel was acquired directly from Tata Steel Europe and underwent casting and hot rolling at Port Talbot, Tata Steel Europe, adhering to standard protocols. Subsequently, hot-rolled coiled samples were obtained post-casting and hot rolling, while hot-band annealed samples were extracted from the same coils after intermediate annealing and pickling at Surahammar Bruks Sweden, Tata Steel Europe.

	C	Si	Mn	Al
B32	0.003	3.2	0.2	0.9

Table 4: Composition of B32 steel investigated within chapter 8, from Tata Steel Europe (wt%)

4.2 Experimental Methods

A variety of experimental methods were utilised in this thesis including, thermogravimetric analysis (TGA), field emission gun-scanning electron microscopy (FEG-SEM), wavelength dispersive spectroscopy (WDS), electron dispersive spectroscopy (EDS) and electron back-scatter diffraction (EBSD).

4.2.1 TGA

Experimental procedures involved oxidation experiments conducted with a thermogravimetric analyser (TGA), shown in figure 9, comprising a vertical tube furnace (55mm bore, 450mm in length, 120mm uniform hot zone) and a micro-balance. The samples were loaded into the TGA, and the experiment involved subjecting them to controlled heating and monitoring their weight changes over time. Data points were recorded every 0.01 second reporting the mass and temperature. Temperature was monitored using a thermocouple placed in the middle of the tube furnace but not in direct contact with the sample. Specific heat treatments are noted in the individual experimental chapter.

Figure 9: TGA furnace used for conducing oxidation experiments

Sample Preparation The samples were machined and ground to a 120-grit surface using adhesive SiC paper to remove any previous oxidation. Sample size and geometry of specimens is noted in the individual experimental chapter. A hole was machined into the sample in order to hang them from the micro-balance in the TGA.

4.2.2 Characterisation

Sample Preparation Oxidised samples were cut in cross section and mounted in resin. Samples were backfilled with resin to maintain the oxide structures during standard grinding and polishing. Final polishing was done with OPS Colloidal silica before the surface was carbon coated with a depth of 10nm.

FEG-SEM Samples were observed using a JEOL JSM-7800F FEG-SEM. The JSM-7800F FEG-SEM incorporates 4 detectors including upper electron detector (UED), upper secondary electron detector (USD), backscattered electron detedctor (BED) and a lower electron detector (LED) [73].

(a) JEOL JSM-7800F machine

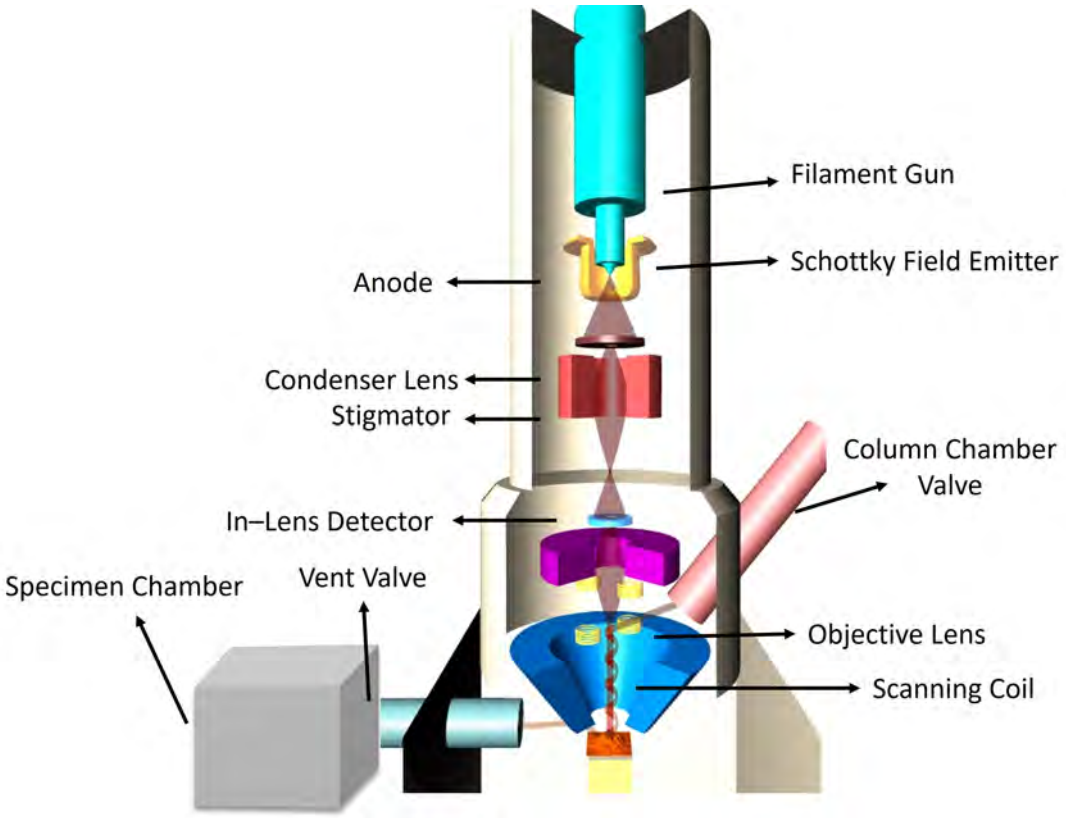

(b) Schematic diagram of a FEG-SEM

Figure 10: FEG-SEM configuration

BED channelling contrast was used the most frequently for analysis of samples. The low angled backscattered electrons allow for high contrast levels and contrast imaging of the samples. The JSM-7800F has a magnification ability of up to X1,000,000 [73]. Oxide precipitates shape and size, oxide thickness, oxide morphology and porosity considerations were some of the key features investigated using BSE.

Phase proportions, grain orientations and oxide chemistry were measured using EBSD, EDS and WDS respectively.

EBSD EBSD analysis was conducted using the JEOL JSM-7800F FEG-SEM. Tests were conducted to determine the phase constituents of the oxide using Kikuchi diffraction patterns. The optimal working distance was established at 18mm, with a 120 Hough resolution and 4*4 binning. Samples were tilted to a 70° angle, and an aperture of f/2 or f/3 was typically chosen. The step size ranged between 0.1-0.05 micron. A voltage of 20-15 kV and a probe current of 15 pA were typically set.

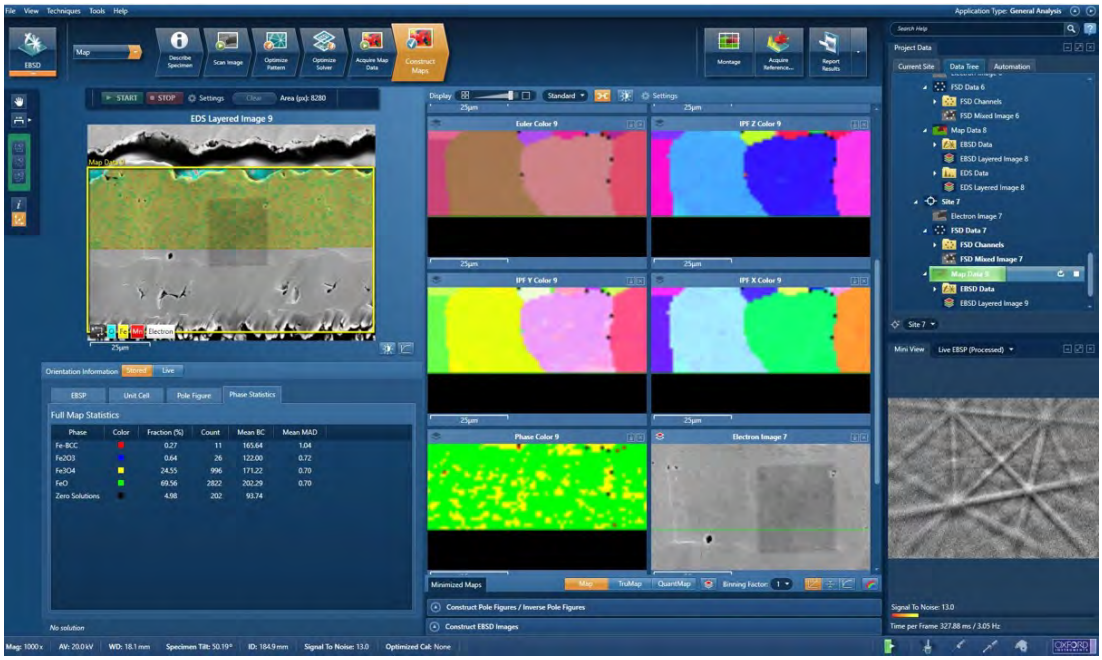

Figure 11: Capture of EBSD control interface and setup during scanning

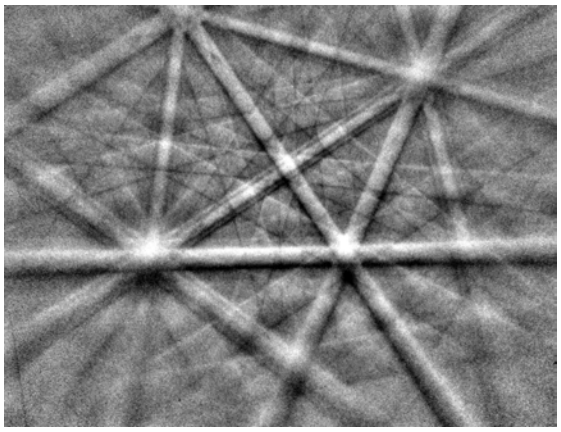

(a) Wustite

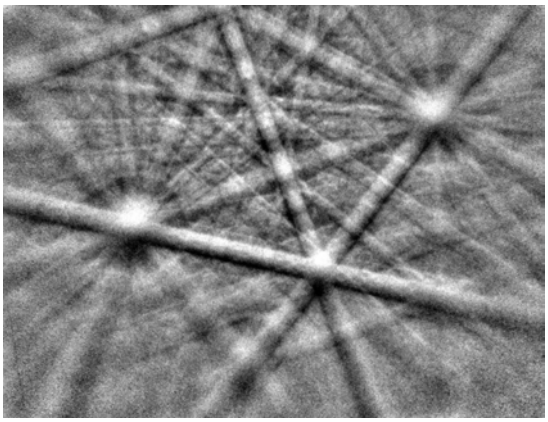

(b) Magnetite

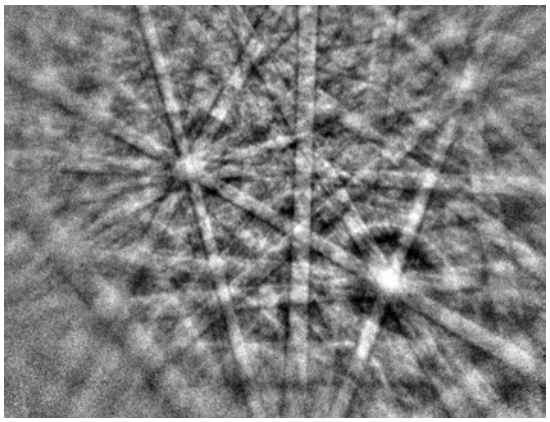

(c) Hematite

Figure 12: Kikuchi patterns captured and saved for referencing during EBSD analysis

WDS/ EDS Electron dispersive spectroscopy (EDS) and wavelength dispersive spectroscopy (WDS) are both techniques that were employed in order to deduce the chemical composition of the phase composition. EDS uses the energy of X-rays in order to deduce the elemental constituents. WDS will utilise X-ray diffraction and Braggs law to separate X-rays of different wavelengths in order to identify the elemental constituents. EDS will measure all X-ray energies simultaneously whereas WDS will measure each X-ray individually. WDS takes significantly longer than EDS to conduct. Nonetheless the spectral resolution and detection limit of trace elements in WDS is far superior to EDS. WDS can accurately identify oxygen wt% in an oxide in order to identify the specific oxide phase.

Analysis using WDS required high signal and probe current. An aperture of f/2 was used with a large probe current and high emission voltage. Background corrections were also conducted relative to the corresponding intensity of the reference material.

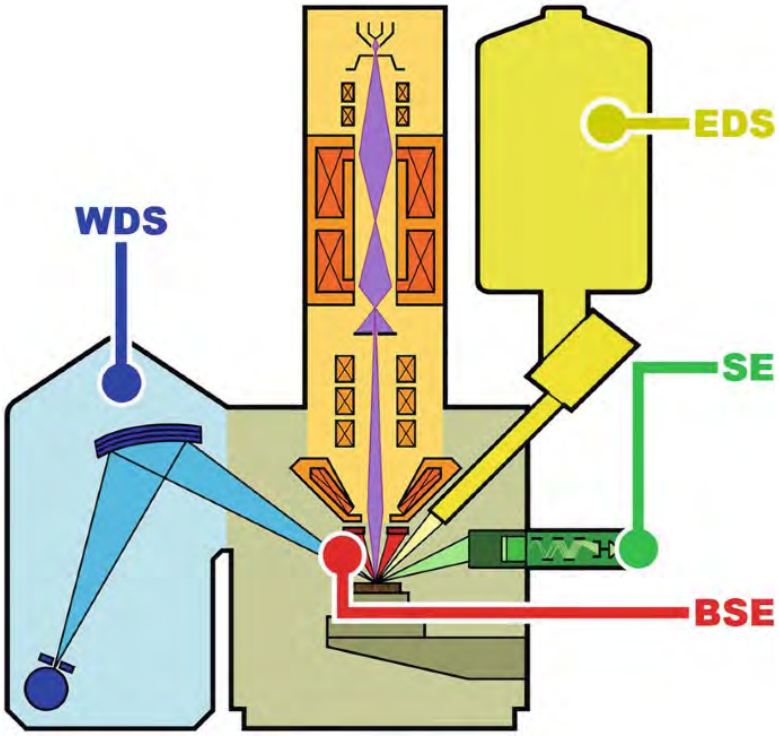

Figure 13: Schematic configuration of an EDS and WDS set-up

5 Oxidation of RAP Samples

5.1 Introduction

The classic iron oxidation system is a complex multiphase system formed of wustite, magnetite and hematite, producing multi-layered scales. Each phase will have independent properties such as thermal coefficients, growth rate and mechanical properties etc [6]. Furthermore, each additional alloying element will have different affinities for oxygen and different mobilities in the oxide phases, so that oxide morphologies are specific to alloy chemistry [19]. Due to the complexity of the multiplex steel alloy oxide, its hard to define the effect of each individual alloying element on the scale formation, adhesion etc. especially when they are interacting with one another. An approach using rapid alloy prototyping (RAP) was selected to help discern the effects of common alloying elements Mn, Si and Mo, on overall scale formation, using a wt% comparable to that seen in high strength industrial grades.

Ordinarily, developing a new alloy is a slow, iterative process, involving high cost and risk to a business. RAP offers a new methodology to efficiently produce and investigate new alloys at low cost and low risk. RAP incorporates a production and processing route from 20g up to 30kg, allowing for new imaginative alloy solutions to be tried and tested. The 20g route is the lowest weight route and assimilates powder, weighing and compaction. Compaction is required to reduce porosity before induction melting [74]. The samples are then melted using induction heating to produce a bar. They are then homogenised at temperature and rolled to the desired thickness. The 20g route allows for multiple samples to be produced quickly and comprehensively. Due to the length scale, it will not conventionally match a hot strip mill route (HSM) nor a finishing schedule reduction and due to the volume of material produced it does not allow for repeatability in comparison to larger scale routes. Nonetheless the 20g route is optimum for oxidation because it only requires a modest amount of material without the need for mechanical testing.

Simple alloying chemistries containing Si, Mn and Mo were developed due to their impact on oxidation and industrial relevance. For example, demand for electrical steels is increasing exponentially as the world transitions to more electrically powered devices with motors, generators, and transformers [75]. Electrical steels are used in the core of electromagnetic devices due to ferromagnetic properties derived from large additions of Si. The drawback is that high levels of Si lead to many deleterious surface defects and additionally make the steel brittle and difficult to work. These surface defects are largely contributed to the formation of fayalite, an oxide phase composed of iron and silicon. The formation of oxide phases associated with Si along with Mn and Mo will be investigated in this chapter and compared to industrial steel grades.

5.2 Experimental Methodologies

5.2.1 Samples

Compositions The RAP compositions produced for this chapter are shown in table 5. The error percentage for the target and measured mass of each sample is located in the appendix.

Sample	Fe	C	Mn	Si	Mo
0.5Mn	99.4	0.1	0.5		-
2Mn	97.9	0.1	2		-
2Mn-0.5Si	97.4	0.1	2	0.5	-
2Mn-1Si	96.9	0.1	2	1	-
2Mn-2Si	95.9	0.1	2	2	-
0.5Mn-0.5Mo	98.9	0.1	0.5	-	0.5
2Mn-0.25Mo	97.65	0.1	2	-	0.25
2Mn-0.5Mo	97.4	0.1	2	-	0.5
2Mn-0.75Mo	97.15	0.1	2	-	0.75
2Mn-1Mo	96.9	0.1	2	-	1
2Mn-1Si-0.25Mo	96.65	0.1	2	1	0.25

Table 5: Composition of alloys produced and investigated via the 20g RAP route *(wt%)*

5.2.2 TGA

Sample Preparation Final sample size and geometry of specimens produced via the 20g RAP route, shown in table 6.

	Width (mm)	Length (mm)	Thickness (mm)
0.5Mn	1.174	3.463	0.202
2Mn	1.2475	3.637	0.201
2Mn-0.5Si	1.12115	3.634	0.204
2Mn-1Si	1.3165	3.575	0.203
2Mn-2Si	1.316	3.63	0.276
0.5Mn-0.5Mo	1.172	6.139	0.146
2Mn-0.25Mo	1.161	6.992	0.139
2Mn-0.5Mo	1.203	6.177	0.142
2Mn-0.75Mo	1.141	6.125	0.148
2Mn-1Mo	1.117	5.961	0.150
2Mn-1Si-0.25Mo	1.176	5.915	0.156

Table 6: Sample size and geometry of specimens machined ready for TGA

Heat Treatment The samples were inserted into the furnace and subjected to continuous heating for 5 minutes and 30 seconds, with a heating rate of 3°C per second, reaching a maximum temperature of 950°C. The heat treatment was designed to discern how the RAP samples would kinetically perform at key temperatures used in a conventional hot-strip mill for rolling. The air velocity during treatment was maintained at 10

litres per minute. Following treatment, the sample was withdrawn from the furnace and allowed to cool in ambient air. Due to the limited material availability and difficulty in repeatability only one sample for each composition was oxidised and examined.

Geometry Effects Figure 14 displays a large, stitched BSE image of sample 2Mn-0.5Si. The sample was hung in a tube furnace in a vertical position. The oxide on top of the sample was extremely brittle, with large cracks travelling through the magnetite layer. The top oxide was thinner and less adherent compared to that of the oxide on the side of the sample. This was because the increased airflow coming through the top of the furnace has resulted in greater oxygen diffusion at the top. The increased oxygen diffusion has enriched the oxide resulting in a thick magnetite layer, making the oxide extremely brittle. The reduced thickness of the top oxide was due to the geometry and decreased surface area of the sample. All analysis has been conducted on the side of each RAP sample to ensure consistency and accuracy.

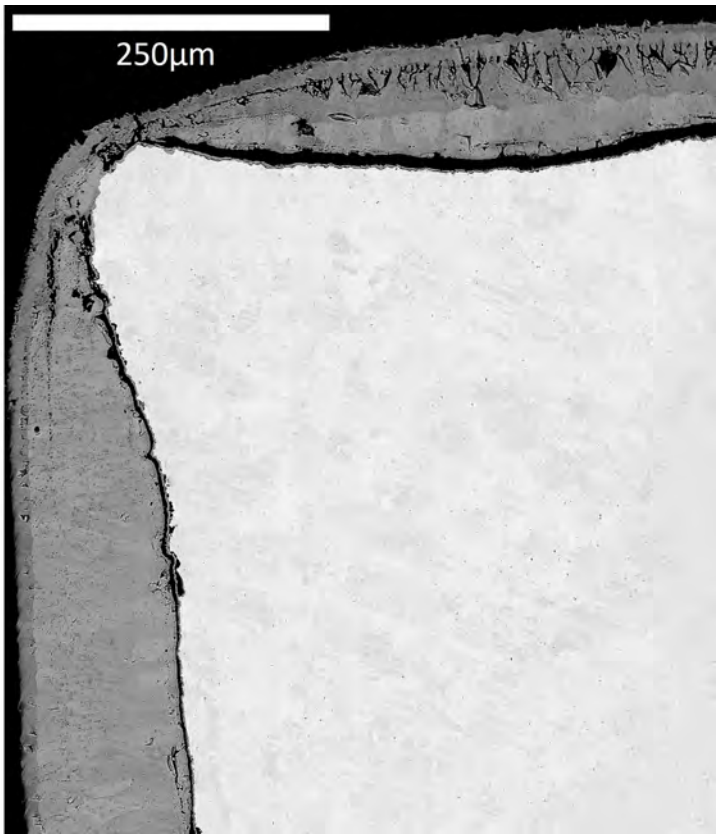

Figure 14: 2Mn-0.5Si Geometry Effect

5.3 Results and Discussion

The results and discussion in this chapter will be split and examined based on RAP composition. The first section will discuss Mn-Si, the second section will discuss Mn-Mo and the third section will discuss Mn-Si-Mo.

5.3.1 0.5Mn

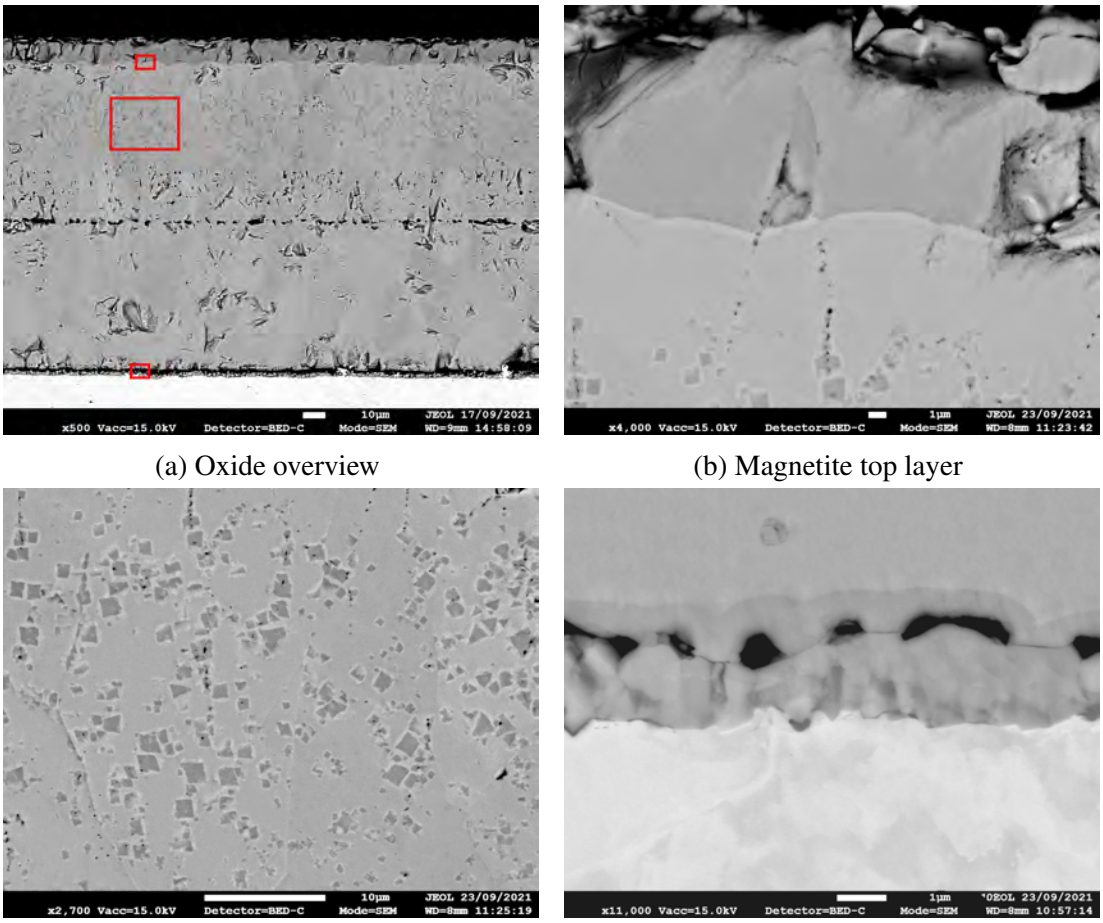

(a) Oxide overview

(b) Magnetite top layer

(c) Magnetite precipitates

(d) Magnetite seam

Figure 15: 0.5Mn Oxide Morphology a) A detailed examination of the oxide through thickness reveals three distinct regions: a dark outer layer identified as magnetite, a thick light grey middle section of wustite with cuboid magnetite precipitates, and a fractured magnetite seam connecting the bulk wustite to the steel matrix b) The outermost oxide layer consists of magnetite attached to the bulk wustite, along with pro-eutectoid magnetite precipitates and vertical lines of porosity extending from the wustite into the outer magnetite layer c) The bulk of the oxide matrix, comprised of wustite with varying sizes of magnetite precipitates d) A magnetite oxide seam attached to the steel substrate, featuring large voids and a lateral crack

Morphology The oxide morphology of the 0.5Mn sample as seen in figure 15, presents as a typical iron oxide consisting of 3 well established oxide layers (refer to literature review figure 7). The oxide thickness was very consistent throughout the sample and was found to be around 148µm. This was considerably higher than any of the other RAP compositions later investigated. The oxide was very continuous and adherent in

nature with a distinct magnetite seam throughout. The thickness of the magnetite seam in figure 15d was 2.63µm and the magnetite top layer, seen in figure 15b, was 11.26µm. Micro-voids and porosity were present within the magnetite seam in figure 15d, creating a line of weakness to which a crack can be seen traversing through. In figure 15a the bulk oxide can be observed to begin detaching at the magnetite seam due to this traversing crack however remains altogether adherent.
Precipitation of magnetite developed predominantly in the top half of the oxide. In figure 15c there was a considerable variance in precipitate size, with the largest reaching over 2µm across and the smallest being 5nm. There was no discernable internal oxidation.

			Wt%		
		Region	Fe	O	Mn
Spectrum	1	Oxide top band	70.46	29.54	
	2	Oxide top band	69.89	30.11	
	3	Oxide bulk top	67.80	23.26	*8.94*
	4	Oxide bulk top	72.65	26.60	0.75
	5	Precipitate	71.02	28.98	
	6	Precipitate	70.66	29.34	
	7	Oxide bulk top	72.09	27.19	0.72
	8	Precipitate	70.19	29.50	0.31
	9	Oxide bulk mid	72.75	26.71	0.54
	10	Oxide bulk mid	72.46	26.99	0.55
	11	Oxide bulk base	72.72	25.64	1.64
	12	Oxide seam	66.02	23.30	*10.16*
	13	Oxide seam	87.65	11.46	0.88
	14	Base Matrix	99.53	0.00	0.47

(a) WDS Points

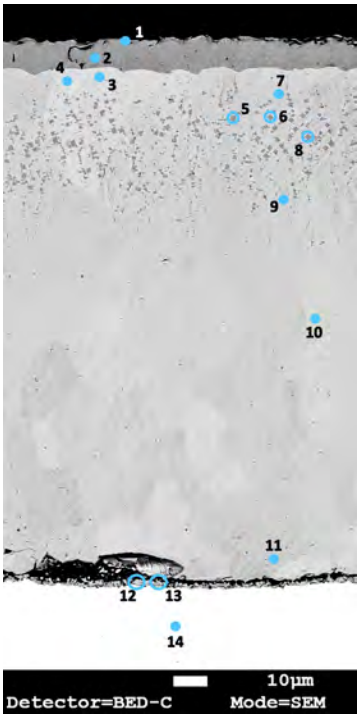

(b) Reference Image

Figure 16: WDS Spectra and reference image for RAP composition 0.5Mn- WDS analysis was performed on a cross-section of the oxide, moving from the outer edge towards the oxide/metal interface to assess its composition in relation to depth *(Highlighted cells EDS)*

WDS WDS spectra of RAP sample 0.5Mn was conducted concurrently throughout the sample. Spectra 14 in figure 16, shows the base matrix was not dissimilar to that of the anticipated composition using RAP. This demonstrates that the 20g RAP route was successful in producing the required alloy composition. Spectra 1 and 2 are within the oxide top band and have a higher oxygen wt.% than any other spectra. The high O concentration and dark contrast of the backscatter image therefore confirm that this was the anticipated magnetite phase. The precipitates in spectra 5, 6 and 8, also have a high oxygen wt.% of roughly 29wt.%. This in addition to the contrast of the backscatter image affirm the presence of pro-eutectoid magnetite precipitates.
Within these magnetite phases there was no presence of Mn, however its present within

the wustite phase. Spectra 4 and 7, taken inside the top region of the wustite phase, show 0.75 and 0.72 wt.% Mn respectively. Spectra 9 and 10, taken towards the middle of the wustite phase, show a slightly lower volume at 0.55wt.%, nonetheless this was still notably higher than that of the base alloy composition. Towards the base of the wustite phase the presence of Mn was further increased at 1.64wt.%. The presence of Mn within the wustite phase was possible because of the fast outward diffusion of Mn [76]. MnO and FeO both have a halite crystal structure with 6 bonds to oxygen, forming a mixture of edge and corner sharing octahedra bonds [77]. Thus Mn^{2+} may displace the Fe^{2+} from FeO forming a $(Fe_{1-x},Mn_x)O$ solid solution, with $0 < x < 1$. The Mn cations dissolved in Wustite will segregate predominately at the scale surface accounting for the increased concentration of Mn towards the base of the Mn [47].
The concentration of oxygen fluctuates throughout the thickness of the wustite. The Fe:O ratio of wustite intrinsically declines as it approaches the outer interface adjoining with magnetite [78]. This increase of oxygen throughout the wustite phase can be observed in spectra 11, 10 and 7 as it increases from 25.64, 26.99 and 27.19 wt.% respectively. The intrinsic stoichiometry gradient also highlights a reduction in the volume of wustite with an increasing distance from the iron substrate [78].

5.3.2 2Mn

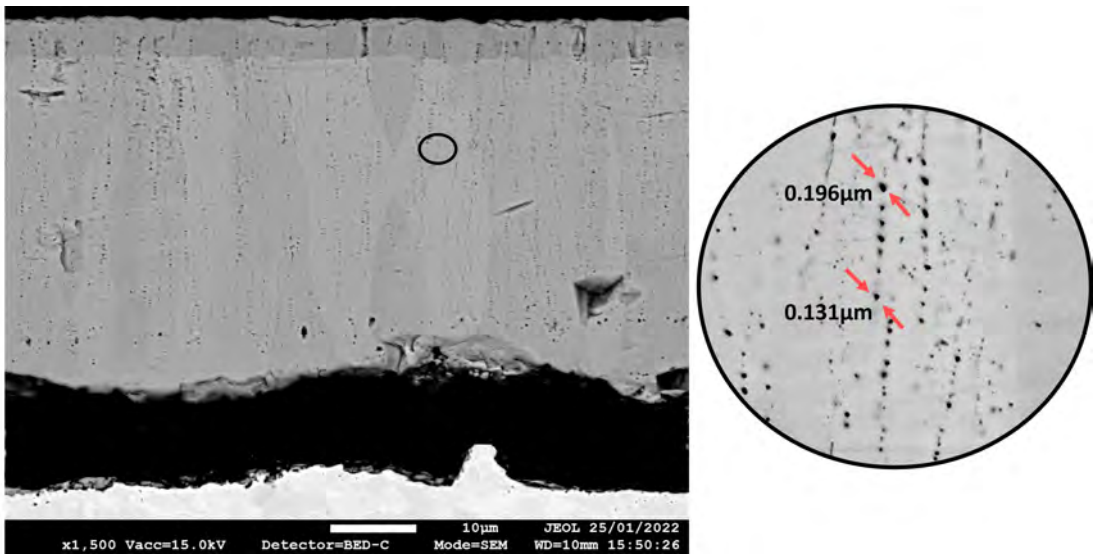

Figure 17: Oxide morphology overview for 2Mn, highlighting the porosity present within the columnar wustite grains - Oxide is broadly in-adherent with the underlying substrate, small internal oxide precipitates are present within the steel close to the metal/ oxide interface (dark spots in internal oxidation zone)

Morphology Its immediately apparent that the oxide morphology of 2Mn, in figure 18a, differs greatly from that of 0.5Mn in figure 15. The additional Mn has produced a substantially thinner oxide of 43.84µm, over 3x thinner than that of the previous sample. The magnetite top layer was also substantially thinner at 4.98µm in comparison to

11.26µm. The magnetite seam was found to be inconsistent throughout the sample but once again was of a considerably lesser thickness. There were no magnetite precipitates present however the overall percentage of magnetite forming the oxide morphology was slightly higher due to the decreased thickness of the oxide. The wustite phase consisted of distinctive columnar grains that varied in both width and length.

			Wt%		
Spectrum		Region	Fe	O	Mn
	2	Top oxide band	67.26	29.94	
	3	Oxide matrix top	67.88	26.16	*2.92*
	4	Oxide matrix top	68.20	26.21	*2.82*
	5	Oxide matrix mid	67.54	26.20	*3.36*
	6	Oxide matrix bottom	68.63	25.43	*3.09*
	7	Oxide matrix bottom	68.25	25.90	*2.84*
	8	Oxide matrix bottom	68.68	25.07	*3.35*
	9	Oxide matrix bottom	68.26	25.89	*2.86*
	10	1µm into sample	95.99		1.33
	11	2µm into sample	94.85		1.01
	12	55µm into sample	94.60		1.59

(a) WDS point scan measurements

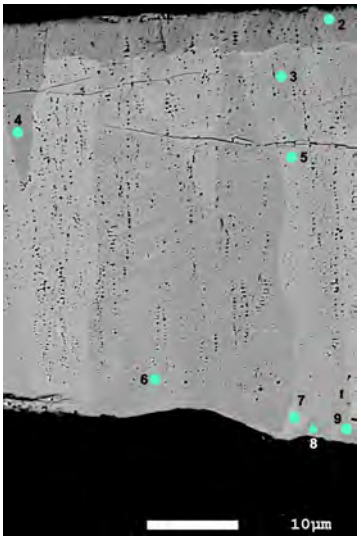

(b) WDS point scane reference images

Figure 18: WDS spectra and reference image for RAP composition 2Mn - WDS analysis was performed on a cross-section of the oxide, moving from the outer edge towards the oxide/metal interface to assess its composition in relation to depth *(Highlighted cells EDS)*

WDS WDS analysis confirms the presence of wustite in spectra 3-9. The oxygen content increases throughout the wustite from 25.07wt.% to 26.16wt.% in a stoichiometric gradient as the wustite approaches the outer magnetite layer. The higher Mn content has resulted in a greater volume of Mn in the wustite increasing the value of x in $(Fe_{1-x},Mn_x)O$. An increased presence of MnO has been found to increase the thermodynamic stability of the wustite phase [79].

Another pre-eminent difference was the formation of internal oxides in 2Mn, notable in figure 5.3.2. The internal oxide morphology of 2Mn was identified as spherical intragranular, with the size ranging from 50nm to 300nm. The depth of oxidation varied sporadically but was approximated at 4 µm. The density of the internal oxide precipitates was very sparse, and the composition composed entirely of MnO. The formation of internal oxide particles was expected due to the higher potential of Mn against Fe. Thermodynamics dictates that the increased reactivity of Mn will result in selective oxidation of Mn, producing internal oxides until a supersaturation limit was reached and oxidation transitions from internal to external [80].

A further distinction between the oxide in 2Mn and 0.5Mn was the large volume of porosity, discernible in figure 18a. Several micro-voids were visible in 0.5Mn however they are of far greater volume in 2Mn. The voids differ in size growing the largest

within the magnetite phase. The average size of these pores was found to be 0.03µm however they can be seen to grow as large as 0.5µm and start to coalesce towards the bottom of the wustite phase. The porosity within the magnetite phase was predominantly due to vacancy defects where iron interstitials will convert to iron vacancies. Porosity may develop due to the displacement of iron from the region [78] whereby the iron was displaced due to its large distance from the bulk steel. Magnetite consumption in the sublayer may also result in porosity, where cationic lattice diffusion of iron ions $Fe^{2+/3+}$ may arise in conjunction with oxygen diffusion through neutral vacancies [78]. The porosity within the wustite phase was also thought to be due to consumption. Evidence of wustite consumption was visible through the wustite phase in spectra 3-9, where the oxygen concentration increases resulting in a stoichiometric gradient and a cation-deficient environment. The porosity observable in figure 18 materialises in a columnar fashion with an increased presence towards the columnar wustite grain boundaries. This was thought to be due to the increased ease of lattice diffusion at the grain boundaries.

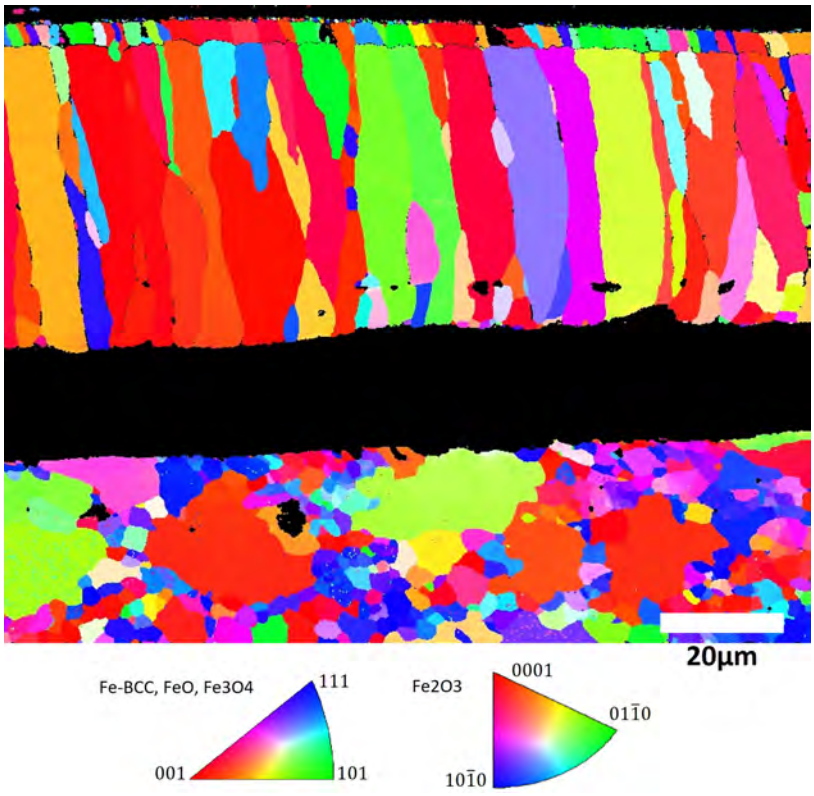

(a) Inverse pole figure-X Map

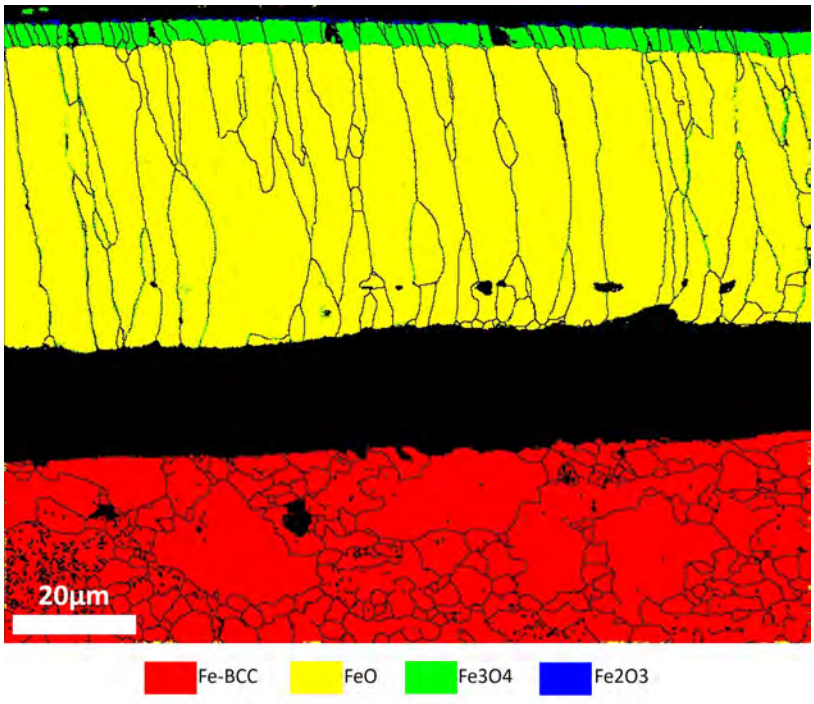

(b) EBSD phase map- Magnetite present at wustite columnar grain boundaries

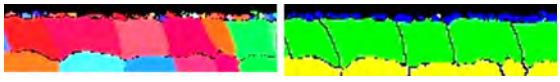

(c) Highlight of outer oxide showcasing thin outer hematite layer

Figure 19: Electron back-scatter diffraction of RAP composition 2Mn- The inverse pole figure X-map and EDS phase map with clearly defined columnar wustite grains, a top magnetite layer and a thin outer hematite layer

EBSD The EBSD phase map in figure 19b identified a thin hematite layer, approximately 1µm in thickness. Seams of magnetite are evident, running along the columnar wustite grain boundaries. Magnetite along the grain boundaries was evidence of oxygen enrichment, this may occur due to the increased ease of lattice diffusion at the grain boundaries. The presence of oxygen enrichment further supports the consumption of wustite (FeO) along the grain boundaries resulting in porosity, discussed previously in figure 18a. The magnetite and hematite layer consists of equiaxed grains unlike the wustite. The wustite grains exhibit columnar growth due to impingement of growth (see Appendix 127). Initially the grains will grow in random directions from the iron substrate however once they start impinging on one another growth direction in the vertical direction becomes preferential [81]. The wustite crystals in figure 19a are randomly oriented.

Blister Phenomena 2Mn was found to produce a very brittle and non-adherent oxide. Figure 20 show a very typical blister morphology. The surface morphology of 2Mn oxide was extremely rough in comparison to that of 0.5Mn. A relationship between deep internal oxidation and rougher surfaces has previously established by [82]. Blister and its formation mechanisms will be discussed in depth in chapter 7.

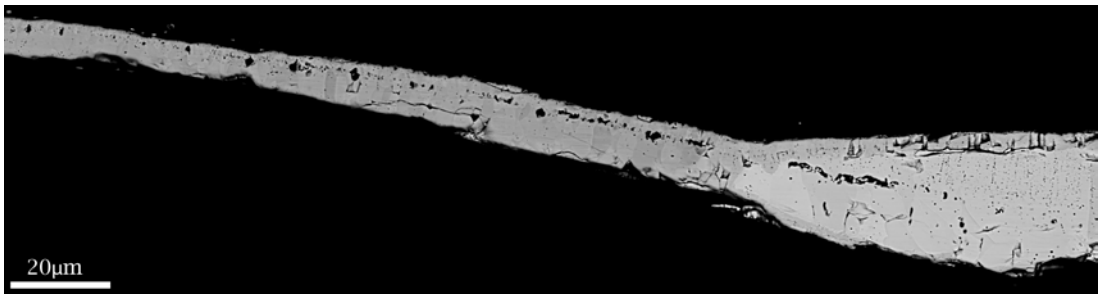

Figure 20: Blister formation on 2Mn

5.3.3 2Mn-0.5Si

Morphology The influence of introducing 0.5wt.% Si into the 2wt.% Mn alloy is depicted in Figure 21a, where it manifests as a characteristic iron oxide structure comprising three distinct oxide layers. Si is commonly incorporated into steel alloys to enhance their magnetic properties and impart oxidation resistance [83]. The incorporation of Si modifies the microstructure of steel, influencing its mechanical properties, such as strength and ductility [52].
The oxide morphology appears similar to that of 0.5Mn however there was one key difference. The oxide morphology in 0.5Mn may be referred to as a type-I morphology [52], where the scale contains primarily retained wustite and pro-eutectoid magnetite precipitates slightly beneath the magnetite layer. The oxide morphology of 2Mn-0.5Si was referred to as a type-II scale, containing magnetite precipitates adjacent to the magnetite seam and slightly beneath the magnetite layer [52].

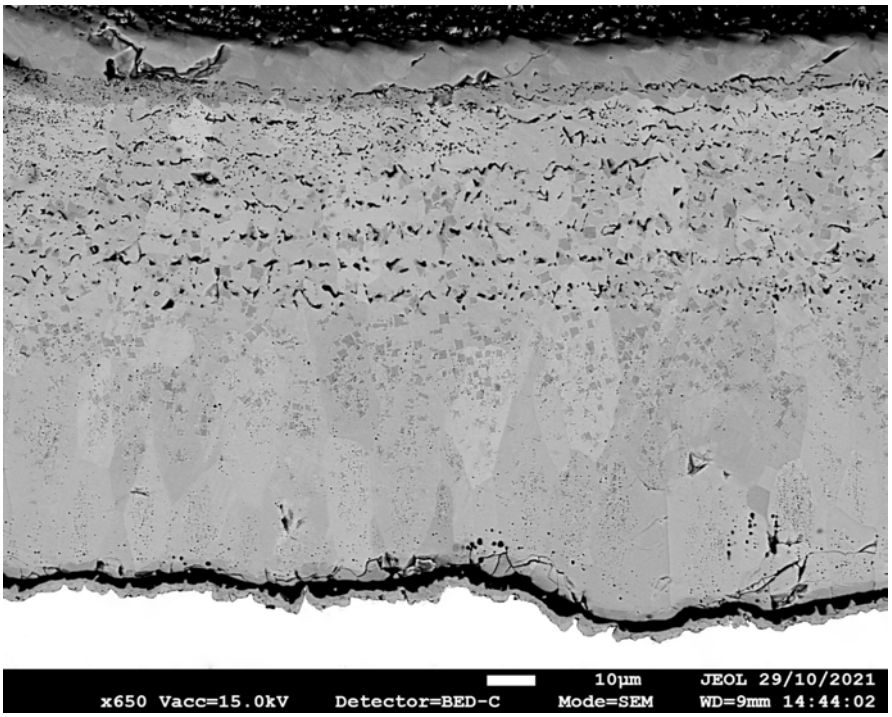

(a) Oxide Overview

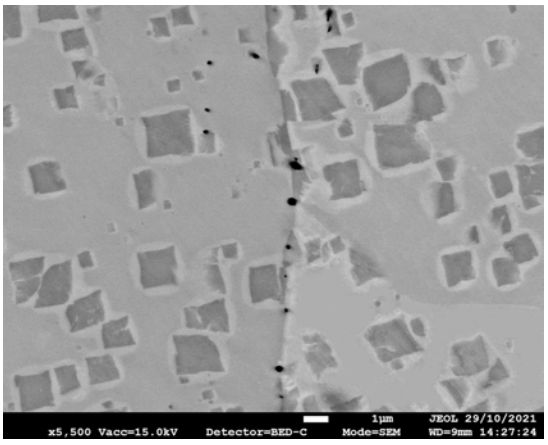

(b) Triple Point Grain Boundary

Figure 21: Through thickness oxide morphology for RAP composition 2Mn-0.5Si - A thick external oxide with clearly defined magnetite seam at the oxide/ metal interface, cuboid magnetite precipitates and large columnar wustite grains

The scale thickness was 117.80µm, the second largest of any of the RAP compositions. This may seem surprising due to the addition of Si, which commonly decreases oxidation, however upon retrospection the volume of Si was presumably too low and thus it is therefore postulated that a complete passivation layer was not formed (see Appendix 129 for Si EDS). The increased volume and thickness of the scale in 2Mn-0.5Si was remarkably more than that of 2Mn. It is presupposed that Si may of tied up a considerable volume of the Mn in a Mn_2SiO_4 phase. Mn possesses a unique ability to rapidly vary its valency state, allowing for high redox flexibility [52] [84] [85]. It has been found to tremendously accelerate the internal oxidation of alloys, allowing for fast diffusion along grain boundaries.

Several spherical internal oxides were observed, however they were not continuous in

nature and only went as deep as 1µm. The sporadic and intermittent internal oxides only served to moderately hinder cation diffusion. The incomplete passivation layer would have allowed for the selective dissolution of Fe to dominate, leading to an increase overall of oxidation kinetics. This effect was comparable to that observed in stainless steel, when an incomplete passivation layer results in an increase of oxidation [86].
The magnetite seam and top layer were 3.22µm and 15.05µm, respectively. The top layer of magnetite was the thickest of all the RAP compositions by a considerable margin. The considerable porosity within the upper half of the oxide was believed to be due to the consumption of wustite and thermal stress cracking upon cooling. The porosity within the top 15-20µm of wustite was composed of a considerable number of microvoids. Below this region the pores are far larger and appear to have coalesced, forming large pores and cracks in an almost banded structure. This band of porosity appears to repeat roughly every 6µm until it extends to the middle of the wustite phase, often surrounded by magnetite. Further into the wustite an increase in the number and density of magnetite precipitates was observed.
Figure 21a shows the interface between 3 wustite grain boundaries, commonly known as a triple point. The magnetite precipitates do not cross over into the neighboring grain, stopping at each of the grain boundaries. This was because the epitaxial growth of the proeutectoid magnetite precipitates was hindered at grain boundaries (see Appendix 128). The magnetite precipitates in 2Mn-0.5Si exhibit a classical faceted structure.

5.3.4 2Mn-1Si

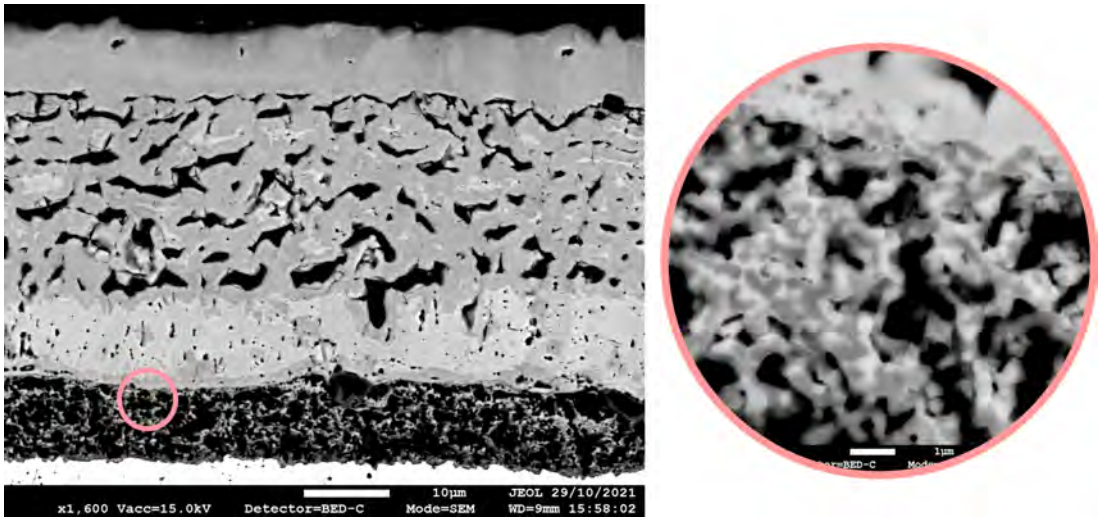

Figure 22: Oxide morphology for RAP composition 2Mn-1Si, highlighting brittle amorphous region located towards oxide/metal interface

Morphology The oxide morphology displayed by 2Mn-1Si, in figure 22, has a distinctive and distinguishable morphology compared to that of the previous RAP compositions. The bulk of the oxide was no longer formed of columnar wustite and was instead composed of a large porous magnetite phase with an amorphous phase between

the substrate and magnetite. There was still a distinctive magnetite top layer separated from the underlying magnetite by a harsh line of porosity and cracking. The magnetite above this region displays equiaxed grains, its accordingly presumed that the magnetite within this region developed first, and the remainder formed from the decomposition of the wustite phase resulting in the large volume of porosity. A small volume of retained wustite was still present towards the surface of the substrate. The retained wustite contained many micro-voids, and a small number of faceted magnetite precipitates. The presence of micro-voids and precipitates suggests that consumption of the phase began but was not completed; this could be due to several reasons. One plausible explanation was that the distance from the surface was too considerable, so the diffusion of oxygen was not great enough. Another was that the amorphous phase beneath has precipitated out a large volume of iron, creating an iron rich oxide band (see Appendix 131).
The amorphous phase present between the substrate and magnetite/ iron oxide was between 9-10 μm thick. Using EDS, the amorphous phase was found to be an amalgamation of Fe, Mn and Si oxides (see Appendix 130). The amorphous phase contains both a light and dark spinel, as seen in figure 22. The lighter spinel phase contained higher levels of iron and lower levels of Mn and Si. In both phases, the Si wt.% was found to be double that of the Mn wt.%. It was identified that the amorphous phase transitioned to more of the darker spinel phase as it approached the substrate. The composition of the amorphous phase will be discussed in the next RAP composition, 2Mn-2Si, with WDS data.
A continuous layer of internal oxidation formed beneath the oxide, penetrating the underlying substrate approximately 6.4μm. The total thickness of the external oxide was 52.99μm, a significant reduction compared to 2Mn-0.5Si.its therefore inferred that the RAP composition 2Mn-1Si produced a complete passivation layer, drastically reducing the external oxidation. A clear link can be established, through which greater internal oxidation will result in lesser external oxidation. Nonetheless it should be noted that a maximum internal oxidation depth will exist for each composition due to oxygens ability to diffuse through the substrate.

EBSD The EBSD maps shown in figure 23, struggled to characterise the amorphous oxide phase, owing to the porosity and brittleness of the phase. Nonetheless the remainder of the oxide was sufficiently characterised and showed a number of interesting trends.
The RAP composition 2Mn-0.5Si, contained a very prominent magnetite seam, however the phase map clearly displays that none was present within 2Mn-1Si, shown in 23b. The formation of a magnetite seam requires a gap between the steel substrate and outer oxide. The gap allows for the inward diffusion of oxygen whilst limiting the supply of iron at the interface, resulting in a proportion of higher oxides [87]. The absence of a magnetite seam may therefore be attributed to the increased adherence of the oxide to the substrate. Furthermore, both Si and Mn will be selectively oxidised before Fe and a richer supply of Si and Mn cations are available due to the close proximity of the

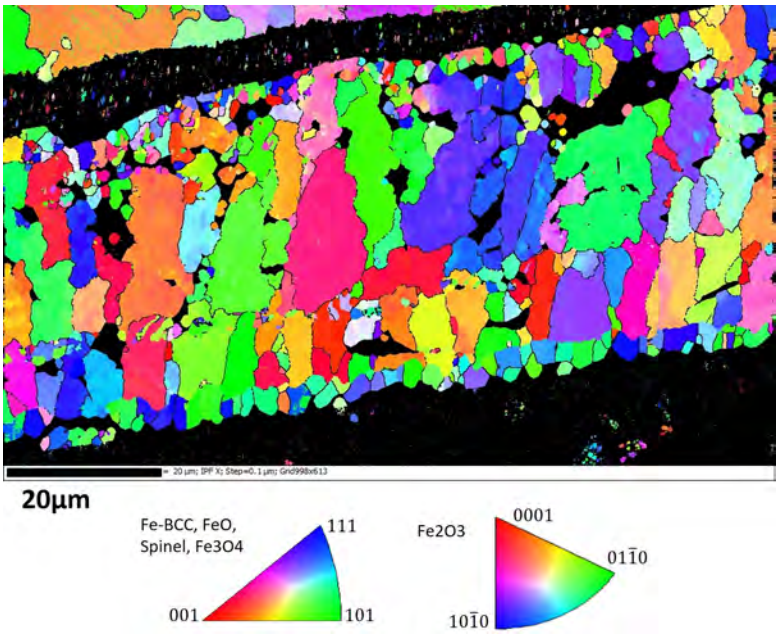

(a) Inverse pole figure-X map- Fe-BCC located at the top of the figure with the oxide located beneath

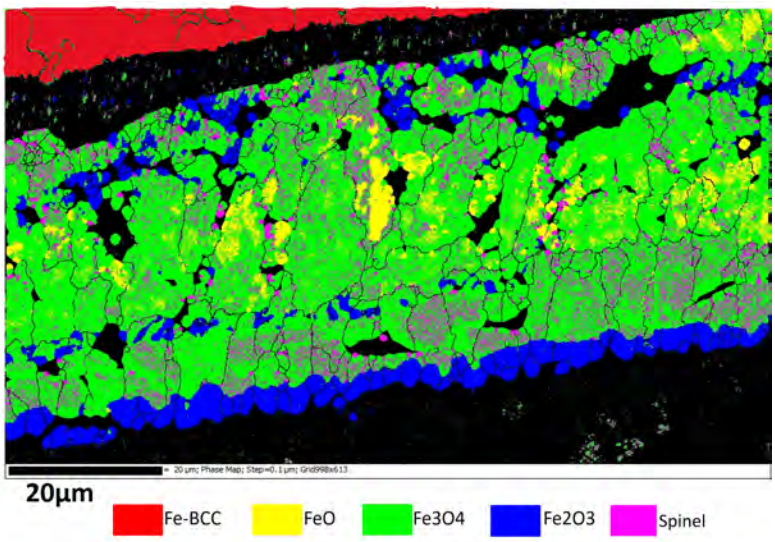

(b) EBSD phase map highlighting the complexity of the oxide produced for RAP composition 2Mn-1Si- Fe-BCC located at the top of the figure with the oxide phase present underneath

Figure 23: Electron back-scatter diffraction phase and IPF map for RAP composition 2Mn-1Si- showcasing an extremely convoluted oxide morphology with multiple oxide phases

substrate surface.

Above the amorphous phase, the IPF map 23a shows a small band of equiaxed magnetite grains, with a limited volume of grains transforming into hematite. The equiaxed grains show no preference of orientation, each appearing random. Its conjectured that this band of small equiaxed grains was the original steel surface. Large magnetite grains are displayed towards the middle of the phase map and once more, exhibit no predilection towards a specific orientation. Several of the large grains contain small islands of

retained wustite, noted previously in figure 22.
The EBSD phase map also identified a very definite hematite layer. The grains are very compacted and show an orientation preference between the $10\bar{1}0$ and $00\bar{1}0$ plane. The thickness of the hematite layer was approximately 3.5-5µm, far thicker than the hematite layer in 2Mn of 1µm. The increased thickness may be attributed to a number of factors, such as the formation of fayalite, found in both the amorphous and internal oxide phase. Fayalite has a lower thermal conductivity than that of the other oxide phases present [88].its plausible to assume that a lower thermal conductivity will bring about a reduction in the cooling rate of the surface, thus resulting in a rise of surface temperature for a prolonged period [88]. The formation of fayalite will also suppress the outward diffusion of Fe ions resulting in a richer oxide. Both of these factors in conjunction with one another will result in a thick hematite layer forming as the outer most scale.

5.3.5 2Mn-2Si

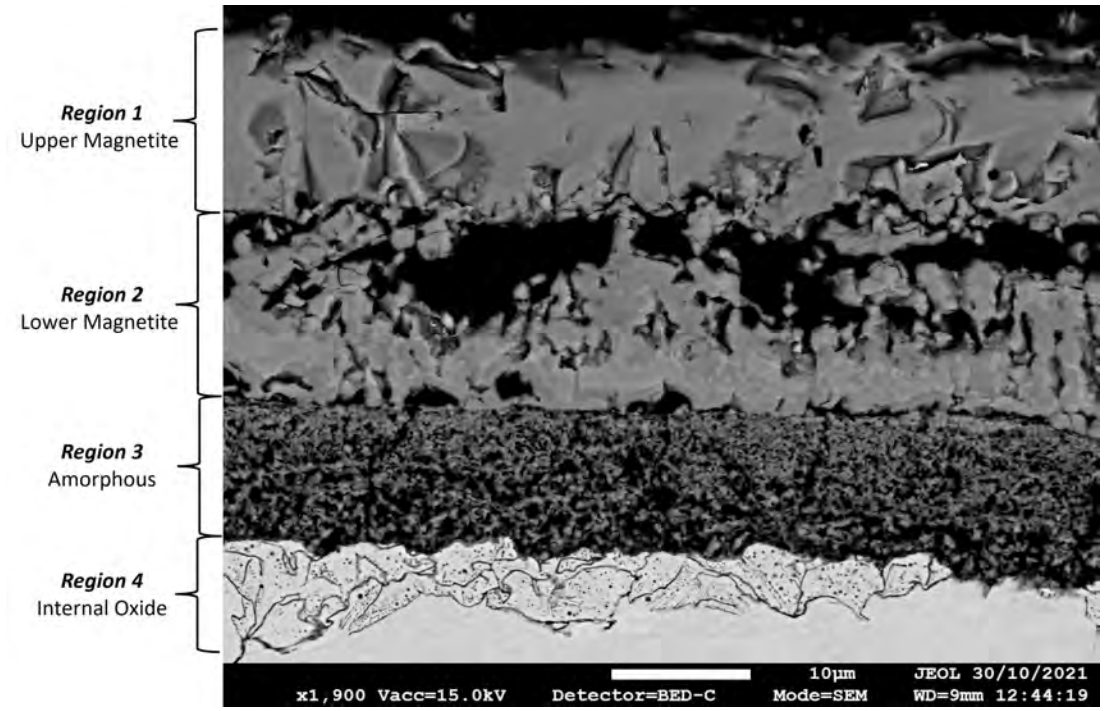

(a) The 4 Distinct Oxide Regions of 2Mn-2Si

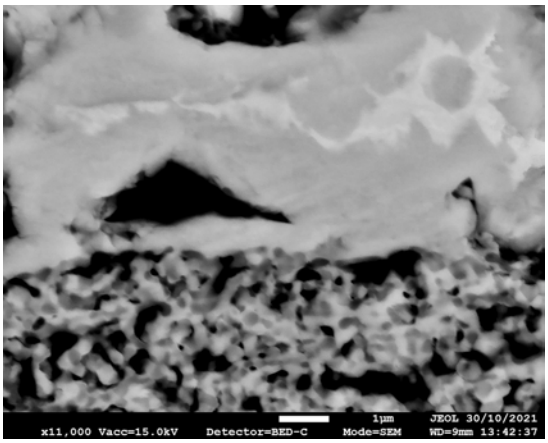

(b) Interface between the Lower Magnetite and the Amorphous Region with Retained Wustite

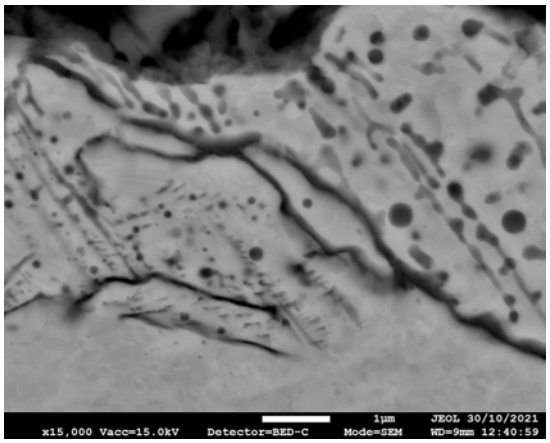

(c) Internal Oxide; Speherical intragranular, Film-like Intergranular, Pertrubed Intragranular Dendrites

Figure 24: Through thickness oxide morphology for RAP composition 2Mn-2Si

Morphology Figure 24 features the oxide morphology of sample 2Mn-2Si. The scale was profoundly convoluted, displaying 4 very distinctive regions, similar to those observed in 2Mn-1Si. The 4 distinct regions will now be categorised as;

1. Upper Magnetite
2. Lower Magnetite
3. Amorphous

4. Internal Oxide

Region 1 and 2 formed a significant proportion of the oxide and was composed of giant magnetite grains. The thickness of the magnetite region for 2Mn-2Si was considerably lower than that of 2Mn-1Si at approximately 27µm and 42µm respectively. The base of this region may be interpreted as the original steel surface; thus, region 1 and 2 can be treated as outer oxidation. Note, that this was separate to external oxidation, which was designated as scale above the substrate surface. Outer oxidation was therefore scale that has formed above the original substrate surface. Within region 1 of the magnetite there was no distinguishable wustite nor a distinctive top layer and there was a much lower volume of retained wustite. This was most likely due to the thinner oxide accelerating the rate of diffusion, increasing the number of higher oxides resulting in a more complete transformation of the wustite.
The islands of retained wustite within region 2 are smaller and more sporadic than those seen in 2Mn-1Si. Figure 24b reveals one of these small islands of retained wustite with a small proeutectoid magnetite precipitate forming within the center. The diffuse interface of the magnetite into the wustite was faceted (planar) producing rough and jagged edges [36]. The rough and jagged edges are a result of the low mobility of the coherent phase (magnetite). The growth of faceted phases was broadly characterised by the lateral movement of ledges across faceted interfaces [36].
The thickness of the amorphous phase in region 3 was very similar for both 2Mn-2Si and 2Mn-1Si at approximately 11µm and 10µm respectively (see Appendix 132). Even though both amorphous regions have a similar thickness, the characteristics they display are somewhat different. A stoichiometric gradient was visible in 2Mn-1Si with a transition from a lighter spinel to a darker spinel phase. This gradient was also visible within 2Mn-2Si however the transition occurs earlier on with a lower percentage of the lighter spinel phase present at the interface. The amorphous region of 2Mn-1Si was extensively more porous than that of 2Mn-2Si. The increased presence of the darker spinel was presumed to be due to the increase of Si.
The internal oxidation region was found to be similar for both 2Mn-2Si and 2Mn-1Si, with an average of approximately 6µm and a maximum penetration depth of 9µm. Nevertheless the density of the internal oxide zone was far greater for 2Mn-2Si with extensive grain and sub grain boundary oxidation.
The oxide thickness of 2Mn-2Si was only 43.5µm, substantially thinner than 2Mn-1si and the lowest of all 11 RAP compositions.Its postulated that the increased density of region 4 extensively hindered cation movement.

WDS The oxygen content in spectra 1-5, designated as oxide phase 1, was markedly higher than that of oxide phase 2 in spectra 6-8. The Fe:O ratio affirms that oxide phase 1 was magnetite and oxide phase 2 was wustite. Thus, the predominant oxide in region 1 was magnetite and region 2 was magnetite with small, retained islands of wustite. Mn had a significant presence within the magnetite and wustite phase, however there

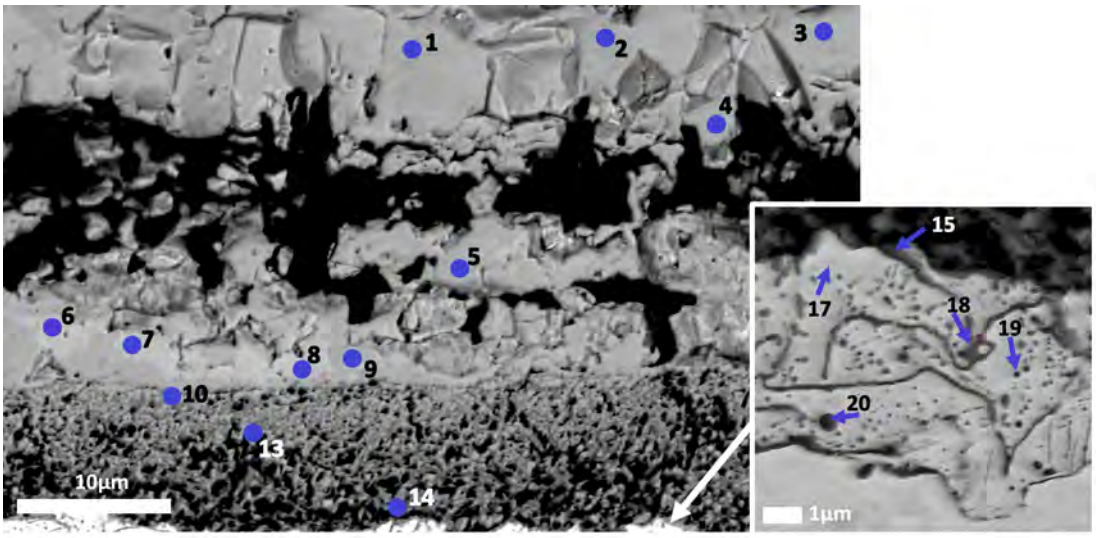

(a) WDS reference image, highlighting internal oxidation zone with spherical intragranular, film-like intergranular, pertrubed intragranular dendrites

			Wt%			
		Region	Fe	O	Mn	Si
Spectrum	1	Oxide phase top 1	68.14	29.50	2.32	
	2	Oxide phase top 1	68.70	29.33	1.92	
	3	Oxide phase top 1	68.74	28.82	2.39	
	4	Oxide phase 1	69.70	28.20	1.99	*0.11*
	5	Oxide phase 1	68.92	28.06	2.99	
	6	Oxide phase 2	71.68	25.40	2.79	*0.10*
	7	Oxide phase 2	71.34	25.32	3.26	*0.06*
	8	Oxide phase 2	71.43	25.40	2.97	*0.18*
	9	Oxide phase 1	68.96	29.79	1.16	*0.08*
	10	Spinel phase 1 (lighter)	66.78	28.57	*1.52*	2.85
	13	Spinel phase 2 (darker)	52.77	31.34	*5.67*	10.21
	14	Spinel phase 2 (darker)	52.38	29.95	4.64	10.96
	15	Internal oxidation	72.62	19.51	3.02	4.72
	17	Internal oxidation	98.97	0.80	0.00	0.21
	18	Internal oxidation	72.95	12.13	6.99	4.25
	19	Internal oxidation	89.72	5.28	1.01	3.98
	20	Internal oxidation	75.28	11.71	6.34	5.20

(b) WDS point scan measurements

Figure 25: WDS spectra and reference image for RAP composition 2Mn-2Si- WDS analysis was performed on a cross-section of the oxide, moving from the outer edge towards the oxide/metal interface to assess its composition in relation to depth (*Highlighted cells EDS*)

were no appreciable levels of Si. The presence of Mn in wustite has previously been discussed in 5.3.2 where Mn^{2+}may displace the Fe^{2+} from FeO forming a $(Fe_{1-x},Mn_x)O$ solid solution, with $0 < x < 1$. The dissolution of Mn within the magnetite phase was slightly more convoluted forming a spinel ferrite complex. It has a $MnFe_2O_4$ structure where the ionic distribution of spinels is commonly written as $(Mn_{1-x}Fe_x)[Mn_xFe_{2-x}]O_4$, with $0 < x < 1$. The parentheses () designate elements sitting within a tetrahedral site and the square brackets designate elements sitting within an octahedral site [89]. The fast outward diffusion of Mn, coupled with the thin outer oxide and the formation of iron oxide compounds resulted in a continuous dispersion of Mn throughout the outer oxide.

Region 3 contained very discernable levels of Si, unlike region 1 and 2. The region was composed of both a lighter and darker spinel phase creating a conglomerated amorphous structure. The darker spinel possessed an exceedingly larger quantity of Si compared to the lighter spinel, with the wt.% of Si within the darker spinel almost a magnitude of fivefold greater. Spectra 10,13-14 also show an enhanced presence of Mn within region 3, notably within the darker spinel. The increased levels of Si and Mn within the darker spinel were in conjunction with a sharp decrease of Fe content. The suggested structure for the amorphous phase was Mn_2SiO_4 + α-Fe + SiO_2 with the darker spinel containing a lower volume of α-Fe.

Region 4 was composed of a continuous layer of internal oxidation beneath the amorphous region. The internal oxide within 2Mn-2Si was denser and more compacted than that of 2Mn-1Si. The denser internal oxide displayed by 2Mn-2Si would have been far more impervious to Fe ions, producing a thinner external oxide. WDS spectra 17 was captured in amidst the internal oxide and consisted of fundamentally pure Fe. Spectra 20 was a globular oxide 0.5µm in diameter with a dark center around 0.1µm. The dark center was conjectured to be pure SiO_2, with an outer shell of $MnSiO_3$. Since SiO_2 is more thermodynamically stable than MnO, it can be conjectured that SiO_2 formed first then as Si was consumed the local Si/Mn activity ratio decreased [82]. Once the ratio was sufficiently low the formation of $MnSiO_3$ became thermodynamically favourable, with Mn in solution reacting at the surface of pre-existing SiO_2 forming a multilayer shell [82]. The center appears darker due to the elemental weight difference between Mn and Si.

Spectra 18 shows that the film like inter granular oxide has a very similar composition to that of the spherical intra-granular oxide. Both 2Mn-2Si and 2Mn-1Si displayed film-like inter-granular and spherical intra-granular oxides however 2Mn-2Si additionally displayed extremely fine perturbed intra granular oxides. These remarkably fine dendritic structures are not commonly observed, and their formation is dependent on inter-facial instability. In figure 25a the fine dendrites appear to be pointing down into the substrate suggesting a preferred growth direction due to the underlying crystal orientation.

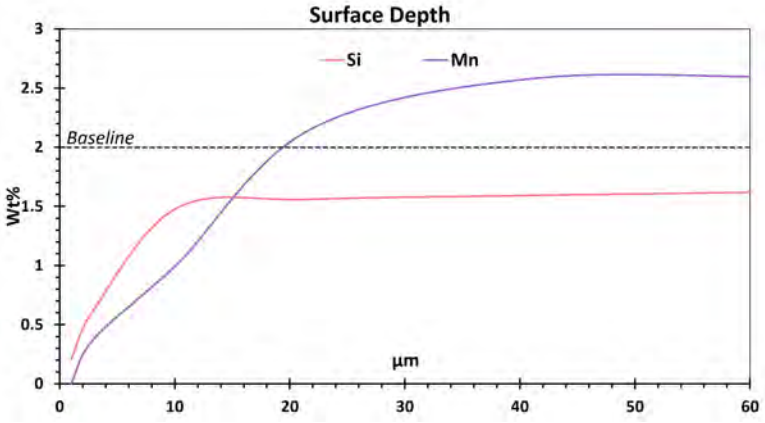

Figure 26: Sub-surface depth WDS analysis *(Measurements were conducted in cross section from the edge surface towards the center)*

Sub-Surface Depletion Figure 26 displays the elemental wt.% vs depth into the substrate (after internal oxidation). A distinct Si/Mn-depletion zone was formed beneath the oxide within the subsurface region. Si levels were found to recover by 10µm into the substrate and then remained constant throughout, however they were slightly lower than estimated at the 2wt.% baseline. Mn levels did not recover until 20µm and then proceeded to further increase past the baseline until 30µm. The increased subsurface depletion of Mn compared to Si was postulated to be due to the increased ability of Mn to diffuse through grain boundaries.

5.3.6 0.5Mn-0.5Mo

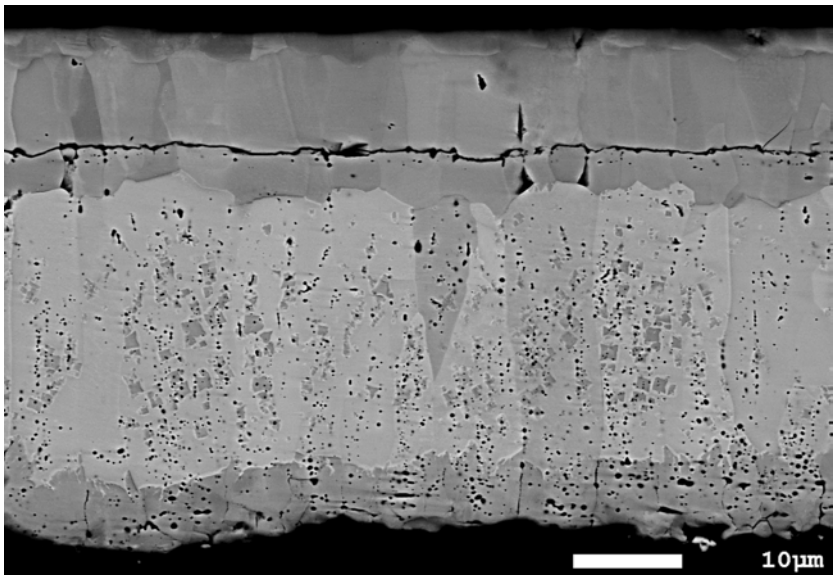

Figure 27: Through thickness oxide morphology for RAP composition 0.5Mn-0.5Mo-Oxide morphology displaying a thick magnetite seam with porosity, a thick outer magnetite layer and porous columnar wustite layer with cuboid magnetite precipitates.

Morphology The oxide morphology displayed by 0.5Mn-0.5Mo in figure 27, presents as a typical iron oxide consisting of 3 well-established oxide layers. There are however a considerable number of key differences compared to previous samples. The oxide thickness was found to reach up to 50µm but was very inconsistent throughout the sample. This was in stark contrast to sample 0.5Mn, which had an exceptionally consistent and thick oxide layer of 148µm. Furthermore 0.5Mn was profoundly adherent to the substrate in comparison to 0.5Mn-0.5Mo, which was non-adherent throughout.
0.5Mn-0.5Mo had a ubiquitous magnetite seam and magnetite top layer of 6.12µm and 14.46µm respectively, predominately greater than 0.5Mn. The percentage of the oxide composed of magnetite was extremely high at 50%, extensively more than any other sample that displayed a typical iron oxide morphology. Pro-eutectoid magnetite precipitates were present throughout the breadth of the sample with a variance in size (see Appendix 134). The precipitates were found to be largest towards the centre of the oxide, presumably due to the thermodynamics of formation of the magnetite seam and magnetite top layer preferentially adsorbing excess oxygen. Significant porosity was visible inside of the magnetite seam and wustite phase. Its presupposed that the porosity within the magnetite seam was due to wustite decomposition and the volatility of the MoO_3 phase [90].
Using EDS, a thin band of Mo was identified at the oxide/ metal interface and within any subsurface cracks, however Mo was not detected through the bulk of the oxide.Its hypothesised that the presence of Mo resulted in embrittlement, inducing sub-surface cracking. It was evident that the Mo/Fe ratio increased drastically at the interface compared to that of the metal and oxide. Formerly it has been reported that Mo increases the activation energy for oxidation and suppresses the inward diffusion of oxygen [91].

This may attribute for the large volume of porosity within the wustite phase with an increased activation energy favouring the growth or iron rich oxides through consumption of wustite [35].
It was presupposed that the low affinity of O for Mo and low diffusivity has resulted in a concentrated band at the interface [92]. This concentrated band has remarkably hindered the inward diffusion of O, drastically decreasing the rate of oxidation and overall oxide thickness. The addition of 0.5Mo resulted in a thinner, richer and more brittle oxide.

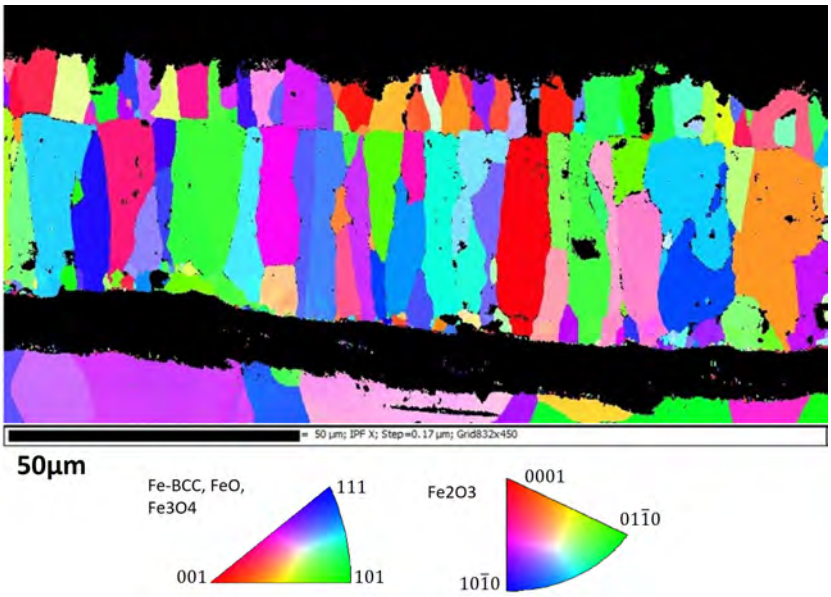

(a) Inverse pole figure-X map

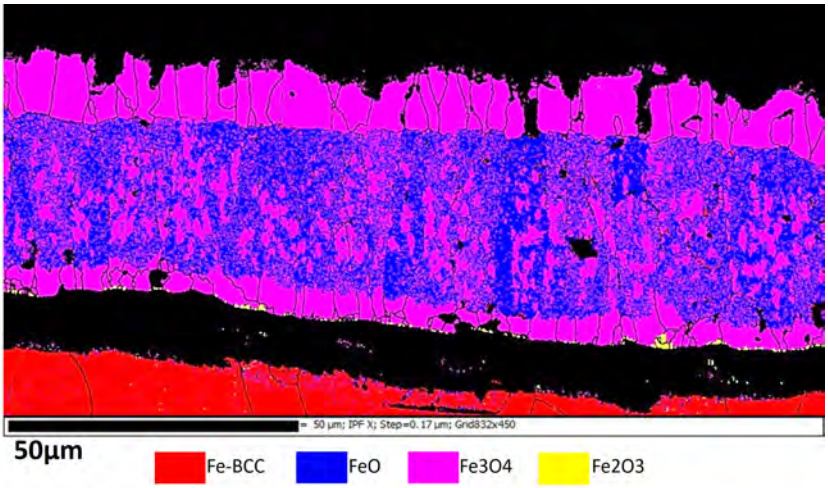

(b) EBSD phase map

Figure 28: Electron back-scatter diffraction phase and IPF map for RAP composition 0.5Mn-0.5Mo

EBSD The EBSD phase map in figure 28a identified a thick magnetite seam and magnetite top layer. No outer hematite layer was detected however small grains of hematite were observed on the underside of the magnetite seam. The minute hematite grains averaged 0.3µm in size and were conjectured to of formed after the break-away of the ox-

ide from the substrate. The break-away will result in enhanced inward diffusion of oxygen with a limited supply of cations. This will drive the decomposition of the wustite phase into magnetite, producing a magnetite seam [6]. When the thermodynamic drive is high enough, the same phenomena will result in the magnetite decomposing into hematite. Previously it has been shown that wustite and magnetite growth was highly dependent on the outward diffusion of metal ions whilst hematite is highly reliant on the inward diffusion of oxygen [93]. The low prominence of hematite is a result of the low diffusion coefficient of iron and oxygen within the hematite phase [52] [94] [19].
The IPF map in figure 28a shows an orientation relationship has been established between the magnetite precipitates and magnetite seam with the underlying wustite. For the orientation relationship to have been established the magnetite seam and precipitates must have developed due to the decomposition of the wustite phase, thus retaining the original wustite orientation. The small grains of hematite did however exhibit a separate orientation to that of the magnetite seam. The individual wustite grains displayed no preferential growth or orientation and neither did the magnetite top layer.

5.3.7 2Mn-0.25Mo

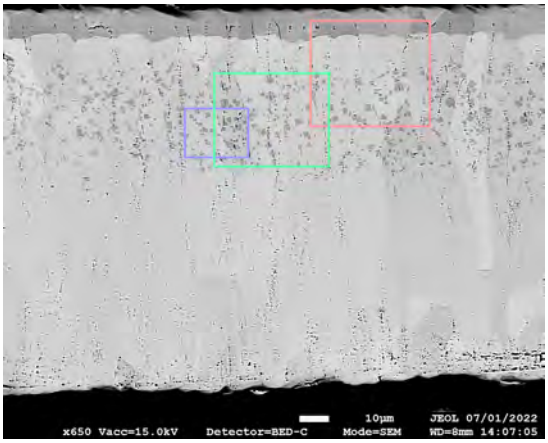

(a) Oxide morphology overview

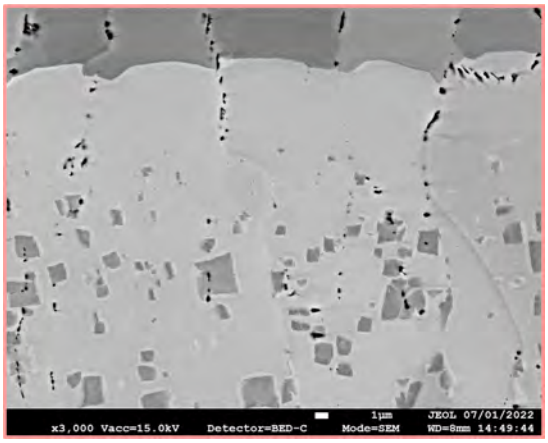

(b) Magnetite precipitates and magnetite outer edge interface

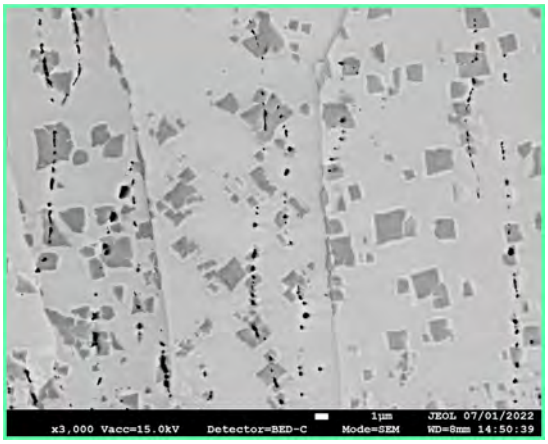

(c) Lines of porosity through wustite and magnetite precpitates

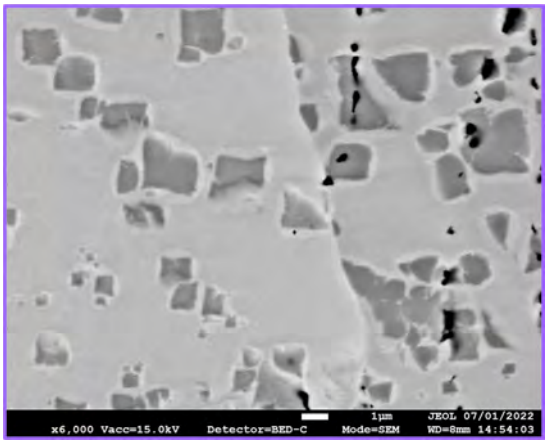

(d) Magnetite precipitates halted at wustite grain boundary

Figure 29: Through thickness oxide morphology for RAP composition 2Mn-0.25Mo- Thick in-adherent external oxide layer with cuboid magnetite precipitates and lines of porosity

Morphology The oxide morphology for 2Mn-0.25Mo was displayed in figure 29. The oxide was overtly thicker than many of the previous RAP samples at 117µm. The minor alloying addition of 0.25Mo appears to have exponentially increased the oxide thickness. This effect was analogous to that observed for 2Mn-0.5Si, where a low alloying addition of 0.5Si acutely increased the oxide thickness due to an incomplete passivation layer. 2Mn-0.25Mo had many discernable characteristics compared to previous samples, especially 2Mn. The oxide thickness of 2Mn was only 45µm, 50% less than that of 2Mn-0.25Mo. Furthermore, 2Mn displayed spherical intra-granular MnO particles, 4µm into the substrate, whereas 2Mn-0.25Mo did not display any internal oxidation. Its presupposed that the intra-granular MnO particles limited cation diffusion and thus reduced the oxide thickness of 2Mn. The absence of an internal oxide region suggests that the addition of 0.25Mo hindered the inward diffusion of oxygen, preventing the formation of any internal MnO particles. Due to the increased oxide thickness of

2Mn-0.25Mo, its inferred that limiting the outward diffusion of cations was of greater consequence than hindering the inward diffusion of anions. Nevertheless even though 2Mn-0.25Mo was a thicker oxide it was not found to blister or produce a discernibly rough surface like 2Mn.
2Mn-0.25Mo also had a thicker oxide compared to 0.5Mn-0.5Mo. This was postulated to be due to the lower Mo/Fe ratio at the interface of 2Mn-0.25Mo. The addition of Mo alters the defect structure of the oxide and affects the overall ion transport properties. The oxidation resistance of an alloy can be increased by doping of a metal ion with a higher valency state than the metal ion in the base oxide [95]. The higher valency state reduces lattice defects and thus slows and suppress growth [95]. 0.5Mo proved to be a sufficient quantity drastically reducing and compacting the oxide. Thus, the addition of 0.25Mo was not sufficient to reduce oxide thickness through doping versus 0.5Mo. Furthermore, Mn has also been shown to enhance lattice diffusion [79], the increased Mn content within 2Mn-0.25Mo may of further counteracted the effect of the Mo.

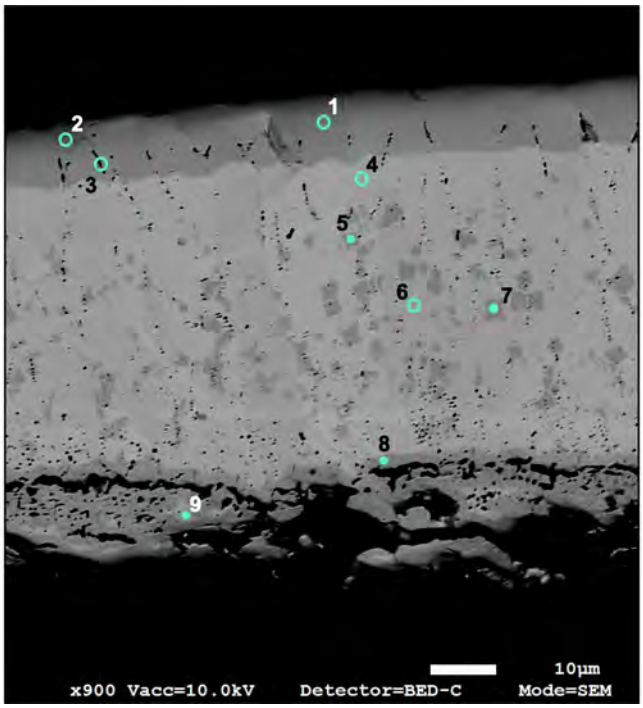

(a) WDS reference image for points 1-9

			Wt%			
		Region	Fe	O	Mn	Mo
Spectrum	1	Oxide top band	72.57	27.43		
	2	Oxide top band	71.63	28.28		*0.09*
	3	Oxide top band	69.40	30.55		*0.05*
	4	Oxide matrix top	71.48	25.76	*2.71*	*0.05*
	5	Precipitate	70.96	29.00		*0.04*
	6	Oxide matrix mid	72.57	25.20	*2.10*	*0.13*
	7	Precipitate	71.49	28.50		*0.01*
	8	Oxide base	69.74	30.22		*0.04*
	9	Oxide base	69.74	25.55	4.55	*0.15*
	10	Oxide seam	72.31	25.72		*1.96*
	11	Oxide seam	46.82	23.91		*29.28*
	12	Base alloy	97.19	*0.82*	1.58	*0.41*

(b) WDS measurements

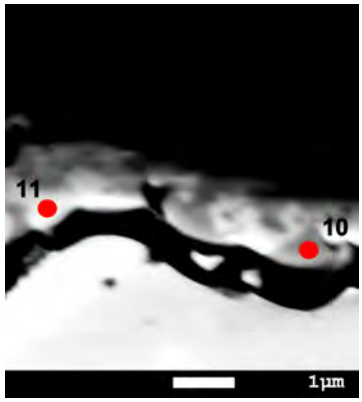

(c) WDS reference image for points 10-11

Figure 30: WDS spectra and reference images for RAP composition 2Mn-0.25Mo-WDS analysis was performed on a cross-section of the oxide, moving from the outer edge towards the oxide/metal interface *(Highlighted cells EDS)*

WDS The oxygen in spectra 1-3, 5, 7 and 8 was markedly higher than that of the oxide in spectra 4, 6 and 9. The Fe:O ratio affirms that spectra 1-3, 5, 7 and 8 were a magnetite phase and 4,6 and 9 were a wustite phase. The magnetite phases are easily distinguished by the darker contrast in the BSE image in figure 30a. Residuals of Mn were present within the wustite phase. The presence of Mn within the wustite phase further substantiates the claim that Mo does not hinder the diffusion of the cations. The base of the oxide has a large volume of porosity and cracking, with the richer magnetite phase surrounding the diffusion pathways. Only trace elements of Mo were seen throughout the oxide however a substantial volume was found within the oxide seam at the interface. The lighter regions of the oxide seam, observed in figure 30c,

contained higher volumes of Mo. Its presupposed that a secondary beta phase has formed however its incomplete and was formed in tandem with an iron oxide.

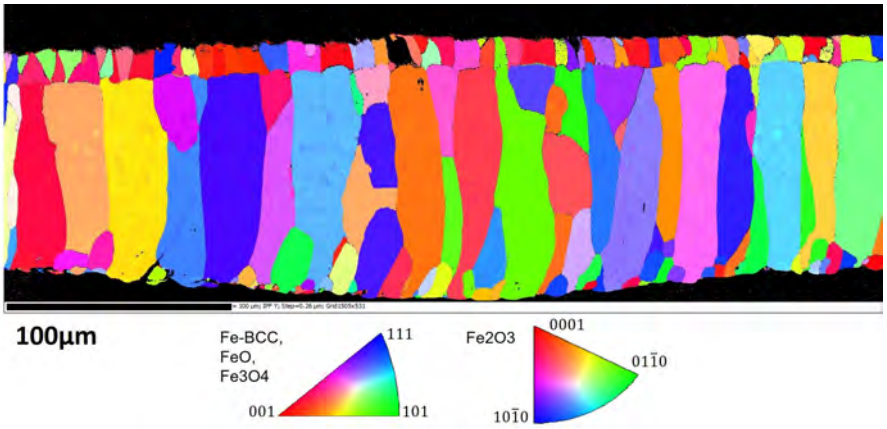

(a) Inverse pole figure-X map

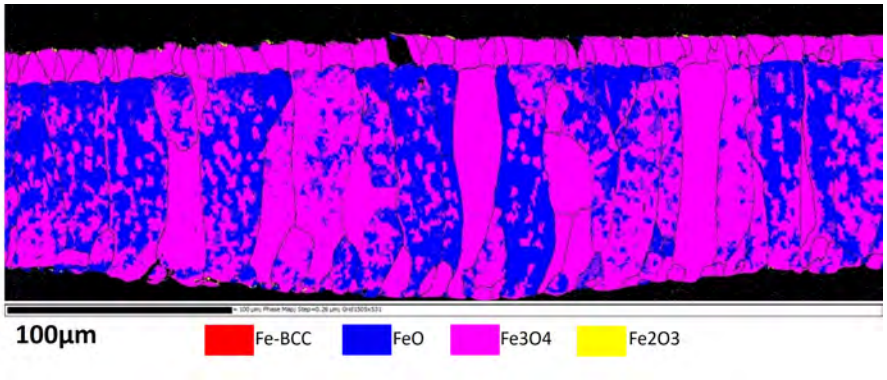

(b) Electron back-scatter diffraction phase map

Figure 31: EBSD for RAP composition of the oxide produced for 2Mn-0.25Mo

EBSD The EBSD phase map in figure 31b identified a definite magnetite top layer but no continuous magnetite seam. The phase map was in accordance with the BSE images in figure 29, which also did not display a continuous magnetite seam. Nevertheless the phase map has become confused in specific grains between the magnetite phase and the wustite phase. A number of grains were incorrectly registered as magnetite, whilst the BSE image shows a long columnar wustite grain with magnetite precipitates. The increased porosity observed within wustite grains of 2Mn-0.25Mo may have resulted in poor indexing of the diffraction patterns. The indexing of the magnetite precipitates was still relatively strong thus its possible the phase map identified the entire grain as magnetite. Furthermore, wustite and magnetite are both cubic structures with similar kikuchi bands leading to further confusion.

The IPF map in figure 31a showed no preferential growth or orientation for the wustite grains or magnetite top layer, suggesting equiaxed cooling. The samples were air cooled after heating allowing for stress dissipation and relaxation. The IPF map revealed an orientation relationship between the magnetite precipitates and the underlying wustite phase, this was also observed in 0.5Mn-0.5Mo.

5.3.8 2Mn-0.5Mo

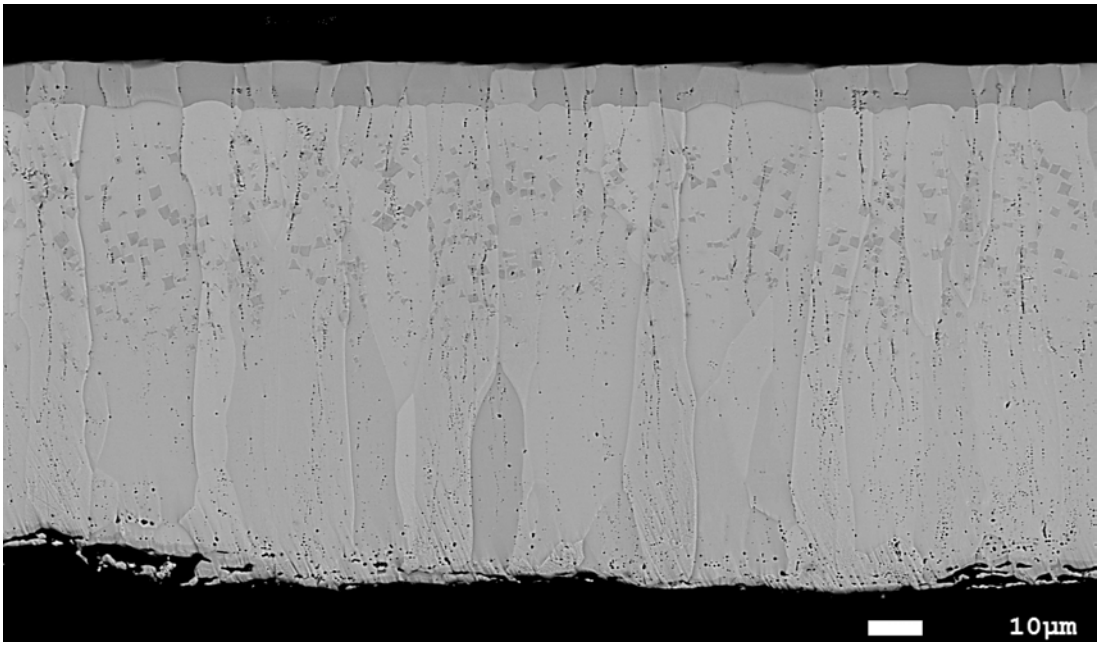

(a) Oxide morphology overview

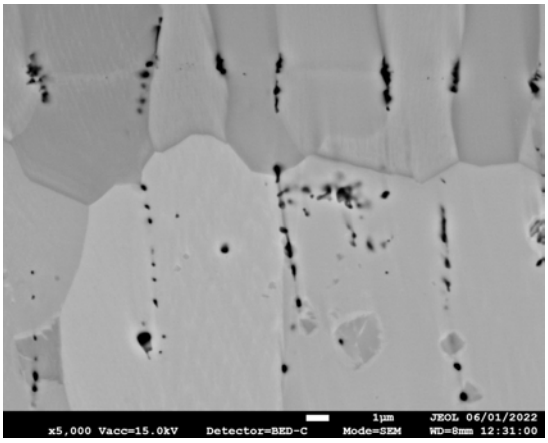

(b) Lines of porisity present at magnetite grain boundaries

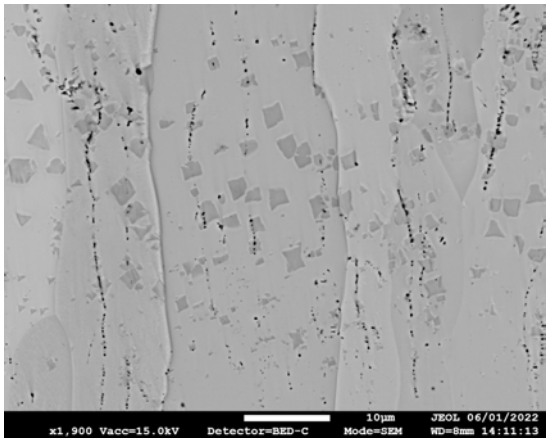

(c) Magnetite precipitates within wustite

Figure 32: Through thickness oxide morphology for RAP composition 2Mn-0.5Mo

Morphology Figure 32 features the oxide morphology of sample 2Mn-0.5Mo. The external scale morphology was remarkably similar to 2Mn-0.25Mo but moderately thinner at 93.7µm. The magnetite top layer was 7.89µm with equiaxed grains. Lines of porosity were present within the magnetite top layer, concentrated at the grain boundaries. The porosity was exceptionally uniform and consistent. Interestingly some of the lines of porosity within the magnetite top layer continued down into the wustite phase beneath. Many of these lines of porosity did not sit at the grain boundaries of the columnar wustite phase (see Appendix 135). The porosity in this instance was most likely due to internal stresses caused by volumetric changes during growth, micro-void formation was then initiated to counterbalance the resulting compressive stresses [78]. Micro-void coalescence will initiate at grain boundaries or around inclusions. Its therefore conjectured that the intra-granular micro-voids, seen in figure 32c, suggest that Mn

acted as an inclusion, initiating micro-void formation.
Intragranular micro-void coalescence within wustite grains was also heavily observed within 2Mn but not within 2Mn-0.5Si. This further supports the assumption that the addition of 0.5Si in 2Mn-0.5Si tied up a large majority of the Mn.
The pores located towards the base of the wustite phase were moderately larger than those observed closer towards the outer scale interface. At the oxide/ metal interface, iron cations move from the substrate into the wustite layer, creating an opposite flux of cation vacancies into the substrate [35]. The process of vacancy injection will then lead to pores [78]. Porosity was also observed within the magnetite seam but was assumed to be due to wustite consumption. Many of the pores coalesced forming cracks parallel to the substrate surface. The average pore size for both 2Mn-0.5Mo and 2Mn-0.25Mo was 0.08µm.
Magnetite precipitates were found continuously distributed throughout the top region of the wustite phase. Many of the precipitates were formed around micro-voids. Voids have an exponential effect on oxidation whereby they act as additional oxygen pathways. Micro-voids may increase the oxygen content of the oxide encompassing them, forming magnetite precipitates. As the precipitates grow, they may then begin consuming the wustite phase, which will then produce further voids. The precipitates were approximately 0.7µm in size for both 2Mn-0.5Mo and 2Mn-0.25Mo.
The thickness of 2Mn-0.5Mo was lesser than 2Mn-0.25Mo but still greater than 2Mn and 0.5Mn-0.5Mo at 93.7µm.Its postulated that the addition of 0.5Mo proved more effective than 0.25Mo due to a greater formation of the secondary Mo phase. The larger addition of Mo will also have a greater effect on the defect structure of the oxide. 2Mn-0.5Mo had a thicker oxide than 0.5Mn-0.5Mo due to the increased Mn content which enhanced lattice diffusion.

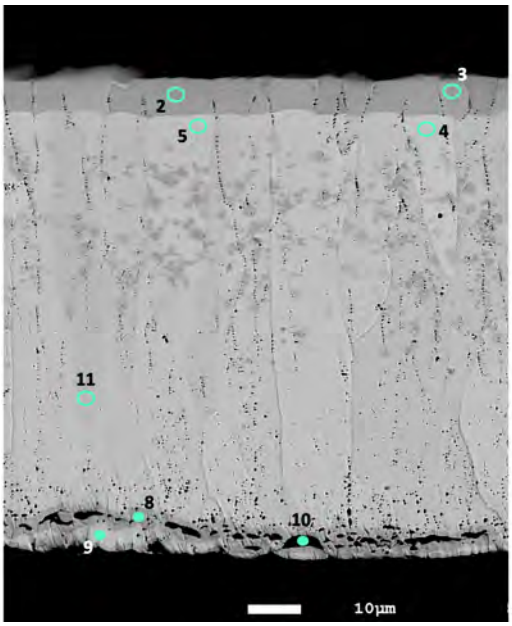

(a) WDS reference image

			Wt%			
		Region	Fe	O	Mn	Mo
Spectrum	2	Oxide top band	69.36	28.52	*2.12*	
	3	Oxide top band	68.82	28.82	*2.19*	*0.16*
	4	Oxide matrix top	68.20	26.92	*4.82*	*0.06*
	5	Oxide matrix top	69.20	25.03	*5.71*	*0.06*
	8	Oxide base	70.12	27.34	*2.38*	*0.16*
	9	Oxide base	69.61	24.27	*5.97*	*0.15*
	10	Oxide base	73.20	26.18	*0.54*	*0.08*
	11	Oxide matrix mid	69.83	24.67	*5.49*	

(b) WDS point scan measurements

Figure 33: 2Mn-0.5Mo WDS analysis - WDS analysis was performed on a cross-section of the oxide, moving from the outer edge towards the oxide/metal interface*(Highlighted cells EDS)*

WDS The oxygen content in spectra 2,3 and 8 was in accordance with the Fe:O ratio for magnetite. Mn was detected within the magnetite unlike 2Mn-0.25Mo. The dissolution of Mn through the magnetite phase will produce $(Mn_xFe_{1-x})[Mn_xFe_{2-x}]O_4$, with $0 < x < 1$. The oxygen content in spectra 4,5,9 and 11 was in agreement with the Fe:O ratio for wustite. The Mn content within the wustite phase was larger than that detected for 2Mn-0.25Mo forming $(Mn_x, Fe_{1-x})O$. Spectra 9 revealed wustite below the band of magnetite towards the base of the oxide. The wustite indicates the oxide may have been attached to the substrate below when the band of magnetite formed, suggesting the transformation was primarily due to the large voids at the base.

5.3.9 2Mn-0.75Mo

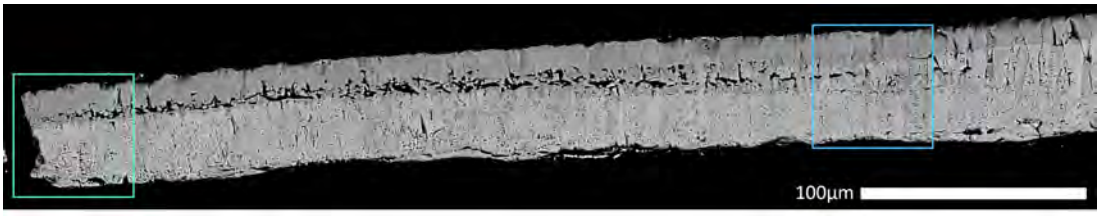

(a) Reference image of detached oxide for RAP composition 2Mn-0.75Mo

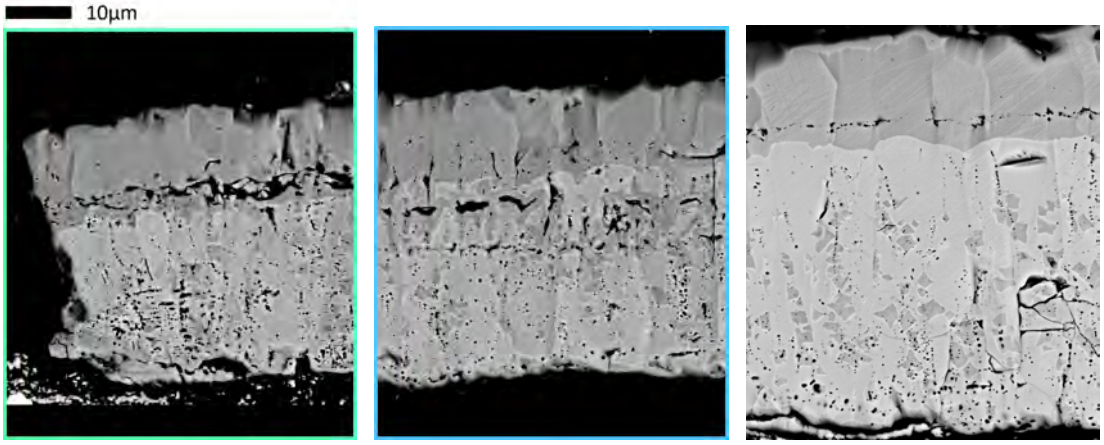

(b) Fractured oxide (c) Enlarged pores (d) Bulk oxide morphology

Figure 34: Oxide morphology for 2Mn-0.75Mo

Morphology Figure 34 shows a large, stitched BSE image of 2Mn-0.75Mo. A large vertical crack was shown traversing through the full thickness of the oxide, creating an open pathway to the substrate below. The crack was intra-granular, indicating that the mechanical failure occurred during cooling [6]. The lack of oxidation on the exposed substrate below further supported this. The effects of the cracking were observed for 380µm adjacent to the fracture point either side. The oxide was richer with greater volumes of porosity through the thickness. Towards the vertical crack the magnetite top layer was moderately thicker, with lateral cracking and increased porosity. The increased ease of oxygen diffusion within this region would have resulted in rapid enrichment of the oxide and increased mixed flux ion transport at the wustite magnetite interface. Thus, the increased growth stresses and wustite consumption would have resulted in large voids coalescing into lateral cracks. Several catastrophic vertical fractures were noted throughout the sample (see Appendix 136). The oxide was found to be exceedingly brittle compared to previous RAP samples.

The bulk of the oxide resembled figure 34. Magnetite precipitates were located towards the base of the oxide unlike 2Mn-0.5Mo and 2Mn-0.25Mo. Nonetheless this was presumably due to the diminished oxide thickness. Precipitates were similar in size to previous samples at 0.84µm. Pores were mainly present within the wustite phase and 0.06µm in size.

The oxide thickness was 57µm, a sizeable reduction compared to 2Mn-0.5Mo and 2Mn-0.25Mo. Minor traces of Mo were detected throughout the oxide thickness using EDS

and a thin band was detected at the oxide/ metal interface. The addition of 0.75Mo compared to 0.5Mo increased the critical temperature of oxidation to 719°C and halved the total weight gain. The mechanical behaviour of the oxide was also altered and the scale was in-coherent with the substrate. In summation it was postualted that 0.75Mo proved effective in reducing oxidation, producing a more compact scale, and producing a brittle, non-adherent scale.

5.3.10 2Mn-1Mo

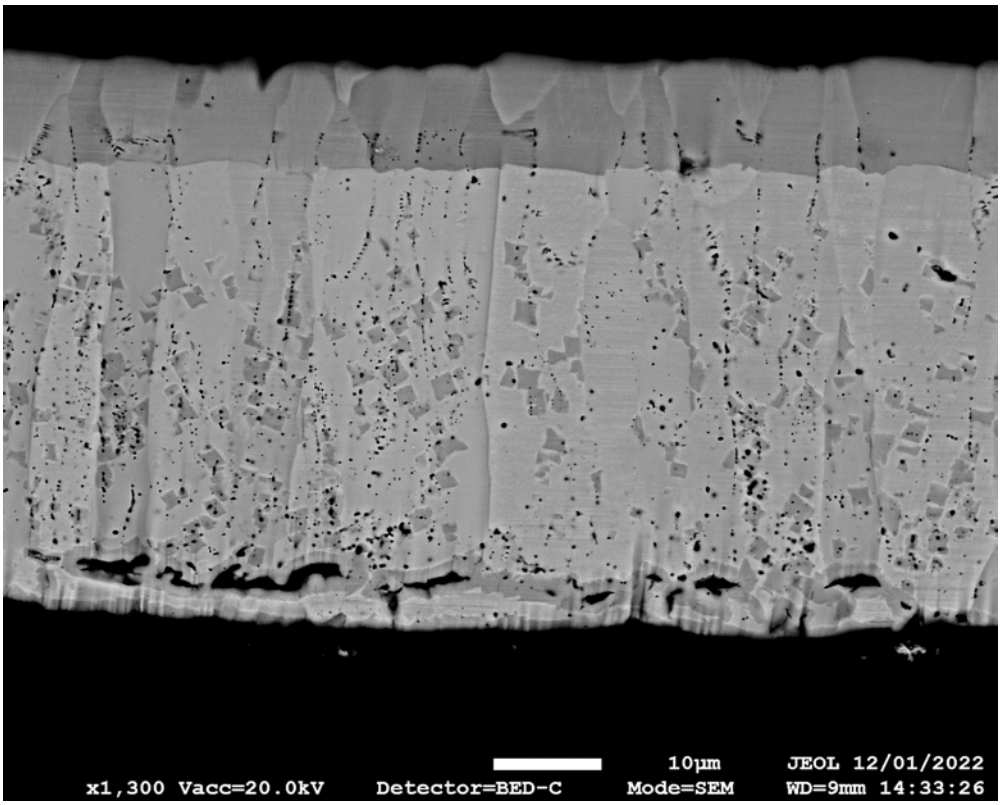

Figure 35: Through thickness oxide morphology for RAP Composition 2Mn-1Mo-Wustite with large cuboid magnetite precipitates, lines of porosity and large coalesced voids located in a seam of magnetite

Morphology 2Mn-1Mo had the largest addition of Mo of the RAP samples. The oxide morphology was profoundly akin to 2Mn-0.75Mo however slightly thinner at 45µm. Large void coalescence was present continually throughout the sample, pointedly near the base of the oxide in a lateral formation, shown in figure 35. Chains of intra-granular micro-voids were observed through columnar wustite grains, with inter-granular micro-voids present in the magnetite top layer. The average pore size was only 0.03µm, the lowest of all the Mo additions. Porosity was more pronounced in 2Mn-1Mo and 2Mn-0.75Mo compared to the lower Mo additions.

The oxide was very brittle and contained many fractures (see Appendix 137). The areas located within a specific vicinity of these fractures experienced oxygen enrichment, similar to the effect observed in figure 34c for 2Mn-0.75Mo. These areas were

converted almost entirely into magnetite and were noticeably thinner. In areas with increased magnetite, lateral bands of cracking were observed, pre-eminently just below and or within the magnetite top layer. The oxide appeared very brittle and non-adherent in nature, with large areas completely detached. Nonetheless, a porous band of oxide remained strongly attached to the substrate, approximately 6µm in thickness. Due to WDS on 2Mn-0.25Mo, shown in figure 33, its presupposed that the band was composed of some form of Mo oxide and an iron oxide.Its presumed the porosity of the phase would be due to volatile Mo species at high temperatures. The evaporation of a Mo species within the secondary oxide phase would create large pores and pinholes, producing a porous brittle structure. The evaporation of the Mo species would trigger the fast outward diffusion of Fe and Mn producing a spinel phase [91]. The appearance of the porous oxide was strikingly similar to the amorphous phase observed in 2Mn-1Si and 2Mn-2Si which contains a spinel structure.
In summation the addition of 2Mn-1Mo effectively and assuredly reduced the oxide thickness compared to other 2Mn-Mo additions. A critical volume of Mo was required to significantly reduce the oxide thickness, approximated at 0.75Mo. An inverse relationship has been established, with the affirmation that oxide thickness was decreased with an increase of Mn:Mo ratio. 0.5Mn-0.5Mo with a 1:1 ratio produced the smallest oxide thickness. 2Mn-1Mo with a 2:1 ratio produced the second smallest oxide thickness.

EBSD The quality of patterns for 2Mn-1Mo was relatively poor. The oxide was brittle and difficult to prepare, making mapping arduous. The IPF map, shown in figure 36a, shows a lateral intra-granular fracture. There was no orientation preference for the wustite or magnetite top layer however a relationship may once again be established between the magnetite precipitates and the underlying wustite phase. No hematite top layer was detected nor a magnetite seam.

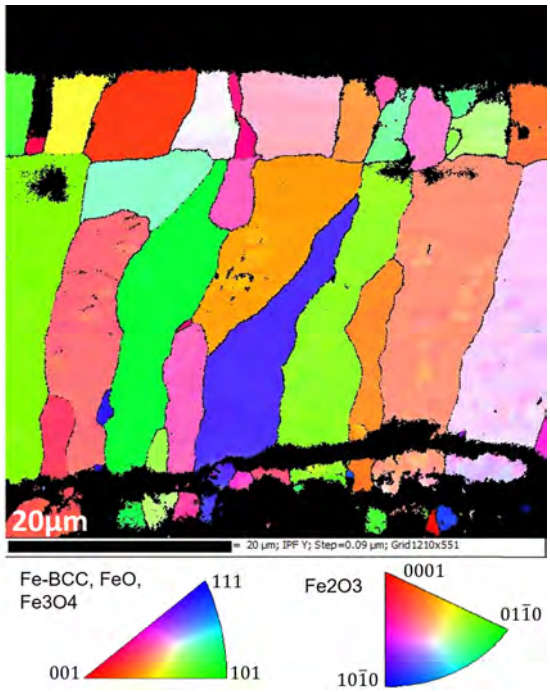

(a) Inverse pole figure-X map

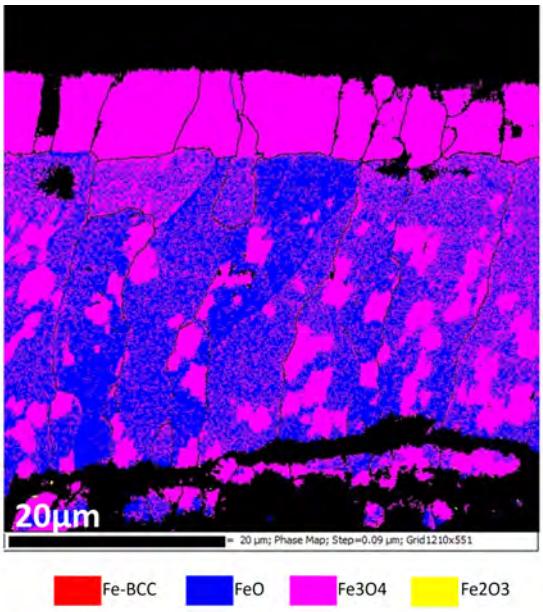

(b) Phase map

Figure 36: Electron back-scatter diffraction IPF-X and phase map for RAP composition 2Mn-1Mo

5.3.11 2Mn-1Si-0.25Mo

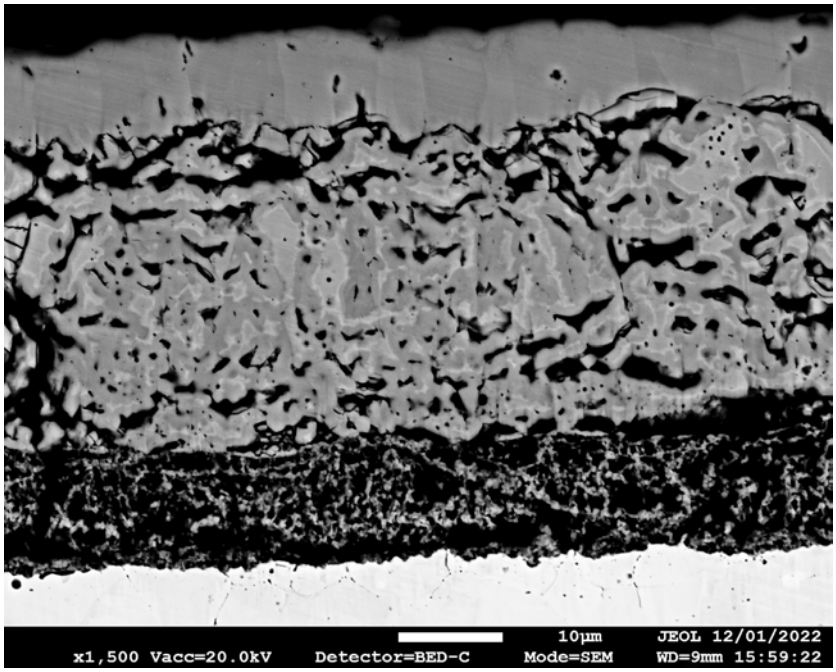

Figure 37: Through thickness oxide morphology for RAP composition 2Mn-1Si-0.25Mo- A convoluted multi-phase oxide morphology displaying 4 distinct regions, an internal oxidation zone with dendritic and precipitate internal oxides, an amorphous and brittle oxide region, a porous magnetite and wustite section and a outer oxide layer

Morphology 2Mn-1Si-0.25Mo was the concluding RAP composition. The oxide morphology displayed in figure 37, was considerably convoluted, with 4 very distinctive regions, similar to those displayed in 2Mn-1Si and 2Mn-2Si. The 4 distinct regions may once again be categorised as;

1. The upper magnetite region
2. The lower magnetite region
3. The amorphous region
4. The internal oxidation region

Region 1 was composed of equiaxed magnetite grains, forming a top layer 8.7µm thick. The top layer was very compact with minimal defects. The small voids observed were different compared to the distinctive inter-granular micro-voids observed in the Mn-Mo additions, appearing sporadically.
Region 2 encompassed a significant proportion of the total oxide thickness, at approximately 31µm. The oxide closely resembles that of region 2 in 2Mn-1Si. Islands of retained wustite are present throughout the thickness of the region, surrounded by a complex of large magnetite grains. Nonetheless, the islands of retained wustite were more evenly dispersed compared to 2Mn-1Si and there was no large band of wustite

present towards the base of the region. This suggest that there was less of a stoichiometric gradient through the magnetite phase, implying a more homogenous transformation of the wustite phase. Another crucial difference was the appearance of micro-voids, notably towards the top right of region 2. These micro-voids were only seen partially in the base of region 2 in 2Mn-1Si and were not seen at all in 2Mn-2Si. Its postulated that these intra-granular micro-voids have formed due to Mn inclusions. This would suggest that the Mn within 2Mn-1Si and 2Mn-1Si was acutely more constrained and tied up than within 2Mn-1Si-0.25Mo.

The amorphous phase within region 3 had an intricate and complex microstructure. The thickness was moderately larger than that reported for 2Mn-2Si and 2Mn-1Si, at approximately 13µm. The amorphous region appears to be a complex conglomerate of spinel phases with a high volume of porosity. A dark and light spinel phase were present, comparable to the ones viewed in 2Mn-2Si and 2Mn-1Si. However, an additional spinel phase with a lighter appearance was observed within 2Mn-1Si-0.25Mo. The lighter contrast of the phase, with the use of BSE, suggests the lighter spinel incorporated the heavier Mo element (see Appendix 138).

Region 4 was composed of a layer of internal oxidation directly beneath the amorphous region. The internal oxidation of 2Mn-1Si-0.25Mo was lower than that reported for 2Mn-2Si and 2Mn-1Si, at approximately 4.6µm and 6.3µm respectively. The internal oxidation in region 4 contained film-like inter-granular and spherical intra-granular oxides.

The oxide thickness was 51µm, a considerable reduction compared to 2Mn-1Si and 2Mn-0.25Mo which were 59µm 117µm respectively.

5.3.12 Mn-Si Kinetics

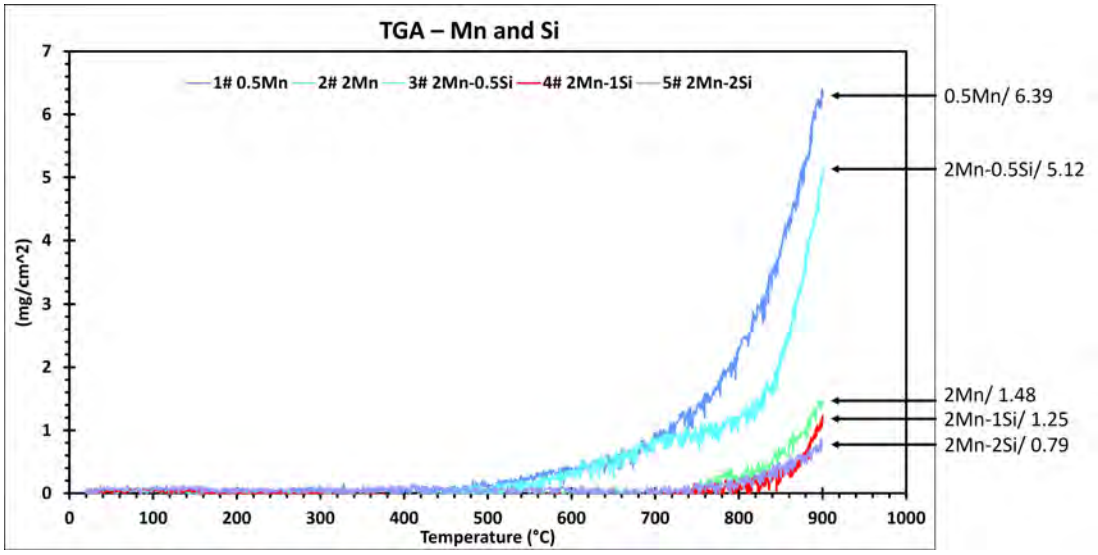

Figure 38: Mass Gain Evolution for RAP compositions containing Mn-Si

Thermo-gravimetric Analysis Figure 38 displays the total mass gain as a function of temperature for RAP samples containing Mn-Si. Throughout this thesis, the y-axis on any figures for thermo-gravimetric analysis (TGA) will be referred to as (mg/cm^2), which stands for mass gain per unit area.

The thermogram allows for the calculation of the critical temperature of oxidation, defined as the temperature at which oxidation of the sample begins [96]. The thermogram for all 5 samples was split into two very distinct sections, with a nil segment and an exponential one. The onset of the exponential segment was distinguished by rapid weight gain of the sample, occurring at the critical temperature of oxidation. All the samples display parabolic behaviour, with the integral limitation of the oxidation kinetics due to a diffusion process.

The total mass gain for all 5 compositions was relatively negligible for the first 500°C then abruptly starts to increase for 0.5Mn at 510°C and 2Mn-0.5Si at 561°C. The increase of mass was due to the formation of the wustite phase, which has a formation temperature of 560°C. The rapid gain of weight for 0.5Mn at 510°C therefore implies that the addition of 0.5Mn has lowered the wustite formation temperature causing rapid weight gain at a lower critical temperature. 2Mn-0.5Si shows a steady weight gain until it approaches 800°C where it aggressively starts to increase. This rapid increase could be due to an increase in kinetic energy, which may enhance the rate of diffusion and/or a phase transformation. 0.5Mn and 2Mn-0.5Si had a total weight gain of 6.39mg/cm^2 and 5.12 mg/cm^2 respectively. 0.5Mn had both the biggest weight gain and the greatest oxide thickness among the five samples, with 2Mn-0.5Si having the second largest.

As expected, the addition of Mn and Si, in the correct additions, has drastically enhanced oxidation resistance. 2Mn, 2Mn-1Si and 2Mn-2Si remained impervious to oxidation for an additional 200°C with only negligible oxidation observed until 700°C. The critical oxidation temperatures were 758°C, 813°C and 790°C for 2Mn, 2Mn-1Si

and 2Mn-2Si respectively. This was in concurrence with a drastic decrease of the total mass gain. Thus, an inverse trend can be established whereby an increase of critical temperature results in a decrease of mass gained.

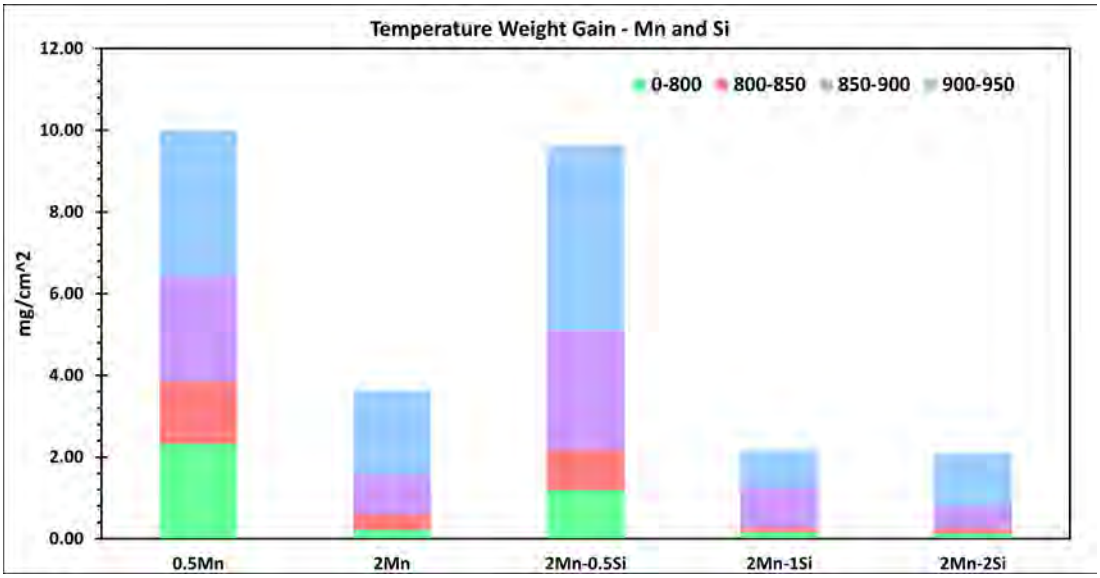

(a) Temperature weight gain chart per increment of temperature bar chart

	0.5Mn	2Mn	2Mn-0.5Si	2Mn-1Si	2Mn-2Si
0-800	2.33	0.22	1.19	0.16	0.13
800-850	1.52	0.39	0.99	0.12	0.12
850-900	2.55	0.96	2.97	0.97	0.54
900-950	3.62	2.06	4.48	0.90	1.28

(b) Mass gain per increment of temperature (mg/cm^2)

Figure 39: Weight gain for RAP compositions Mn-Si, displaying weight gain for each individual increment of temperature

Mass Gain The total weight gained per increment of temperature, for the Mn-Si RAP samples, are displayed in figure 39. Mass gain was the greatest for all samples between 900-950°C, with the exception of 2Mn-1Si in which 850-900°C saw the largest mass gain. The 900-950°C temperature band saw double the mass gain compared to the 850-900°C band for Samples 2Mn, 2Mn-0.5Si and 2Mn-2Si. Both 2Mn-1Si and 2Mn-2Si only saw negligible weight gain until the 850-900°C temperature band.

5.3.13 Mn-Mo Kinetics

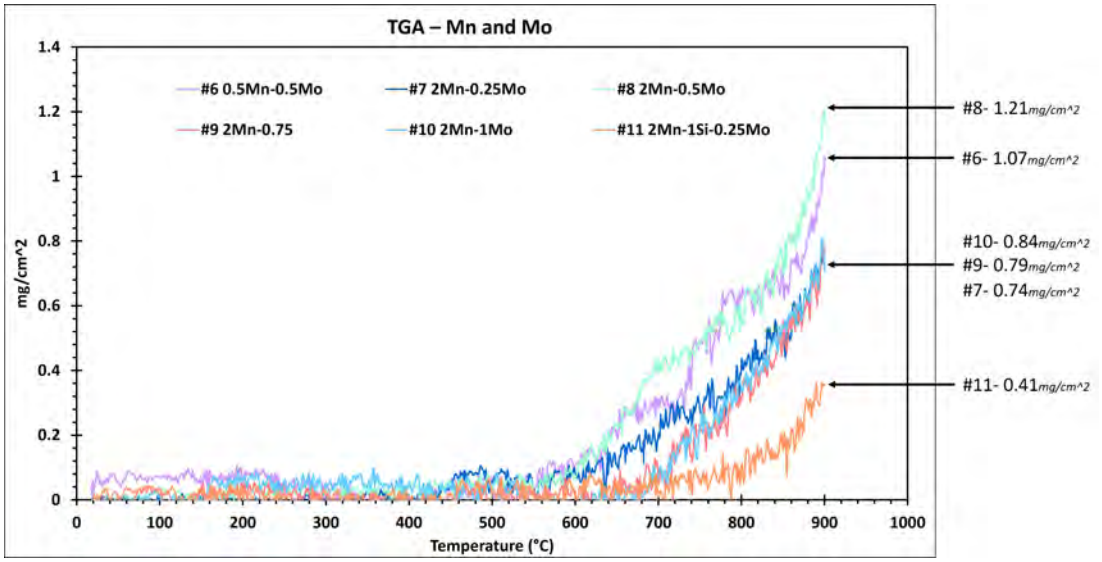

Figure 40: Mass Gain Evolution for RAP compositions containing Mn-Mo

Thermo-gravimetric Analysis Figure 40 displays the total mass gain as a function of temperature for RAP samples containing Mn-Mo. Throughout this thesis, the y-axis on any figures for thermo-gravimetric analysis (TGA) will be referred to as (mg/cm^2), which stands for mass gain per unit area. All the samples display parabolic behaviour, with the integral limitation of the oxidation kinetics due to a diffusion process.
The mass gain curves of the 2Mn-xMo compositions are all very similar in appearance however 2Mn-0.75Mo and 2Mn-1Mo had a higher critical temperature of oxidation. The addition of Mo above 0.75wt.$\%$ was found to drastically increase the critical temperature of oxidation from 586°C to 719°C for 2Mn-0.5Mo and 2Mn-0.75Mo respectively. The total mass gain was also halved for 2Mn-0.75Mo.

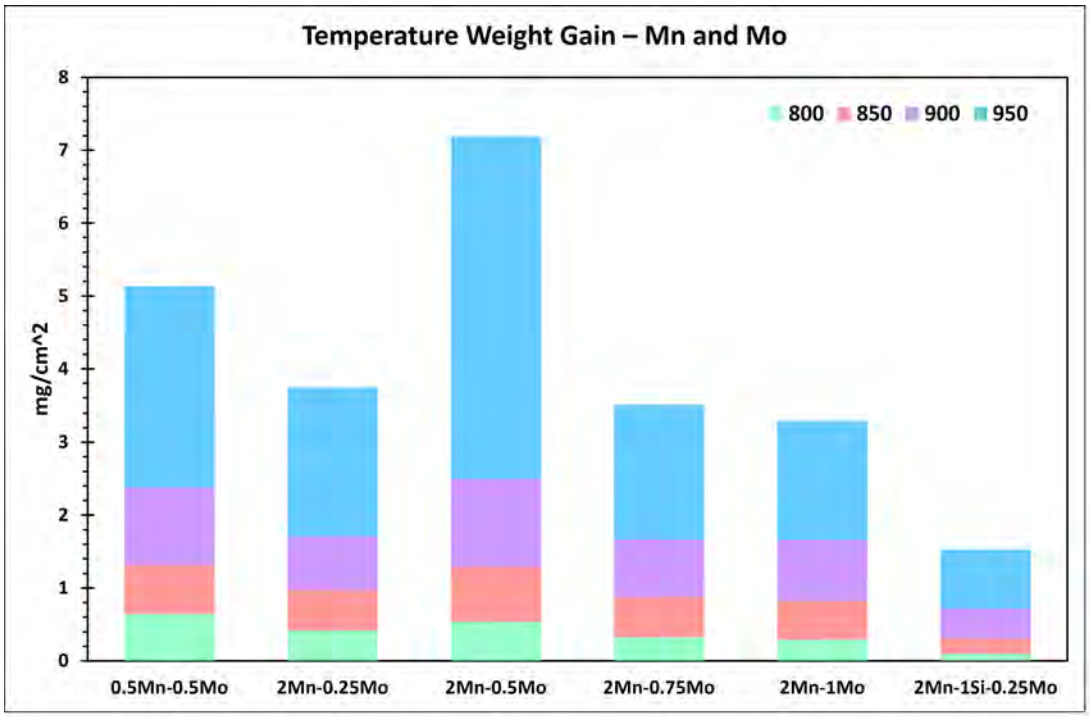

Figure 41: Weight gain for RAP compositions Mn-Mo, displaying weight gain for each individual increment of temperature

Mass Gain The total weight gained per increment of temperature, for the Mn-Mo RAP samples, are displayed in figure 41. The Mo additions experienced exponential gain between 900-950°C, often more than doubling in mass gain. The increased mass gain between this period was likely due to the increased ease of lattice diffusion with the increase of temperature.

2Mn-0.25Mo appears to be an anomaly displaying a peculiarly low weight gain although the oxide thickness was extremely large. The average thickness of the oxide was 117.16µm, the third highest, and far thicker than 2Mn-0.75Mo which displayed a similar mass gain. Possible explanations are an extremely high porosity resulting in a low-density oxide. Although the oxide contained porosity it was not thought to be of great enough volume to account for the exceptionally low mass gain. Its therefore conjectured that oxide predominantly grew during cooling once it was removed from the furnace.

5.3.14 Summary

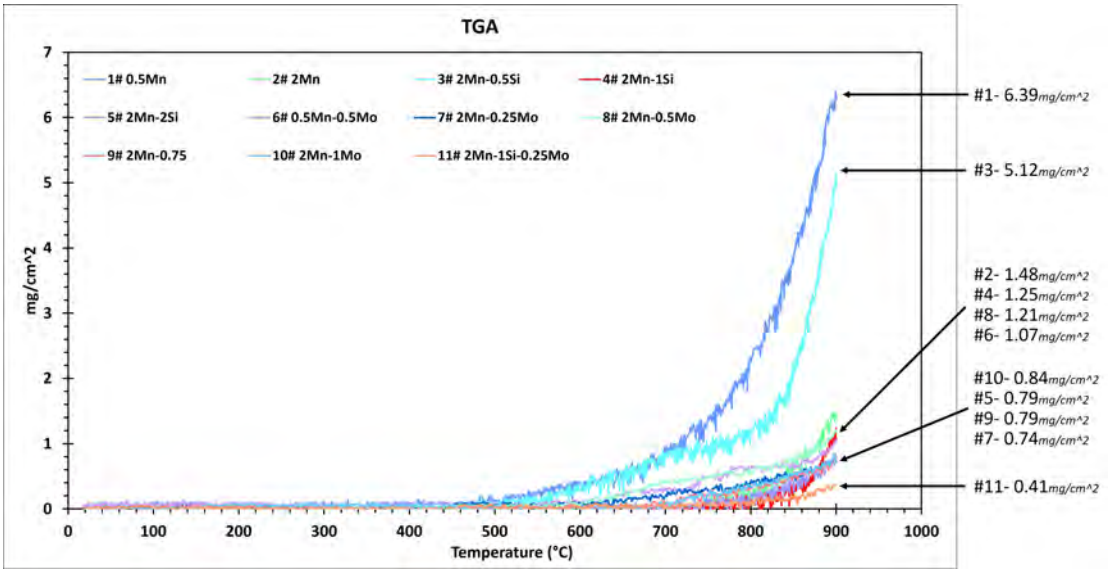

Figure 42: Mass gain as a function of temperature after continuous heating for 5 mins

Rate of Oxidation The TGA curve for the 11 RAP compositions investigated are displayed above; with the total mass gain operating as a function of temperature. Throughout this thesis, the y-axis on any figures for thermo-gravimetric analysis (TGA) will be referred to as (mg/cm^2), which stands for mass gain per unit area. The thermogram can help ascertain the influence of an alloying element on the thermodynamic and kinetic properties of the alloy. The critical temperature of oxidation was once again defined as; the temperature at which oxidation of the sample begins with a transition from a nil to an exponential segment.

The total mass gain for the 11 samples was negligible for the first 500°C then abruptly started to increase for 0.5Mn and 2Mn-0.5Si as previously discussed. The critical temperature of oxidation was also relatively low for 0.5Mn-0.5Mo and 2Mn-0.5Mo at 561°C and 587°C respectively. The mass for 0.5Mn-0.5Mo differs from the other compositions with a staggered oxidation curve. After a small initial volume of mass gain, the curve plateaus, holding just below 0.2mg/cm^2 until 720°C. The sample once again gains weight between 720°C -780°C, then plateaus until 860°C whereafter the trend continues. One possibility to explain this phenomenon was break-away; the composition was found to be extremely porous and brittle, its plausible that the oxide may have fractured/ broken away in sections allowing for rapid oxidation until a passive layer was reformed. Another plausibility could be due to an increase in kinetic energy, which may enhance the rate of diffusion and/or a phase transformation. Despite the early onset of external oxidation in 0.5Mn-0.5Mo, due to the low critical temperature of oxidation, the mass gain was still considerably less than that of 0.5Mn and 0.5Mn-0.5Si.

The final RAP composition, 2Mn-1Si-0.25Mo had the lowest weight gain of 0.41mg/cm^2 and the highest critical temperature of oxidation at 864°C. This further supports the in-

verse trend identified in figure 38 whereby an increase in the critical temperature of oxidation results in a decrease of total mass gained.

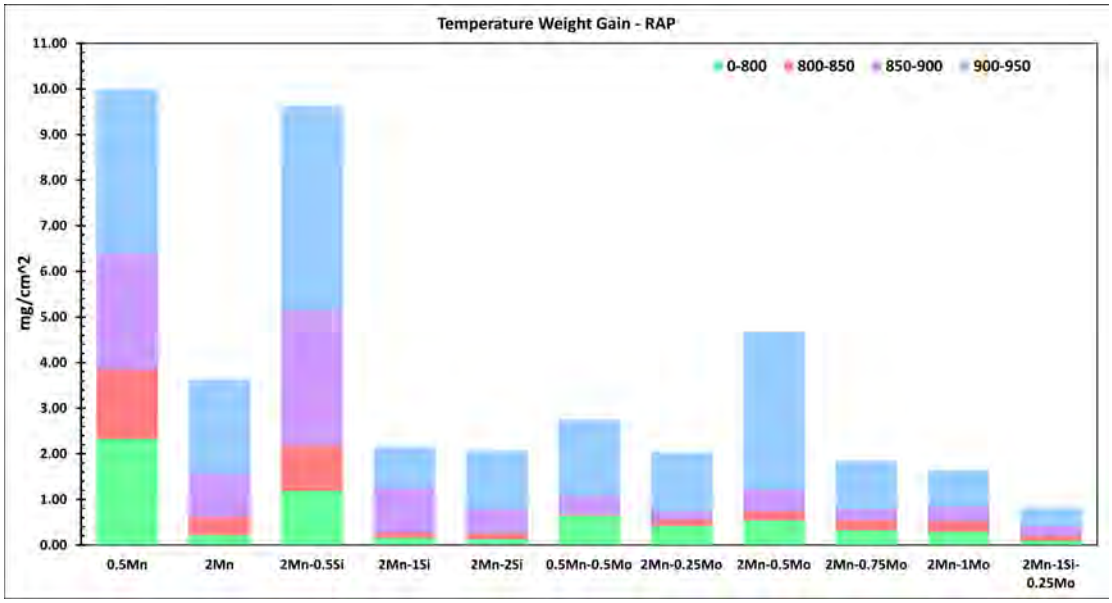

Figure 43: Temperature weight gain per increment of temperature

Mass Gain The total mass gain per increment of temperature was displayed in figure 43. Mass gain was the greatest for all samples between 900-950°C apart from 2Mn-1Si. The mass gain for Si additions above 1wt.% was negligible between 0-800°C, with sizeable mass gain not observed until 850-900°C.

2Mn-1Si-0.25Mo experienced the lowest total mass gain, with a relatively thin and adherent oxide. Although 2Mn-1Si-0.25Mo had the lowest mass gain it was not the thinnest. Thus, the results of the TGA weight gain should not be considered in isolation. The oxide was extremely porous, principally within the amorphous region. The high volumes of porosity would of formed a low-density oxide, accounting for the low mass gain and relatively thick oxide. 2Mn-2Si was the thinnest oxide but had a mass gain over 2x larger than 2Mn-1Si-0.25Mo. The higher mass gain of 2Mn-2Si may be due to the greater depth and density of the internal oxide region, which would have resulted in mass gain during formation and hindered external oxide growth. 2Mn-2Si also had a lower volume of porosity compared to 2Mn-1Si-0.25Mo of 18% and 29% respectively. 2Mn-1Si was of a similar thickness to 2Mn-1Si-0.25Mo however had a mass gain almost 3x greater. Similar to 2Mn-2Si, 2Mn-1Si had a lower volume of porosity compared to 2Mn-1Si-0.25Mo at 15% and a thicker band of internal oxidation.

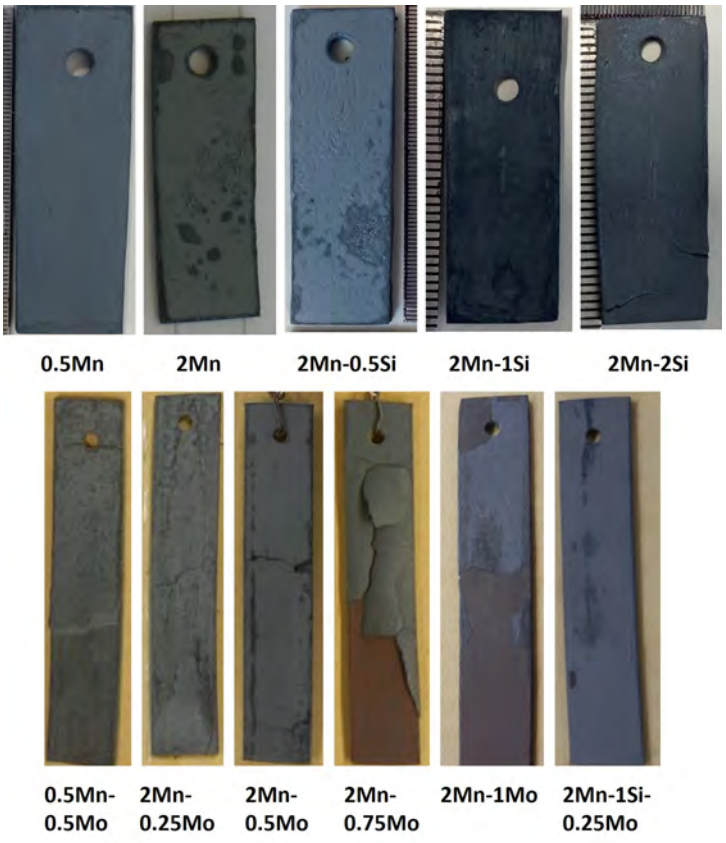

Figure 44: Samples after heat treatment and air cooling

Topography Post heat-treated samples are shown in figure 44. 2Mn underwent severe blistering with large blisters observed across the surface. An industrial standpoint would deem the topography of 2Mn to be extremely unfavourable, with the blister potentially resulting in rolled in defects. The formation of blister will be discussed comprehensively in chapter 7. Both 0.5Mn-0.5Mo and 2Mn-0.25Mo also blistered in a number of regions, however to a much smaller extent than 2Mn.
The increasing additions of Mo produced an increasingly brittle oxide with low mechanical stability. 2Mn-0.75Mo was observed to fracture in multiple places with 2Mn-1Mo experiencing the greatest area of failure with much of the oxide removed exposing the underlying metal. The additions of Si above 1wt.% produced very adherent oxides.

Morphology and Thickness The oxide thickness for the RAP compositions were scaled to size and displayed in figure 45. BSE images were used to represent the differences in oxide morphology. The graph illustrates the stark contrast between the developed oxide morphology for each composition. The additions of Si above 1wt.% produced convoluted and intricate oxide morphology's whilst the Mn and Mo additions produced a relatively simple and quintessential iron oxide. The increasing Mo additions drastically reduced the oxide thickness from 117µm to 45µm and substantially raised the critical temperature of oxidation, shown in table 7. The thickness of the magnetite top layer did not experience any considerable modifications and no internal oxidation was observed.

An internal oxide region approximately 6µm in thickness was observed for 2Mn-1Si and 2Mn-2Si, however their morphologies and density of oxidation differed. Both produced internal oxides containing intra-granular and inter-granular oxidation. 2Mn-2Si produced a greater density of spherical intra-granular oxides and extremely fine perturbed intra-granular oxides. The extremely fine dendritic structure was conjectured to be the growth front of the oxide.

	Oxide Thickness (µm)	**Magnetite Top Layer (µm)**	**Internal Oxide Depth (µm)**	**Weight Gain 0-950°C (mg/cm^2)**	**Critical Temperature (°C)**
0.5Mn	148.2	11.3	0.0	10.0	510.0
2Mn	44.8	5.0	1.0	3.6	758.0
2Mn-0.5Si	117.8	15.1	0.0	9.6	561.5
2Mn-1Si	59.4	9.2	6.4	2.2	813.5
2Mn-2Si	43.5	11.9	6.2	2.1	790.3
0.5Mn-0.5Mo	46.0	14.5	0.0	2.8	561.4
2Mn-0.25Mo	117.2	9.1	0.0	2.0	636.7
2Mn-0.5Mo	93.7	7.9	0.0	4.7	586.6
2Mn-0.75Mo	57.3	7.0	0.0	1.8	719.3
2Mn-1Mo	45.1	9.9	0.0	1.6	712.8
2Mn-1Si-0.25Mo	55.6	8.7	4.6	0.8	854.0

Table 7: Analysis of RAP samples

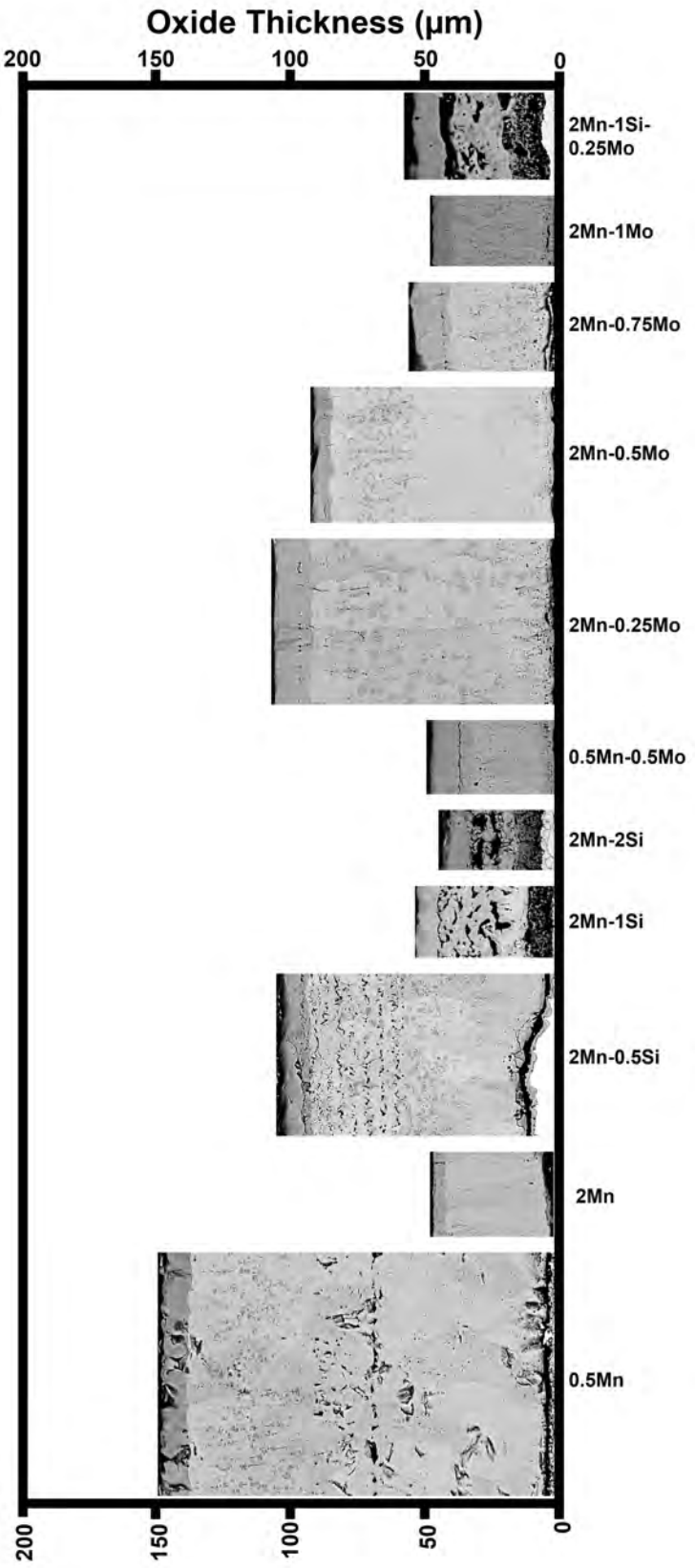

Figure 45: Scaled images used to show oxide thickness

5.4 Conclusions

RAP was used to investigate the formation of oxides associated with Mn, Si and Mo. The oxide thickness was shown to vary significantly depending on the alloying additions, ranging from 45µm to 148µm. The addition of 2Mn-2Si formed the thinnest external oxide and 0.5Mn formed the thickest external oxide. A pronounced magnetite top layer was present for all samples ranging from 5µm to 15µm in thickness.

- TGA analysis showed an inverse relationship between oxide thickness and the critical temperature of oxidation.
- 0.5Mn and 2Mn-0.5Si both exhibited external oxide layers over 100µm thick, with moderately low critical oxidation temperatures of 510°C and 560°C respectively.
- External oxide development was delayed in 2Mn-1Si-0.25Mo which exhibited the highest critical oxidation temperature at 854°C resulting in a substantially reduced oxide thickness of 56µm.
- Internal oxidation was observed within Si additions above 1wt.%, with a depth of approximately 6µm when paired with Mn.
- No measurable internal oxidation was recorded for the Mn-Mo additions.

Manganese

- Mn was present within the wustite phase and magnetite phase of all samples, often producing a negative stoichiometric gradient from the interface to outer oxide layer.
- Sub-surface depletion of Mn was detected near the oxide/ metal interface for 10µm, with a similar phenomenon observed with the Si compositions.

Silicon

- The addition of Si produced a complex and intricate oxide composed of many regions; however, a minimum fundamental addition of 1wt.% was requisite. Below 1wt.% it was found that an incomplete passivation layer was produced.
- The addition of 0.5Si in 2Mn-0.5Si was found to increase oxidation, seemingly due to an incomplete passivation layer resulting in the selective dissolution of Fe. The oxidation rate was drastically accelerated, and the critical temperature of oxidation was lowered.
- The addition of 1Si in 2Mn-1Si raised the critical temperature of oxidation from 521°C to 813°C and dramatically reduced the oxide thickness. The resulting scale was a complex porous oxide with 4 distinct regions:

1. The upper magnetite region
2. The lower magnetite region
3. The amorphous region
4. The internal oxidation region

- The amorphous region was composed of 2 distinct spinel phases, with the lighter spinel containing a lower volume of Si and the darker spinel containing a higher volume.
- A transition was noted from light to dark spinel as the oxide/ metal interface was approached. WDS analysis was used to highlight the stoichiometric gradient of Si through the amorphous region.
- The addition of Si promoted porosity in the external oxide, decreasing the density of the scale. Thus, the results of TGA weight gain should not be considered in isolation.

Molybdenum

- Mo was combined with 2Mn in increasing additions from 0.25-1 wt%. An inverse relationship was established whereby increased Mo content resulted in a decrease of oxide thickness from 117μm to 45μm.
- Oxide thickness was also decreased with an increase of the Mn:Mo ratio; 0.5Mn-0.5Mo had the highest ratio of 1:1 and produced the thinnest oxide. A higher Mn:Mo ratio was also found to decrease the adherence of the oxide to the underlying substrate.
- A considerable raise in the critical temperature of oxidation was detected between 2Mn-0.5Mo and 2Mn-0.75Mo, rising from 586°C to 719°C. The significant increase in critical temperature of oxidation was also accompanied by a decrease in oxide thickness from 94μm to 45μm. Additions above 0.75Mo produced a definite porous band of oxide at the scale/ metal interface, hindering the growth of oxide.
- 2Mn-1Mo produced the most advantageous scale from an industrial standpoint. The oxide was non-adherent and light, resulting in low yield loss, with a critical temperature of oxidation above 700°C. Furthermore, 2Mn-1Mo experienced a depressed weight gain between 900-950°C; a key critical industrial working temperature.

2Mn-1Mo produced the best oxide scale morphology from an industrial standpoint of the 11 compositions examined.

6 Oxidation of Industrial Steels

6.1 Introduction

The hot rolling of steels represents a crucial step to achieve a finished product of high surface quality. The ever increasing demands to increase throughput and quality of material produced by hot-strip mills has resulted in very specific regimes and scheduling rules [97].

The phenomena of oxidation at high temperature was due to the thermodynamic instability of a base metal or alloy. Under most conditions pure metals and alloys are thermodynamically unstable. Thus, due to the high processing temperatures of hot-strip mills oxidation was both inevitable and toilsome to govern.

Oxidation within hot-strip mills lowers the surface quality of strip products and may result in numerous defects; producing cutbacks and potential customer rejections along with possible customer litigations.

Tertiary scale produced prior to the finishing mill was of the utmost importance because of the severity of defects it may cause. Tertiary scale was at risk of fracture and becoming embedded during rolling in the finishing mill resulting in rolled-in scale. The mechanical behaviour of scale was still poorly understood [97].

Oxidation will occur because the atoms at the surface of a respective base metal have fewer respective neighbours than those within the bulk of the metal matrix [6]. The atoms at the surface of the metal are thence highly reactive and will react to produce a more thermodynamically stable product. The reactant product will be unique for each steel grade and composed of a multitude of phases.

Thus, in order to keep productivity and quality of a hot-strip mill as high as possible its essential understand the effects of chemical composition, temperature and elapsed time reaction on scale formation. Thermodynamic investigation of a number of key industrial steel grades characterised by distinct chemical compositions was conducted within this chapter in order to gain a better understanding of the kinetics and of the reactant products formed. An increased emphasis of analysis was placed on DP800 due to its importance in industry and in-order to better understand the oxidation rates observed.

6.2 Experimental procedures

6.2.1 Steel compositions

This chapter endeavours to investigate various steel grades characterised by distinct chemical compositions to discern the influence of composition on oxidation rates. Notably, these steel grades are known to suffer from detrimental defects resulting from oxidation during processing at Tata Steel. Table 8 shows the compositions of the industrial steel grades investigated within this chapter. All material was sourced and provided by Tata Steel Europe.

	C	Si	Mn	Al	Cr	Typical use
Interstitial Free (IF)	0.004	0.019	0.1	0.004	-	Drawability Applications
Low Carbon	0.047	0.019	0.230	0.036	-	Low Cost Application
3812	0.150	0.100	0.860	0.036	0.028	Tinplate and Tubes
S63	0.080	0.150	1.140	0.026	0.370	High Strength Steel
DP800 Hyperform	0.155	0.440	2.032	0.589	0.028	Automotive
B32	0.003	3.200	0.200	0.900	-	Electrical Steel

Table 8: Composition of steels grades investigated within this chapter (wt%)

6.2.2 TGA

Heat Treatments for IF, Low Carbon, 3812, S63 and B32 The heat treatments were designed to discern how the industrial steel grades would kinetically perform at key temperatures used in a conventional hot-strip mill for rolling. Each sample was sequentially inserted into the furnace. To prevent oxidation, they were all purged with argon and heated in an argon atmosphere. Once the target temperature was reached, the samples were held at that temperature under argon for 5 minutes. Following this, oxygen was introduced into the furnace at a rate of 10 litres per minute. After a duration of 600 seconds, the samples were extracted from the furnace and allowed to cool in ambient air. Temperatures investigated include 800°C, 900°C, 1000°C, 1100°C and 1200°C for all compositions. S63 underwent additional testing at 1050°C, 950°C, 850°C, 700°C and 500°C. B32 underwent additional testing at 1120°C, 1140°C, 1180°C and 1200°C and was held for 700s to investigate the formation of fayalite.
One continuos heat treatment was conducted on interstitial free (IF) steel in order to discern the critical temperature of oxidation and to serve as a comparison for the RAP compositions investigated in chapter 5. The sample was inserted into the furnace and subjected to continuous heating for 5 minutes and 30 seconds, with a heating rate of 3°C per second, reaching a maximum temperature of 950°C.
Sample geometry was 65mm x 25mm x 2mm for all samples. Due to the large number of heat treatments and time constraints no repeats were conducted.

Heat Treatments for DP800 DP800 underwent more extensive testing compared to the other industrial steel grades examined, owing to its significant industrial relevance

and its critical role as a key ultra-advanced high-strength steel.
Several isothermal heat treatments were carried out on DP800 samples. To prevent oxidation, all samples were flushed with argon and heated in an argon atmosphere. Upon reaching the desired temperature, the samples were maintained at that temperature under argon for 5 minutes. Subsequently, oxygen was introduced into the furnace at a flow rate of 10 litres per minute. After the specified duration, the samples were removed from the furnace and air-cooled. Temperatures investigated at 5mins and 12mins include 800°C, 900°C, 1000°C, 1100°C, and 1200°C. One pro-longed isothermal heat treatment was conducted at 800°C for 2 hours.
One continuos heat treatment was conducted in order to discern the critical temperature of oxidation. The sample was inserted into the furnace and subjected to continuous heating for 5 minutes and 30 seconds, with a heating rate of 3°C per second, reaching a maximum temperature of 950°C.
For short oxidation tests lasting 10 seconds or less, the sample geometry size was approximately 10mm x 10-20mm x 2mm. Temperatures investigated at 10s include 800°C, 850°C, 900°C, 950°C and 1000°C. All other heat treatments followed dimensions of 10mm x 60mm x 2mm. Due to the large number of heat treatments and time constraints no repeats were conducted.

6.3 Results and Discussion

The results and discussion will be split into 2 sections for this chapter on industrial grades of steel. Part 1 will discuss the results obtained using characterisation techniques and part 2 will discuss the results obtained using TGA.

6.3.1 IF

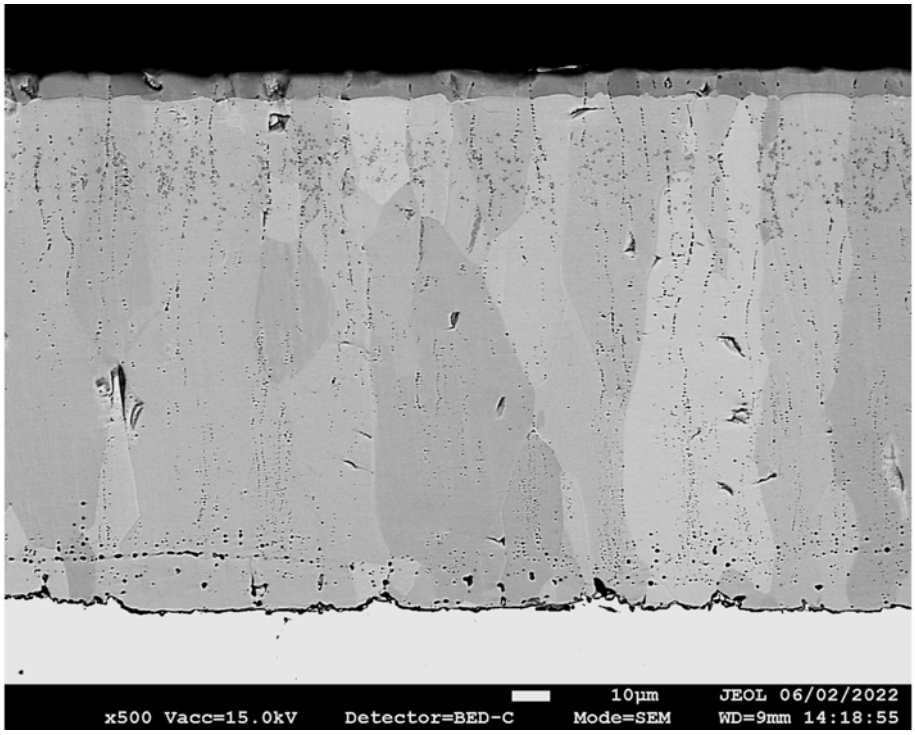

(a) Oxide overview

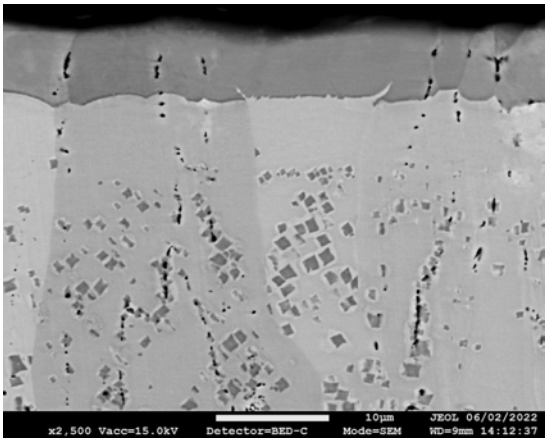

(b) Magnetite precipitates and magnetite top layer

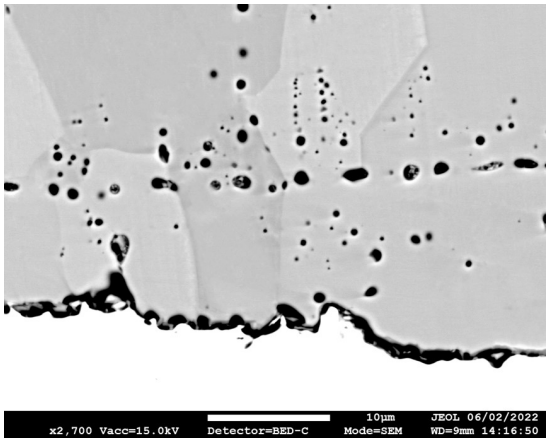

(c) Porosity located at oxide-surface interface

Figure 46: Oxide morphology of IF steel

An interstitial free (IF) steel was heat treated and investigated in order to use as an industrial standard reference due to its low alloying chemistry. The IF steel underwent a continuous heat treatment for 5 minutes, with a heating rate of 3°C per second; the same as the RAP samples. The oxide morphology of the post heat treated IF steel

		Wt%	
	Region	**Fe**	**O**
1	Oxide Top Band	72.6	27.4
2	Oxide Matrix Top	71.6	25.9
3	Oxide Matrix Bottom	74.5	25.5

Table 9: WDS point scan measurements on IF Steel

displayed in figure 46. The oxide was very simplistic, producing a thick adherent scale consisting of 3 well established oxide layers. The sample was profoundly like that of RAP sample 0.5Mn figure 5.3.1, which contained the lowest volume of alloying additions from chapter 5. The oxide thickness was very consistent throughout and was found to be around 141µm.

The IF steel contained significant porosity appearing in lateral bands towards the base of the oxide and vertical intra-granular bands throughout the wustite phase. The formation of these pores was discussed previously in 2Mn-0.5Mo figure 5.3.8, with the lateral bands of porosity conjectured to form due to vacancy injection and the intra-granular pores due to internal stresses. The average pore size was recorded at 0.117µm.

Magnetite precipitates were found consecutively distributed through the top 50 µm of the wustite phase, averaging at 0.387µm in size. The observed precipitates in the IF steel were on average smaller than the precipitates observed in 0.5Mn and less numerous. Another distinction between the 2 was the magnetite seam. A clear and definite magnetite seam was present throughout the 0.5Mn sample while the IF steel did not contain one. As previously discussed in 2Mn-0.5Si figure 21, magnetite seams generally form after a gap develops between the steel substrate and outer oxide. The absence of a magnetite seam in the IF steel may be attributed to the close adherence of the oxide to the steel. Its conjectured the well adhered interface has resulted in an iron oxide rich in cations; evidenced by the diminished presence of magnetite precipitates and lack of a magnetite seam.

A distinct magnetite top layer was observed, as with all the RAP samples. The magnetite top layer was 7µm in thickness, substantially thinner than the RAP compositions with an oxide thickness above 100µm. The WDS analysis confirms the presence of the magnetite and wustite phases.

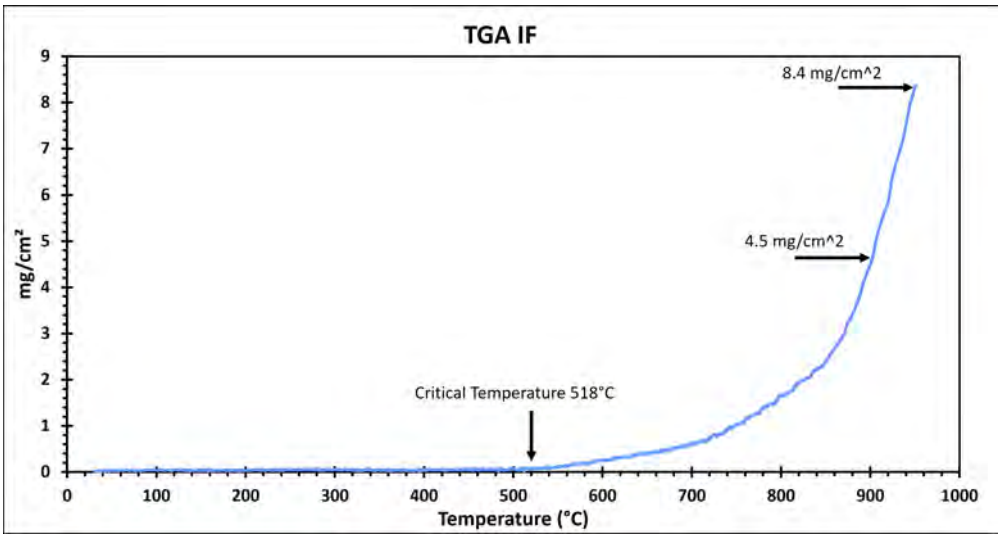

Figure 47: Continuous heating curve of IF steel

The total mass gain as a function of temperature for the IF steel is displayed in figure 47. The critical temperature of oxidation was 518°C, slightly lower than the established wustite temperature of formation of 560°C [98]. IF steel has a low addition of Mn at 0.1wt.%. MnO has been shown to stabilise the wustite phase, potentially lowering the critical temperature of oxidation for wustite. This phenomena was also observed in 0.5Mn which had a critical temperature of oxidation of 516°C [79]. The total weight gain at 950°C was 8.4mg/cm^2.

6.3.2 DP800

DP800 A number of isothermal heat treatments were conducted to deduce the oxide formation of a dual phase steel. The samples produced an exceptionally low rate of oxidation. The morphology and topography of the samples was investigated.

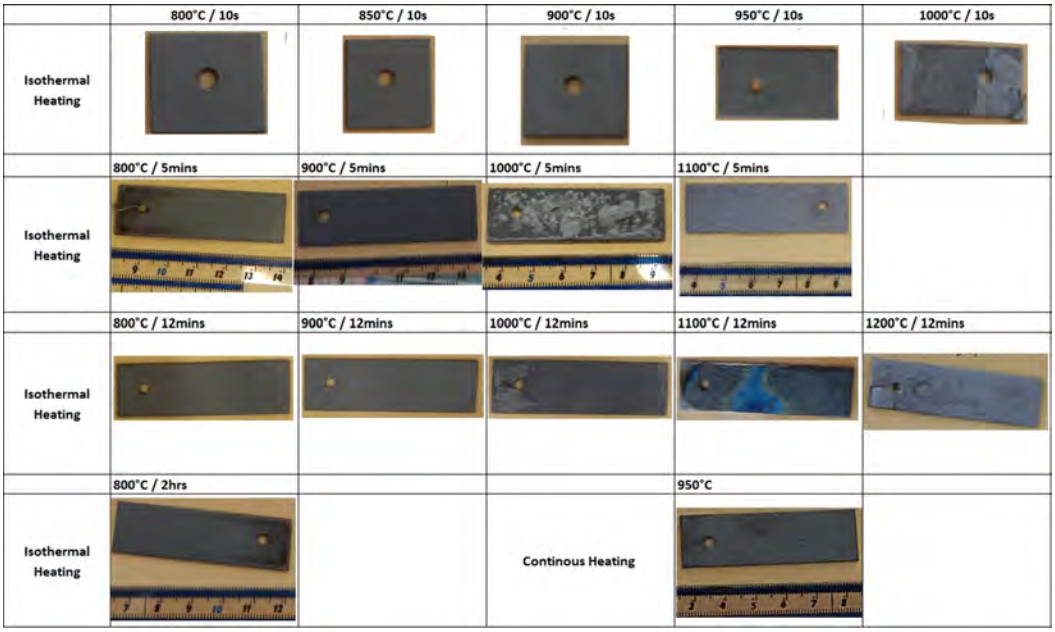

Figure 48: DP800 samples after heat treatment and air cooling

Topography of heat treated samples Post heat treated samples are shown in figure 48. At higher temperatures breakaway of the oxide was observed. Above 1000°C the oxide began to blister severely and spallation of the surface occurred. The lifetime of the oxide at 1000°C was extremely short with failure noted from heat treatments as short as 10s. An industrial standpoint would deem the topography of the surface at 1000°C to be unfavourable due to the risk of rolled in scale. At 800°C the scale was smooth and adherent providing an optimal surface for rolling even after 2hrs of heating.

6.3.3 DP800 10s

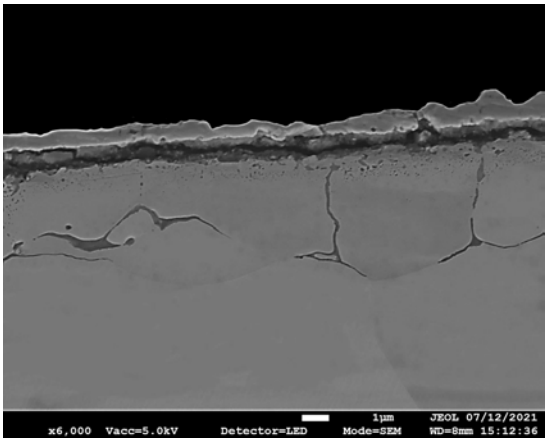

(a) Oxide morphology at 800°C after 10s

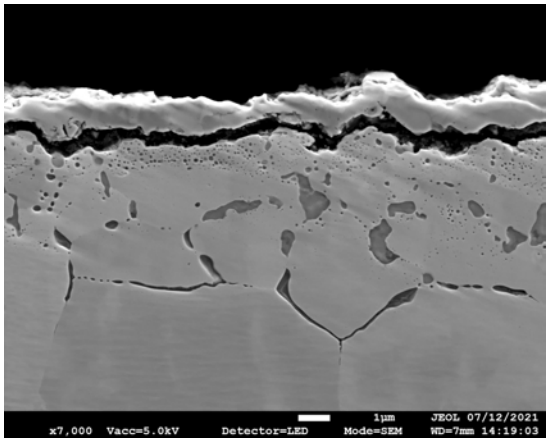

(b) Oxide morphology at 850°C after 10s

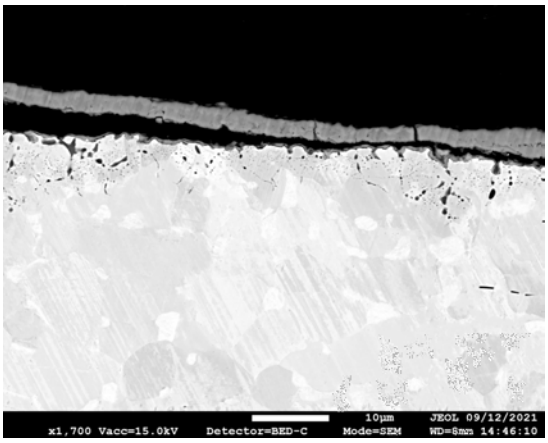

(c) Oxide morphology at 950°C after 10s- Blister

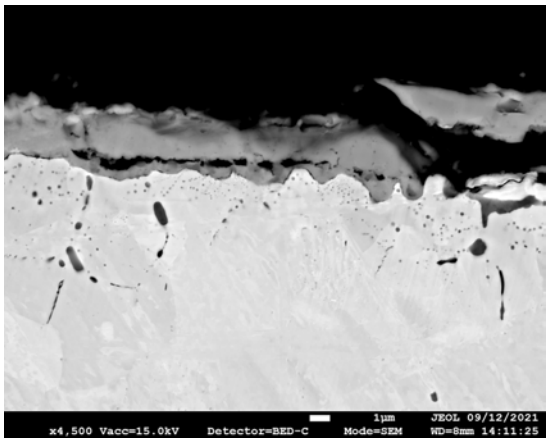

(d) Highlight of oxide morphology at 950°C after 10s showcasing IOZ

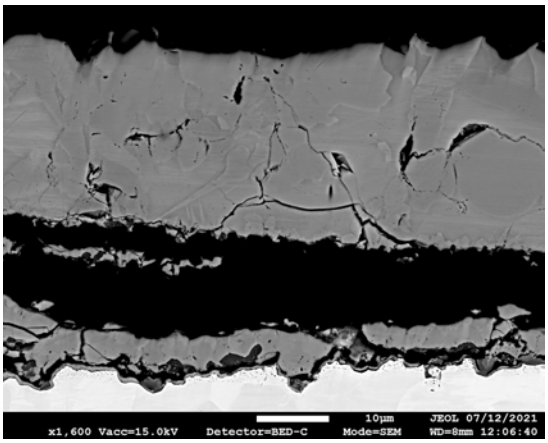

(e) Highlight of oxide morphology at 1000°C after 10

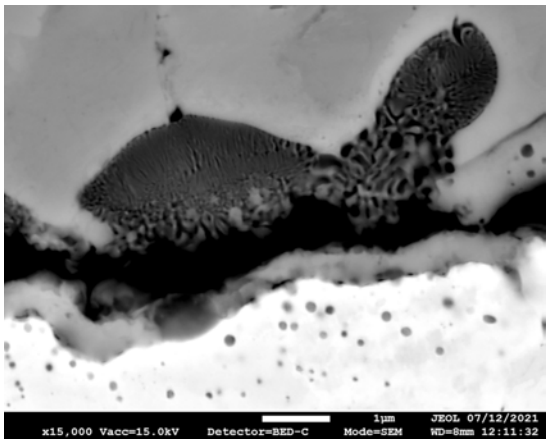

(f) Highlight of oxide morphology at 1000°C after 10s showcasing IOZ

Figure 49: Oxide morphology of DP800 after 10s

A number of DP800 samples were heat treated under isothermal conditions for 10secs at varying temperatures. Samples were ground and polished prior to heat treatment to remove any pre-existing oxides. External and internal oxidation was apparent within all heat-treated samples; evident within figure 49.

The sample oxidised at 800°C produced a moderately thin and continuous external

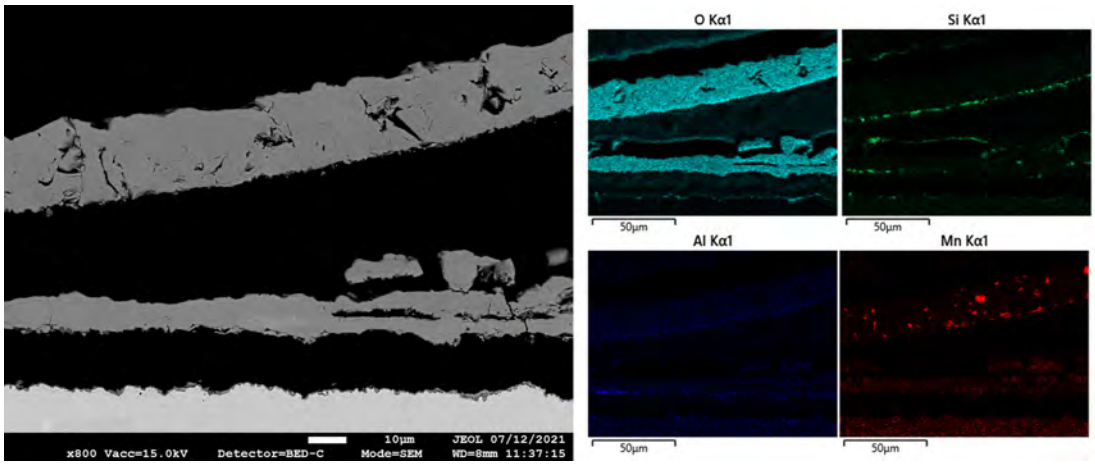

Figure 50: EDS scan conducted on blister formed on DP800 at 1000°C for 10s

oxide of 1µm (see Appendix 139). The external oxide thickness was recognised to increase with temperatures to 1.5µm at 850°C, 2.6µm at 900°C, 3.0µm at 950°C and 26.4µm at 1000°C (see Appendix 140). A summary of the oxide thickness was displayed in table 10.

The external oxides contained no magnetite precipitates and had little or no porosity. At 950°C several blisters were observed through the oxide. The oxide morphology for 1000°C varied greatly compared to the lower temperatures and was markedly thicker. The external oxide segregated into multiple regions splitting throughout the thickness and creating blisters, shown in figure 50. The oxide was found to fracture and split around a spinel phase that was not present at lower temperatures. Using EDS, the spinel phase was predominantly found to be from Si and Al (see Appendix 141). The spinel phase observed in figure 49f, tended to be located at the interface between the external oxide and the internal oxide. Its conjectured that this spinel phase was previously internal oxidation that grew and was dragged by the moving interface [99].

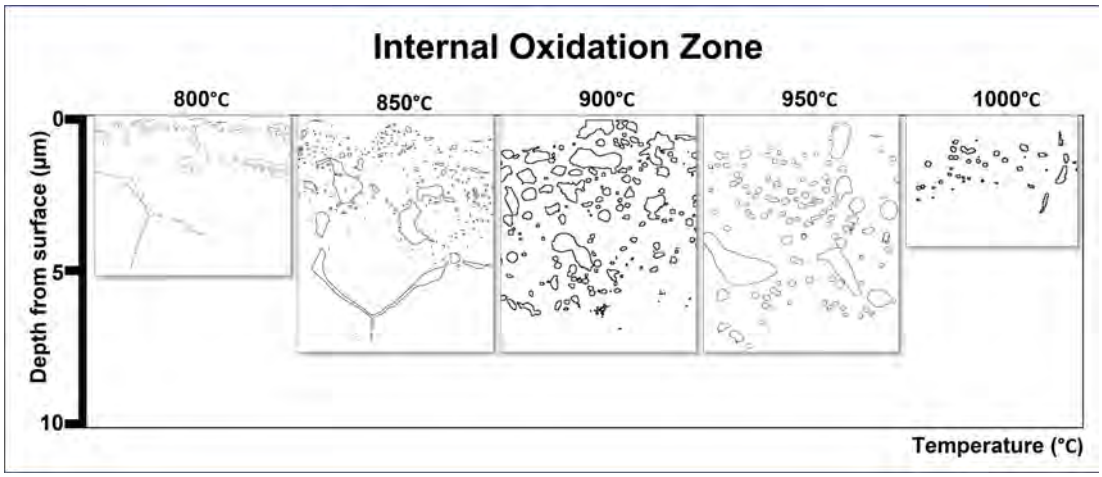

Figure 51: Internal oxidation depth measurements for DP800 after 10s heating produced using image J

Internal oxidation was detected within all of the heat-treated samples. At 800°C the depth of internal oxidation was more than twice the thickness of the external oxide. The

internal oxidation permeated the substrate deepest along the grain boundaries, forming a film like inter-granular oxide, visible in figure 51. A lateral band of spherical intra-granular oxides were present close to the interface but did not penetrate the subsurface as far as the inter-granular oxidation at the grain boundaries. This phenomenon may be explained due to the increased ease of diffusion at grain boundaries. The oxygen may travel faster along these grain boundaries resulting in a greater concentration of solute oxygen further into the alloy.

At 850°C the oxidation also permeated the substrate deepest along the grain boundaries. The average depth of internal oxidation was twice that of 800°C at 5.6µm compared to 2.7µm. The external oxide was also thicker at 850°C but not by a substantial amount.

At 900°C and 950°C the oxide shifted to more of a globular morphology and increased in permeation depth to 7µm and 7.2µm respectively. The largest oxides were noted at the grain boundaries however intra-granular oxides were also present throughout the thickness of the IOZ.

The oxide morphology shifted again at 1000°C to an almost completely spherical morphology with a considerably reduced permeation depth of 1.73µm. In contrast the external oxide was staggeringly thicker at 26.4µm; almost 10 times more than 950°C which had a thickness of 2.95µm.

	Temperature (°C)	Oxide Thickness (µm)	Internal Oxidation Depth (µm)
10s	**800**	1.01	2.72
	850	1.52	5.63
	900	2.64	7.02
	950	2.95	7.22
	1000	26.42	1.73

Table 10: Oxide thickness measurements for DP800 samples heat treated for 10s

6.3.4 DP800 5mins

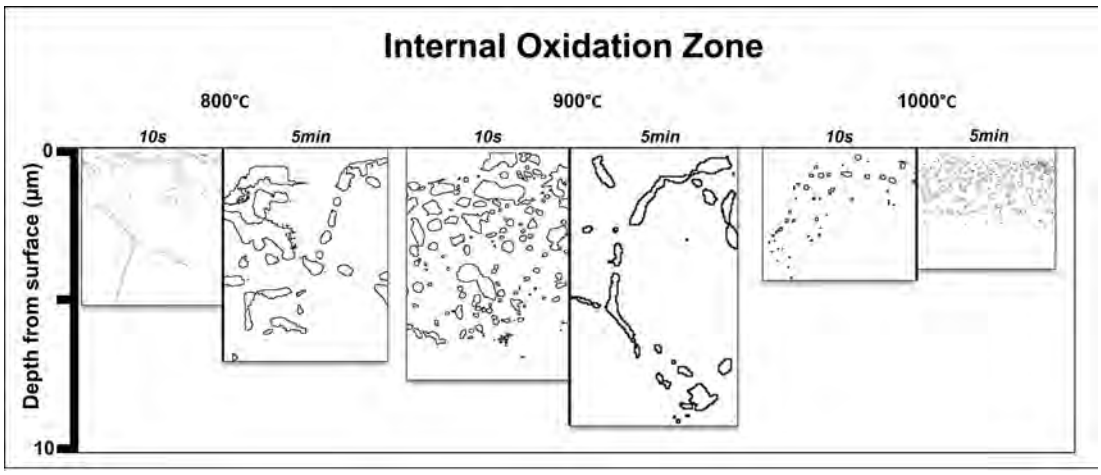

Figure 52: Internal oxidation depth measurements for DP800 after 5mins heating produced using image J

Internal oxidation was observed for all the DP800 samples heat-treated for 5 minutes. The internal oxidation was coarser and on average permeated deeper into the substrate

than that of the previous 10 second heat-treated samples. Correspondingly, the external oxide was significantly thicker at 5 minutes, increasing from 1µm to 9.7µm for 800°C, 2.64µm to 11.5µm for 900°C and 26.4µm to 41.5µm for 1000°C. A summary of the oxide thickness was displayed in table 11.

The increase in external oxide thickness was significantly greater than the increase in internal oxidation. This was in agreement with Wagners [100] proposal that a critical volume fraction of internal precipitates will govern the transition from internal to external oxidation and internal oxidation will reach a maximum penetration depth.

During the initial stages of linear growth oxygen diffusion was the key driving factor. Internal precipitates will rapidly start to form and eventually begin to inhibit the inward diffusion of oxygen [101]. Nuclei will then start to coalesce and grow laterally forming a dense layer of oxide [99]. This effect was observed for 800°C at 10 seconds, where the internal precipitates at the interface can be seen to form sideways with some coalescing. Deeper into the IOZ, oxidation only follows the grain boundaries. Once the critical volume fraction of precipitation occurs, oxygen diffusion becomes blocked and scale formation will transition almost entirely to external. Internal oxidation will reach a maximum permeation depth due to the decrease of solute oxygen with the increasing depth of the IOZ. Thus, the driving force for oxide precipitation at the internal reaction front will decrease with depth into the IOZ [47]. At 800°C for 5 minutes the internal oxidation was extremely coarse, and the external oxide moderately thicker affirming Wagner's proposal.

The IOZ behaved differently for 1000°C at both 10 seconds and 5 minutes compared to the lower temperatures investigated. The IOZ and precipitates were smaller than those of 900°C and 800°C. It was inferred that the higher temperature resulted in an increase ease of diffusion for both anions and cations. The result was a thinner but thicker lateral band of internal precipitates, shown in figure 52.

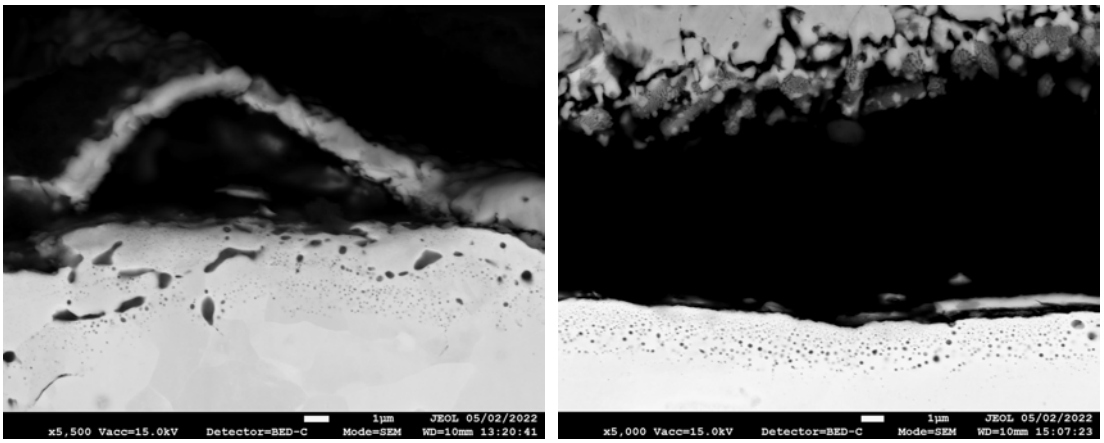

(a) Small blister produced after heating at 900°C 5mins

(b) detachment of oxide scale after heating at 1000°C 5mins

Figure 53: Internal oxidation zone of DP800 after heating for 5mins

Time	Temperature (°C)	Oxide Thickness (µm)	Internal Oxidation Depth (µm)
5min	800	9.70	6.41
	900	11.53	7.72
	1000	41.50	2.28

Table 11: Oxidation thickness measurements for DP800 samples heat treated for 5mins

6.3.5 DP800 1200°C for 12mins

The oxide morphology for a DP800 sample, isothermally heat treated at 1200°C for 12 minutes, was displayed in figure 54. The subsequent oxide was an extraordinarily intricate and complex multi-phase scale. Due to the profoundly convoluted nature of the oxide will be categorised into 4 distinctive regions. The 4 regions will now be categorised as;

1. Upper External Oxide
2. Lower External Oxide
3. Interface
4. Internal Oxidation Zone (IOZ)

The upper external oxide includes the outer magnetite layer and the adjacent wustite with small magnetite precipitates, shown in figure 54c. The lower external oxide was the area below figure 54c. The thickness of the oxide greatly surpassed all other DP800 samples, averaging at 331µm, a catastrophic volume of oxidation.
In region 1 the outer magnetite layer was approximately 120µm, with an increased thickness towards less adherent areas. An additional outer oxide layer, supposed to be hematite due to the dark contrast in the BSE image, was measured at 24µm. The magnetite precipitates within the wustite zone varied in morphology and size. The larger precipitates had a flower like formation and the smaller precipitates a classic square face. The larger precipitates are likely the result of localised nucleation through the decomposition of wustite during the cooling process [102]. The large precipitates formed roughly 30µm below the magnetite top layer favouring, higher growth rates and lower nucleation rates. The flower like precipitate in the centre of figure 54c has a number of dendritic arms growing outwards into the wustite. The oxidation temperature was below that of the liquidus temperature suggesting the dendritic morphology of this larger precipitate was a solid-state transformation [26]. The similar cubic crystal structures of wustite and magnetite would result in low inter-facial energies and fast kinetics, ensuring a smooth interface. Thus, the solute diffusion of the magnetite from the supersaturated wustite would produce a precipitate shape similar to that of the dendrites found in solidification [103].
Region 2 was a complex amalgamation of many phases. Fayalite was observed throughout the region and was often encompassed by magnetite. Fayalite would have been liquid at the oxidation temperature of 1200°C; liquid fayalite phase was evident at the

metal/ scale interface and travelled upwards through the external oxide towards the outer environment. Due to the encompassing magnetite surrounding the fayalite phase, its presumed that during the liquidus stage the fayalite acted as an oxygen highway, rapidly enriching the surrounding oxide and helping form the large magnetite islands observed within the lower external region. Figure 54c shows further evidence of this phenomena in the bottom right hand corner of the BSE image; with dendritic magnetite growing outwards into the wustite from the fayalite phase.

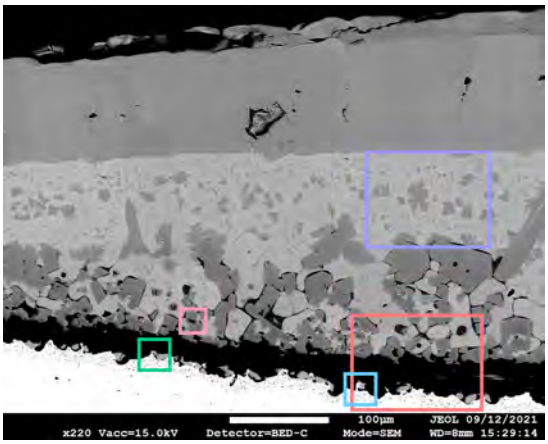

(a) Through thickness oxide morphology

(b) Lower external oxide

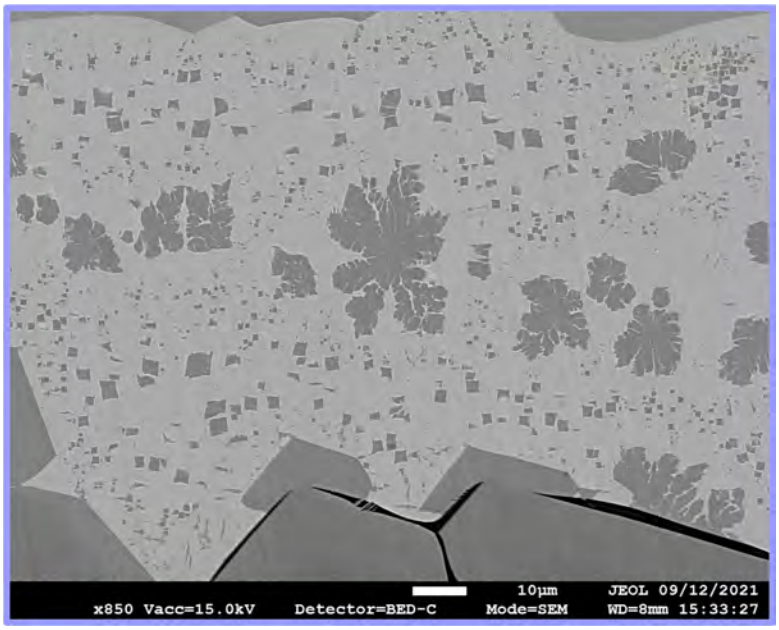

(c) Upper external oxide

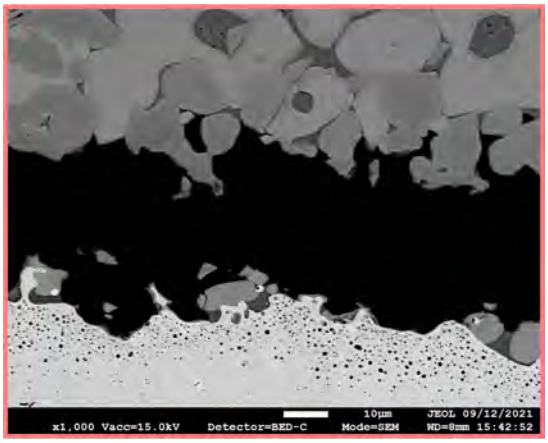

(d) Multiphase region

(e) Interface and IOZ

Figure 54: Oxide morphology of DP800 steel after heating for 12mins at 1200°C- Thick convoluted oxide containing multiple oxide phases

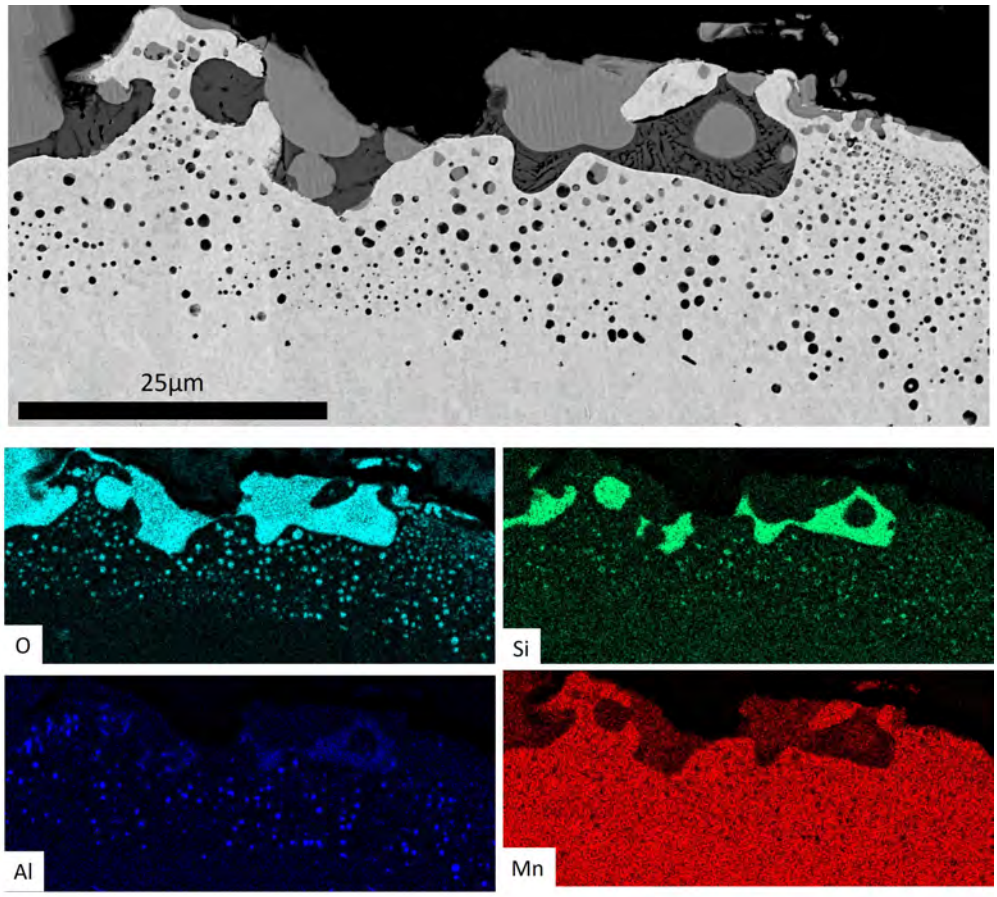

Figure 55: EDS map conducted on the internal oxidation zone of DP800 after heating at 1200°C for 12mins

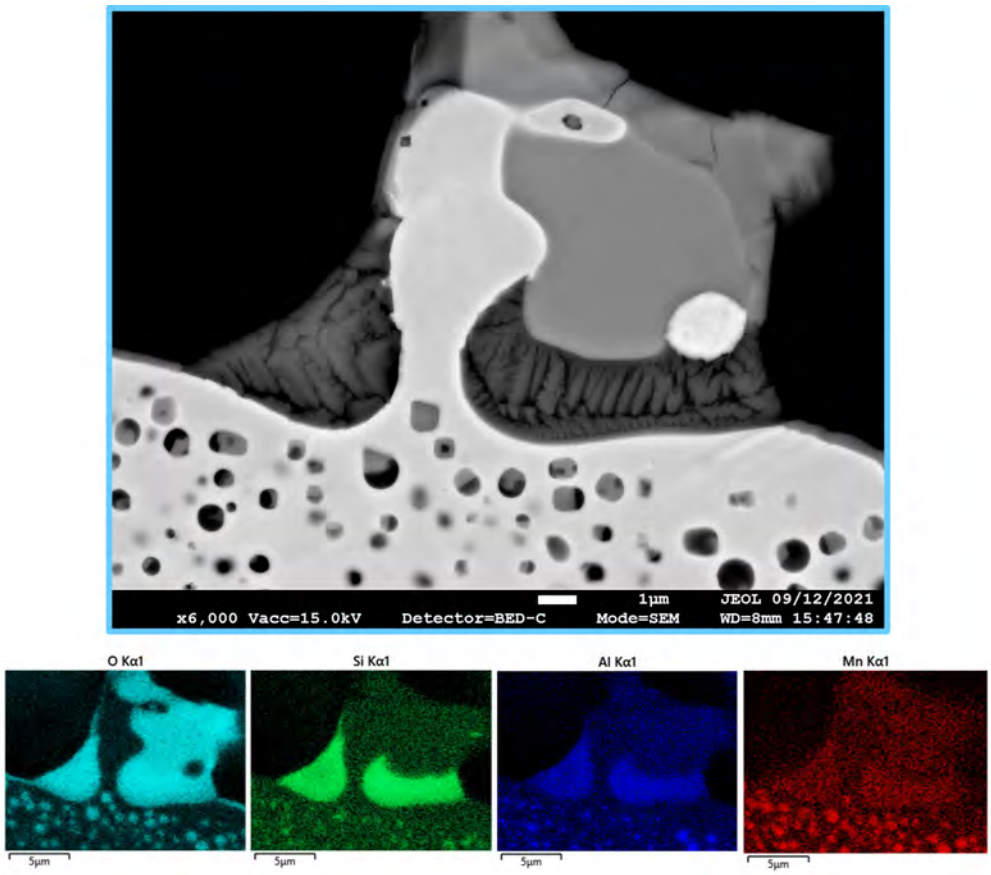

Figure 56: EDS map conducted on DP800 interface region between oxide and substrate after heating at 1200°C for 12mins

Region 3 was a convoluted formation of many different oxides. The interface was an extremely brittle region with the external oxide shearing off and becoming completely in-adherent throughout most of the sample. The brittleness within this region was attributed to the formation of oxides with Al. The EDS and WDS measurements in figures 56 55, show the presence of Al throughout the interface, notably in the darker oxide and internal oxide precipitates. The presence of Al was not detected at any discernable levels within the external scale.

A complex eutectic was formed between the fayalite and Al rich oxide, with the Al rich oxide producing a dendritic structure within the liquid fayalite background matrix. Its conjectured that the formation of the eutectic phase resulted in large in-coherencies between the eutectic and the surrounding the oxides. The large in-coherencies resulted in break away and mechanical failure of the oxide scale. The EDS maps show regions of entrapped iron completely encompassed by the surrounding oxides. The regions of entrapped iron were surrounded by both magnetite and the fayalite eutectic. The remaining oxide attached to the substrate was patchy and approximately 6µm in thickness.

An internal oxidation zone formed beneath the inter-facial region. The depth of internal oxidation was substantially greater in comparison to that of the DP800 samples oxidised at lower temperatures. The morphology of the internal oxide precipitates was closely related to that of the samples oxidised at 1000°C.

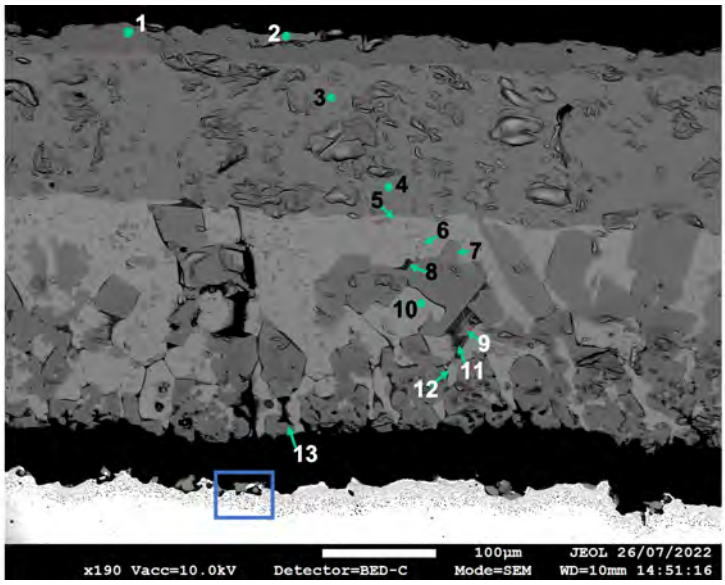

(a) WDS reference image for points 1-13

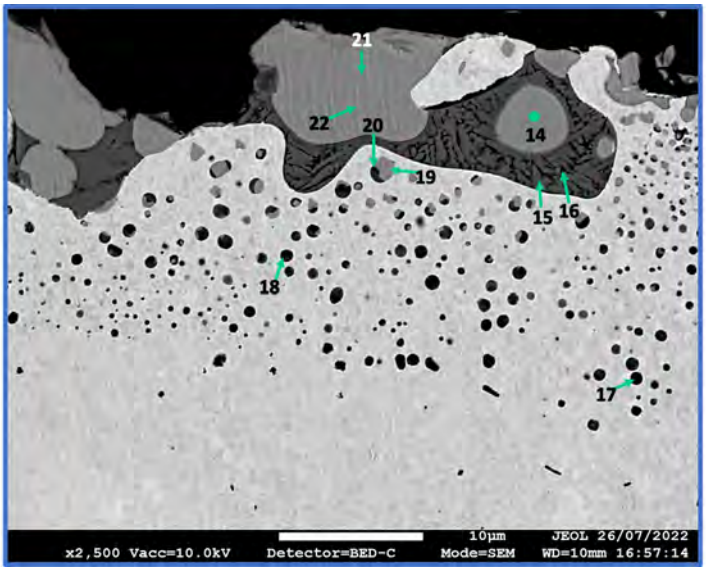

(b) WDS reference image for points 12-22

		Wt%							Wt%				
		Fe	O	Si	Al	Mn			Fe	O	Si	Al	Mn
Spectrum	1	70.93	29.07				Spectrum	12	68.40	25.96	*0.47*	*0.14*	*5.03*
	2	70.72	29.28					13	67.77	29.17	*0.42*	*1.84*	*0.80*
	3	71.41	28.59					14	69.78	24.98	*0.20*	*0.56*	*4.48*
	4	69.83	30.17					15	45.66	32.88	*15.07*	*2.50*	*3.90*
	5	72.51	27.49					16	60.32	19.22	8.82	4.56	7.08
	6	70.77	29.23					17	20.66	24.99	1.90	24.59	27.85
	7	70.58	29.42					18	27.22	24.76	3.95	14.46	29.62
	8	46.89	32.31	11.53		9.27		19	65.27	23.55	0.16	0.27	10.75
	9	69.01	28.44	*0.45*	*1.03*	*1.07*		20	38.11	23.95	5.78	18.15	14.02
	10	69.07	24.71	*0.33*	*0.09*	*5.80*		21	70.04	*25.52*	*0.20*	*0.59*	3.65
	11	45.94	33.01	12.22	*0.17*	8.67		22	71.13	*24.56*	*0.22*	*0.58*	3.51

(c) WDS point scan measurements

Figure 57: WDS analysis conduced on DP800 heated at 1200°C for 12mins *(Highlighted cells EDS)*

At temperatures examined below 1000°C oxidation was primarily inter-granular, however above this threshold it transitioned to intra-granular. The internal oxide precipitates were smaller at higher temperature, favouring higher nucleation rates with lower

growth rates. The more uniform dispersion and size at high temperature was probably a result of the increased flux of anions. At high temperatures the entropy of the system was increased, and both the anions and cations may move with increased freedom. This was due to heightened kinetic energy and thus transport of ions was not solely limited to areas of high inter-facial energy such as grain boundaries. WDS and EDS analysis show that the internal oxide precipitates are primarily a mixture of Mn and Al oxides.
In figure 57, WDS spectra 1-7 prove that region 1, the upper external oxide, was entirely composed of iron oxides. Spectra 8 and 11 show the presence of fayalite within the lower external oxide, primarily alongside magnetite. The compositional structure of the fayalite was $(Fe_{1-x}, Mn_x)_2SiO_4$.
Spectra 17-20 were used to identify the different compositions of the internal oxide precipitates. The BSE image in figure 57b shows 3 different internal oxide precipitates; darker, lighter and a combination of the two. The darker precipitates in spectra 17 and 18 were primarily found deepest into the substrate and contained a large wt% of Al and Mn. The lighter precipitates were observed closest towards the inter-facial region primarily towards the fayalite. It was assumed that the precipitates close to the interface were depleted of Al, Si and Mn due to the formation of richer phases, such as fayalite depleting the local area. Spectra 19 and 20 highlight this phenomenon, where spectra 19, closest to the eutectic fayalite phase, was reduced but spectra 20 still contained a large wt% of Al. The result was a number of fully depleted internal oxide precipitates and some partially depleted precipitates.

6.3.6 DP800 800°C 2hrs

The morphology of a DP800 sample oxidised at 800 for 2hrs was displayed in figure 58. Even with an extended period of oxidation the scale was substantially thinner than that of the sample oxidised at 1200°C for 12mins at 22.41µm and 331.3µm respectively. The internal oxidation was primarily focused along the grain boundaries similar to that of the previous samples oxidised at 800°C for 10s and 5mins. The lower half of the external oxide has seemingly coarsened, producing a porous amorphous structure.
WDS spectra 6 and 7 in figure 59 indicated the presence of Si, Al and Mn within the amorphous region. The amorphous region darkened as it approached the metal/ scale interface, illustrating an increase in Si, Al and Mn content. Several lateral cracks were observed within the darkened amorphous region rich in Si.
The WDS results indicated that the top region of the external oxide was entirely composed of magnetite. The grains also appeared equiaxed and relatively even in size compared to the frequently observed columnar wustite grains. This indicates that oxide growth was hindered.

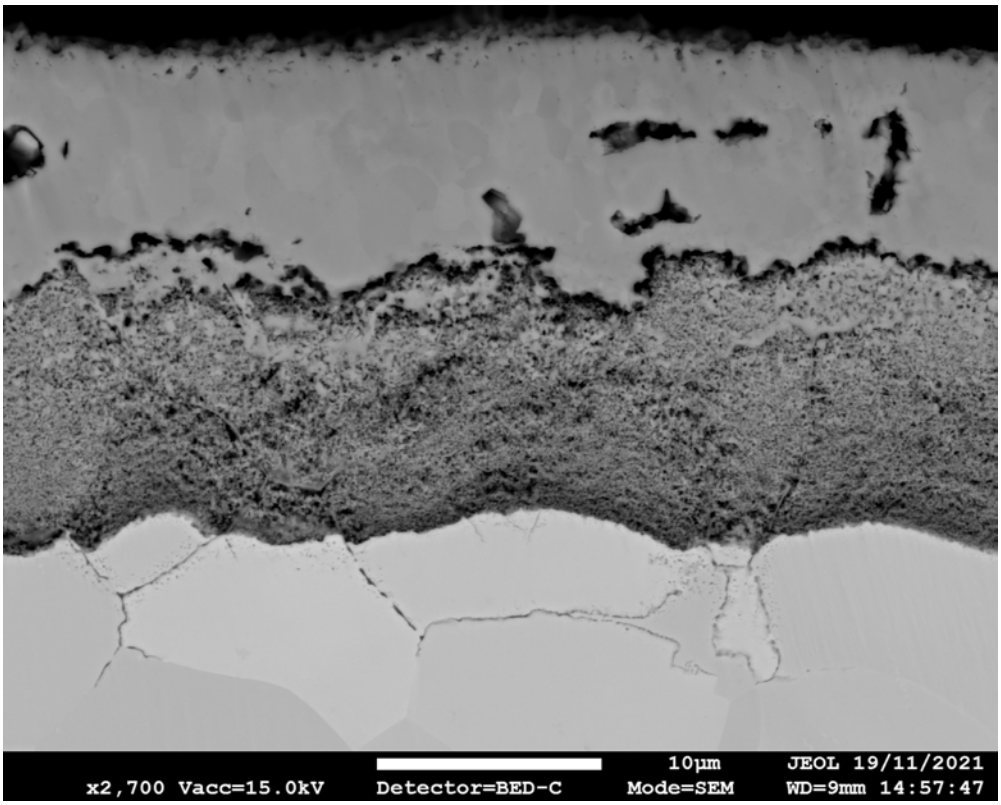

Figure 58: Oxide morphology after heat treating for 2hrs at 800°C

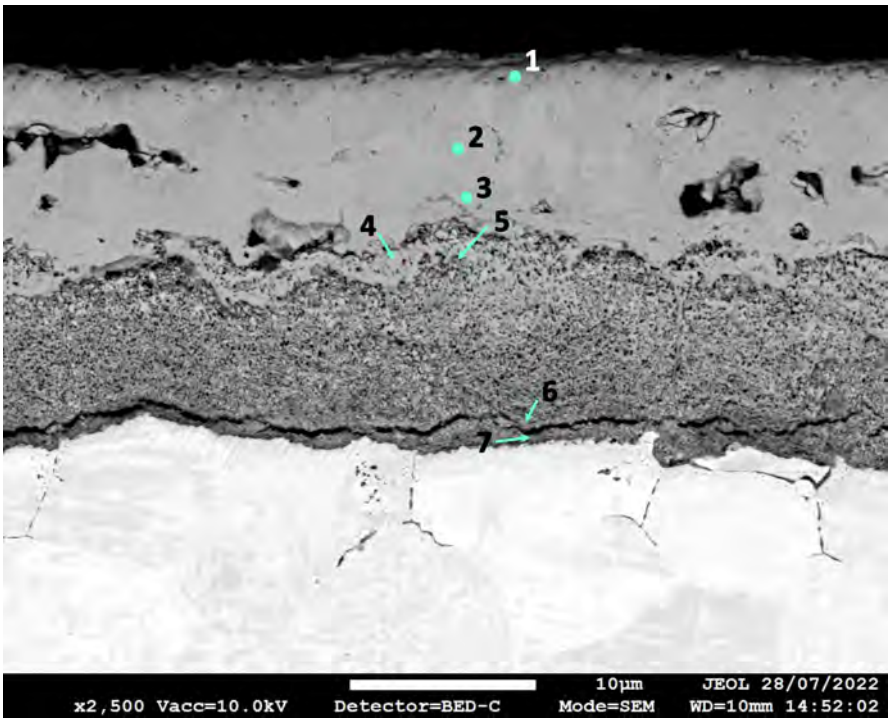

(a) WDS point scan reference image

			Wt%				
		Region	Fe	O	Al	Si	Mn
Spectrum	1	Oxide matrix top	33.78	64.56			
	2	Oxide matrix mid	67.99	31.99			
	3	Oxide matrix mid	67.62	26.6			*5.72*
	4	Oxide/ Spinel interface	69.4	29.25			*1.28*
	5	Oxide/ Spinel interface	69.83	29.06	*0.68*	*0.44*	
	6	Spinel	63.71	27.26	2.79	2.41	*3.82*
	7	Spinel	68.86	17.68	2.87	0.54	*10.05*

(b) WDS point scan measurements

Figure 59: WDS analysis conducted on DP800 heated at 800°C for 2hrs *(Highlighted cells EDS)*

6.3.7 DP800 TGA

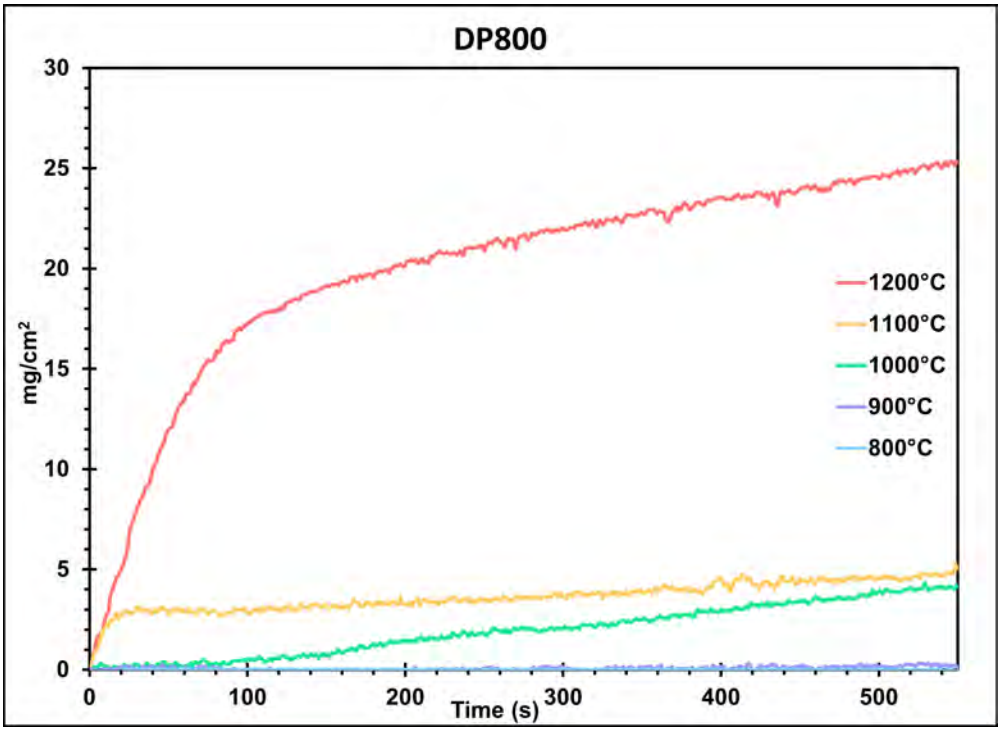

Figure 60: Mass gain curve of DP800 steel at 800°C, 900°C, 1000°C, 1100°C, 1200°C

Figure 60 illustrates the results obtained in thermogravimetric analysis (TGA) for DP800. Samples were oxidised over a temperature range of 700-1200°C for 600s. The rate of oxidation can clearly be observed to increase with increases of temperature. At higher temperatures the first stage of oxidation was characterised by a distinct linear regime whereby the growth was directly proportional to time. The limiting constituent within a linear regime was the reaction rate, which may be defined by the amount of oxygen delivered at the outer scale surface in unit time [62]. At 1100°C and 1200°C the linear regime was distinctly pronounced before a second stage of oxidation occurred with a transition to a parabolic regime. As the oxide growth transitions to a second stage of oxidation with a parabolic regime, the limiting constituent will become the diffusion of cations through the oxide layer. The diffusion of cations will become increasingly hindered as the oxide thickness increases. The oxidation below 1000°C was almost non-existent. The lack of oxidation below this temperature was conjectured to be due to the presence of internal oxide precipitates at the metal scale interface [104]. This was in agreement with the reduced oxide thickness's observed below 1000°C at both 10s and 5mins in figure 52. The increase in oxidation rate at 1000°C and above was surmised to be a result of the decreased internal oxidation depth, allowing for an increase in oxide thickness and weight gain.

The weight gain at 1200°C was almost five times greater than that of 1100°C, at 24.5mg/cm^2 and 4.58mg/cm^2 respectively. The substantially enhanced weight gain at 1200°C was thought to be due to a complete transition from a solid to a liquid fayalite phase, allowing for rapid oxidation.

6.3.8 Low Carbon TGA

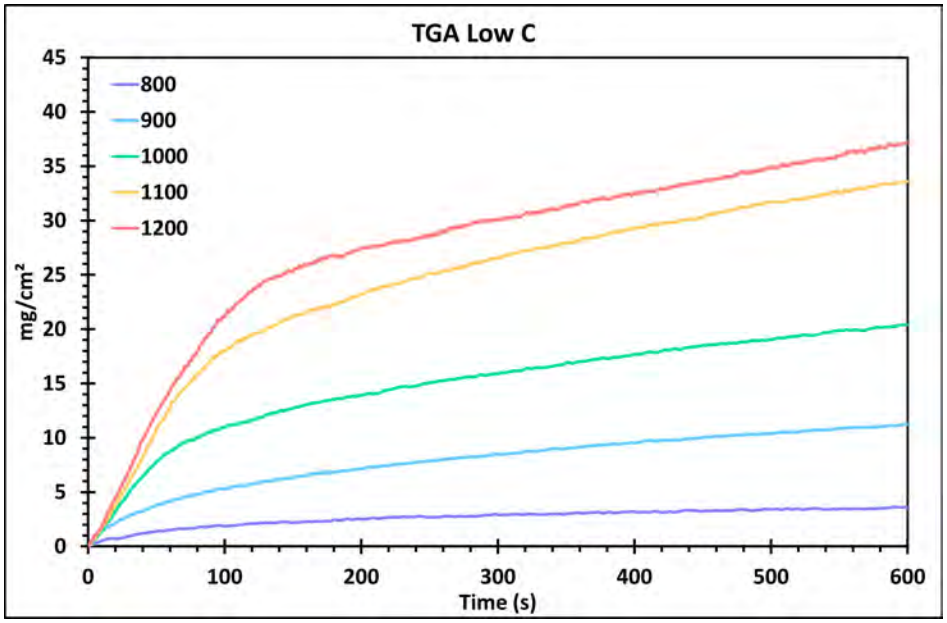

Figure 61: Mass gain of Low C steel at 800°C, 900°C, 1000°C, 1100°C, 1200°C

The effect of temperature on oxidation for a low carbon steel was investigated due to its broad range of applications. Low carbon steels are commonly used for various reasons: they offer excellent weldability, enhanced machinability, high ductility, cost-effectiveness, and in certain environments, they provide better resistance to corrosion due to their reduced carbon content [105].

The TGA results for the low C steel differed remarkably to that of the DP800. The results displayed in figure 61, show a 2 stage oxide growth behaviour, similar to that of the DP800 at 1100°C and 1200°C. The weight gain even at 1200°C for the low C steel was still substantially greater than the DP800 sample at 35.1 mg/cm2 and 24.5 mg/cm2 respectively. Thus even with the liquid fayalite phase enhancing oxidation of the DP steel the low alloying additions within the low C steel allowed for greater movement of cations and a greater rate of reaction. The DP800 steel wholly outperformed the low C steel.

At the lower temperatures of 800°C and 900°C the oxide transitions from stage one linear to stage 2 parabolic behaviour almost immediately, in approximately 10seconds. The parabolic regime quickly tailed off, with a substantially lower weight gain per unit of time in comparison to the linear regime; this phenomenon was consistent across all temperatures. The linear regime was significantly extended at higher temperatures, estimated at 70s, 100s and 140s for 1000°C, 1100°C and 1200°C respectively.

6.3.9 3812

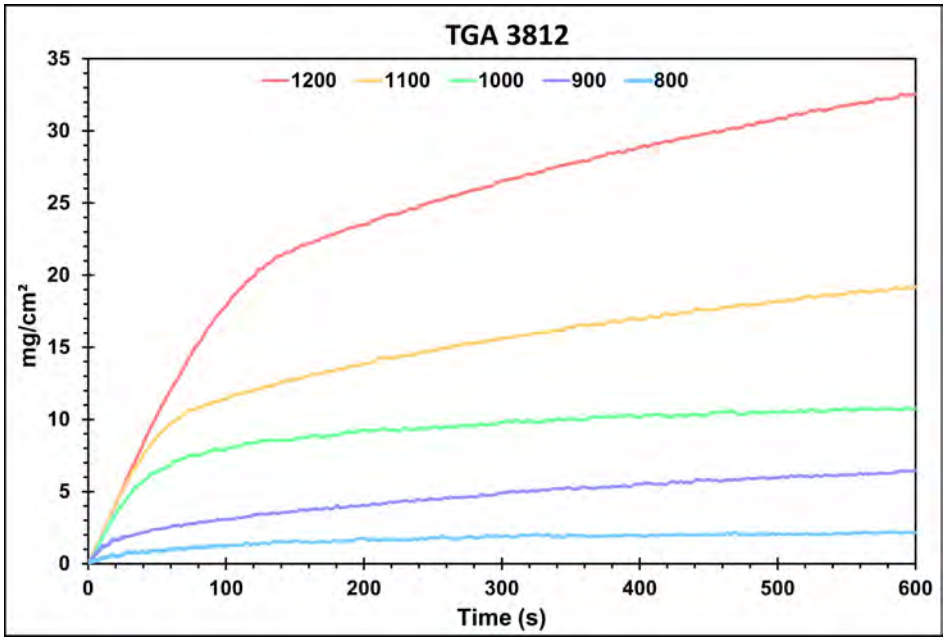

Figure 62: Mass gain curve of 3812 at 800°C, 900°C, 1000°C, 1100°C, 1200°C

The mass gain per unit surface for the 3812 steel grade is reported in figure 62. This steel grade is specifically chosen for its relevance in various industries, including packaging, construction, and automotive sectors. With its corrosion-resistant properties and versatility, it serves as a benchmark for understanding oxidation behaviour in practical applications [105]. The TGA results appear very similar to that of the low C results, with a 2 stage oxide growth. The linear behaviour in stage one at 800°C and 900°C was very short and not distinctly pronounced, similar to that of the low C steel. Nonetheless the weight gain of 3812 at 800°C and 900°C was significantly lower than that of the low C steel at 2.07 mg/cm2 and 5.97 mg/cm2, compared to 3.56 mg/cm2 and 10.38 mg/cm2 respectively.

The largest volume of weight gain for 3812 was observed between 800°C and 900°C, with an increase greater than 2.5x in mass. The volume increase of mass gained between temperatures decreased linearly with increases in temperature; meaning that the mass gain difference between 1100-1200°C was less than the volume gain between 1000-1100°C.

The 3812 steel performed well and had the second lowest mass gain of all of the steel grades at 1200°C. The samples did experience significant detachment of the oxide scale, thought to be due to the higher C content of the steel. This will be discussed in chapter 7, when discussing blister formation mechanisms.

6.3.10 S63

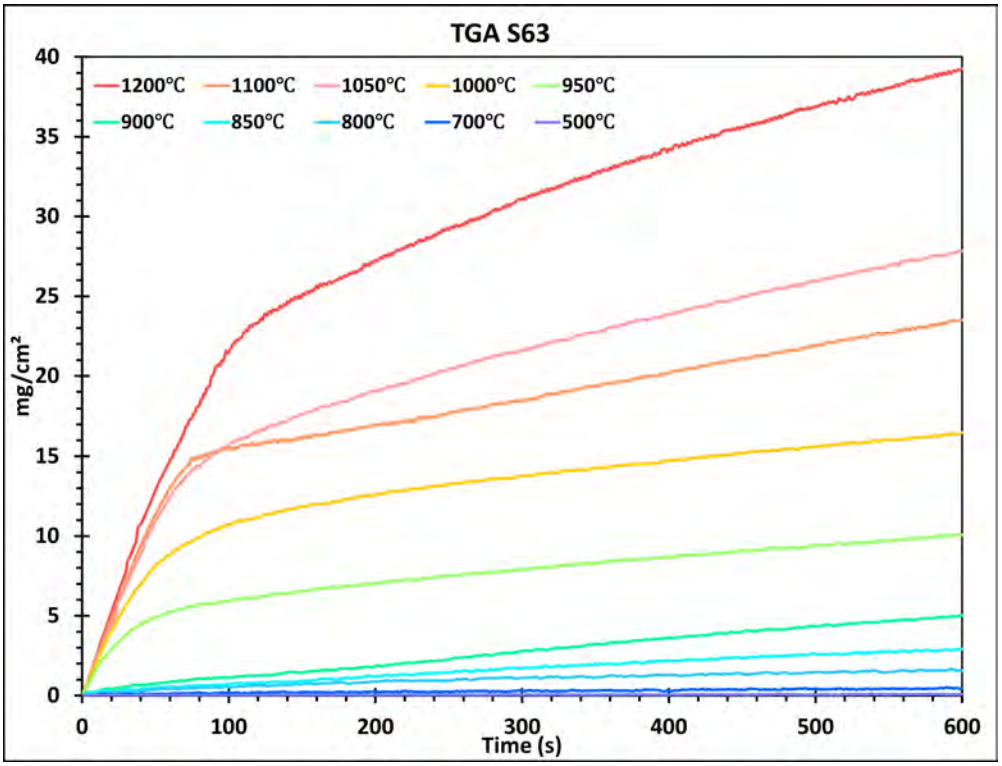

Figure 63: Mass gain curve of S63 at 500°C, 700°C, 800°C, 850°C, 900°C, 950°C, 1000°C, 1050°C, 1100°C, 1200°C

The weight gain for the high strength steel (HSS) grade S63 was shown in figure 63. The samples displayed a typical 2 stage oxide growth with both linear and parabolic behaviour. In stage one, at temperatures below 950°C, the period of linear oxidation was short, akin to that of the low C steel and 3812. At 500°C the sample was almost completely devoid of any mass gain, due to the low kinetic energy. At 700°C oxidation did occur; however the rate of reaction was extremely slow and only a small amount of mass was gained by 500s.

At higher temperatures the linear oxidation period was extended. At 1100°C the total mass gained at 500s was 21.89mg/cm^2, higher than that of both 3812 and DP800. At 1100°C the transition to parabolic behaviour was very sharp with an almost immediate change at 80s, however at 1050°C the transition occurs gradually over a period and the total mass gained was far higher.

6.3.11 B32

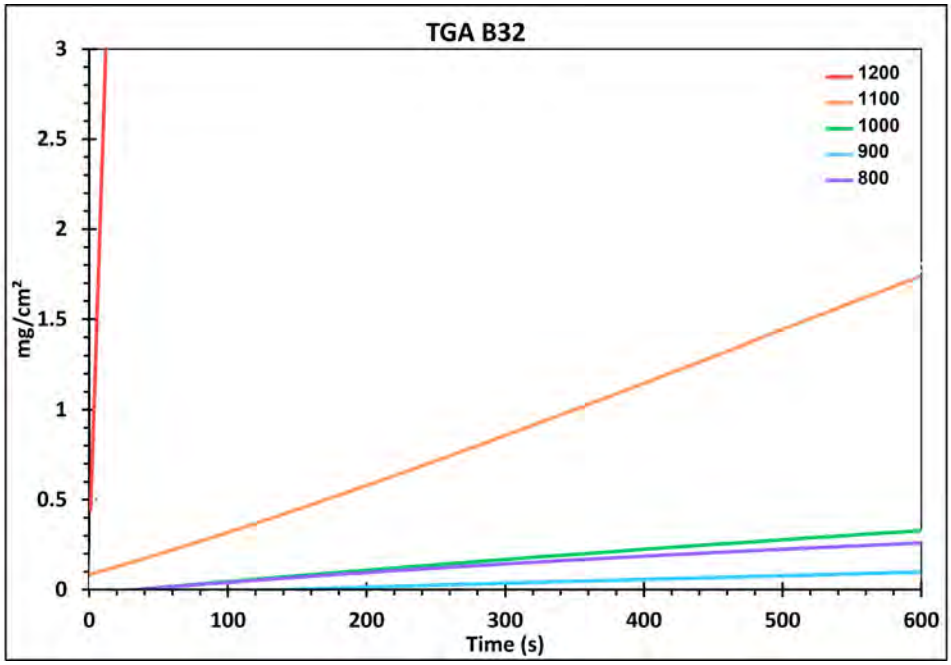

(a) Mass gain curve for B32 scaled up

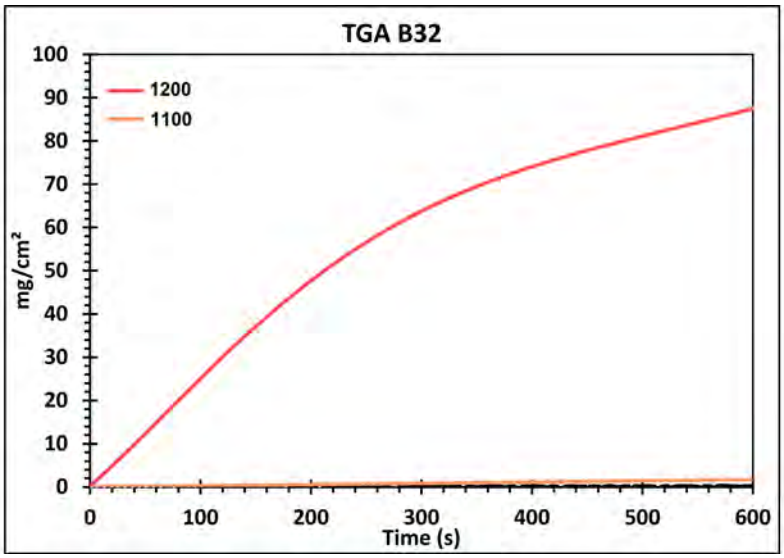

(b) Mass gain curve for B32 at 1200°C and 1100°C

Figure 64: Mass gain curves for B32

The TGA results for the high silicon steel are displayed in figure 64. This high Si steel grade, commonly known as B32 steel grade, exhibits unique behavior compared to other steel grades. Specifically engineered for applications requiring magnetic properties, such as in electrical transformers and motors, high silicon steels like B32 are designed to minimise energy loss through eddy currents. Therefore, understanding their oxidation behavior is crucial for ensuring long-term performance and reliability in electrical applications [23].

Figure 64a will be used to discuss temperatures below 1100°C and figure 64b to discuss the results for 1200°C. At the lower temperatures of 1000°C, 900°C and 800°C

the onset of oxidation was delayed, due to a passivation period. The total volume of oxidation was extremely low and the mass gain was under 0.5 mg/cm2. The passivation period was due to the formation of a passivation layer, composed of a thin adherent silica layer. The thin silica layer hindered the diffusion of iron ions, limiting the reaction rate and preventing an early onset of oxidation. A similar phenomena was observed for the DP800 TGA results, with oxidation suppressed below 1100°C due to the formation of internal oxide precipitates. Nonetheless the effect of the passivation layer was far more prominent for B32 because of the increased Si and Al content.
The effect of the passivation layer was absent after 1100°C, due to the transformation of the fayalite phase from a solid to a liquid. The author conjectures that this liquid fayalite phase rapidly increased the ease of diffusion for cations; expeditiously advancing the formation of the external and internal oxidation. The external oxide repeatedly consumed the internal oxide, resulting in the microstructure containing liquid fayalite dispersed intermittently throughout the external oxide. This was observed within the DP800 microstructure and was further discussed for B32 steel in chapter 7.

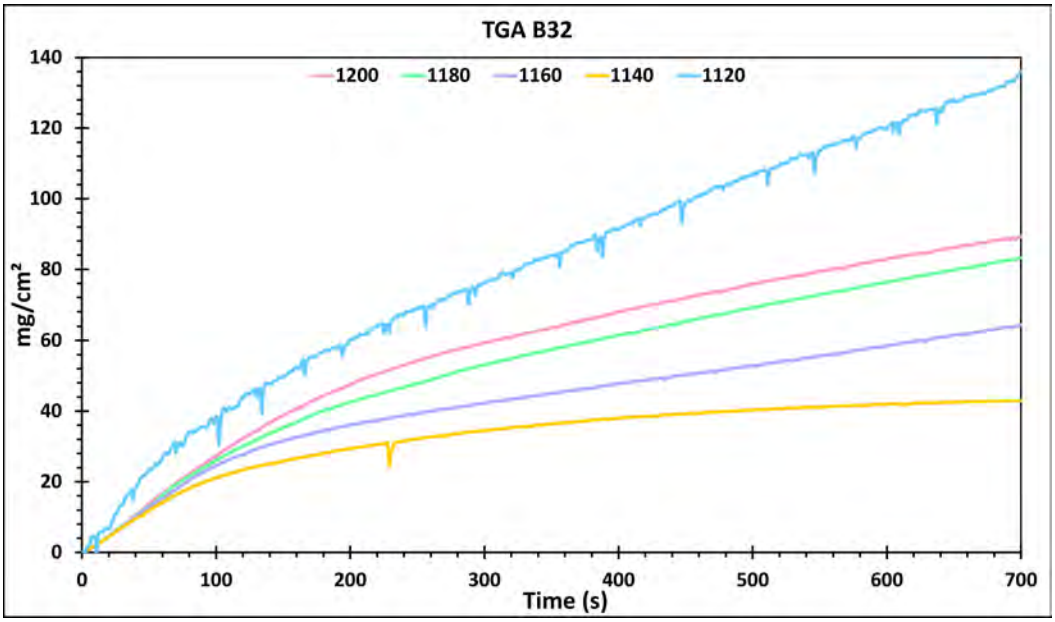

Figure 65: Mass gain curves for B32 above 1120°C

The TGA results for B32, close to the liquid fayalite temperature reported in literature [106] [107], are shown in figure 65. The mass gain and rate of oxidation was lowest at 1140°C but was still inordinately more than temperatures at 1100°C and lower. The weight gain at 1000°C for 500s was only 0.88 mg/cm2 and for 1140°C 40.37 mg/cm2. This incredible difference highlights how considerable the increase in oxidation was once the liquid fayalite temperature was approached. There was a large amount of noise recorded for 1120°C however it had decidedly the greatest mass gain of any samples examined at 104.91 mg/cm2 for 500s. The noise may conceivably be due to localised regions of failure within the sample, resulting in breakaway of the oxide and exposing a fresh underlying surface.

6.3.12 Comparison of Industrial Steel Grades

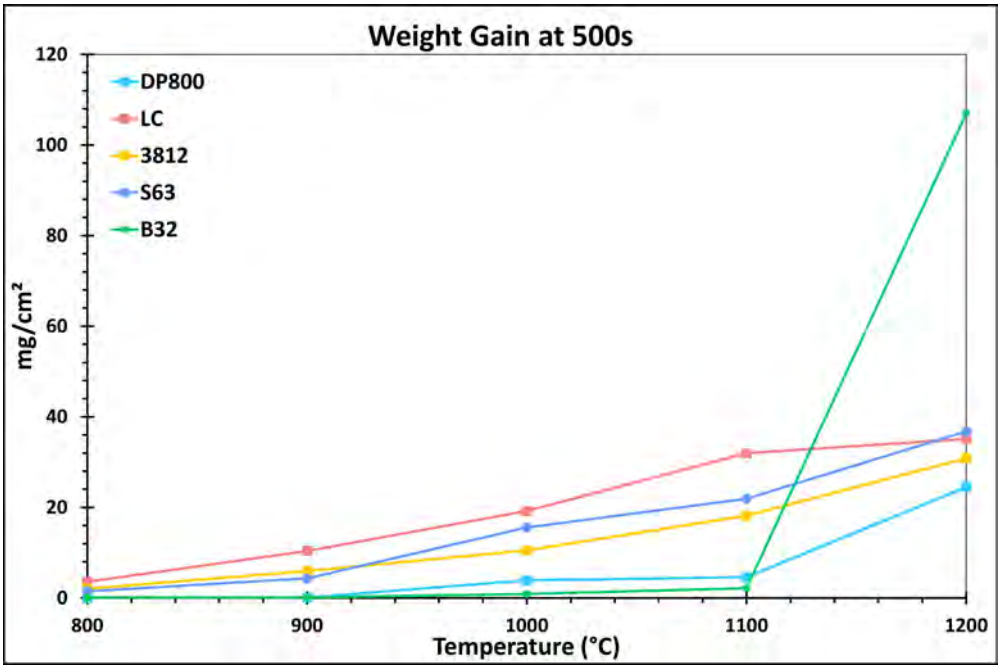

Figure 66: Comparison of the mass gain at 500s for DP800, LC, 3812, S63 and B32 at 800°C, 900°C, 1000°C, 1100°C and 1200°C

The Weight gain at 500s for each steel composition are plotted in figure 12. The steel grades all displayed different oxidation rates and mass gain attributed to the difference in chemistries. All alloying compositions displayed the largest mass gain and a rapidly accelerated rate of oxidation at 1200°C.

	800	900	1000	1100	1200
DP800	0.0	0.1	3.9	4.6	24.5
LC	3.6	10.4	19.2	32.0	35.1
3812	2.1	6.0	10.5	18.2	30.8
S63	1.5	4.3	15.6	21.9	36.8
B32	0.1	0.1	0.2	2.2	107.0

Table 12: Mass gain measurements at temperature for each steel grade

B32 and DP800 experienced the most prominent mass gain at 1200°C, especially when considering the mass gain at lower temperatures. The low rates of oxidation at lower temperatures were surmised to be due to the comparatively high alloying content of the samples. The total alloying content was 4.3wt% and 3.1wt% with Si at 3.2wt% and 0.44wt% for B32 and DP800 respectively. The passivation effect and depressed oxidation rates at temperatures below 1200°C, was stronger for B32 due to the greater Si content. It should be noted that the high Mn in DP800 would have also played a crucial role in suppressing oxidation, however previous work in chapter 5 shows it would not have as large an effect.

At 1200°C the effect of the passivation layer was negated, and oxidation was rapidly accelerated due to the melting of the fayalite phase. The liquid fayalite was evident in the BSE image in figure 67d with the darkest elemental contrast. Dendritic arms of

FeO formed within the liquid fayalite phase. The liquid phase was clearly evident at the metal/scale interface and travels all the way through the external scale towards the outer surface. The mass gain for B32 at 1200°C was more than triple all other compositions, including those with very low total alloying content. Thus Si not only stops providing oxidation resistance at higher temperatures but may in fact expeditiously accelerate oxidation.

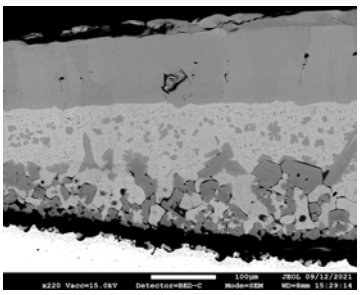

(a) DP800

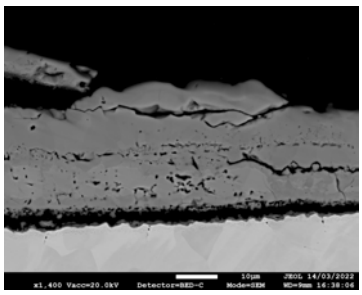

(b) 3812

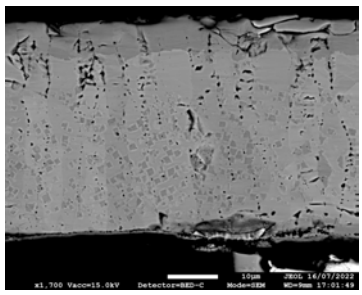

(c) S63

(d) B32

Figure 67: Microstructure examples of steel compositions analysed using TGA - a)DP800 1200°C for 12mins b) 3812 900°C for 5mins c) S63 900°C for 5mins d) B32 high temperature sample

The DP800 had the lowest mass gain at 1200°C performing best out of all the compositions. In Figure 67d the microstructure of DP800 contains a conspicuous region of internal oxidation. A high wt% of Mn and Al was found within the internal oxide precipitates using WDS; figure57c, spectra 17 and 18. Al2O3 and MnO have a melting point of 2072°C and 1840°C respectively; significantly higher than that of fayalite at 1200°C. Due to the high melting temperature of the internal oxide precipitates the IOZ continued to provide resistance to cation movement at 1200°C reducing oxidation. Figure 67b and 67c show no IOZ.

6.4 Conclusions

A thermodynamic study of industrially pertinent steel grades was conducted in order to understand the kinetics of reaction and the resulting product of formation. The composition of the steel was discovered to have a considerable impact on the rate of oxidation. An emphasis was placed on the characterisation and analysis of DP800 in order to understand the low rates of oxidation observed. Temperature was found to have an extremely significant impact on the rate of oxidation and internal oxidation depth of DP800.

DP800 Internal Oxidation

- Internal oxidation was present at 800°C-1000°C after isothermal heating for 10s. 950°C showed the greatest depth of internal oxidation at 7.22µm with the lowest depth recorded for 1000°C at 1.73µm.
- A clear shift was noted in both morphology and thickness of the internal oxide at 1000°C to smaller more spherical precipitates. The morphology below 1000°C was primarily inter-granular nucleating along grain boundaries however this transitioned to intra-granular at higher temperatures. The precipitates were also substantially smaller on average; supposedly favouring higher nucleation rates and lower growth.
- The decrease in internal oxidation at 1000°C was coupled with the promotion of a thick external oxide layer; almost 10 times larger than the other samples investigated.
- Internal oxidation depth was marginally greater for 5mins compared to 10s. At 5mins the internal oxidation zone was far coarser and more consistent; 900°C showed the greatest depth of internal oxidation with the lowest recorded at 1000°C.
- shows itnernal oxidation grows rapidly then doesnt develop much more

DP800 Oxide Morphology

- At 1200°C the DP steel showed an extremely thick and convoluted oxide morphology composed of 4 distinct regions. The increased thickness and complexity of the oxide scale was due to a liquid fayalite phase which rapidly enhanced oxidation.
- At temperatures below 1200°C the external scale was composed of a brittle, predominantly magnetite oxide.

TGA

- LC, 3812 and S63 samples showed substantial oxidation at 900°C and above. Oxidation curves displayed 2 step oxidation growth with a linear and parabolic region. Oxidation rates increased with increases of temperature

- DP800 showed no appreciable oxidation below 1000°C due to an internal oxide layer limiting external oxidation growth. Between 1100-1200°C a massive increase in the rate of oxidation was seen for DP800 due to liquid fayalite. Nevertheless the total rate of oxidation was still substantially lower than the total oxidation for the other 4 alloys. DP800 had the lowest total weight gain.
- B32 had the lowest mass gain at temperatures below 1100°C, however at 1200°C it was triple that of all other samples investigated.
- High Si content will stop providing oxidation resistance at higher temperatures and will then begin to expeditiously accelerate oxidation.

7 External Oxidation Blistering

7.1 Introduction

Oxide scale growth is an inevitable byproduct of the high temperature processing of steel. Blister is a phenomenon that occurs due to oxide growth, where high temperatures result in the swelling of surface scale producing a bubble-like feature, shown in figure 68. Blisters can subsequently become embedded in the steel substrate during hot rolling in the finishing mill. This rolled in scale defect causes havoc within industry, not only with wear on machinery but loss of customer satisfaction, poor surface finish, loss of material and profit.

Figure 68: Large complex blister observed on a high Si steel after heating at 1180°C for 30s

Even though blister was a highly prevalent issue there is still much that is not known or understood. The classic iron oxidation system is a complex multiphase system formed of wustite, magnetite and hematite producing multi-layered scales. Each phase will have independent properties such as thermal coefficients, growth rate and mechanical properties. Furthermore, each additional alloying element will have different affinities for oxygen and different mobilities in the oxide phases, so that oxide morphologies are specific to alloy chemistry. Therefore, blister regimes can be unique to each steel grade resulting in a diverse range of formation mechanisms [83] [53].
Blister has been reported to have both a nucleation and growth process where the scale detaches from the substrate and blisters after a very short period. There was some debate over the exact mechanisms of nucleation and growth of Blisters. Two main mechanisms have formerly been proposed for blistering. One relating to growth stresses and the other relating to formation of gases at the steel oxide interface [61] [108] [109] [110] [62].
Matsuno related blister to an imbalance in adhesive forces, growth forces and the relief of internal stresses during isothermal oxidation [58]. Pilling and Bedworth postulated that stress within scale was a result of the volume dilatation of metal to its oxide [111] [112]. The Pilling-Bedworth Ratio (PBR) considers the volume of metal consumed and the volume of oxide formed. If the PBR > 1, the oxide was under compression and

the metal in tension, and vice versa for PBR < 1. The iron oxidation system PBR $>$ 1, therefore, during oxide growth, compressive stress was present in the scale. In this situation, the compressive stress may form blisters if the critical value necessary to lift the scale was reached [58]. The PBR will only give an indication of the sign and not the magnitude of stress of the system.

Kondo has suggested that compressive stress was not a main factor for blister initiation. It was reported that the pressure of the CO, CO2, and N2 gas generated at the interface between the scale and matrix was sufficient to produce a blister. The outer hematite layer helps to increase gas pressure due to its low permeability and porosity and thus, creating a pressure build up large enough to detach the scale from the substrate [108]. Mechanical stresses, such as those reported by Robertson et al. [4] and Basabe [62] can also result in scale detachment and blister formation. Its more likely that blistering was a combination of these factors resulting in different formation mechanisms for various alloy grades.

In both cases above, once nucleated the steel substrate exposed inside of the blister is further oxidised in the reducing atmosphere of the blister. However, the atmosphere within the blister was highly dependent upon the porosity of the blister crown and was often unique to each steel grade due to variations in alloying chemistry. Each additional alloying element will have different affinities for oxygen and different mobilities in the oxide phases. Of particular interest are Si and Al that produce brittle complex internal oxides and spinel structures [110].

This chapter 7 aims to determine the formation mechanism of blister for 3 industrial steel grades. The effect of temperature and time on blister formation along with the severity of the blister are of utmost importance.

7.2 Experimental Procedure

7.2.1 Composition

Table 13 shows the compositions of the industrial steel grades investigated within this chapter. Material was sourced and produced by Tata Steel Europe

	C	Si	Mn	Al	Cr
3812	0.150	0.100	0.860	0.036	0.028
DP800 Hyperform	0.155	0.440	2.032	0.589	0.028
B32	0.003	3.200	0.200	0.900	-

Table 13: Composition of steels grades investigated within this chapter (wt%)

7.2.2 TGA

Blister Regime Heat Treatment for 3812 The oxidation tests were selected to simulate hot rolling conditions with a freshly descaled surface and the approximate formation of secondary and tertiary scales in a finishing mill stand. Each sample was sequentially inserted into the furnace. To prevent oxidation, they were all purged with argon and heated in an argon atmosphere. Once the target temperature was reached, the samples were held at that temperature under argon for 5 minutes. Following this, oxygen was introduced into the furnace at a rate of 10 litres per minute. Times and temperatures investigated include 4s at 900°C, 10s at 800°C, 900°C, 1000°C and 1100°C, 30s at 800°C, 900°C, 1000°C, 1100°C and 1200°C, 60s at 800°C, 900°C, 1000°C, 1100°C and 1200°C and 600s 800°C, 900°C, 1000°C, 1100°C and 1200°C. An image was captured of the samples after they were immediately extracted from the furnace; figure 69. The blisters appear as dark spots within figure 69 due to the detachment of the oxide scale. Sample geometry was 65mm x 25mm x 2mm for all samples. Due to the large number of heat treatments and time constraints no repeats were conducted.

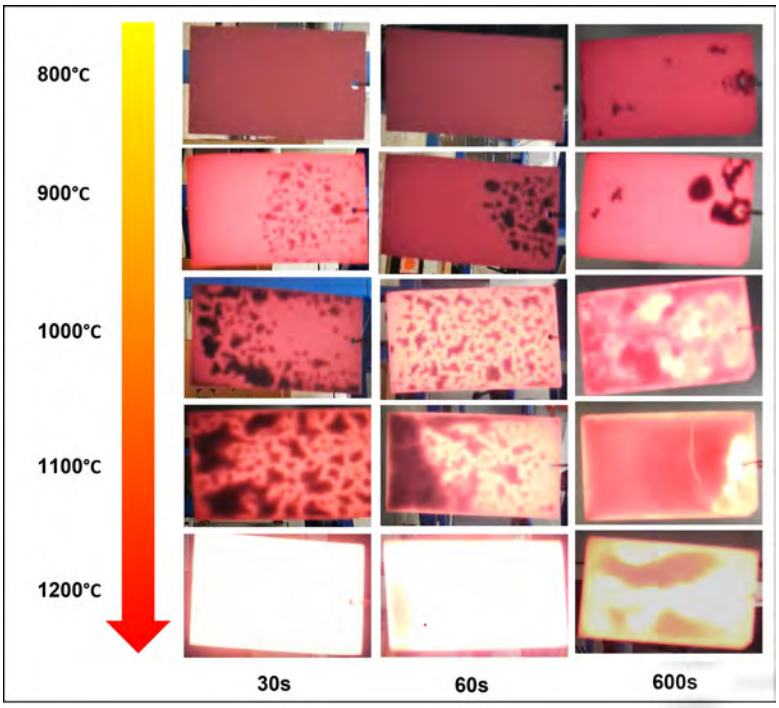

Figure 69: Samples by heat treatment and time after immediate removal from the furnace

DP800 Several isothermal heat treatments were carried out on DP800 samples. To prevent oxidation, all samples were flushed with argon and heated in an argon atmosphere. Upon reaching the desired temperature, the samples were maintained at that temperature under argon for 5 minutes. Subsequently, oxygen was introduced into the furnace at a flow rate of 10 litres per minute. After the specified duration, the samples were removed from the furnace and air-cooled. Temperatures investigated at 5mins and 12mins include 800°C, 900°C, 1000°C, 1100°C, and 1200°C. Temperatures investigated at 10s include 800°C, 900°C and 1000°C. One pro-longed isothermal heat treatment was conducted at 800°C for 2 hours.

B32 Blister heat treatments were conducted by V.Basabe on a 3.2wt.% electrical steel [62]. A blister regime was then produced and samples were characterised in this thesis.

7.2.3 Characterisation

Focused Ion Beam (FIB) Milling A Carl Zeiss CrossBeam 550 FEG-SEM was utilised for FIB-milling, a process that employs a focused ion beam to precisely mill materials. This technique facilitated the creation of a cross-sectional view of a blister dome, allowing for in-depth analysis. Gallium ions were used for milling due to their high ionisation energy and minimal damage to the sample. Following the milling process, cross-sectional analysis was conducted, which involved examining the structure and composition of the sample in detail. Additionally, Energy Dispersive X-ray Spectroscopy (EDS) examination was performed to further analyse the elemental composition of the sample. The detailed parameters utilised during these processes are

meticulously documented in the figures presented throughout this chapter.

7.3 Results and Discussions

7.3.1 3812

Modes of Blister Previously V.Basabe reported that there are two key modes of blistering [62]. In Mode 1 it was ascertained that the stresses produced by oxide growth would increase with increasing oxide thickness. Therefore, in Mode 1 the incubation time for blister formation was shortened by increasing the temperature [62].
In Mode 2 increase in temperature would result in an oxide with high ductility and high porosity. The high oxide ductility and/or porosity would accommodates for the intrinsic stresses from oxide growth [62]. Thus, Mode 2 was the inverse of Mode 1 and incubation time was increased with temperature. Upon observation both of these modes could be affiliated with the results produced from 3812.

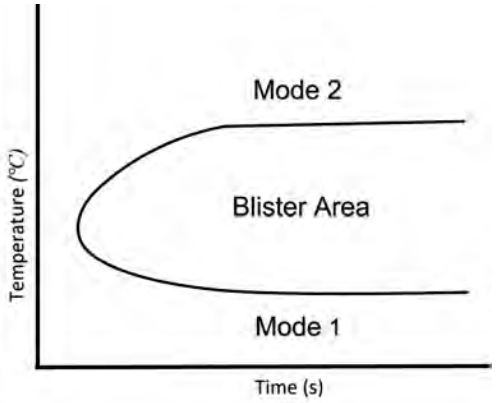

(a) A model used to describe the two key modes of blistering

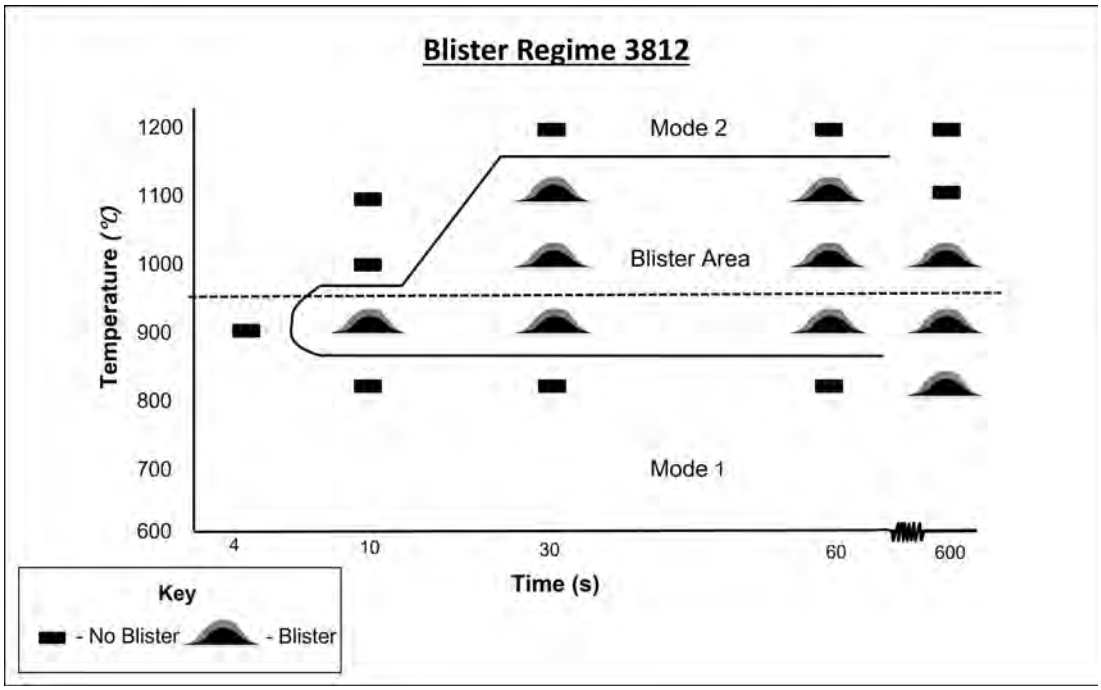

(b) Blister regime for 3812 - *Blisters produced upon heating*

Figure 70: Blister time temperature graph for 3812

Blister Regime The resulting blister regime after being heat treated for steel grade 3812 is depicted in figure 70. At temperatures below 1000°C blister was associated with mode 1; above it was associated with mode 2. The nose of the blister curve was found to at 10s for 900°C. Blister did not occur above 900°C for 10s, thus it was inferred that the blister had shifted to mode 2 at 1000°C and thus a longer incubation time was required. For the temperature 900°C, figure 69 shows the blisters were most severe at 60s, with many of the blisters conglomerating together to form a larger detached region. At 900°C for 600s the only one large blister formed towards the top of the sample. Nonetheless upon cooling, many smaller blisters formed across the sample.
At 1000°C the formation of blisters was within mode 2, with the increase of temperature resulting in greater ductility and longer incubation times. The blisters were highly pronounced and distributed across the length of the sample. The blisters at 1000°C were larger than those at 900°C, with a number of them amalgamating together. At 30s there was a greater presence of blisters towards the edges of the sample with some very small blisters forming towards the centre of the sample. The blisters towards the centre were far smaller and more spherical in shape. At 60s the blisters were more uniform and evenly distributed across the sample, displaying a more random shape. It was inferred that the smaller blisters towards the centre of the sample at 30s had only just begun to nucleate and were juvenile in their development.
Blister was also present at 1100°C in mode 2, however only at 30s and 60s. Figure 69 shows that the blisters, similar to 1000°C had an increased prominence towards the bottom edge of the sample, presumably due to the geometry of the sample. At 30s there were many individual blisters with a number of them amalgamating together.
At 60s this effect became more pronounced, with the blisters presumably merging to create one large in-adherent region at the bottom of the sample. At 600s there were no discernable blisters upon removal from the furnace. It was conjectured that similar to 60s, the oxide had become detached from the substrate however due to the increased heating time the effect was more pronounced and the entire oxide lifted away. The oxide at 600s remained attached at the edges but fractured towards the top right hand corner, exposing the surface beneath.
No blisters upon heating were detected at 1200°C, nevertheless upon cooling a multitude of blisters were observed across the sample, similar to those observed at 900°C. These blisters will be refereed to as blisters upon cooling and will be designated as mode 3. This is a new and unreported phenomena and will be discussed later on in the chapter.

7.3.2 30s heating

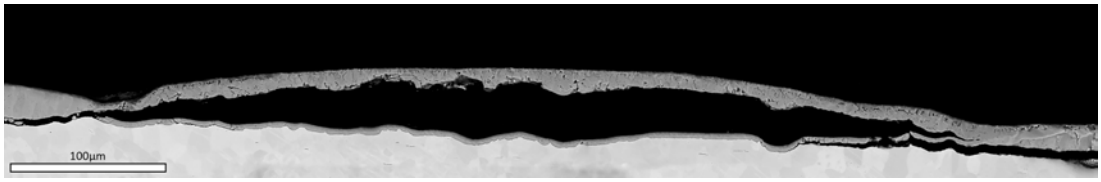

Figure 71: Blister formed upon heating at 900°C for 30s

900°C Figure 71 shows the cross section of a large blister that formed during heating at 900°C for 30s. The blister was 559µm across in diameter with a crown thickness of approximately 16µm. This crown thickness was found to be consistent with other blisters throughout the sample. The bulk of the oxide was 25-30µm thick and the oxide beneath the blister was 3-4µm thick. The oxide beneath the blister appeared to be composed of magnetite with some minor regions containing wustite. The BSE image in figure 71 shows the lighter wustite phase closest to the substrate with the wustite remaining very well adhered. The blister regime in figure 70b found that blister would nucleate after 10s at 900°C.

It was postulated that after the initial blister nucleation the exposed steel surface within the blister would then begin to oxidise. The blister would produce a reducing environment [61], limiting the oxygen to the exposed surface and resulting in slow scale growth of the exposed surface. The blister crown itself would be restricted in growth after uplift, due to the increased distance required for cations to migrate.

The morphology of the blister crown was notably dissimilar to that of the bulk of the oxide. The bulk of the oxide was primarily composed of columnar wustite grains with a distinctive top layer of equiaxed magnetite and hematite grains. Nonetheless, the blister crown was composed almost entirely of equiaxed magnetite grains with small regions of retained wustite. The right hand side of the BSE image in figure 71 clearly portrays the transition of the blister crown to the bulk of the oxide. Its inferred that the restricted movement of the cations and surplus of anions resulted in the formation of an oxygen rich scale, with any wustite within the initial blister crown being reduced almost entirely to magnetite. The bulk of the oxide would of simultaneously continued to grow producing a thicker classic oxide scale.

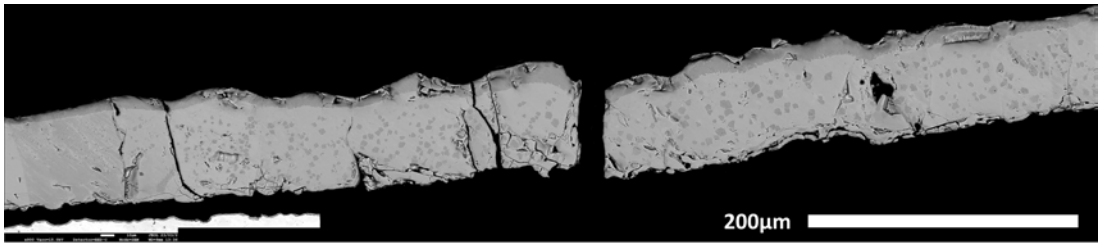

Figure 72: Blister formed upon cooling at 1200°C for 30s

1200°C Figure 72 shows the cross section of a blister formed at 1200°C for 30s upon cooling. The blister had many fundamental differences compared to the blister formed upon heating at 900°C. One pre-eminent difference was the crown thickness which was over four times greater than 900°C; in excess of over 70µm. The blister was also far greater in diameter and had an eminently different morphology. The morphology of the blister crown at 1200°C was predominantly wustite with many smaller magnetite precipitates dispersed throughout (see Appendix 142). The magnetite precipitates varied in size ranging from sub-micron to over 16µm and were faceted in nature (see Appendix 143). The bulk of the oxide that remained well adhered did not contain any magnetite precipitates greater than 1µm. Its conjectured that the multiple fractures and cracking observed through the blister acted as oxygen highways, accelerating oxidation through the crown as the sample further cooled.

Another key dissimilarity was the difference between the blister crown thickness and the bulk oxide thickness. The thickness of the bulk oxide at 1200°C was approximately 75µm, around the same as that of the blister crown. At 900°C the bulk oxide was 10µm thicker than the blister crown, due to the early nucleation of the blister stunting any further through thickness growth while the remaining bulk oxide continued to grow unhindered. The comparable thicknesses between the blister crown and oxide at 1200°C further supports that the blister formed upon cooling after the oxide had predominantly completed growth.

7.3.3 60s heating

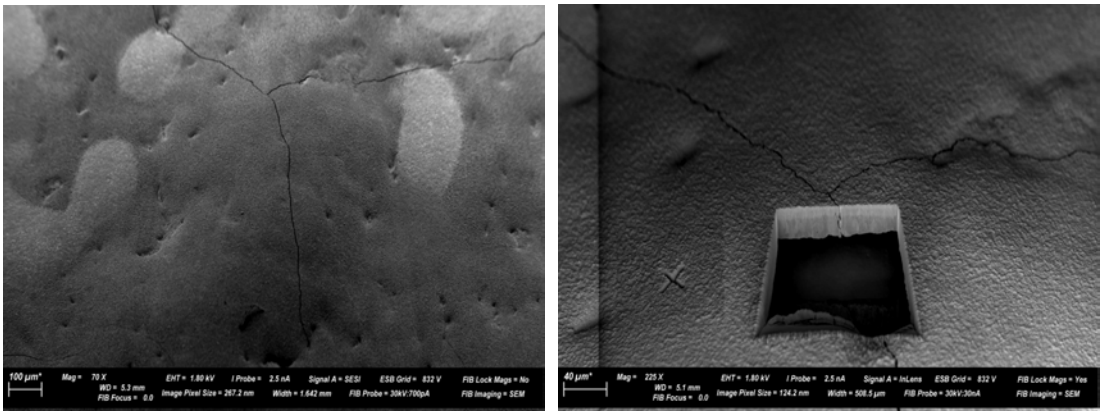

(a) Overview of blister crown before milling- Triple point crack extending from the center of the blister dome

(b) Overview of the blister crwon after FIB-milling

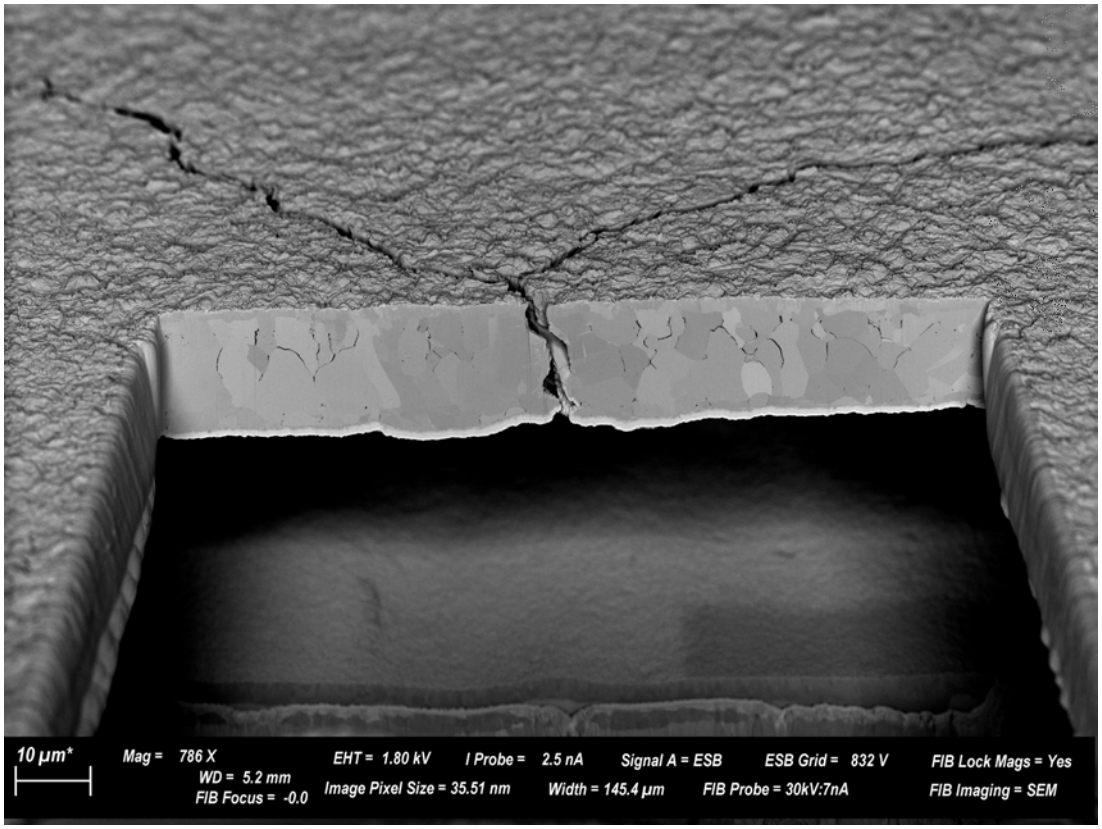

(c)

Figure 73: FIB milled cross section of a blister formed upon heating at 900°C for 60s

900°C The heat treatment at 900°C for 60s resulted in a substantial number of large cavernous blisters. Figure 73 features one of these blisters after being milled by FIB in order to examine the cross sectional area of the crown. It was not possible to determine the bulk oxide thickness using this technique however the blister crown was determined to be approximately 18µm. A large triple point crack was detected on the apex of the blister, presumably forming during the uplift of the blister due to tensile stresses. The cross section shows a considerable number of inter-granular cracks along the oxide

grain boundaries in addition to some smaller pores located towards the base of the oxide. The EDS map of the milled region detected a thin lateral band of Mn, roughly 1-1.5µm thick at the base of the oxide (see Appendix 144).

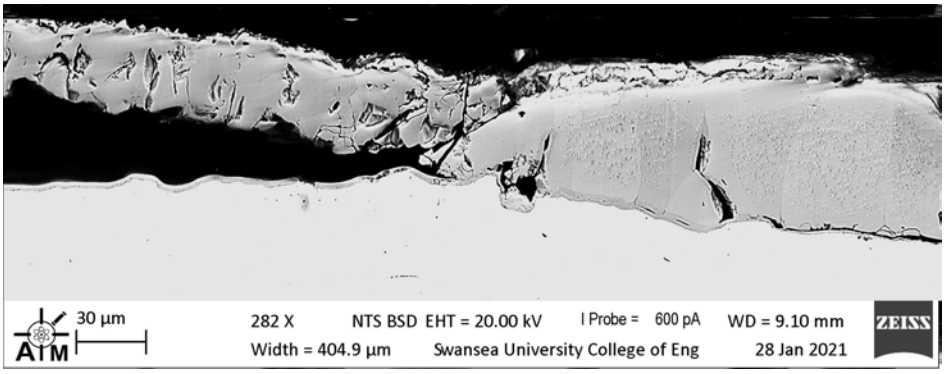

Figure 74: Blister formed upon heating at 1000°C for 60s

1000°C Figure 74 shows a blister that formed at 1000°C for 60s. It was determined that the blister had nucleated upon heating, however the blister crown was substantially thicker than that formed at 900°C at 35µm and 18µm respectively. The increased thickness of the blister crown was presumed to be due to the higher temperatures and the transition from mode 1 to mode 2. The bulk oxide was approximately 90µm thick and had a magnetite seam of 4µm. A thin oxide developed within the blistered region and had a thickness of 3µm.

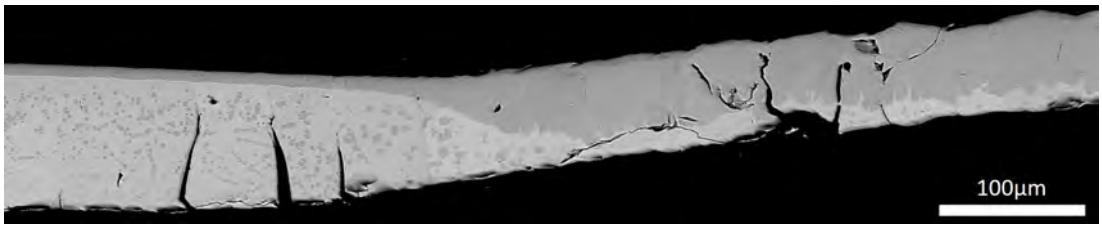

(a) Oxide overview

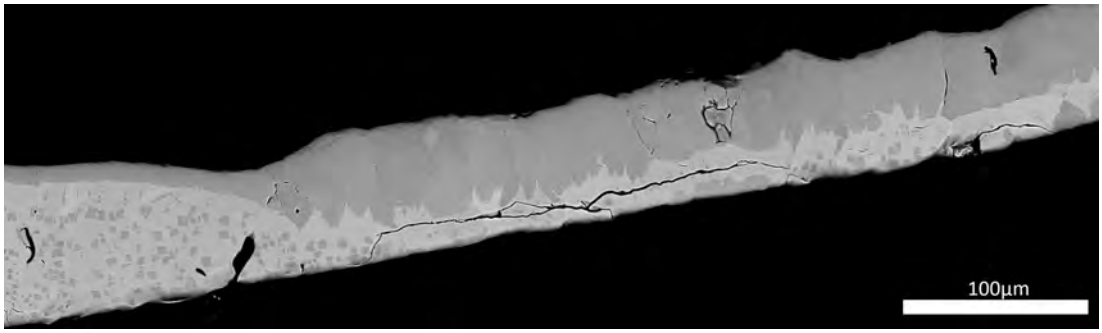

(b) Oxide overview

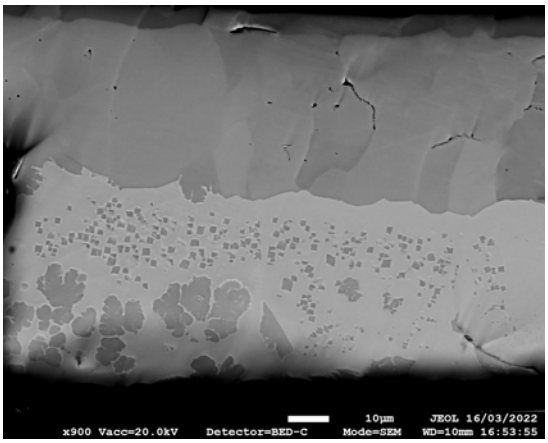

(c) Blister crown

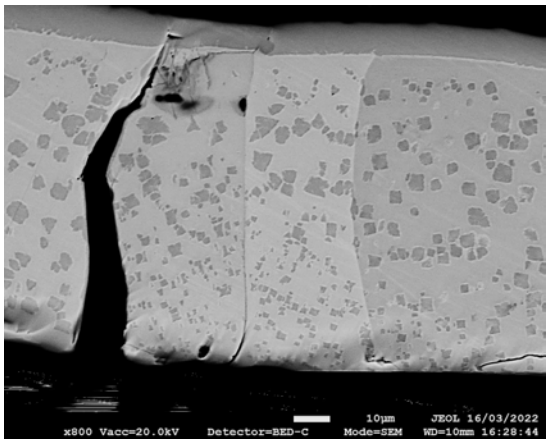

(d) Large lateral crack through wustite grain

Figure 75: Blister formed at 1100°C for 60s

1100°C At 1100°C for 60s several blisters were observed to nucleate upon cooling however the large majority formed upon heating. The blister produced in figure 75 had a crown thickness of 73µm and a bulk oxide thickness of approximately 101µm. The ratio between the blister crown thickness and the bulk oxide was far greater at 1000°C; thus it may be inferred that the oxide reached the required growth stress for blister nucleation far earlier on in oxide development. The blister crown was composed of a thick outer magnetite layer and an inner layer of retained wustite and magnetite precipitates. Figure 75a showed that as the distance from the bulk oxide increased the proportion of retained wustite within the blister crown decreased. A number of lateral fractures through the wustite phase were observed as seen in figure 75d. The fractures were located within the bulk oxide close to the blister crown and presumed to of occurred during uplift of the blister crown. Figure 75d revealed the fracture front travelling upwards through the wustite phase and halting at the outer magnetite. The fracture initiated at the point of blister nucleation during the uplift of the blister crown. The bulk oxide was composed predominately of large columnar wustite grains with an

assortment of magnetite precipitates and a 10µm thick outer magnetite layer.

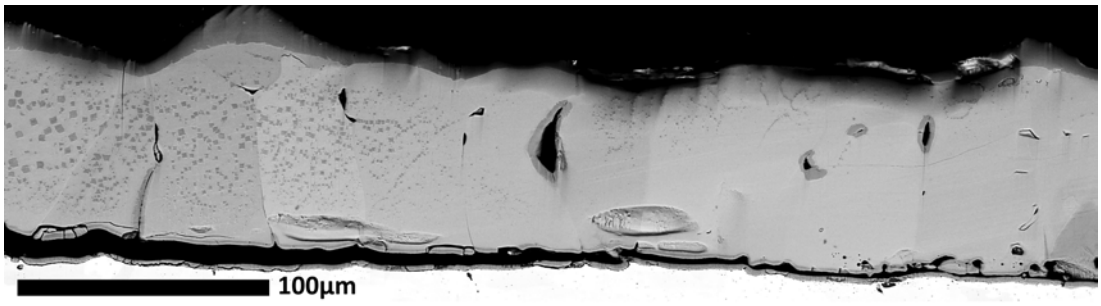

(a) Oxide overview

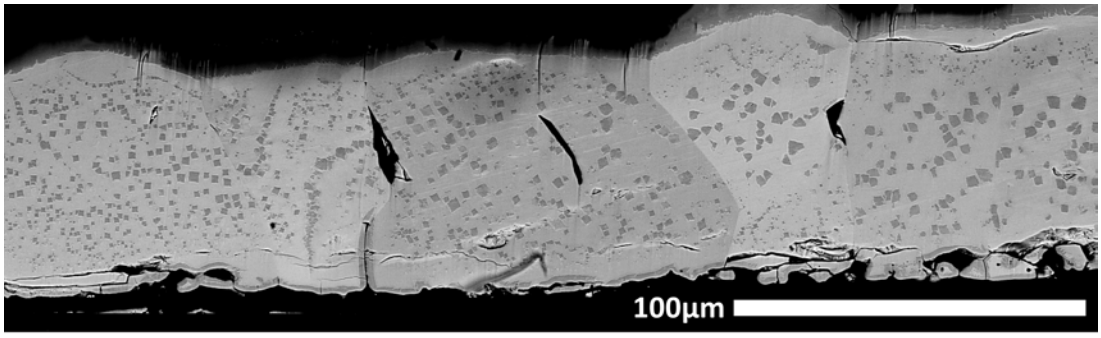

(b) Blister crown

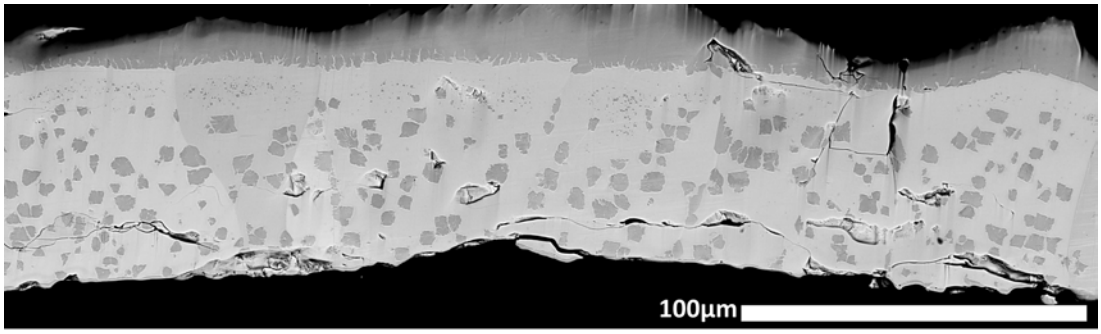

(c) Apex of the blister crown

Figure 76: Blister formed upon cooling at 1200°C for 60s

1200°C The cross section of the oxide and blister formed at 1200°C for 60s was displayed in figure 76. The crown thickness of the blister was approximately 77µm and the bulk oxide thickness within the vicinity of 81µm. The blister crown was of a similar thickness to the blister produced at 1100°C, however the blister at 1200°C contained a far greater volume of retained wustite. The large volume of retained wustite was due to the blister lifting during cooling, allowing for a very short period of wustite decomposition. The blister shape was not well distinguished in comparison to those produced at 1000°C and 900°C. The blister produced at 1200°C for 60s was profoundly similar to that produced at 1200°C for 30s, with both presupposed to nucleate via the same formation mechanism during cooling.

7.3.4 600s heating

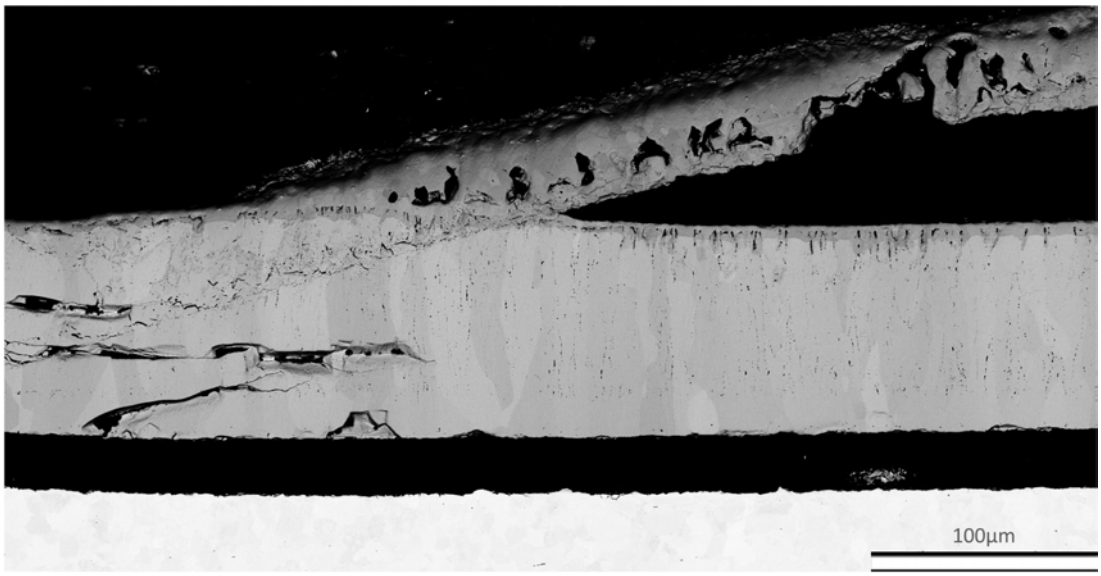

Figure 77: Blister formed upon heating at 900°C for 600s

900°C Figure 77 depicts a large blister produced at 900°C after 600s. The blister was 1021µm across in diameter with a crown thickness of 38µm, more than double that of the blister produced at 900°C after 60s. The blister crown was composed of brittle equiaxed magnetite grains with some of the grains appearing to have fallen out during preparation of the sample (see Appendix) 145. The bulk oxide was formed primarily of large columnar wustite grains and recorded at 101µm in thickness.
A substantial difference at 600s was the large volume of porosity noted throughout the wustite phase of the oxide. Lines of porosity were noted throughout the wustite phase but were heavily concentrated within areas of close proximity to the blisters. Studies have shown that porosity will dramatically increase with increases of time in the wustite phase. Pores are thought to of been heavily generated due to the consumption of wustite in order to further enable the growth of magnetite and hematite [78]. Porosity was also thought to of been heavily generated due to internal stressed generated during volumetric changes triggered by growth. Microvoid formation may of then been initiated to counterbalance these compressive stresses [112] [78]. The average pore size was 0.5µm although many of the pores had coalesced.
The thick layer of wustite beneath the blister crown was surmised to of formed once the antecedent blister had nucleated, lifting the blister as the oxide beneath continued to grow. The oxide layer beneath the blister crown was 91µm in thickness.

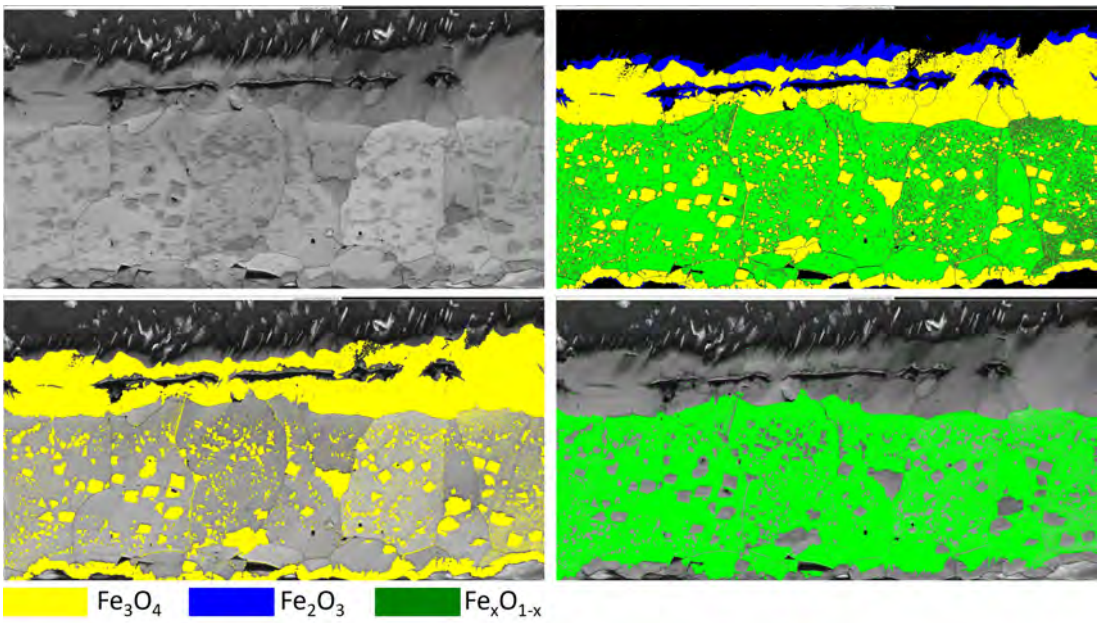

(a) Phase Map

(b) IPF-X Map

Figure 78: EBSD of the Bulk Oxide at 900°C for 600s

900°C EBSD Bulk Oxide The EBSD phase map in figure 78a identified a classical 3 phase iron oxide system. A number of exceedingly fine hematite grains were detected on the underside of the magnetite seam. The presence of fine hematite grains was indicative of oxide break-away from the underlying substrate, resulting in a limited supply of cations. The limited supply of cations will increase the thermodynamic drive for the decomposition of wustite into magnetite and subsequently magnetite into hematite [98].

The IPF map in figure 78b revealed that the magnetite seam did not display a particular orientation preference nor did the columnar wustite grains. Nonetheless an orientation relationship could be established between the pro-eutectoid magnetite precipitates and the underlying wustite crystal. In order to establish such a relationship the magnetite precipitates must have developed due to the decomposition of the wustite phase and thus retained the underlying crystal orientation. The fine hematite grains showed

no oritentation relationship with the magnetite seam. Additionally the outer hematite layer and top magnetite layer shared no obvious orientation relationship. A large horizontal fracture through the magnetite top layer has enhanced the oxidation process and resulted in a number of hematite grains nucleating within the oxide phase.

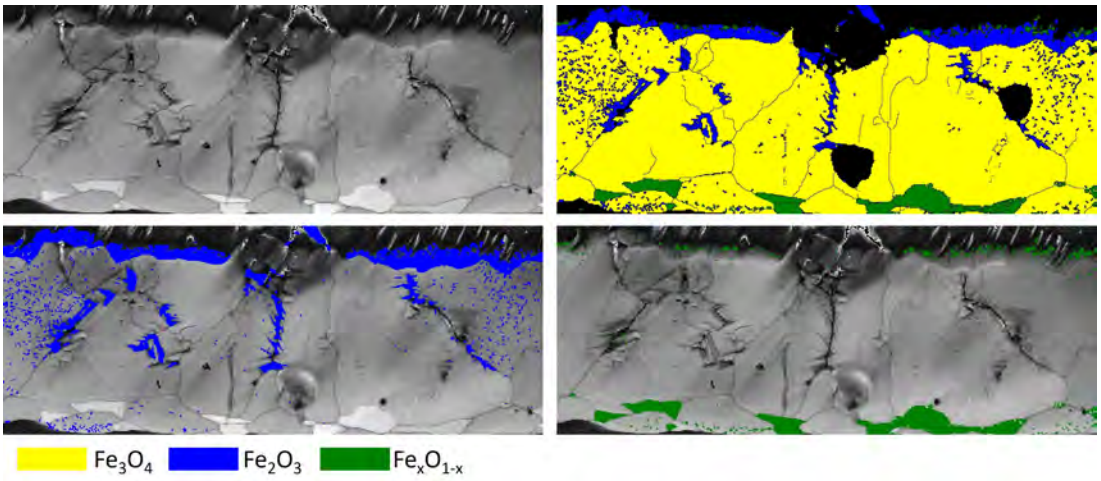

(a) Phase Map

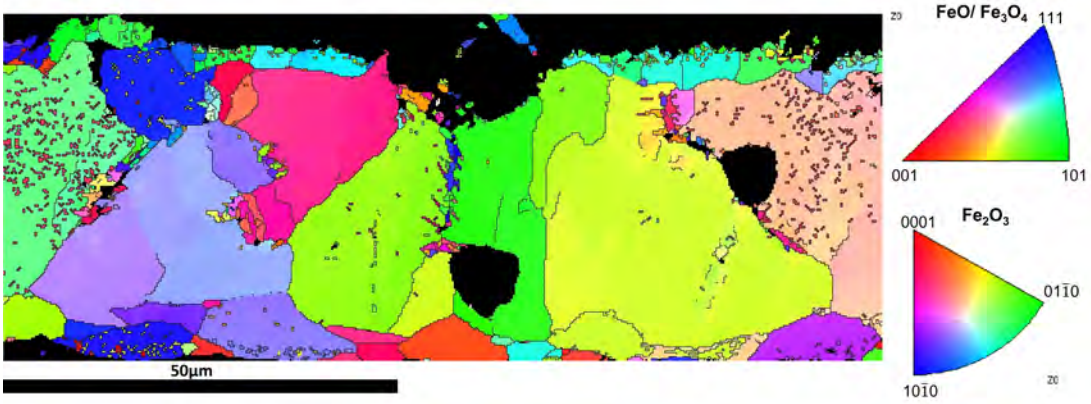

(b) IPF-X Map

Figure 79: EBSD of the Blister Crown at 900°C for 600s

900°C EBSD Blister Crown The EBSD phase map for the blister crown was shown in figure 79a. The oxide morphology was distinctly different to that of the bulk oxide and was found to be principally composed of magnetite. A small intermittent band of retained wustite grains were present along the base of the oxide. The retained wustite grains did not have the classical columnar shape commonly observed for wustite and seen within the bulk oxide. The IPF map in figure 79b shows an orientation relationship between the retained wustite grains and a number of the respective neighbouring magnetite grains.

A number of minute cracks formed along the grain boundaries of the magnetite phase. The hematite phase map shows that the hematite grew along the cracks with a number of small hematite nuclei precipitating through the magnetite grains.

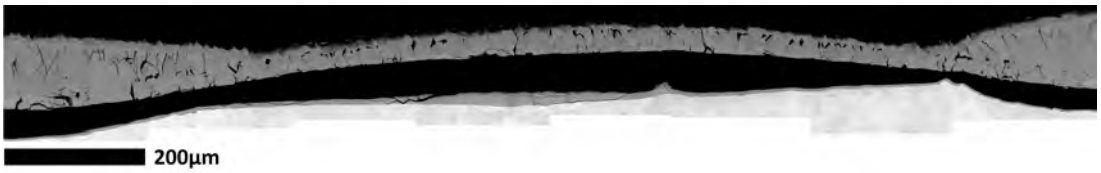

(a) Large scale overview

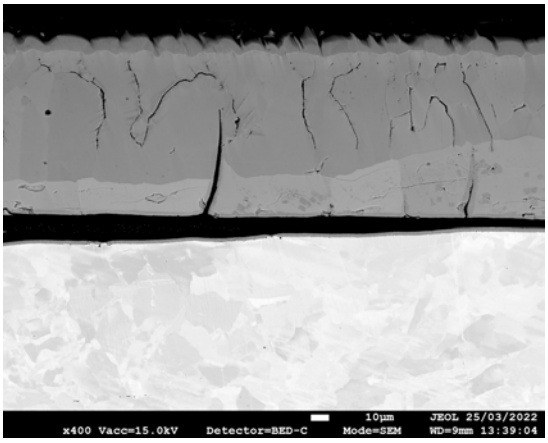

(b) Bulk oxide

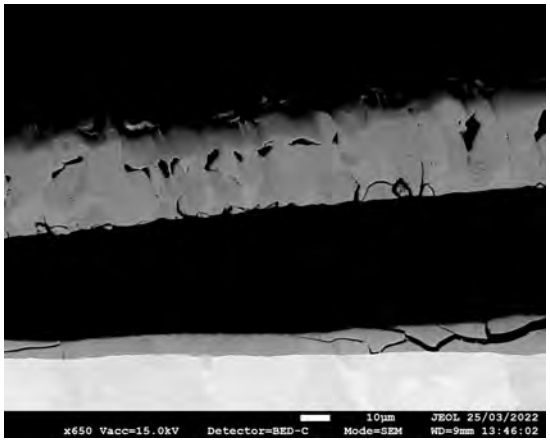

(c) Blister crown

Figure 80: Blister formed upon heating at 1000°C for 600s

1000°C The oxide morphology for the blister produced at 1000°C for 600s was displayed in figure 80. The blister examined was 993µm across in diameter and had a crown thickness of 40µm. The oxide produced was very in-adherent.

The bulk oxide thickness was 103µm and was very close to that produced at 900°C, however the morphology was found to differ quite dramatically. At 1000°C, magnetite was the primary phase and made up the largest volume of the bulk oxide. Thus, in spite of the similar oxide thicknesses, the scale at 1000°C was decidedly richer in oxygen. The magnetite phase differed in thickness throughout the bulk oxide but was approximated at 46µm. The darker phase visible above the magnetite phase in figure 80b was conjectured to be hematite. The thickness of the hematite phase was recorded at 7.8µm and was relatively constant throughout the bulk oxide.

The oxide beneath the blister ranged from 4-18µm in thickness and was detached from the bulk oxide. Upon close inspection it was found that the oxide consisted of a two layer scale.

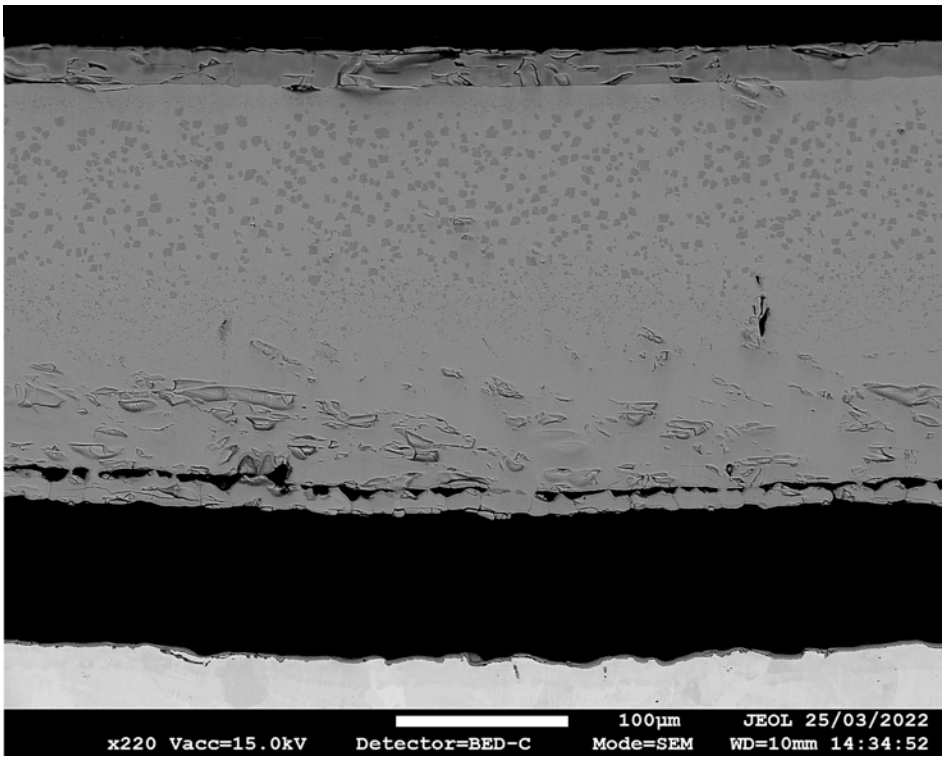

(a) Oxide morphology

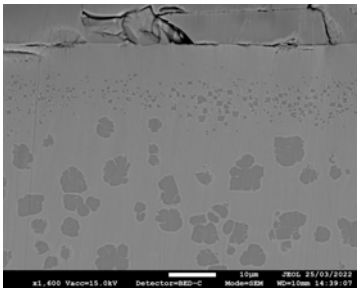

(b) Magnetite precipitates towards outer edge

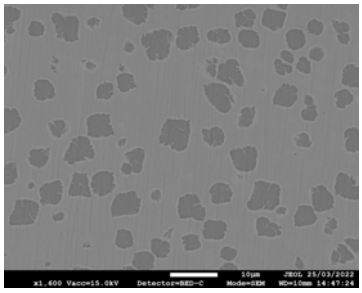

(c) Magnetite precipitates towards center of oxide

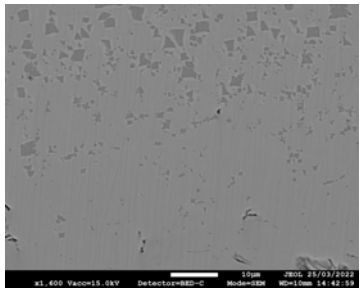

(d) Magnetite precipitates towards interface

Figure 81: Oxide morphology formed at 1100°C for 600s

1100°C Figure 81 features the oxide produced at 1100°C for 600s. The oxide morphology presents as a typical iron oxide consisting of well established oxide layers. The oxide thickness was profoundly greater than that of any of the prior bulk oxides investigated at approximately 264µm. The extensive majority of the oxide was formed of wustite however a continuous and significant magnetite top layer of 24µm was detected and a magnetite seam of 6µm.

Precipitation of magnetite developed predominantly throughout the top half of the wustite phase. The magentite precipitates formed in 3 specific lateral bands. The first band appeared roughly 10µm below the magnetite top layer and many of the precipitates were sub-micron. The band of sub-micron precipitates was shown in figure 81b and was around 10µm in thickness. It was postulated that the sub-micron precipitates were hindered in growth due to the close proximity to the magnetite top band. The magnetite top band would adsorb a large quantity of the excess oxygen that would help promote the magnetite precipitate growth. Beneath the sub-micron layer a region of

substantially larger magnetite precipitates evolved. Many of the precipitates within this region were greater than 5µm in diameter. The large precipitates within this region had dendritic arms and less of cuboid structure indicating they had grown sizably since nucleation. Below the larger magnetite precipitates, towards the middle of the wustite phase, the magnetite precipitates once again decreased in size .
The long heating period at 1100°C produced a thick oxide that did not blister. The resulting oxide was very fragile and in-adherent. Due to the large volume of retained wustite it was conjectured that the oxide detached during cooling.

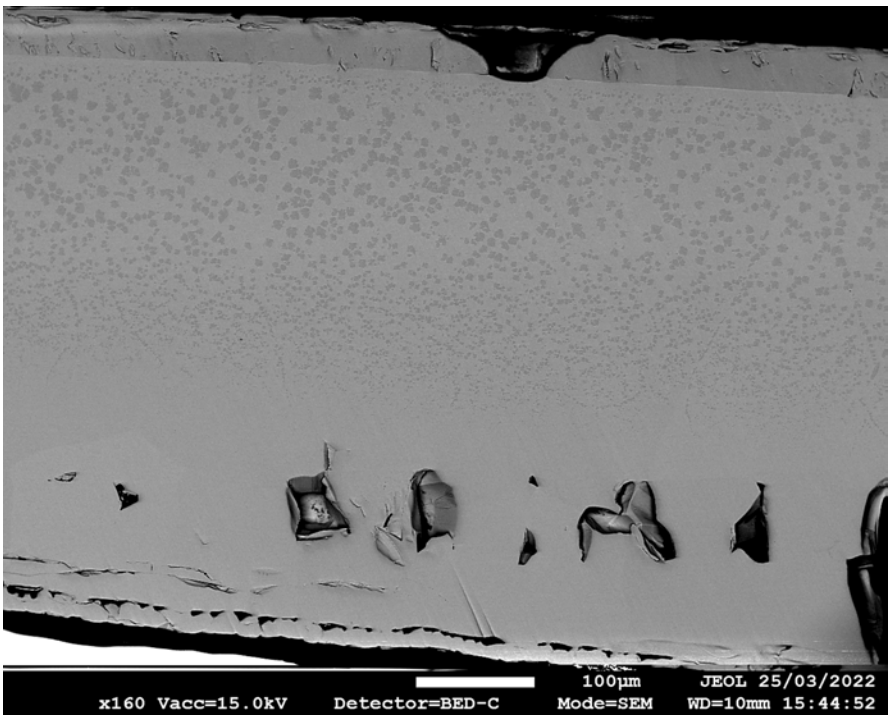

Figure 82: Oxide morphology for 1200°C for 600s

1200°C The oxide produced at 1200°C for 600s did not blister and was the largest by a substantial factor. The thickness of the oxide displayed in figure 82 was approximately 526µm and the top magnetite layer was 41µm. The morphology was very similar to that of the oxide created at 1100°C.

7.3.5 Formation Mechanisms

Whiskers Figure 83 depicts a whisker formed within a blister at 1000°C after 60s. The blister dome was ion beam milled in cross section, exposing the interior of the blister and surprisingly unveiling a number of oxide whiskers. The whiskers varied in size ranging from 6-30µm in length and around 3µm across in width. The oxide whiskers protruded from the sample surface towards the reducing atmosphere retained within the blister [109] [40]. The whiskers often had a kinked and seemingly random shape, developing more of a grooved outer face as they grew larger. Pyramid structures were repeatedly observed on whiskers that were smaller in length. Often the whiskers appeared to have seemingly erupted from the underlying surface (see Appendix 146).

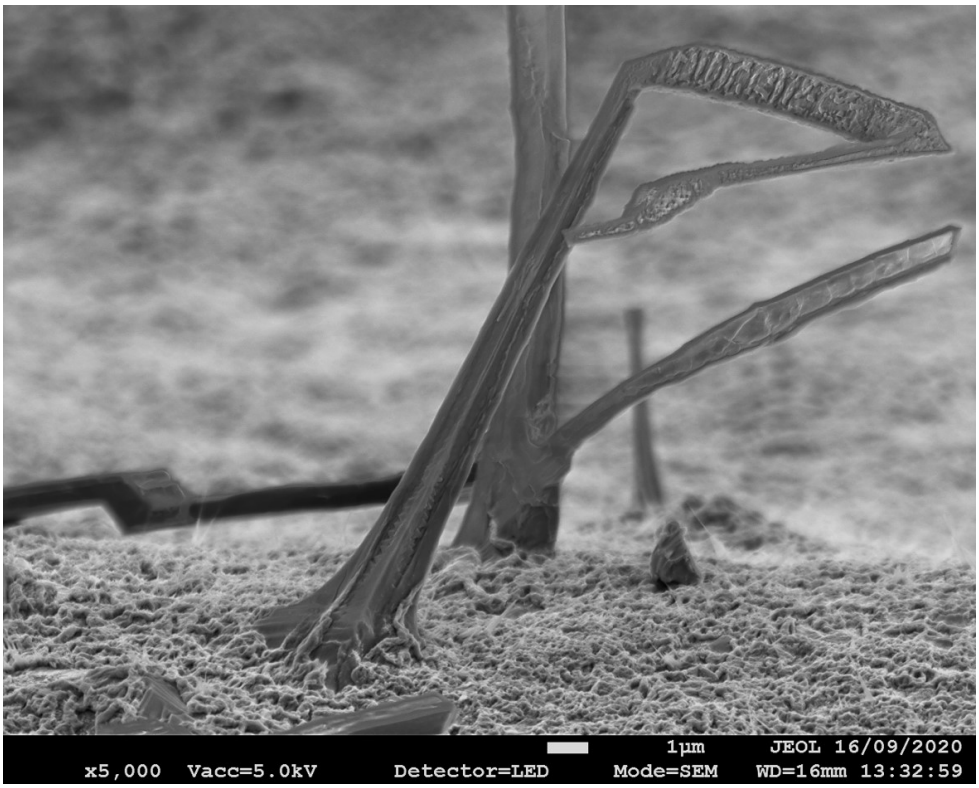

(a) Overview of oxide whisker

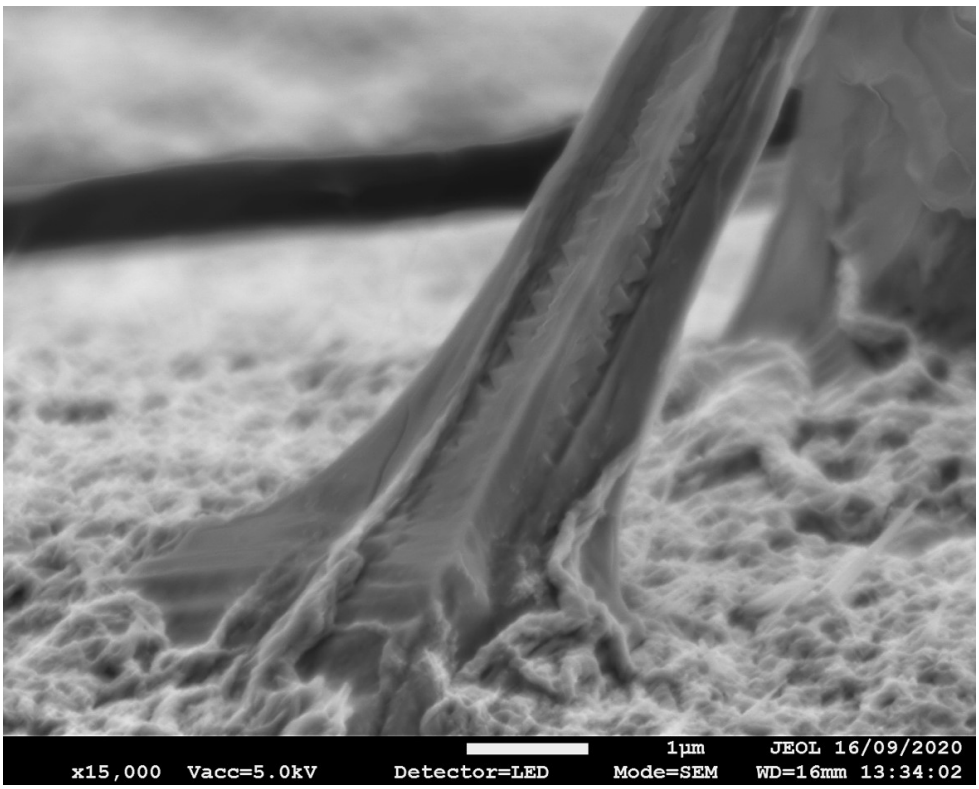

(b)

Figure 83: Whisker formed on sample heated at 1000°C for 60s within a blister environment

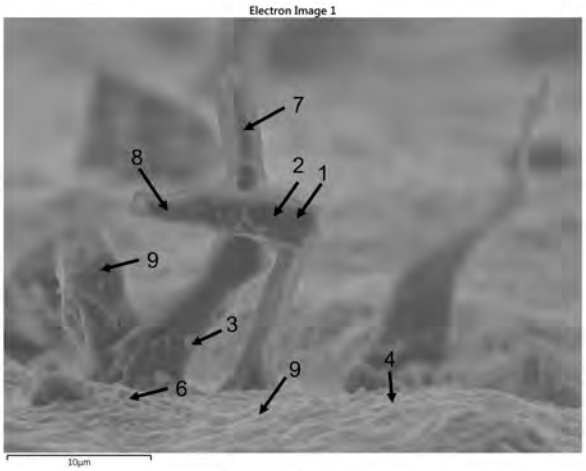

Spectrum	1	2	3	4	5	6	7	8	9
O (%)	25.34	25.7	6.8	26.46	28.05	27.11	7.56	26.49	24.09
Fe (%)	73.91	73.72	92.64	72.97	71.52	72.59	91.61	72.29	75.4

Figure 84: EDS point scan of oxide whiskers developed within blister environment

The growth direction of the whiskers was assumed to have originated from a preferential plane. A number of formation mechanisms for whisker growth have been proposed through literature but the underlying mechanism was still not well understood for many materials [113]. One key formation mechanism proposed was the anisotropic growth rate of a preferred crystallographic direction leading to an elongated crystal [51]. This mechanism requires a nucleation source and a whisker growth rate limited by a gas-solid interface reaction [51]. Initiation sites may be sources of stress such as screw dislocations at the substrate surface. Outwards scale growth of the whisker will then occur in order to diffuse the stress at the substrate surface [114] [113]. EDS analysis found the whiskers to be composed of iron oxide with a Fe:O ratio akin to wustite. The source material of the whisker was found to be iron, with the transport mechanism supposed to be primarily grain boundary diffusion. Diffusion has previously been reported at both the root and tip of the whisker [113] [51] but due to the pyramidal shape and thicker base of many of the whiskers observed it was assumed diffusing atoms aggregated at the root. Whisker growth once initiated was rapid and profuse [113].

Classical Modes of Blistering As previously discussed, mode 1 blistering was characterised by shorter incubation times for formation at higher temperatures [62]. Mode 2 blistering was characterised by longer incubation times for formation at higher temperatures [62].

Figure 85 depicts timestamped images of samples after removal from the furnace at specific temperatures. Figure 85a shows an oxidised sample without any blister. At 800°C after 30s the oxide produced was smooth and adherent with the temperature and heating time too low to result in blister. Nonetheless at 800°C after 600s, blister was observed on the sample, demonstrated in the heat treated samples in figure 69. The longer incubation time resulted in blister, thus samples oxidised at 800°C were characterised by mode 1.

The timestamped images for blister formation within mode 1 were shown in figure 85b; for 900°C at 30s. The increase of temperature raised the stress within the oxide, hence the critical

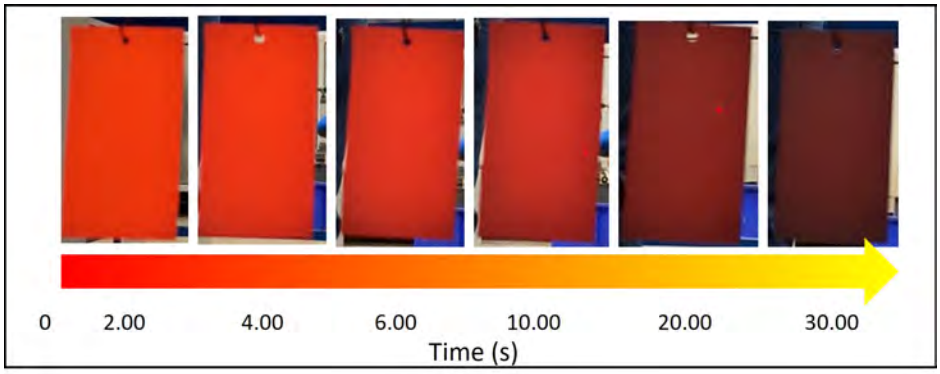

(a) Mode 1 - No Blister (800°C 30s)

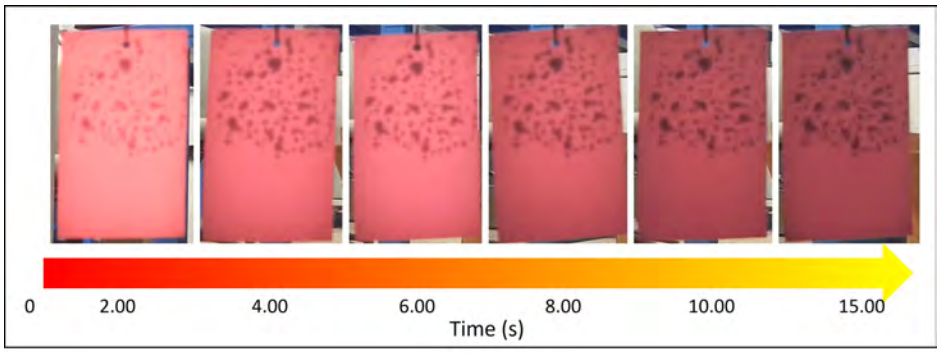

(b) Mode 1 - Blister - (900°C 30s)

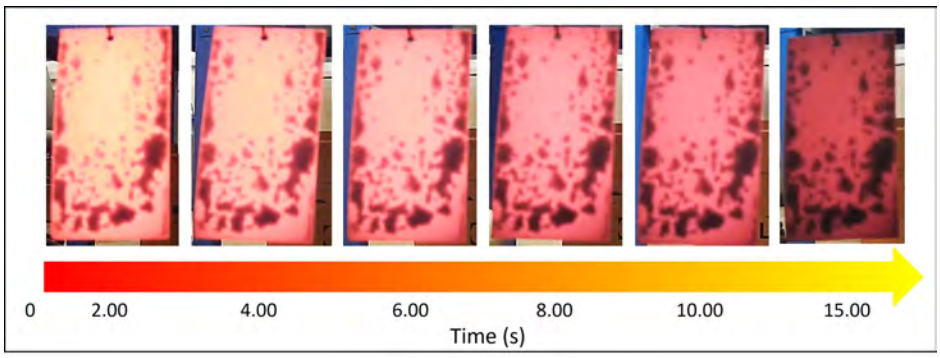

(c) Mode 2 - Blister - (1000°C 30s)

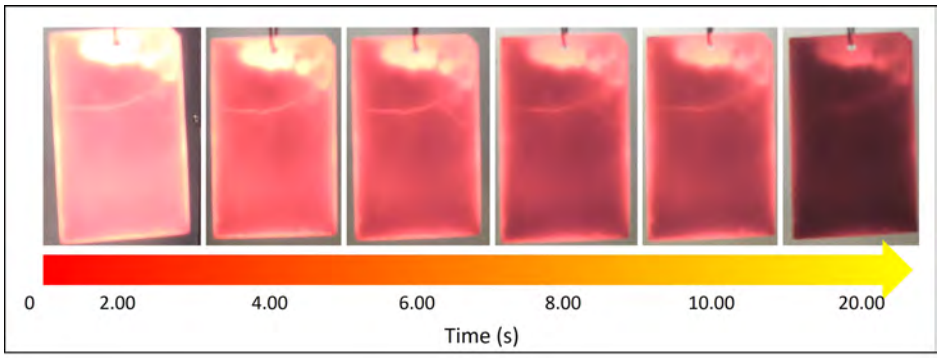

(d) Mode 2 - No Blister (1100°C 600s)

Figure 85: Timestamps showing samples after removal from the furnace

stress for blister initiation was obtained quicker. The blisters produced grew moderately after removal from the furnace but were limited towards the top half of the sample.
Figure 85c shows the formation of blisters within mode 2. Blister was characterised by mode 2 at 1000°C due to the longer incubation time required for blister to be observed. The blisters were far more significant upon removal from the furnace within mode 2 and found to be far more prominent and evenly distributed across the surface.
Samples heated at 1100°C were also treated as mode 2 however due to the prolonged heating time at 600s the oxide did not form any blisters and detached from the surface as whole.

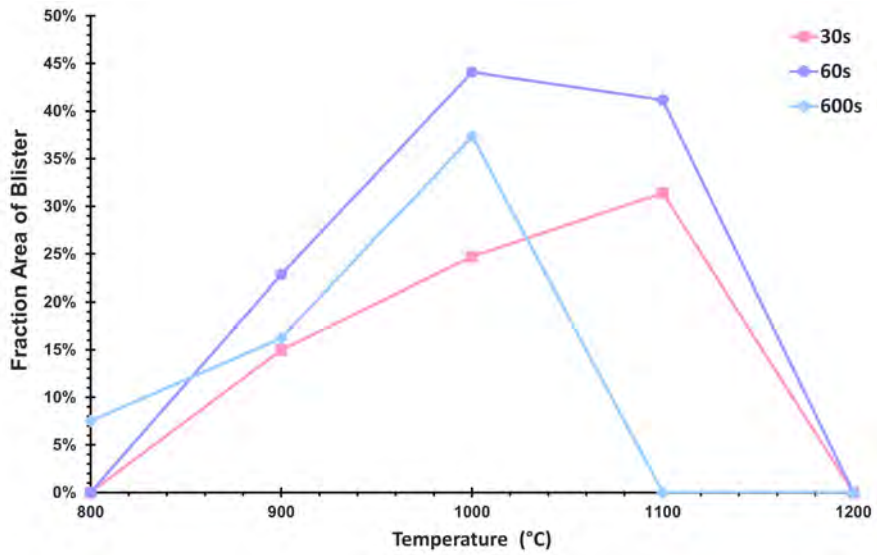

Figure 86: The area fractions of blister formed on scale surface immediately after removal from the furnace - Blister upon heating

	800	**900**	**1000**	**1100**	**1200**
30	0%	15%	25%	31%	0%
60	0%	23%	44%	41%	0%
600	8%	16%	37%	0%	0%

Table 14: Fraction area of blister formed upon heating

The area fraction for blister upon heating was reported in figure 86. Pertaining to the investigated temperatures, 800°C produced the lowest volume fraction of blister; only blistering after a longer incubation time of 600s.
The volume of blister significantly increased within mode 2, with the fraction area almost doubling between 900°C to 1000°C. The lower volume of blister observed at 900°C further supports that blistering was less severe within the mode 1 temperature regime.
For 30s of heating, the fraction area of blister increased linearly with temperature excluding 1200°C. Blister did not occur during heating for any of the investigated times at 1200°C. The fraction area of blister was most severe at 1100°C for 30s at 31%.

For 60s of heating, a different scenario was observed. The fraction area of blister was more of a normal distribution peaking at 1000°C and dropping off after 1100°C. The percentage of blister at 60s was commendably greater than that of the other 2 specified heating periods at temperatures of 900°C 1000°C and 1100°C. Sample 1000°C for 60s retained the largest volume of blister from the entire sample set at 44%.
The lower volume fractions observed at 600s further aids the hypothesis that prolonged heating times, within the mode 2, will result in a more malleable and ductile scale, ultimately reducing blister upon heating.

Mode 3 - Cooling A new and previously unreported mode of blister was observed and substantiated during air cooling on a number of 3812 samples. The new phenomena will henceforth be refereed to as blister upon cooling. Figure 87 presents the blister upon cooling phenomena at 1200°C for 30s and 60s.

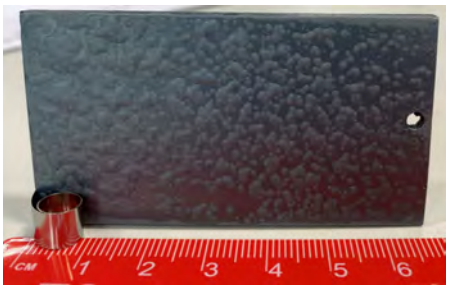

(a) Sample prior to mounting (1200°C 30s)

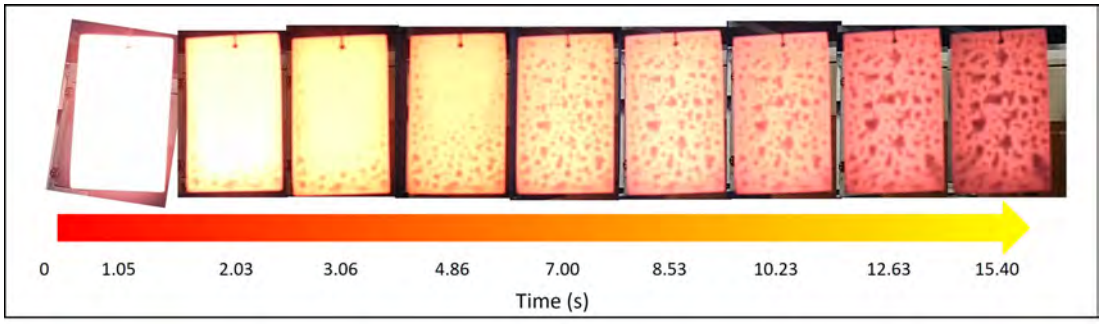

(b) Mode 3 - Blister on Cooling (1200°C 30s)

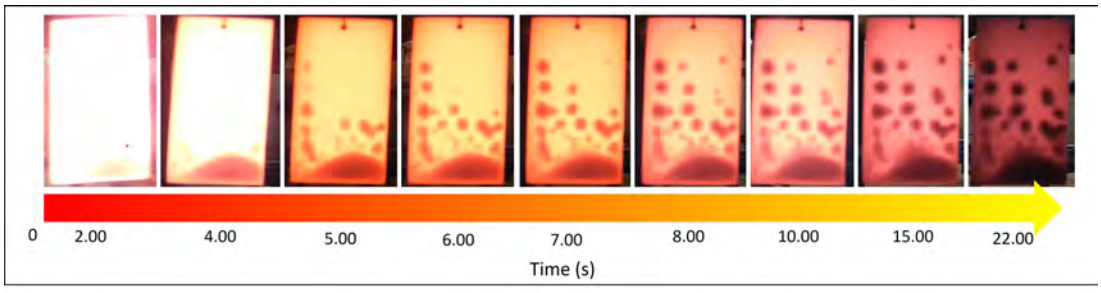

(c) Mode 3 - Blister on Cooling (1200°C 60s)

Figure 87: Blister on Cooling- Timestamps showing samples after removal from the furnace depicting

In Figure 87b, observed at 1200°C for 30s, the immediate post-furnace removal surface of the sample appeared clean. However, within 3 seconds, blistering commenced at the

bottom edge, a phenomenon observed both visually and through camera monitoring. Notably, the blisters emerged once the sample cooled from its white-hot state, indicating they were absent prior to removal from the furnace. Subsequently, at the 4-second mark, blister nucleation progressed inward toward the sample's center. By the 7-second mark, blistering encompassed the entire sample. Similarly, Figure 87c, taken at 1200°C for 60s, exhibited a comparable progression, initiating at the edges before extending toward the sample's center. The timestamped images show that the sample heated for 30s blistered significantly faster compared to 60s after removal from the furnace. The blisters produced at 30s were smaller and far more numerous than those produced at 60s. There was no discernable difference in size of the blisters across either sample.

The blister was thought to nucleate firstly towards the outer geometry of the sample due to preferential cooling. Preferential cooling of the sample would firstly occur towards the edges of the sample due to the large volume of exposed surface area, resulting in fast heat loss.

During cooling stresses are generated due to the differing thermal expansion coefficients of the oxide phase and the underlying alloy [78]. The differing thermal expansion coefficients will result in non-uniform thermal stresses and high inter-facial stress. Blister upon cooling was postulated to occur due to thermal stresses initiated upon cooling, whereby a critical volume of high inter-facial stress was reached. Upon reaching a critical volume of stress, the oxide will become incoherent with the substrate and lift to alleviate the inter-facial stress [115].

Blister upon cooling was principally observed at the higher temperatures within the mode 2 region. The samples that displayed the largest volume of blister upon cooling did not exhibit any blister upon heating. It was conjectured that due to the increased temperature, upon heating, any resulting stresses or gases could be easily distributed through the ductile scale [97]. Nonetheless as the scale cooled, any generated or residual stresses would not be distributed through the oxide and the inter-facial stress would build. Thus, in order to alleviate the increasing inter-facial stress the scale would lift, producing blister upon cooling.

Further supporting this theory were the many key differences observed in oxide morphology and thickness in blisters upon heating versus cooling. The blister crown produced upon cooling was of a similar thickness to the bulk oxide whereas, upon heating the crown was considerably thinner than the bulk oxide. Blister crown growth would be limited once lifted from the substrate due to the limited availability of cations. Hence, it would be expected that the growth of blisters upon heating would be stunted due to the early uplift of the blister crown; producing a blister crown substantially thinner than the bulk oxide [116]. Furthermore, upon heating the blister crown was composed predominantly of magnetite, while the blister upon cooling was formed primarily of retained wustite [117]. The large volume of retained wustite upon cooling was owed due to the blister lifting during cooling allowing for a very short period of wustite decomposition [97].

Modes of Blister Steel grade 3812 produced blister across a range of temperatures and heating times, with a number of formation mechanisms. The resulting blister regime after heat treatment and subsequent air cooling was depicted in figure 88 for the 3 identified modes of blister. The nose of the blister curve was found at 900°C for 10s. At temperatures below 1000°C, blisters were primarily mode 1 and above they were a combination of mode 2 and 3.

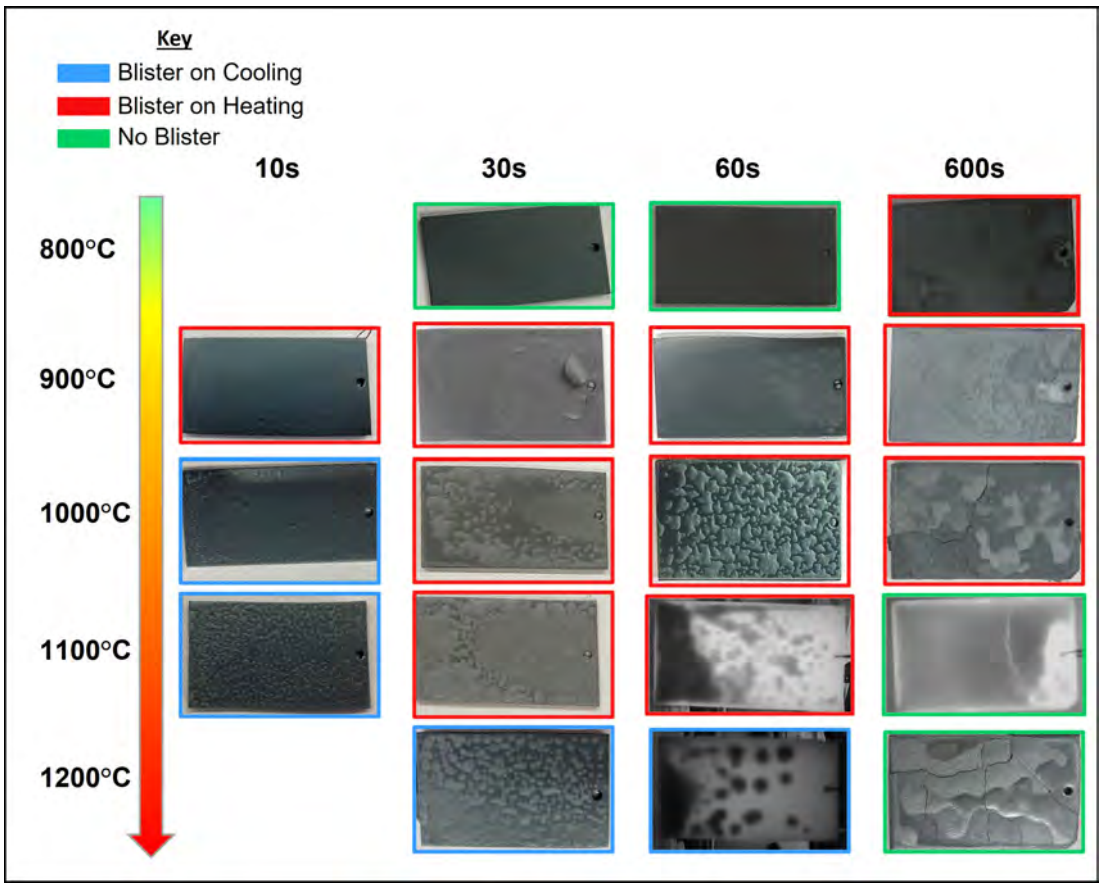

Figure 88: Samples after heat treatment and air cooling categorised by heat treatment

	30s	**60s**	**600s**
900°C	30	x	103
1000°C	x	90	101
1100°C	117	101	264
1200°C	75	81	526

Table 15: Bulk Oxide Thickness (µm)

	30s	**60s**	**600s**
900°C	16	18	39
1000°C	x	35	40
1100°C	84	73	No blister
1200°C	70	77	No blister

Table 16: Blister Crown Thickness (µm)

Bulk oxide thickness and blister crown thickness were shown to increase with increments of heating time, shown in table 16 15. The largest gain was for the bulk oxide between 60s to 600s at 1200°C, with an increase of 81µm to 526µm. The considerable increase in oxide thickness resulted in the elimination of blister.
Blister upon heating was evident at 900°C due to the discrepancy between the blister crown and the bulk oxide thickness. A 1:2 ratio was established between the crown and bulk oxide. As heating times were extended the ratio increased for blister upon heating. Blister upon cooling was clearly discernable at 1200°C due to the comparable thickness of the blister crown and bulk oxide. Blister upon cooling translates into a rough 1:1 ratio for the crown and oxide thickness.

7.3.6 DP800

Blister Regime The resulting blister regime after heat treatment was depicted in figure 89. Samples were isothermally heat treated and then lifted out of the vertical tube furnace and filmed as they air cooled.
The isothermal heat treatments were designed in order to obtain TGA data and deduce the oxide morphology in chapter 6. Nonetheless blister was noted on a number of samples upon examination and a partial blister regime was produced (see Appendix 147, 148, 149, 150). Future works should include further heat treatments on larger samples in order to identify the volume fraction of blister, the blister regime nose and the transition temperature between mode 1 and 2.
A number of very interesting phenomena were observed within the DP800 samples including blister within blister. This will be discussed in the results below

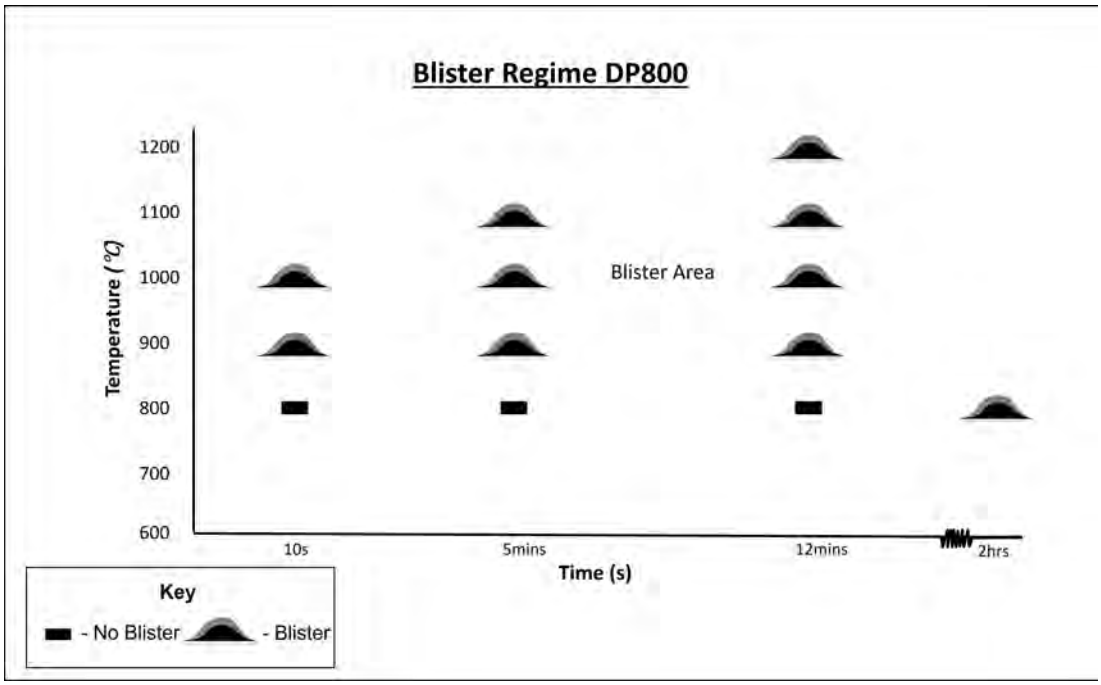

Figure 89: Blister regime DP800

7.3.7 5 minutes

900°C 5mins The blister and oxide formed after heating for 5mins at 900°C was shown in figure 90. The diameter of the blister in figure 90b was 13.5µm with a height of 5µm. The height was measured from the base of the substrate to the apex of the blister dome. The height of the blisters was found to be analogous throughout the sample, producing a rough but repetitive surface topography. The diameter of the blisters varied far more substantially than the height with the measured diameters in figure 90a ranging from 10µm to 23µm. The bulk oxide thickness was measured at 11.5µm and the blister crown thickness at 1.5µm. The crown thickness was extensively thinner than any blisters produced previously on the 3812 steel grade. The previously obtained TGA results indicated that DP800 had a fiercely lower rate of oxidation at 900°C, hence a thinner blister crown and oxide was not of surprise.

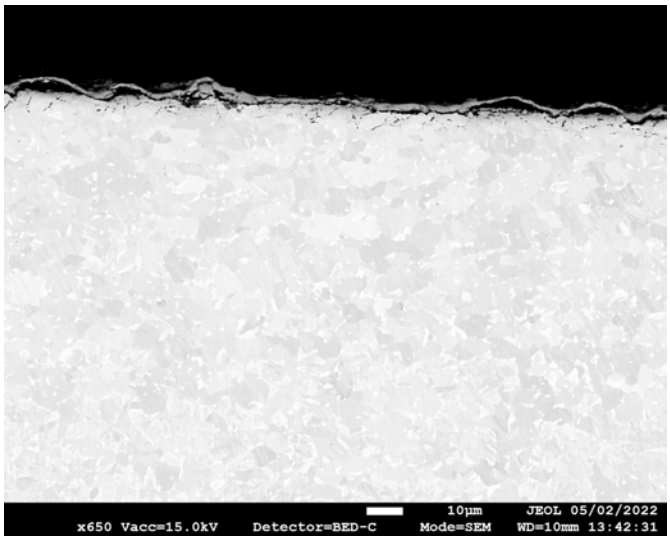

(a) DP800 microstructure overview with regions of internal oxidation and numerous blisters

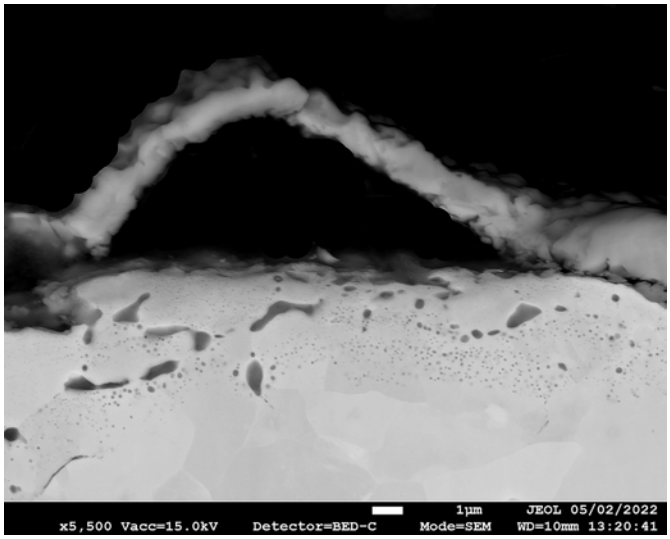

(b) Singular blister

Figure 90: Microstructure and oxide formed after heating at 900°C for 5mins

1000°C 5mins The blister and oxide morphology formed after heating for 5mins at 1000°C was far more complex and convoluted than that produced at 900°C. Figure 91 exhibits an intricate and multi-phase oxide with a thin region of internal oxidation. The bulk oxide was 41.5µm in thickness, consisting of wustite, magnetite and a complex spinel phase.

The blister crown displayed in figure 91a was approximated at 7µm and had a thick layer of oxide beneath. The oxide beneath the blister appeared to have split in multiple regions with large lateral cracks appearing to initiate the lifting of a secondary layer of oxide. This will be referred to as secondary blister and is discussed in detail later on.

Figure 91c shows that adjacent to the blister crown was a fine channel of small eutectic particles formed of an Al-Si oxide. These produced a spinel phase and formed throughout the oxide in a banded structure but were not present at 900°C.

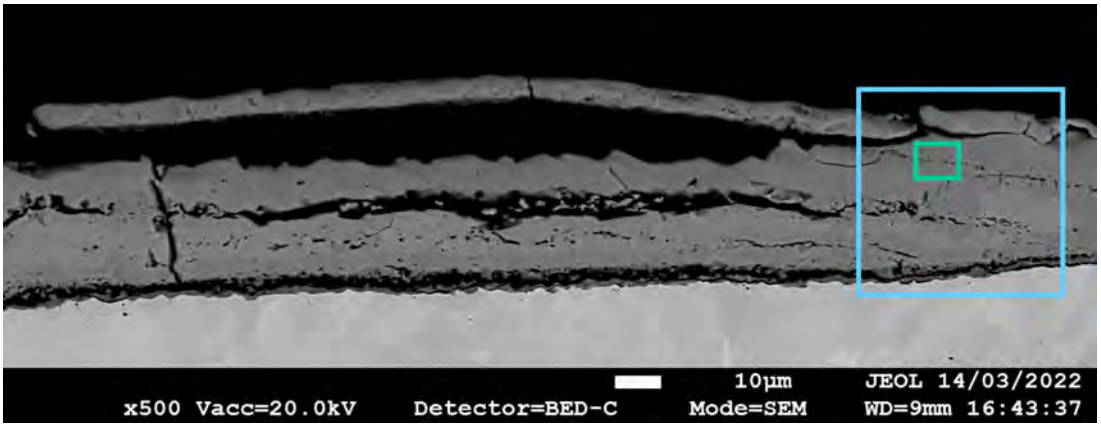

(a)

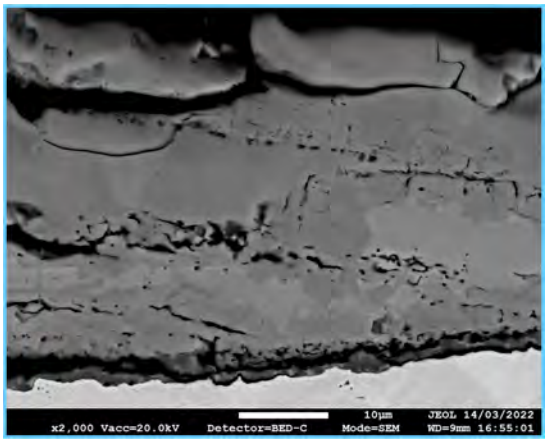

(b)

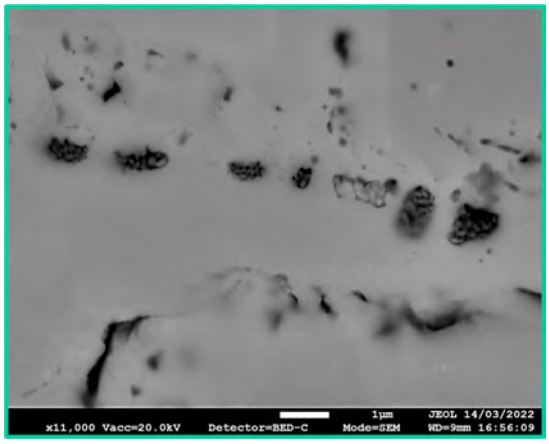

(c)

Figure 91: Blister formed after heating at 1000°C for 5mins

It was conjectured that the eutectic particles of Al and Si were previously internal oxide precipitates that were dragged by a moving interface as the oxide continued to grow [99]. It was postulated that as the internal oxide precipitates were dragged into the external oxide, incoherency with the surrounding oxide increased. Incoherent phases often experience enhanced mobility and thus as the precipitates became more mobile they migrated towards one another producing larger particles within an intermittent

banded structure [118] [119].

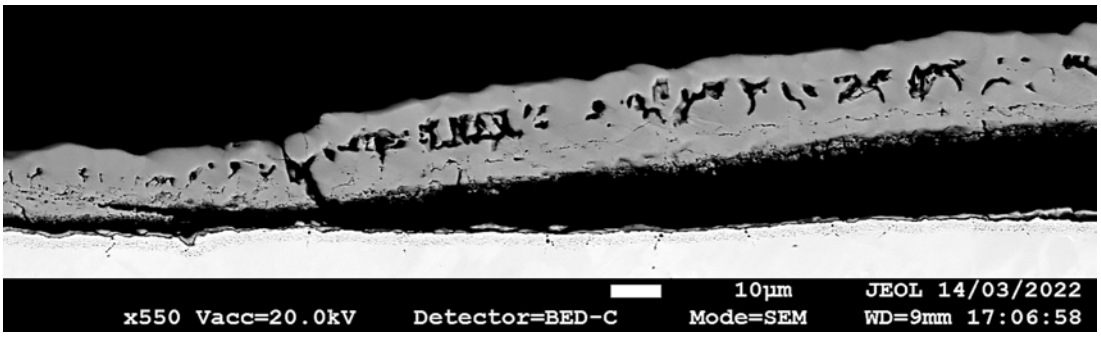

(a)

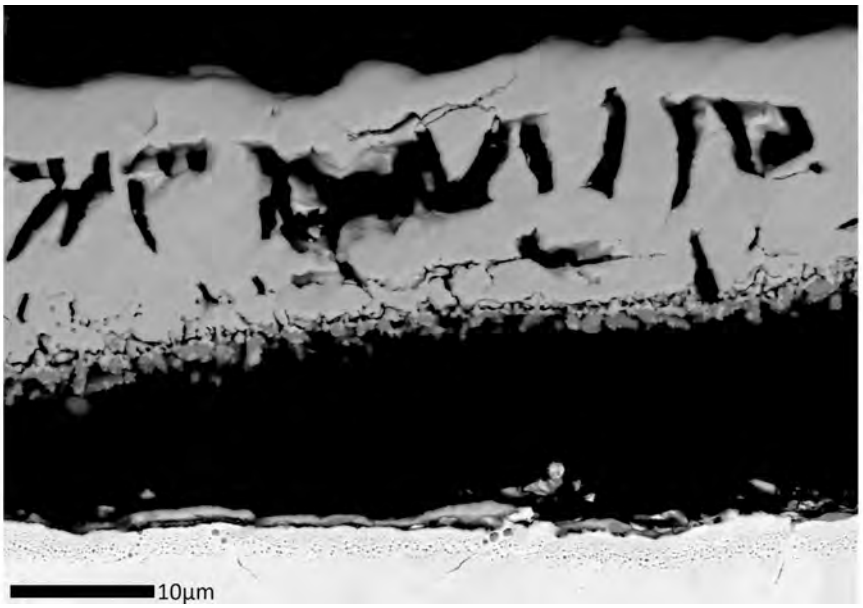

(b)

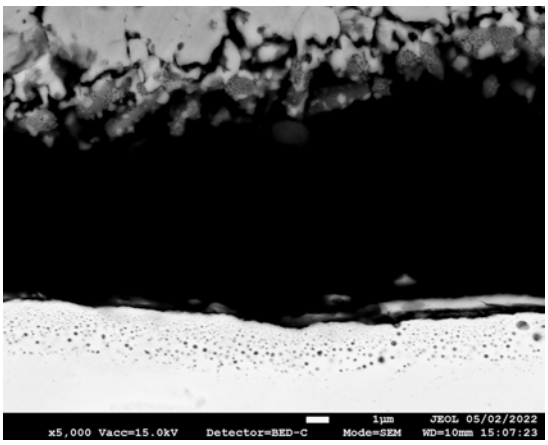

(c)

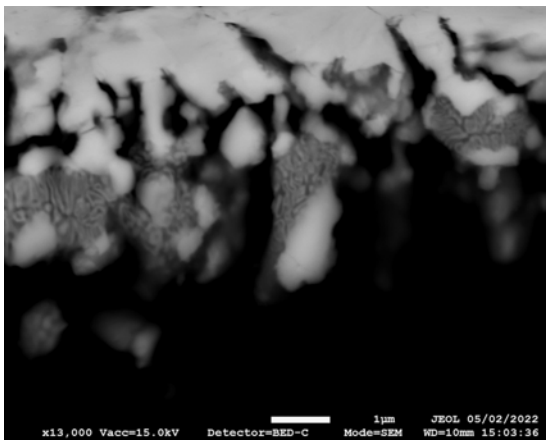

(d)

Figure 92: Blister formed upon heating at 1000°C for 5mins

Figure 92 displays another blistered region formed after heating at 1000°C for 5mins. As previously noted in the blister for figure 91, a spinel phase was observed throughout the external oxide. The spinel was detected on the underside of the blister crown, with a lamella structure shown in figure 92d.

The conglomerated spinel phase would create a large volume mismatch with the sur-

rounding iron oxide phase. The incoherent interface would then produce a large volume of strain within the surrounding area allowing for rapid crack propagation due to the banded structure of the precipitates [120]. The brittleness within this region allowed for break away and mechanical failure of the oxide scale, with the uplift producing a blister.
A key difference ascertained between the two blisters observed for 1000°C for 5mins was the difference in blister crown thickness. The blister in figure 92 had a blister crown thickness of approximately 23µm. A thicker blister crown implies that the blister lifted later on during oxide growth development or potentially during cooling. This was further supported by the distinct lack of oxide beneath the blister. The blister crown was composed brittle equiaxed magnetite grains with some of the grains appearing to have fallen out during sample preparation.

WDS Extensive WDS analysis was conducted on the DP800 blister samples in order to deduce the phase composition within the multiphase scale.
WDS points 3,4 and 5 show that the bulk of the oxide was composed of magnetite. Islands of retained wustite were present within the lower half of oxide shown spectra 6 and 17. The high volume of magnetite throughout shows that cation transport was likely suppressed resulting in an oxygen rich scale. The cation transport would have been hindered due to the internal oxidation zone noted throughout DP800 samples as outlined previously in chapter .
Spectra 9, 13, 14, 21, 22, and 26 were used to identify the composition of the blister crowns and were all found to be magnetite and hematite. An oxygen content around 30wt% was indicative of hematite, 27wt% was indicative of magnetite and below was indicative of wustite.
The underside of the blister crowns was found to be extremely rich in Si. Spectra 11 and 23 show that the spinel identified in figure 92d was a rich in Si and Al producing a complex eutectic phase. The WDS results show that although the blister crowns may differ in size and appearance the bulk of the oxide were all composed of iron oxides.

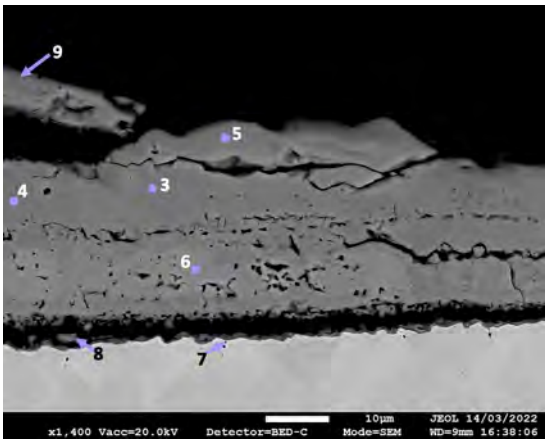

(a) Reference area 1

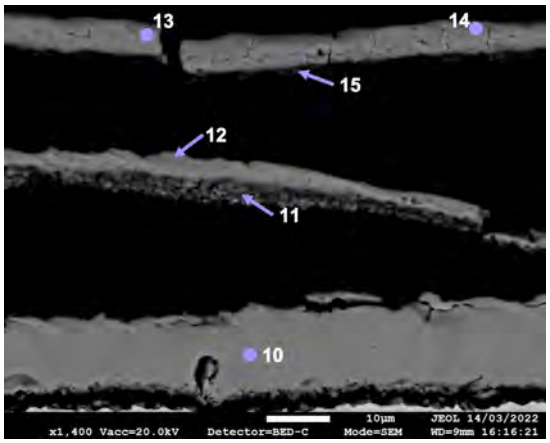

(b) Reference area 2

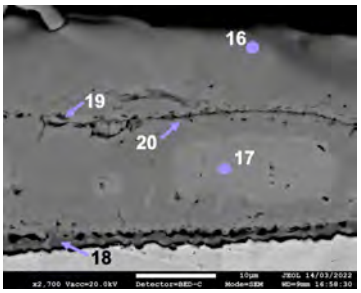

(c) Reference area 3

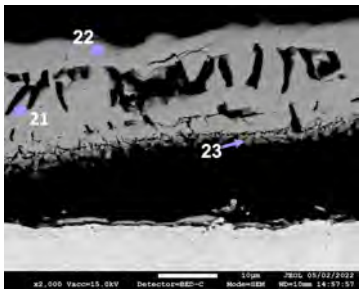

(d) Reference area 4

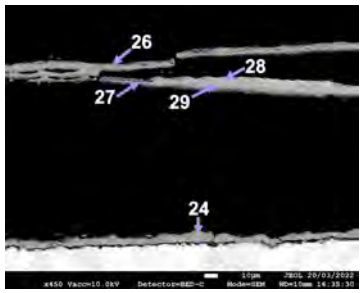

(e) Reference area 5

			Wt%				
		Region	Fe	O	Al	Si	Mn
Spectrum	3	Oxide matrix mid	70.60	29.27	0.07	0.06	
	4	Oxide matrix mid	65.89	28.85	0.02	0.02	
	5	Oxide matrix top	70.32	29.44	0.03	0.08	
	6	Oxide matrix 2nd phase	73.07	26.63	0.23	0.06	
	7	Oxide interface	73.85	14.27	2.77	4.59	4.51
	8	Oxide interface	54.26	33.82	2.93	8.99	0.00
	9	Blister	68.89	30.71	0.27	0.13	
	10	Oxide beneath blister crown	69.86	29.89	0.20	0.05	
	11	Blister crown underside	65.74	29.25	0.87	4.14	
	12	Blister crown below secondary blister	72.78	26.10	0.53	0.60	
	13	Secondary blister crown	66.90	32.31	0.44	0.35	
	14	Secondary blister crown underside	68.22	31.24	0.36	0.18	
	15	Secondary blister crown	67.59	28.36	1.21	2.61	0.23
	16	Oxide matrix top	64.12	35.53	0.25	0.11	
	17	Oxide matrix secondary phase	70.92	26.88	0.23	0.06	1.91
	18	Oxide interface	55.85	33.34	5.42	5.40	
	19	Oxide crack	60.12	31.14	0.55	5.74	2.44
	20	Oxide crack	56.49	32.15	0.57	7.21	3.53
	21	Blister crown	69.41	29.66	0.28	0.65	
	22	Blister crown	69.85	29.87	0.20	0.09	
	23	Blister crown underside	48.24	34.69	3.73	13.34	
	24	Oxide beneath blister	69.63	29.78	0.43	0.16	
	26	Blister crown split top side	69.61	29.70	0.27	0.27	
	27	Blister crown split bottom side	70.68	28.47	0.63	0.22	
	28	Blister crown split bottom side	64.81	31.72	1.10	2.36	
	29	Blister crown split bottom side	71.98	27.85	0.04	0.13	

(f) WDS point scan spectra

Figure 93: WDS conducted on DP800 at 1000°C for 5mins

7.3.8 Double Blistering Phenomena

Paper Presented at the oxi conference 2022

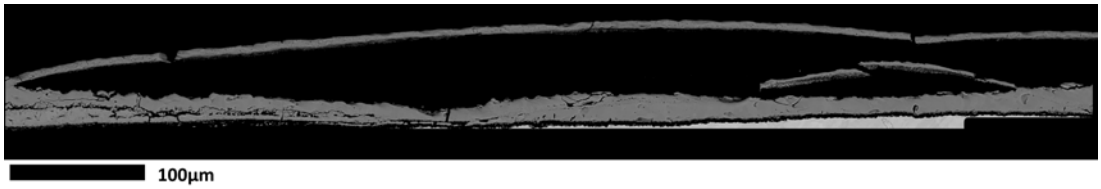

(a) Through thickness oxide morphology- Substanatial oxide growth beneath primary blister propogating a smaller secondary blister

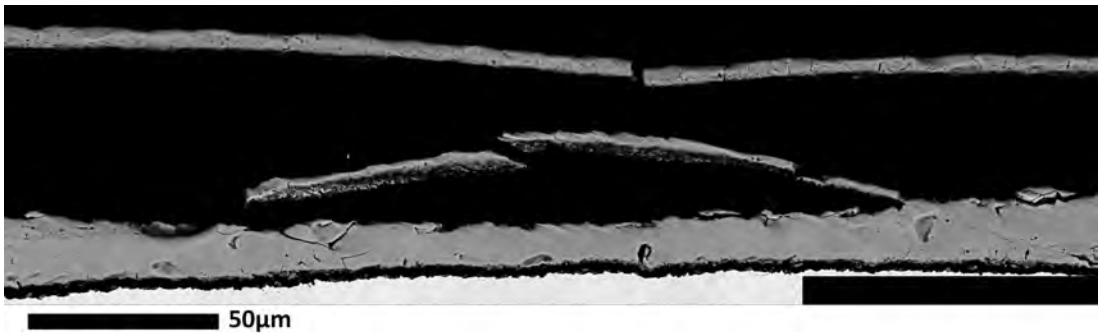

(b) Highlight of secondary blister within primary blister

Figure 94: Double blister phenomena

Figure 94b shows the cross section of a large blister over 900µm in size with a smaller secondary blister within the primary blister zone. The phenomenon of secondary blister was seen multiple times throughout the sample. The primary blister has a crown thickness of 7.98µm, with the secondary blister having a comparable crown thickness of 7.49µm. This was found to be consistent with other primary and secondary blisters throughout the sample. The bulk of the oxide was found to be 41.5µm in thickness and the area underneath the primary blister 22.2µm. The primary blister crown was concaved in regions, thought to be due to the relaxation of the crown once the gases from decarburisation have been released.

Due to the double blistering phenomena in figure 94, nucleation must be considered as two separate stages, with the initial primary blister developing within the first stages of oxidation. Its postulated that the oxide beneath then continues to grow, until eventually conditions allow for a secondary Blister to nucleate. The oxide morphology in 94b consists primarily of a loosely adherent iron oxide with areas of internal oxidation between the oxide scale and the metal substrate. A spinel phase rich in Al and Si can be noted on the undersides of both blisters and can be seen to continue permeating into the iron oxide below. Bands of the same spinel phase appear roughly every 5-7µm throughout the oxide as globular spheres less than 1µm in diameter. They are extremely brittle in nature and are surmised to be acting as initiation sites for failure, allowing for quick crack propagation through the oxide due to the banded nature.

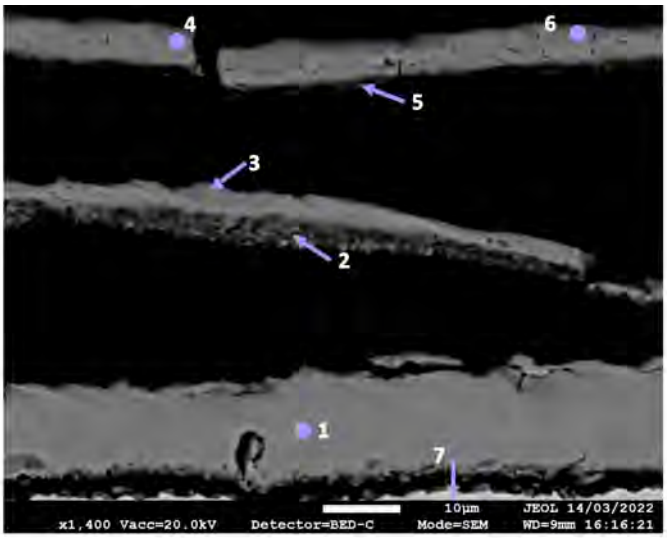

		Wt%			
	Region	Fe	O	Al	Si
1	Oxide beneath blister crown	69.86	29.89	0.20	0.05
2	Blister crown underside	65.74	29.25	0.87	4.14
3	Blister crown below secondary blister	72.78	26.10	0.53	0.60
4	Secondary blister crown	66.90	32.31	0.44	0.35
5	Secondary blister crown underside	67.59	28.36	1.21	2.61
6	Secondary blister crown	68.22	31.24	0.36	0.18
7	Internal oxidation zone	60.32	19.22	8.82	4.56

Figure 95: WDS conducted on the cross-section of a secondary blister

Chemical analysis confirms the presence of a spinel phase high in Si – 4.14 wt% and Al – 0.87wt% at both the metal/scale interface and under the blister crown (points 2, 6 and 7, in figure 95). If the presence of the brittle spinel phase acts as a line of weakness for blister formation, then this suggests that the segregation of the Si and Al must also occur early in the oxide scale development. Oxide development is often reported to be guided by the ionic transport of cations ($Fe^{2}+$, $Fe^{3}+$) and anions ($O_{2}-$) with cation transport largely dominating resulting in an outward growth [19] [121]. In DP800 steel, the alloying additions of Si and Al results in selective oxidation, reducing the outward diffusion of cations and resulting in local enrichment of Si and Al at the metal/scale boundary [122]. This results in the formation of a thin Hematite layer at the oxygen rich surface. This selective oxidation of Si and Al typically lowers oxidation rates of steel producing a passivation layer.

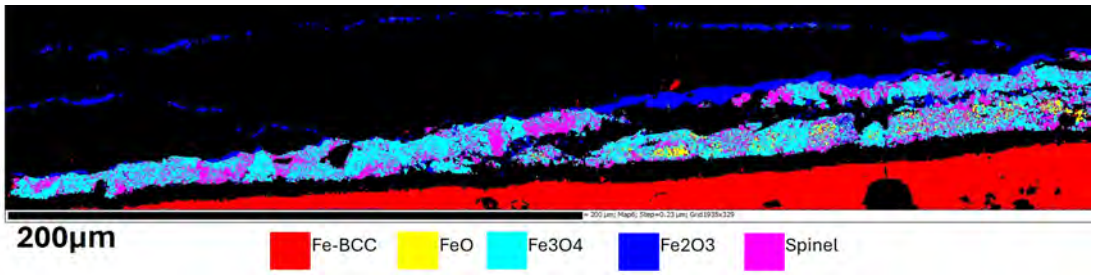

(a) Phase map

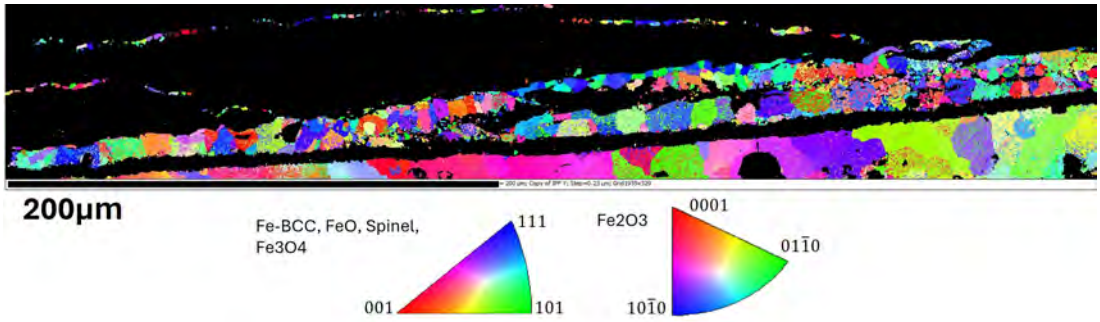

(b) IPF-X map

Figure 96: EBSD conduced on DP800 double blister area 1000°C for 5mins

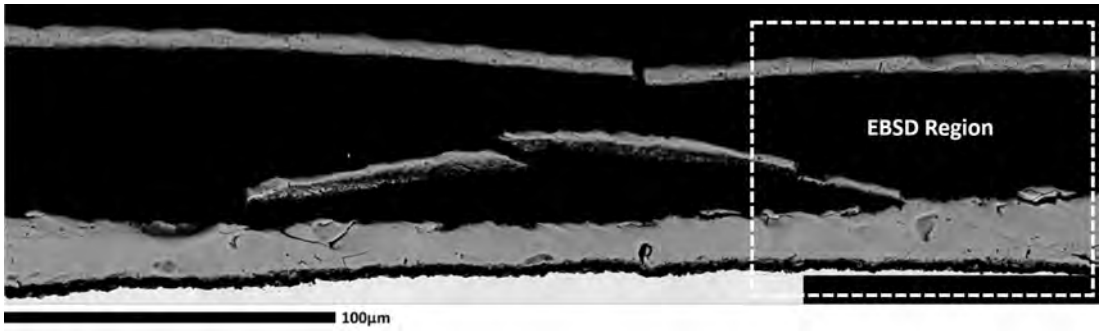

Figure 97: EBSD reference area

The EBSD phase map in figure 96a shows a banded structure with the primary and secondary blister crowns both composing of hematite and the thicker oxide scale comprised of magnetite, iron oxide, and a spinel phase. The presence of hematite in both blister crowns suggests that the mechanism for blister formation in this case was predominantly due to decarburisation. Hematite has poor permeability and acts as a barrier for gas diffusion resulting in gases at the metal/scale interface producing pressure that assists in lifting the scale upwards [53] [109]. Some of the Si and Al rich spinel phase was carried up with the blister crown allowing for the formation of another thin hematite layer within the blister. Nonetheless, the difference in the secondary blister formation was that it forms due the dissociative mechanism suggested by Kondo [109], where hematite forms from the dissociation of oxygen from both the CO and CO_2 gases present in the blister micro-environment. As before, once the hematite layer was formed the remaining build-up of gases causes the secondary blister to develop.

The EBSD IPF map in figure 96b shows no preferred grain orientation for the oxide scale in general, however there are some regions of preferred orientation in the high-

lighted hematite region. The preferred (0001)Hem shown in the EBSD IPF//X map 96b was similar to that reported by Oliveria et al. [123], that proposed a relationship of (111)Mag // (0001)Hem between the two phases. However, in this case the relationship was not continued in either of the hematite blister crowns.

Double Blister Conclusions

- The early formation of a thin Hematite layer in DP800 acts as a barrier for gas diffusion due to its poor permeability. The subsequent build-up of gas pressure causes the scale to blister at the metal/scale interface which was weakened by the presence of a brittle Si and Al rich spinel phase.
- The dissociation of oxygen from the CO and CO_2 rich atmosphere within the initial blister allows a secondary layer of hematite to grow, forming a new gas barrier which can then nucleate a secondary blister.

7.3.9 Blister Crown Split

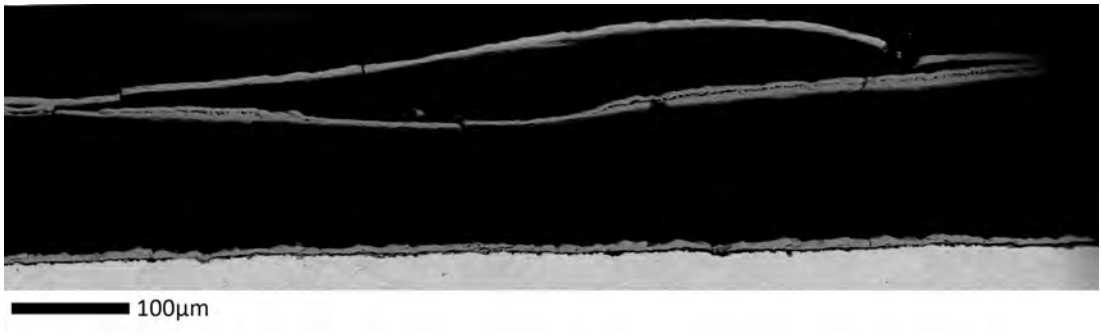

(a) Overview of blister crown that has split into 2 sectons

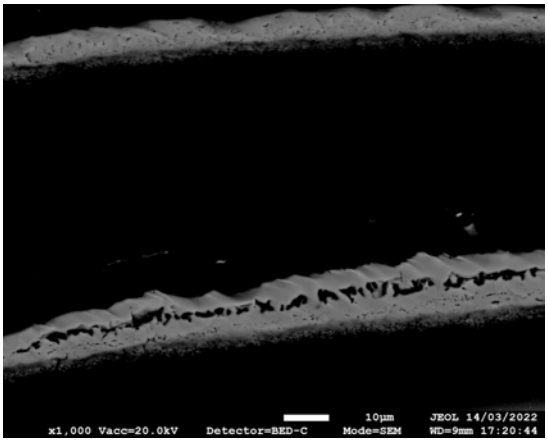

(b) Blister crown split

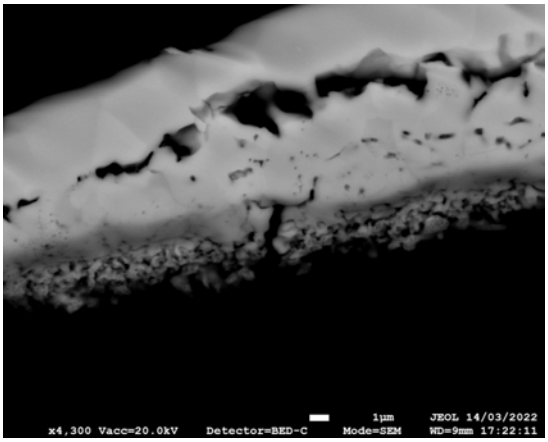

(c) Area beneath secondary blister crown

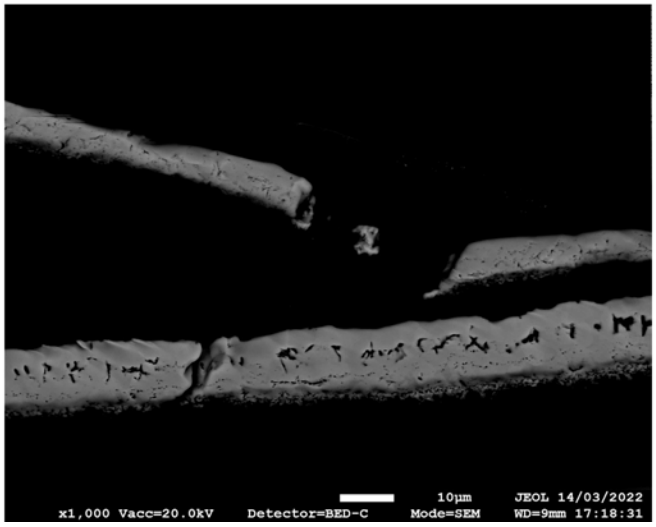

(d) Initiation point of seperation

Figure 98: Blister crown that has split in to two sections forming a blister on top of the primary blister

The lateral fracture of the blister crown was another unusual phenomena observed on the DP800 steel grade heated at 1000°C for 5 minutes. Figure 98 shows a blister crown which has partially fractured width ways and produced another smaller blister on top of the original blister. The bottom section of the blister crown was thicker than the top section at approximately 13µm and 7µm respectively. The base of the blister crown

was con-caved and sagging, presumably due to relaxation of the crown once gases from decarburisation have been released.

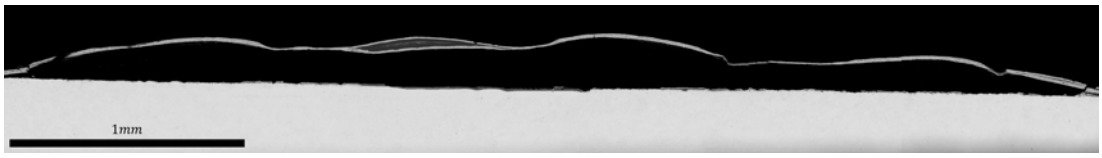

Figure 99: Stitched image of large blister displaying blister crown splitting

The conglomerated spinel phase, previously observed on multiple blisters throughout the sample, was evident on the undersides of both sections of the blister crown in figure 98c. The evidence of the spinel along the fracture lines suggests that it once again allowed for rapid crack propagation and acted as an initiation site for fracture.
It was hypothesised that a blister crown similar to that shown in figure 92 was uplifted, containing a band of spinel precipitates. A form of stress has then acted on the blister crown, causing it to fracture at the highly stressed interface between the iron oxide and spinel phase.

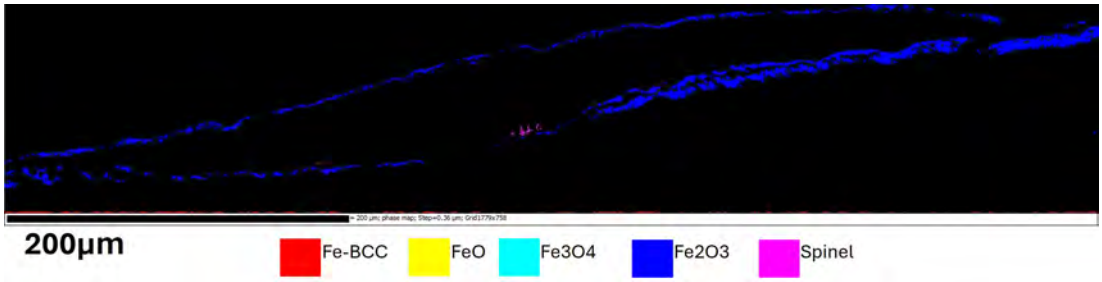

(a) Phase map

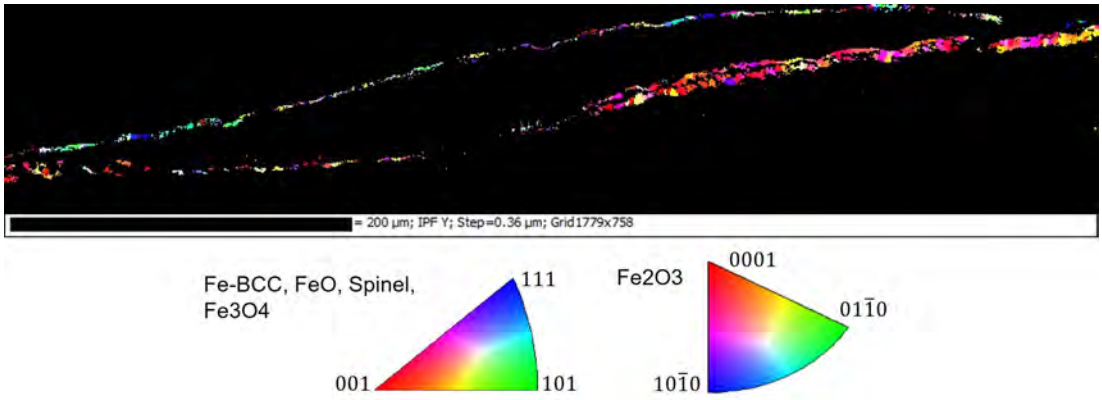

(b) IPF-X map

Figure 100: EBSD conducted on blister crown split

EBSD was conducted on the blister crown in figure 98, in order to gather further information on the failure mechanism. The EBSD IPF map in figure 100b showed no preference for a specified orientation. A slight predilection was shown towards the (0001) plane in the base of the crown towards the right hand side, however the remainder of the crown was seemingly randomly orientated.

The EBSD phase map identified that the composition of the blister crown was almost entirely formed of hematite. Small regions of the spinel phase were observed however the actual volume observed in the BSE images was far higher. The lower volume identified in the phase map was presumed to be due to poor indexing.
The strong presence of hematite indicates that blister nucleation was initiated through decarburisation. The poor permeability of hematite may result in pressure build up within the blister crown, initiating failure along weak points within the crown.

7.3.10 B32

Blister Regime A blister investigation was conducted by V.Basabe on a 3.2wt% electrical steel referred to as B32 [62]. A blister regime was produced from this work and was shown in figure 101. It was found that a silica passivation layer prevented the formation of blisters at temperatures below 1100°C [62]. Above 1100°C blisters were found to form within the mode 1 region and blister was absent within the mode 2 region. Mode 2 was presumed to be absent due to the high ductility of the oxide at the elevated temperatures. A number of these samples were then passed on and analysed within the scope of this thesis.

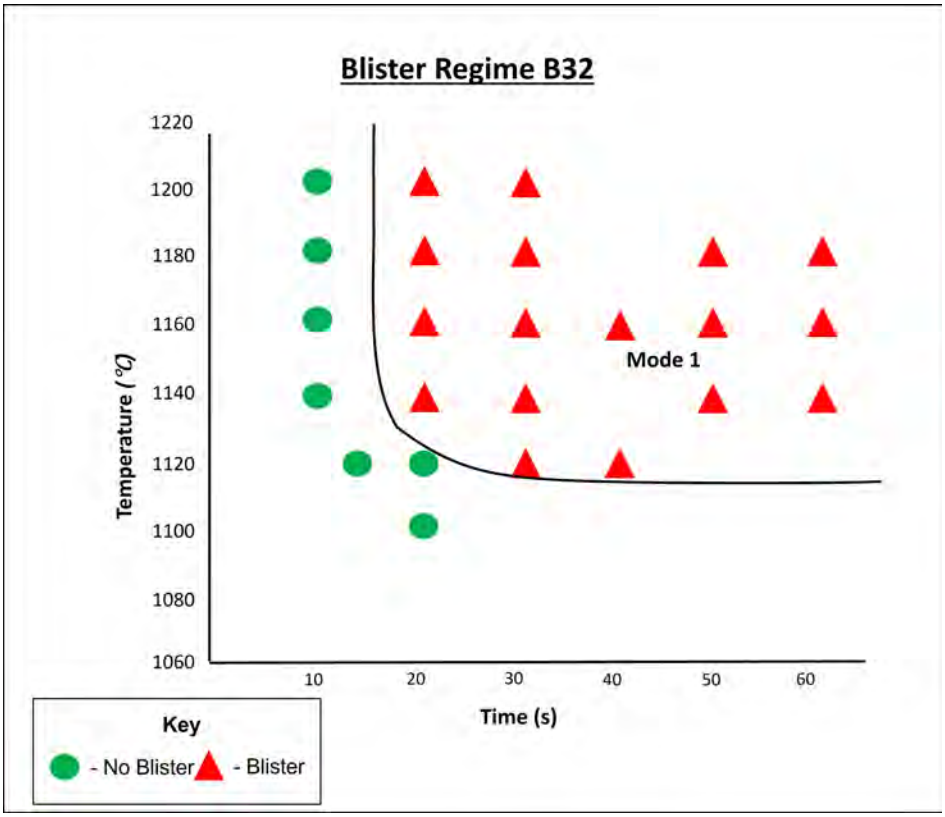

Figure 101: B32 Blister Regime produced by V. Basabe [62]

7.3.11 30 seconds

(a) Oxide morphology of large blister produced upon heating at 30s for 1180°C

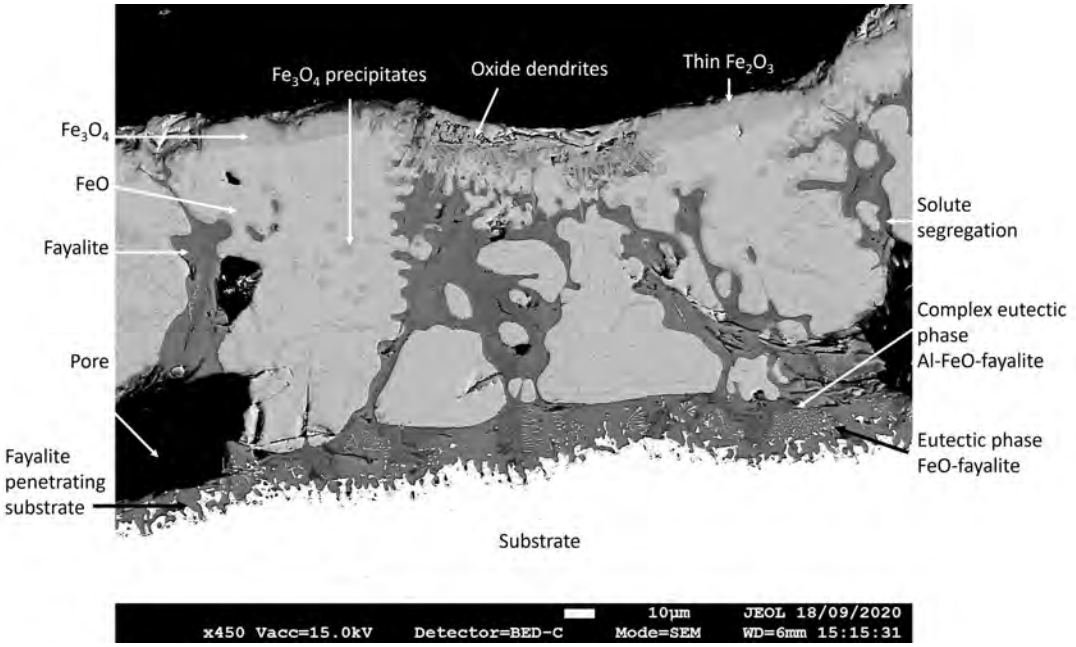

(b) Through thickness oxide morphology detailing oxide phases and oxide characteristics

Figure 102: B32 blister oxide morphology

Oxide Morphology A distinctive and distinguished blister produced at 1180°C after 30s was displayed in figure 102a. The diameter of the blister was very broad measuring at 943µm. The blister crown appeared sturdy and tough remaining intact and unbroken during sample preparation and handling. The crown thickness was approximately 120-150µm. The height of the blister was around 200µm but there was a noticeable depress, presumably due to shrinkage upon cooling.

Figure 102b shows the morphology of the bulk oxide for the heat treated sample. The B32 oxide was inordinately more complex and intricate than any of the previously examined oxide morphology's. A multitude of oxide phases were detected within the microstructure. The large number of varying phases was due to the high alloying content of the B32 grade.

As previously discussed the growth of the oxide layer was affected by the presence of

alloying elements, with silicon having an exorbitant effect due to the formation of the stoichiometric compound fayalite [124].
Fayalite anchors penetrated deep into the substrate forming well adhered tendrils previously shown to drastically reduce de-scalability [107]. A complex ternary eutectic was observed close to the interface within the fayalite phase. The ternary eutectic was formed of Si, Al and Fe oxides [125]. The darker bands within the fayalite phase were rich in Al whilst the lighter phase was rich in Fe. Further into the external oxide a large volume of solute segregation was evident with islands of iron oxide within the fayalite. The islands of iron oxide were primarily composed of wustite and varied in size.

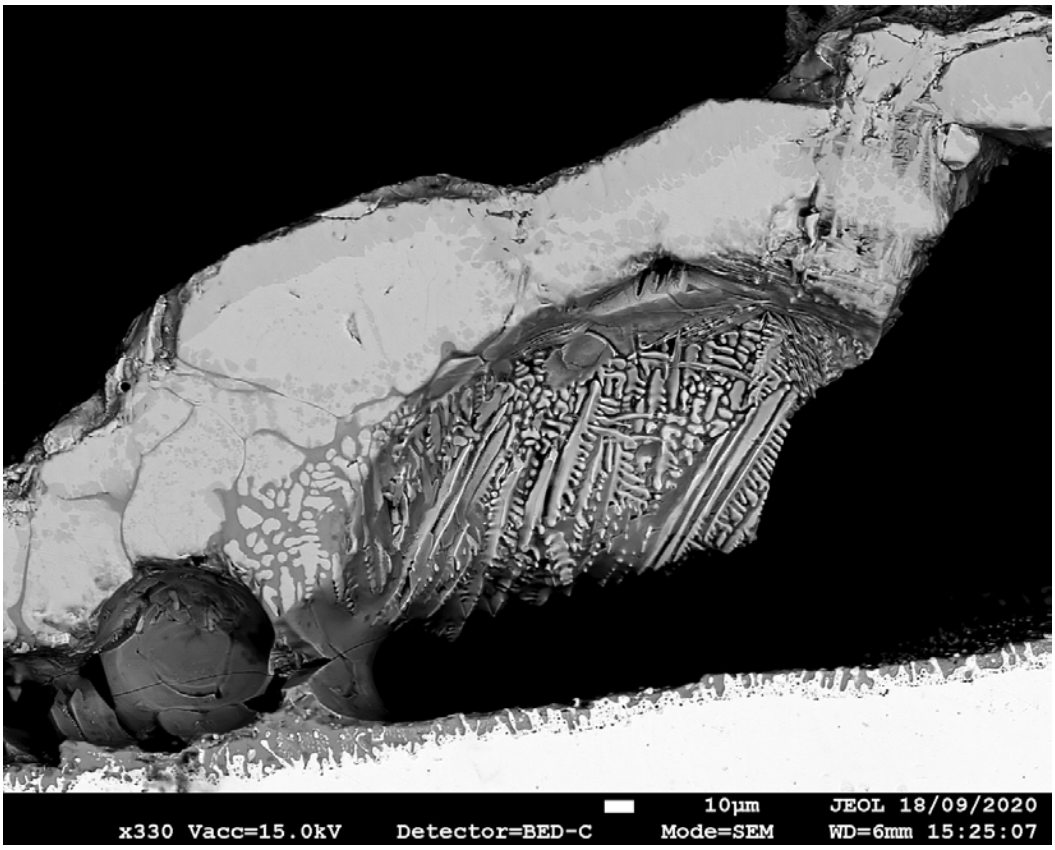

Figure 103: B32 blister with remarkable liquid fayalite and dendritic iron oxide structure

Figure 103 depicts the remarkable and striking oxide morphology of a blister formed at 1180°C. The blister displayed outstanding iron oxide dendrites within a fayalite matrix. Prominent secondary and tertiary dendrites were noticeable throughout the blister dome.
The formation of the dendritic iron oxide was a result of liquid fayalite attack. The eutectic temperature of fayalite and FeO was reported at 1173°C [107]. The heat treatment conducted at 1180°C resulted in liquid flow of fayalite into the external scale, forming a net distribution throughout the external scale [126]. The liquid oxide attack promotes rapid and destructive oxidation, enhancing oxidation rates significantly; further affirming the B32 TGA results discussed in chapter 6. The effect of the liquid oxide attacks was further enhanced as the volume of Si increases as a larger quantity of

liquid becomes available [124] [127].

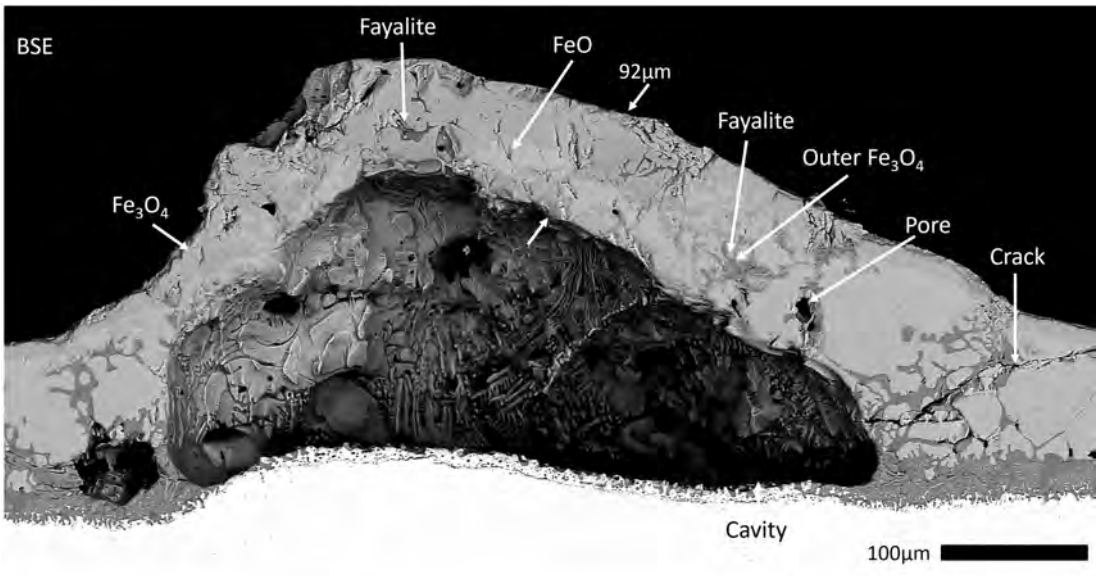

(a) Large blister cavity with complex multiphase oxide dome

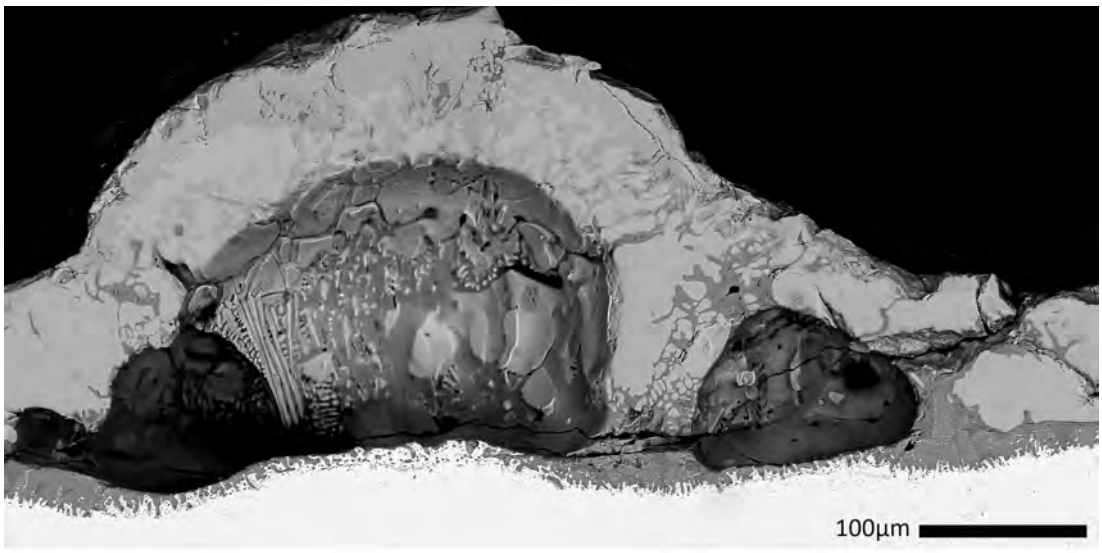

(b) Large blister dome next to an underdeveloped smaller blister

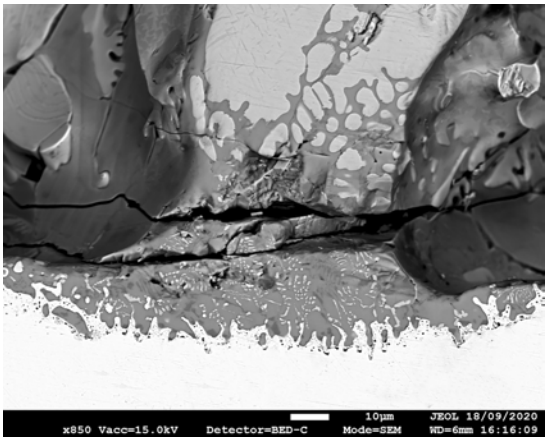

(c) Highlight of fracture through fayalite phase located between the large blister dome and under developed smaller blister

(d) Highlight of fracture through fayalite phase travelling from blister cavity towards outer surface

Figure 104: Numerous B32 blister displaying brittleness through fayalite

The liquid oxide has been shown to first form at the interface [106]; this was in con-

junction with observations at lower temperatures, were fayalite was only present at the interface of the oxide. This was due to the low diffusion coefficients of Al and Si through iron oxide. Once the fayalite has become a liquid it will then rupture the scale and attack from below, consuming and dissolving the oxide [106]. The liquid oxide will create a transport network for reactants and oxidation; hence rapidly enhancing oxidation growth. Its hypothesised that as the iron oxide content increases the liquid phase will become unstable and re-crystallises. The resulting microstructure was a fayalite matrix containing islands and dendrites of iron oxide [106].

Figure 104 shows another series of blisters formed on the B32 steel. The apex of the blister crowns contained very minimal quantities of fayalite. Larger volumes of fayalite were present through the lower sections of the blister crown once again containing dendrites of iron oxide. The inner blister dome in figure 104b phenomenally displays the transition of a liquid fayalite phase with dendritic islands of iron oxide to pure iron oxide. The dendrites of iron oxide were far more prominent towards the interface of the oxide.

A number of large pores were noted throughout the fayalite phase. The pores observed within the fayalite were attributed to the contraction of the liquid oxide during cooling [124]. Cracking was repeatedly observed at the interface of the iron oxide and the fayalite phase, presumably due to the low coherency between the two phases and the contraction of the liquid fayalite during cooling. Wustite and magnetite are both cubic crystal structures whilst fayalite was an orthormbic crystal structure.

The initiation point for nucleation of a blister was reported to be the center point (assuming two have not joined together) [109]. The base of the blisters examined, below the apex of the blister crown, show fewer and smaller fayalite anchors compared to the surrounding oxide. The center of the blister crown were fewer fayalite anchors are present was assumed to be the original nucleation point. One hypothesis for the lack of fayalite anchors was that the blister nucleated relatively early on before a large volume of liquid fayalite was present. As more liquid fayalite was produced it then travelled up the sides of the blister to reach the external surface. The small volume of fayalite present within the blister crown was conjectured to of been present before the blister was formed. The blister crown was moderately thinner than the surrounding bulk oxide and richer in magnetite, further supporting the hypothesis.

Figure 104d shows that as the fayalite approaches the external surface the surrounding scale became richer in oxygen, transforming into a higher order oxide [124]. This effect was attributed to the engrossment of the oxide, were a thicker scale will require a higher ion transport to sustain growth [128] [37]. Therefore the ratio of ferrous to ferric ions will shift as the distance from the substrate increases, becoming increasingly ferric. The presence of the liquid fayalite close to the surface will then act as an oxygen highway; further decomposing the wustite. [124].

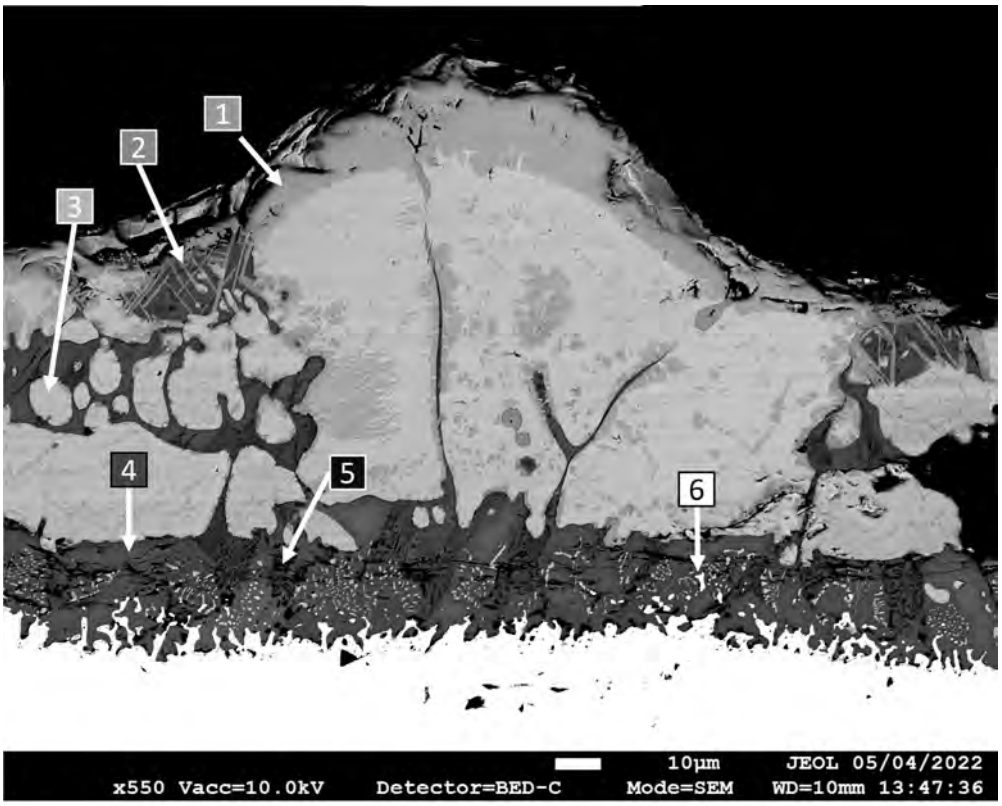

	Fe	O	Si	Al	Mn
1	69.82	29.23	0.17	0.04	0
2	63.17	28.79	5.55	1.51	0.2
3	69.17	24.97	0.04	0.94	4.89
4	51.28	32.32	15.29	1.11	0
5	36.87	34.82	3.04	25.27	0
6	94.72	0.58	4.45	0.26	0

Figure 105: WDS point scan for B32 (wt%)- WDS analysis was performed on a cross-section of the oxide, moving from the outer edge towards the oxide/metal interface

WDS was conducted concurrently throughout the sample and was shown in figure 105. The colour contrast of the BSE image has been used to identify the phases in the WDS spectras. The Fe:O ratio and oxygen content in spectra 1 confirms that the thick outer band of oxide was magnetite.

The phase analysed in spectra 3 formed the vast majority of the bulk oxide. The oxygen content substantiates that the phase was wustite, however a considerable quantity of Mn was also detected. As previously discussed in chapter 5, Mn may commonly exist within the wustite phase forming $(Fe_{1-x},Mn_x)O$ [47]. Mn will form a stoichiometric gradient through the wustite phase, with a higher concentration of Mn towards the interface. An increased presence of MnO has been found to increase the thermodynamic stability of the wustite phase [79].

The phase in spectra 2 appears to be an amalgamation between magnetite and fayalite. The wt% of Fe in fayalite was 54.8 wt%, significantly lower than that recorded in spectra 2 at 63.17 wt%. Additionally the oxygen content recorded at 28.79wt% was above that of wustite and below that of fayalite. The composition of spectra 4 matches that of fayalite and appears significantly darker in the BSE reference image than the

phase in spectra 2. Spectra 6 shows region of pure iron that have been entrapped by the liquid fayalite phase.

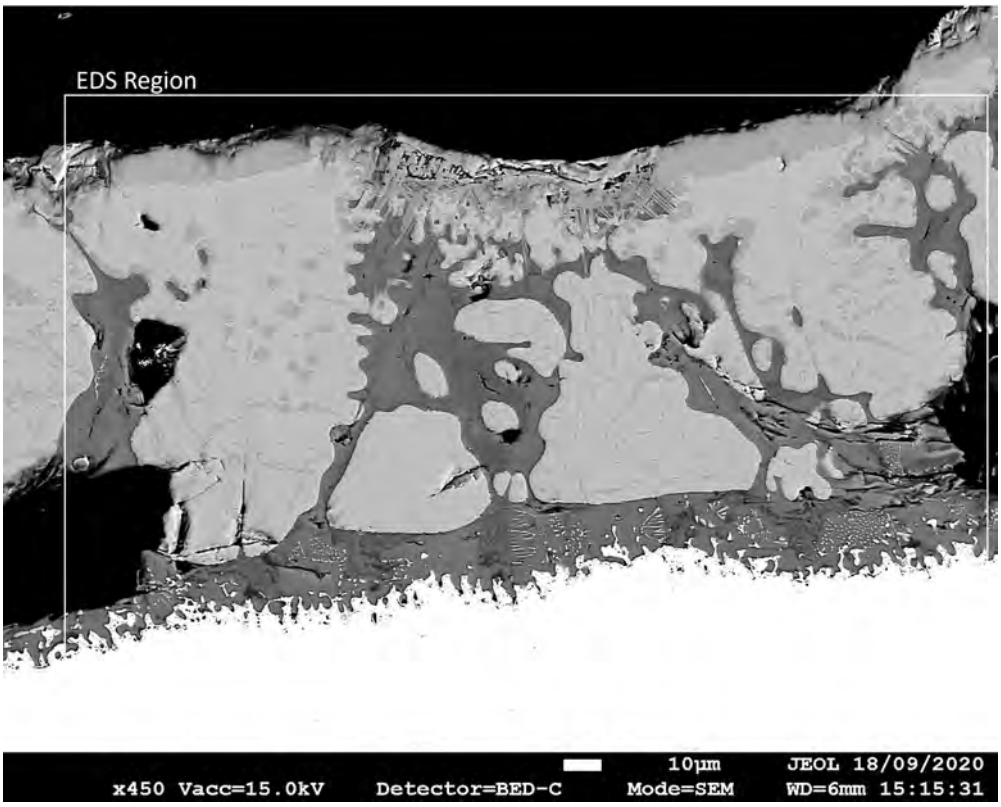

(a) The through-thickness oxide morphology of B32 steel- Exhibits complex structure characterised by multiple oxide phases. Large islands of retained wustite are interspersed within a matrix of oxides rich in silicon and aluminum.

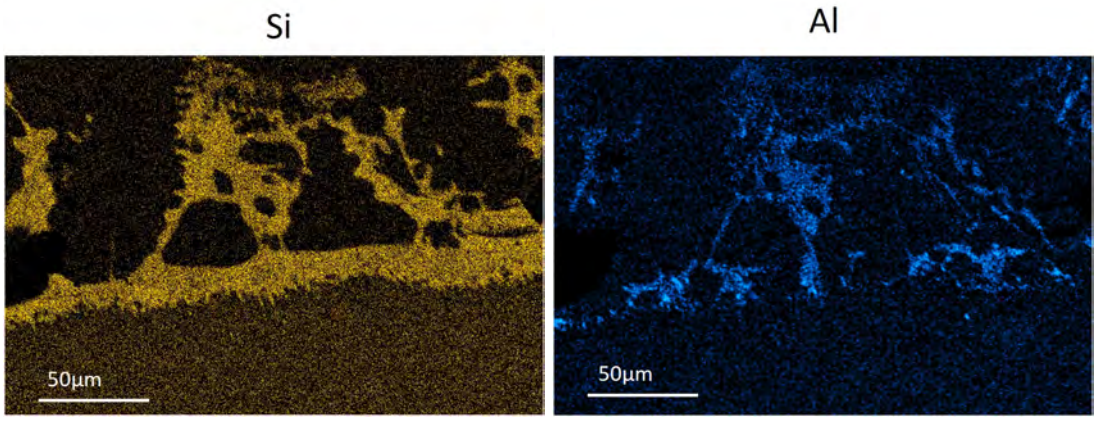

(b) Silicon map (c) Aluminium map

Figure 106: EDS map of B32 bulk oxide

The phase in spectra 5 was part of a ternary eutectic within the Al_2O_3-FeO-Fe_2O_3-SiO_2 system [20]. The Al_2O_3-FeO-Fe_2O_3-SiO_2 oxide system was highly complex, with multiple phases competing for growth [106]. Spectra 5 was rich in Al and had the darkest BSE contrast. The darker contrast was a result of the high Al content and the phase was only present towards the oxide interface. The oxide was conjectured to be corundum (M_2O_3), (Al_2O_3, Fe_2O_3) [20].

Wustite was precipitated out of the fayalite phase alongside corundum close to the interface. Solute segregation resulted in excess Fe and O within the liquid phase forming wustite. Solute segregation also resulted in excess Al, Fe and O within the liquid phase forming corundum (see Appendix 152, 151). The ternary eutectic was formed of fayalite, corundum and wustite. Corundum was not found high within the fayalite phase presumably due to lower concentrations of Al away from the oxide interface. The EDS map in figure 106 shows that within the fayalite matrix Si levels remain relatively constant however the Al was heavily biased towards the interface of the oxide.

7.3.12 Summary

A mechanism has been proposed for blister nucleating under stress; highlighted in figure 107. Its supposed that as the oxide grows stress was generated at the interface between the oxide and the substrate. As the oxide grows a critical stress was reached whereby the oxide was lifted off the substrate in order to alleviate the high stress. Steel grade 3812 was exclusively linked to blister nucleating under stress however differing modes were generated depending on temperature and time.

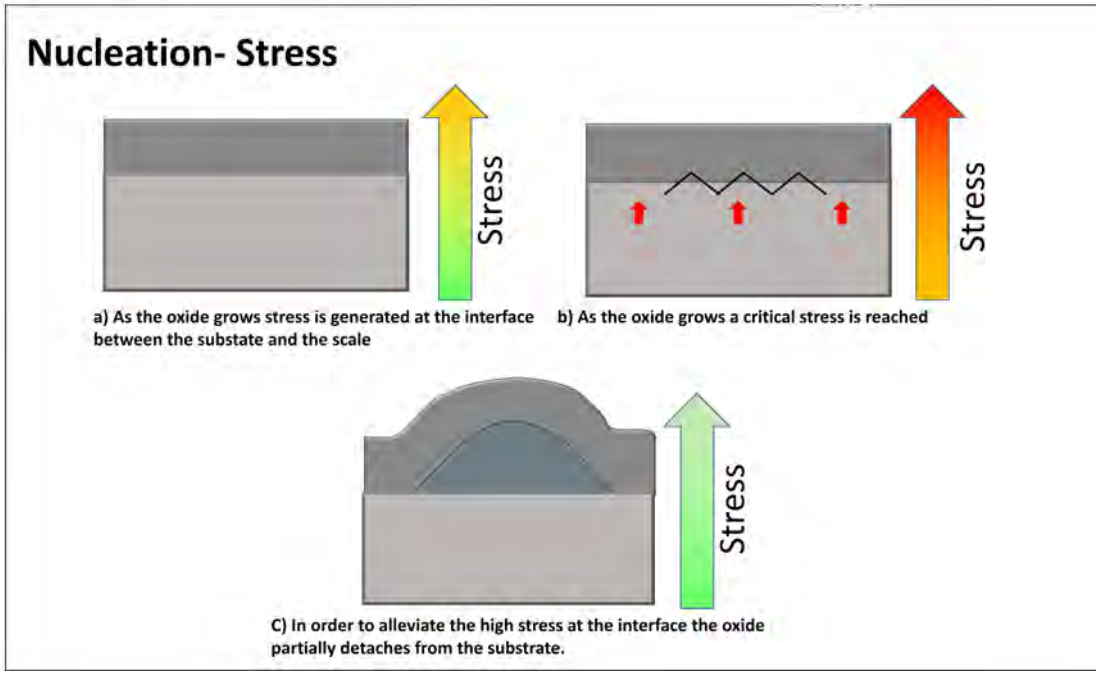

Figure 107: Formation mechanism proposed for generic blister formation- Oxide growth results in stresses at oxide/metal interface, critical stress results in delamination

A blister formation mechanism involving decarburisation has been suggested in figure 108. The mechanism suggests that upon heating a thin layer of C was produced at the oxide-substrate interface; commonly known as C-enrichment. Oxygen from the oxide scale will then permeate down into the C enriched layer, forming CO [108]. Once formed the gas will not be able to diffuse out through the oxide due to a non-permeable hematite layer. The gas will then lift the oxide, initiating a blister. Once lifted, the gas will either dissociate back into the substrate and oxide, or escape into the atmosphere. The blister crown may crack during uplift due to the stresses generated allowing the trapped gases to escape.

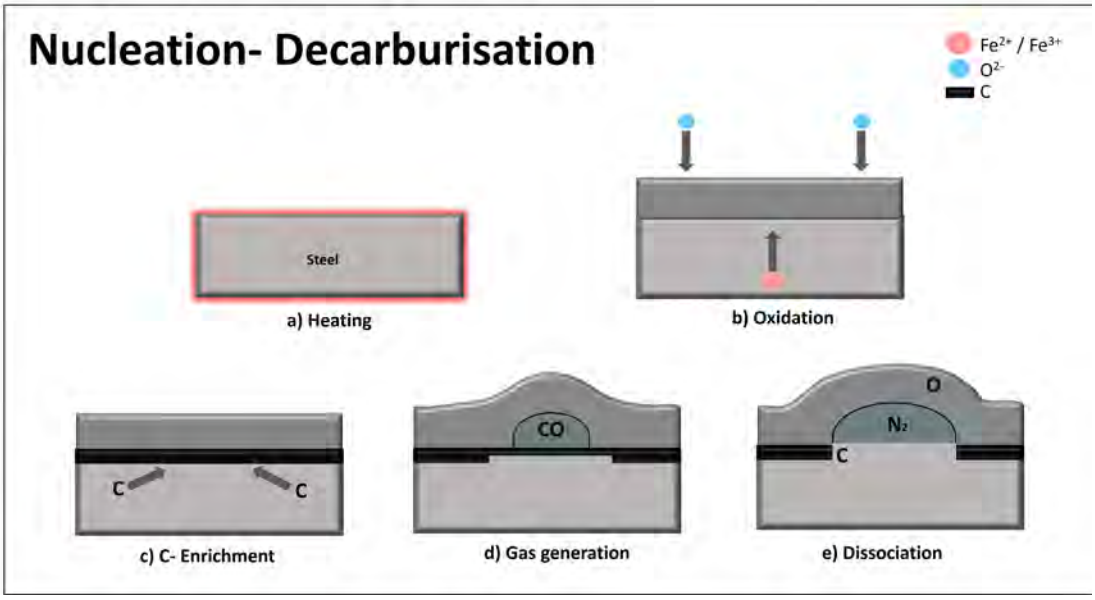

Figure 108: Formation mechanism proposed for DP800 blister- Oxide growth and generation, C-enrichment at oxide/metal interface, gas generation resulting in blister formation, gas dissociation

Double blistering was observed on DP800 with a secondary blister nucleating inside of a larger primary blister. The double blistering phenomena was previously unreported and a new formation mechanism for secondary blister has been proposed in figure 109. Double blistering must be considered as 2 separate stages with 2 distinct nucleation stages. After nucleation of the primary blister, oxide within the blister dome will continue to grow. Due to high Al and Si content a brittle spinel phase formed a secondary phase in a banded structure throughout the oxide. The spinel phase will create a large volume of mismatch and stresses throughout the oxide layer. Upon generation of gases or stresses the brittle spinel phase will act as an initiation site for failure. A secondary blister will then nucleate once the fracture of the newly formed oxide was initiated in order to alleviate any stresses.

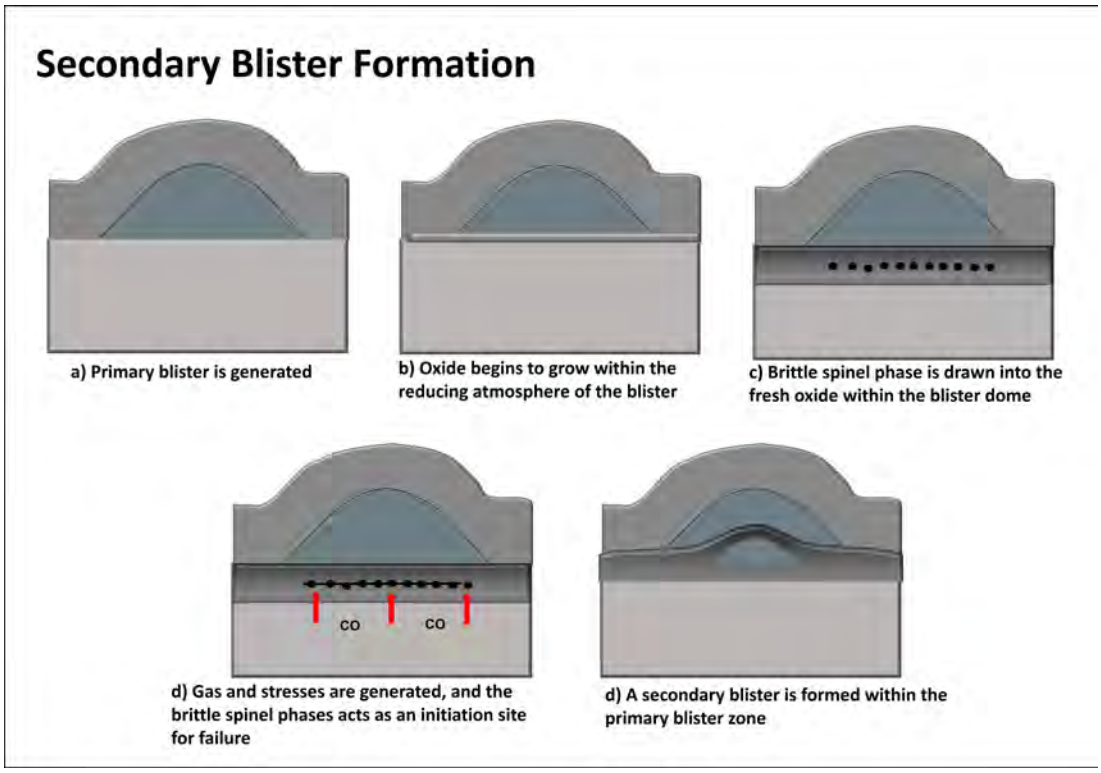

Figure 109: Formation mechanism proposed for DP800 double blister- Primary blister generation, continued oxide growth, secondary spinel phase present within freshly developed oxide, initiation of secondary blister

7.4 Conclusions

An oxidation study of industrially pertinent steel grades was conducted in order to deduce the blister formation mechanisms. The composition of the steel had an astronomical effect on the morphology of the blister produced and the formation mechanisms. Higher alloyed steels produced substantially more complex blister morphologies.

3812

- A blister regime was successfully produced for steel grade 3812 and 3 keys mode of formation were identified.
- Mode 1 was exclusively identified below 1000°C and was characterised by short incubation times.
- Mode 2 was ascertained to develop at 1000°C and above. Blister crown thickness and bulk oxide thickness were found to be greater than those of mode 1.
- A new and previously unreported mode of blister was observed and substantiated during air cooling on a number of 3812 samples; referred to as blister upon cooling or mode 3. Mode 3 was observed at temperatures above 1000°C.
- The area fraction of blister was greater in mode 2. The highest area fraction observed was at 1000°C for 60s at 44% coverage. A heating time of 60s produced the strongest degree of blister across 900°C, 1000°C and 1100°C. A lower volume fraction was observed at 600s due to the prolonged heating time resulting in a more malleable scale. The nose of the blister curve was located at 900°C for 10s.

DP800

- Blister was observed on a large number of DP800 samples with different heating times and temperatures; from 900°C for 10s to 1200°C for 12mins. The blisters contained a multitude of phases and were smaller than that of the blisters produced on the 3812 samples.
- Blister formation on DP800 was conjectured to be by cause of stress and decarburisation. The blister crown was predominantly hematite which acted as a barrier for gas diffusion due to its poor permeability. Subsequent build-up of gas pressure resulted in the up-lift of scale at the brittle-scale interface. At 1000°C a spinel phase rich in Al and Si initiated failure and breakaway of the oxide.
- The presence of a conglomerated spinel phase and hematite in the outer oxide resulted in a multitude of unique and new phenomena such as blister crown splitting and secondary blister; figure 109.

B32

- Blisters formed on B32 had a distinctive and distinguished oxide morphology. The exterior scale contained a complex ternary eutectic phase containing Al-Si-Fe.
- B32 blister will only occur at high temperatures with the aid of a liquid fayalite phase to promote growth.

8 Internal Oxidation

8.1 Introduction

During hot rolling, strip-steel will exit a finishing mill between a temperature range of 820-910°C, depending on the required properties and chemistry [129]. Once the strip-steel has exited the finishing mill its rapidly cooled by water sprays on a run-out table. A tertiary scale will develop during this processing and is not removed prior to coiling. The strip-steel is then coiled at a specified temperature; thereafter, the steel will cool to the ambient room temperature. A diagram displaying the hot rolling process at Port Talbot, Tata Steel Europe is displayed in figure 110.

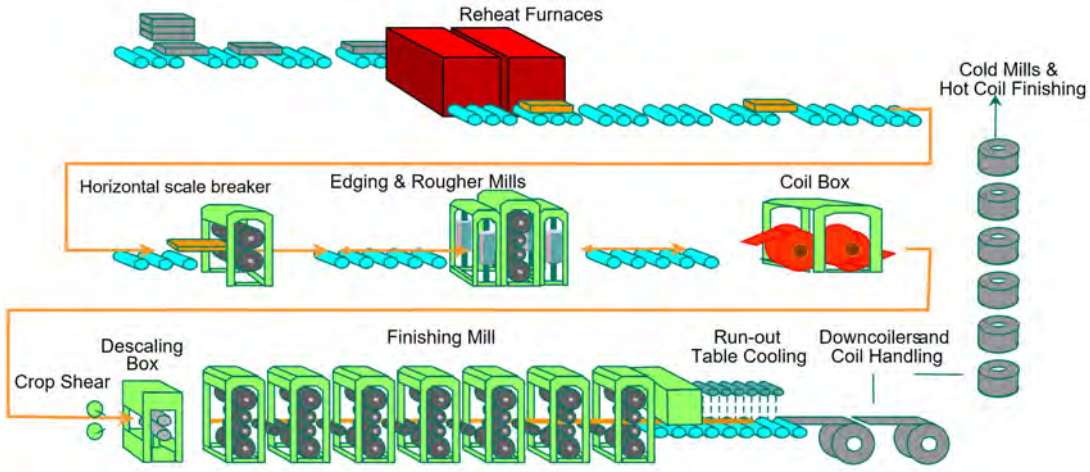

Figure 110: Schematic of the hot-strip mill process at Port Talbot, Tata Steel Europe

The final morphology and composition of external oxide scale are known to be influenced by coiling temperatures after hot rolling [130]. As the strip enters the finishing mill and run-out table, a tertiary external scale typically forms at finishing temperatures. This oxide typically consists of a classic three-layered scale, with wustite decomposing during cooling. The ultimate morphology of this scale is dependent on factors such as cooling rate, coiling temperature, and composition.
In electrical steels, the oxide scale produced is highly complex due to the high alloying content of the composition. Oxidation within the hot-strip mill yields both external and internal scales. Internal oxidation occurs due to selective surface oxidation of reactive alloying elements such as Si and Al. This selective surface oxidation reduces de-scalability due to lower thermal stresses produced at the inter-facial boundaries [88]. The internal scale can significantly impact the magnetic properties of the steel and lead to various production issues. In extreme cases, problems such as dirt formation may arise during cold rolling, resulting in poor final annealing and undesirable product appearance. As the steel is rolled thinner during the manufacturing process, internal oxide precipitates may detach from the surface due to mechanical stresses. These detached precipitates can then accumulate on the surface of the rollers, leading to a phenomenon known as dirt build-up. This build-up of oxide particles on the rollers can affect the

quality of the rolled steel and may require frequent cleaning and maintenance of the rolling equipment to ensure smooth and efficient production operations [131]. Moreover, the presence of these detached oxide precipitates can also contribute to surface defects in the final product, impacting its overall appearance and performance [131]. To mitigate these issues, it is crucial to optimise the oxide scale. While internal oxidation is suspected to continue developing after hot coiling, it has not been extensively studied.

This study aims to investigate the effect of coiling temperature on the internal oxidation region to enhance surface quality for further processing. Plant trials have been conducted with reduced coiling temperatures to explore potential improvements. The designated coiling temperatures for the trial were applied to two distinct electrical steel runs within the hot-strip mill at Port Talbot.

8.2 Experimental materials

8.2.1 Coiling Temperature Trial

Plant trials were conducted at the hot-strip mill in Port Talbot, Tata Steel Europe, with the experimental variable being the coiling temperature after hot rolling. To ensure robustness in the findings, these trials were split into two separate runs. This approach served two purposes: firstly, to minimise potential risks to downstream customers, and secondly, to allow for a thorough assessment of the initial run. Notably, temperatures X°C and X-75°C were repeated in both trial runs to enhance the reliability and confidence in the obtained results.

Following hot rolling and coiling at Port Talbot, coils were shipped to Surahammar, Sweden. Upon arrival at the intermediate annealing-pickling line in Surahammar, the coils designated for the coiling temperature trials were divided into two equal halves. Samples were extracted from the mid-position of each coil, both before and after annealing, in their original hot-rolled condition.

The first set of samples, referred to as hot rolled coil (HRC) samples, aimed to determine the impact of coiling temperature on the depth of internal oxidation. Subsequently, samples were taken after intermediate annealing and pickling, denoted as hot-band annealed (HBA) samples, to evaluate the influence of internal oxidation depth on the pickle-ability of the steel.

Throughout the hot-strip mill and annealing-pickling processes, standard best practices were followed, and the coils were processed in the order of receipt. No notable increase in brittleness was observed due to changes in coiling temperature, and no significant effects on magnetic properties were expected.

The coiling temperatures were designated as X°C for the highest temperature and X-A°C for subsequent lower temperatures, with A°C representing the difference between the two coiling temperatures. Detailed specifications are provided in Table 17. Images of the coils post hot-band annealing are presented in Figure 111.

Trial	Coiling Temperature
1	X°C
2	X°C
1	X-45°C
2	X-50°C
1	X-75°C
2	X-75°C
2	X-100°C
1	X-115°C

Table 17: Table displaying plant trials conducted and coiling temperatures

Figure 111: Coils as sampled from plant after sandblasting and pickling

8.3 Results and Discussions

X°C Trial 1 and 2

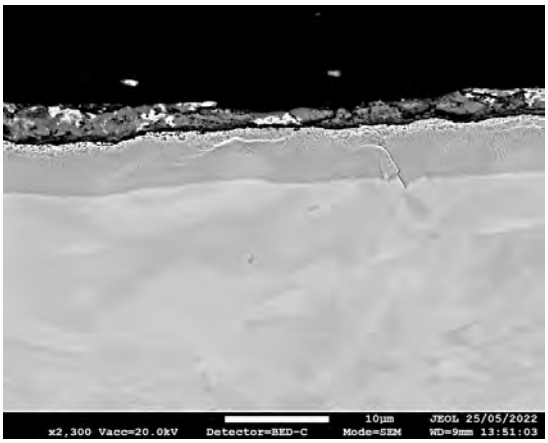

(a) Oxide morphology overview displaying a layer continous internal oxidation Trial 1

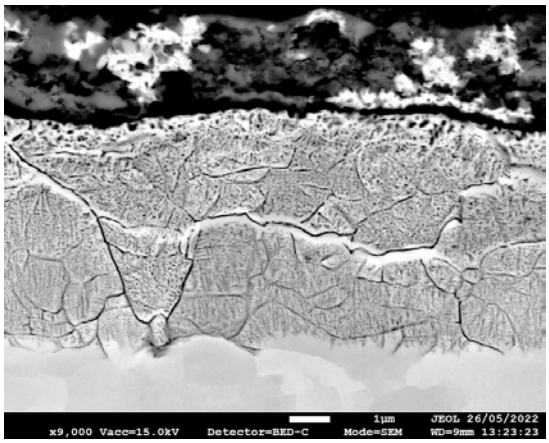

(b) Consumption of underlying iron grains beneath the IOZ Trial 2

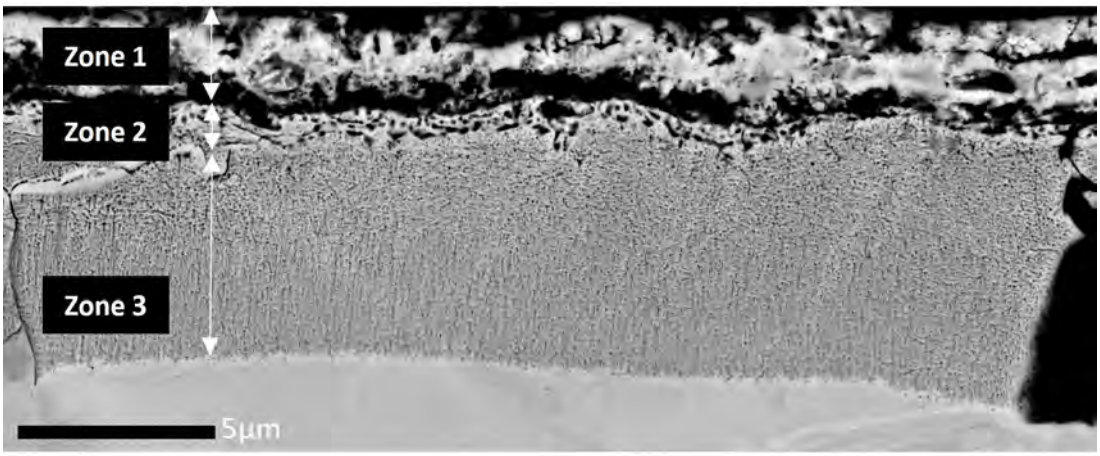

(c) Morphology overview with labelling of regions Trial 1

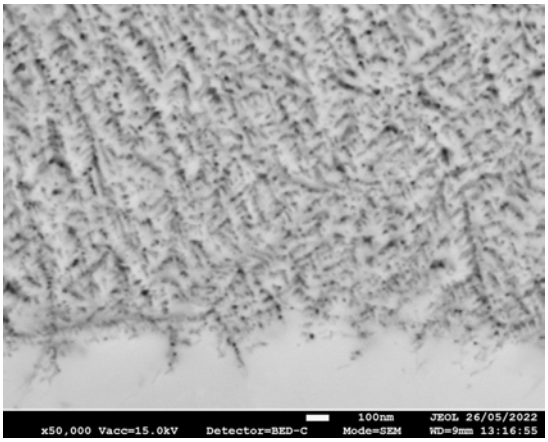

(d) Internal oxidation growth front Trial 1

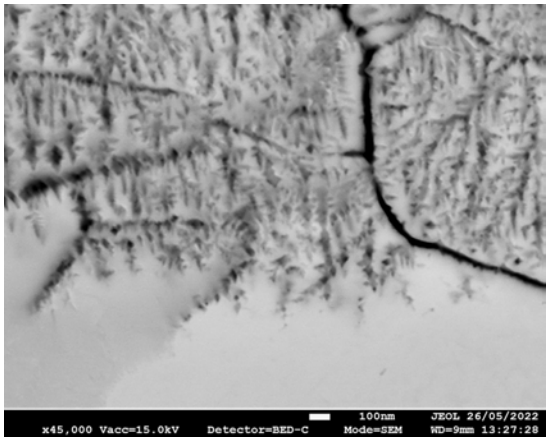

(e) Fine dendritic particles of silica along the growth front of the IOZ Trial 2

Figure 112: Oxide morphology after coiling at X°C Trial 1 and Trial 2

Figure 112c unveils the intricate nature of oxide morphology, particularly within the region where internal oxidation takes place. Here, a notable phenomenon emerges as the internal oxide layer undergoes a transition from the banded structure observed in

zone 3 to a coarser, more globular morphology observed in zone 2. This transition, occurring over a distance of less than 0.5 µm, hints at a change in the oxidation dynamics, possibly influenced by local variations in composition and oxygen availability.
The interface between zones 1 and 2 exhibits a sporadic and non-adherent nature, suggesting a potential influence of the internal oxide layer on the external oxide. It is conceivable that the internal oxide layer, being closer to the steel substrate, acts as a preferential sink for oxygen, thereby impacting the growth and morphology of the external oxide layer. This dynamic interplay between the internal and external oxides adds layers of complexity to the oxidation process.
The thickness of the internal oxidation zone measured consistently at 9-12 µm for both trial 1 and trial 2. Additionally, in BSE figures 112a and 112b, the reduced iron oxide islands within the external oxide layer are highlighted. The depletion and presence of these iron islands suggest that oxygen was consumed during the formation of the internal oxide.

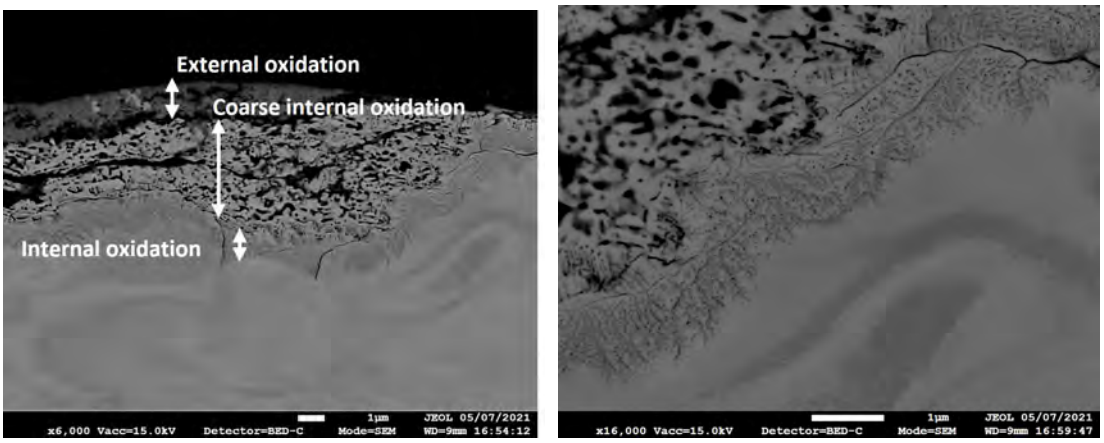

(a) Morphology overview with labelling of regions Trial 2

(b) Transition between spherical to dendritic growth of internal oxide Trial 2

Figure 113: Edge oxide morphology after coiling at X°C

Both figure 113a and 113b were taken from the edge of the coil. The thickness of the internal oxide at the edge of the coil was significantly less than that of the centre at 4.8µm; shown above in figure 112. This was because the coil edge loses heat far faster than the middle section, thus growth was halted quicker due to thermodynamics.
The interface between the coarse internal oxidation and fine internal oxidation was more clearly defined towards the edge of the coil. A crack can be seen travelling through the globular IOZ. The crack extended and joined through the brittle precipitates.

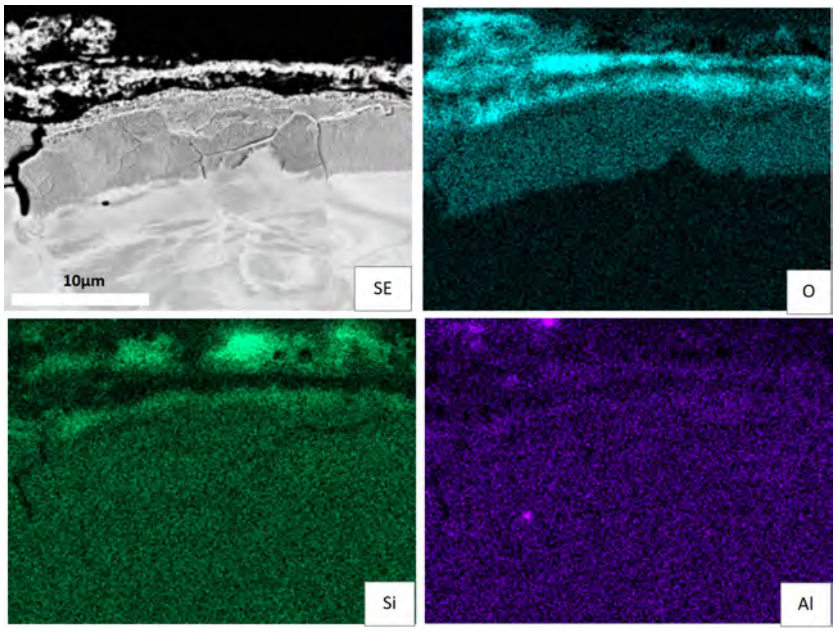

Figure 114: EDS conducted on oxide after coiling at X°C Trial 1

Figure 114 affirms that an IOZ was present by virtue of the increased presence of O beneath the steel surface. The EDS map in figure 114 shows high counts of both Si and O within the same region, displaying a sub-layer of SiO_2. This rich region has created a Si-depleted sub-layer within the IOZ. Oxygen has dissolved into the steel creating a supersaturated layer just below the steel surface. The super-saturated layer created a high entropy zone promoting the internal oxidation of elements with a high affinity for O_2, such as Si, depleting the region of the high affinity element below.

X°C HBA After hot-band annealing (HBA), dense oxidation was still present after sand blasting and pickling in the annealing-pickling line. Figure 115b and 115c shows coarse remaining internal oxidation. The oxide was loosely adherent but still present throughout the strip.

The morphology of the oxide was drastically different compared to the hot-rolled coil (HRC); shifting from a rod like dendritic structure to coarser more globular shape. The globules were all relatively uniform in size and composition.

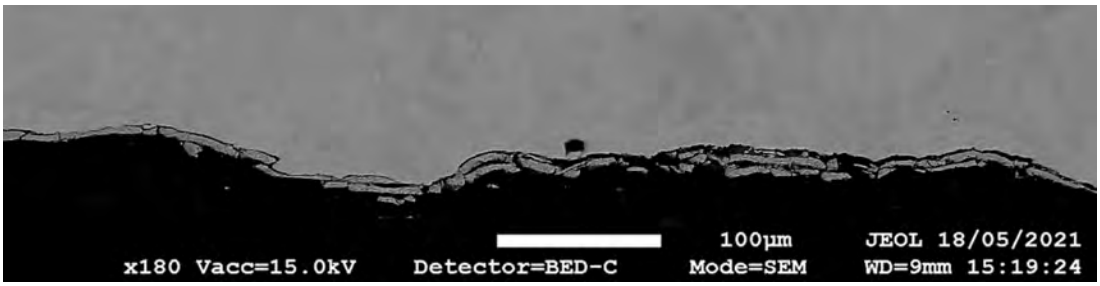

(a) Oxide morphology overview displaying continuity of persisting coarsened internal oxide Trial 1

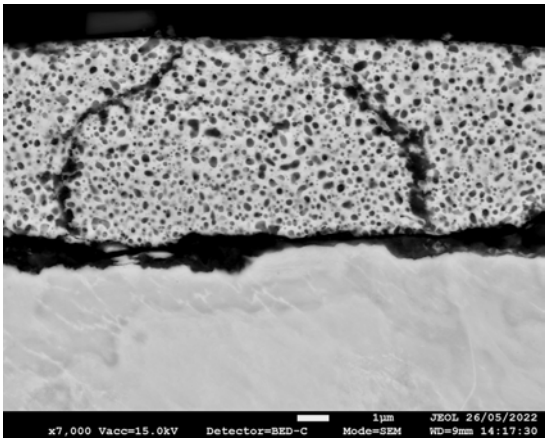

(b) Coarsened internal oxide Trial 1

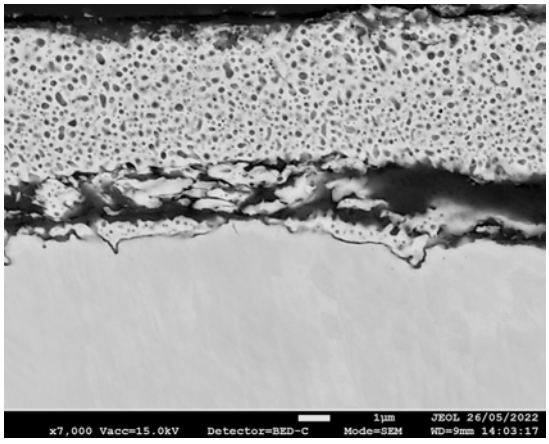

(c) Coarsened internal oxide Trial 2

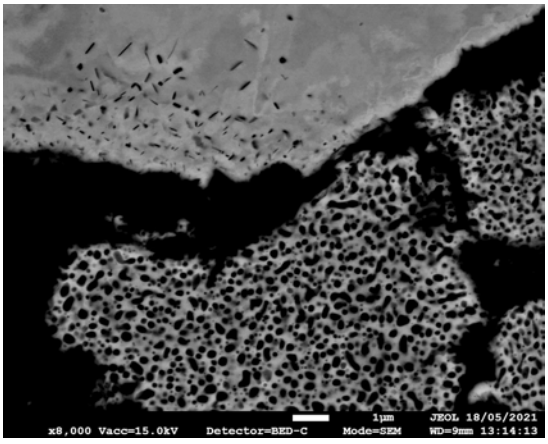

(d) Highlight of coarsened internal oxide breaking away from underlying substrate and AlN particles Trial 1

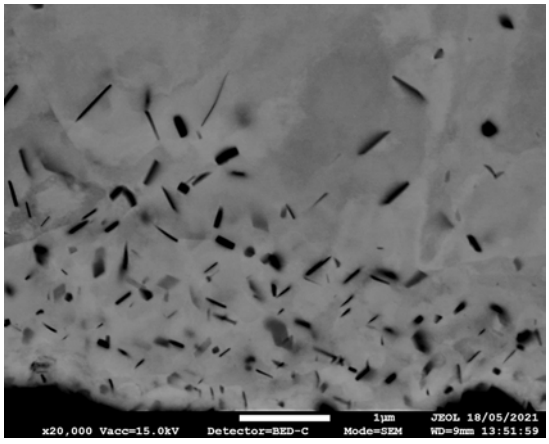

(e) Highlight of fine subsurface AlN particles Trial 1

Figure 115: Oxide morphology of retained coarsened internal oxide after sand blasting and pickling for X°C Trial 1 and Trial 2

EDS analysis was performed on the HBA samples coiled at temperature X°C, as illustrated in figure 116. The analysis confirmed the presence of coarsened oxide, as indicated by the oxygen concentration map. Additionally, Al was detected near the oxide interface, although it appeared sporadically. The morphology of these aluminum precipitates suggested that they could potentially be aluminum nitride (AlN). However, definitive confirmation using EDS was challenging due to its limited sensitivity to low-weight elements such as nitrogen [23] [69].

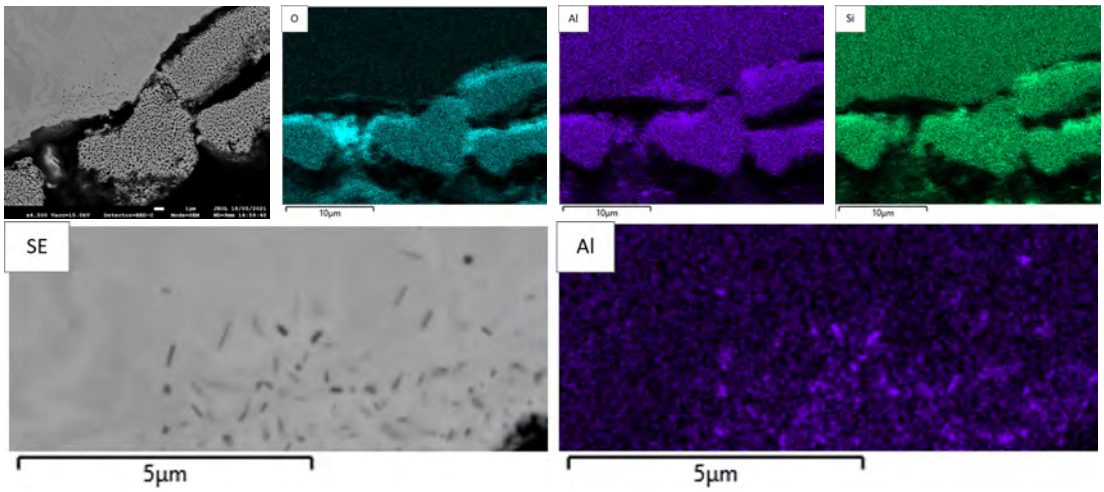

Figure 116: EDS conducted after HBA on sample coiled at X°C Trial 1

X-45°C Trial 1

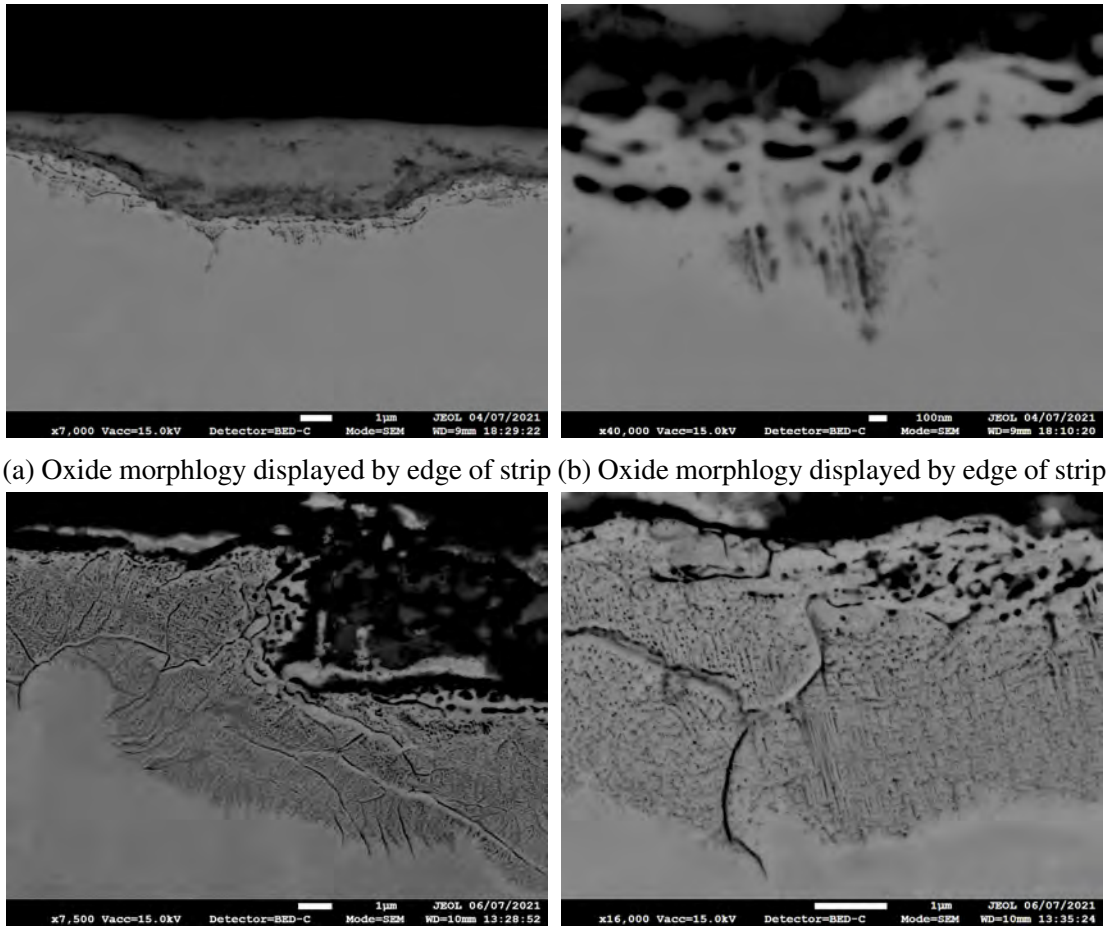

(a) Oxide morphlogy displayed by edge of strip (b) Oxide morphlogy displayed by edge of strip

(c) Highlight of fine dendritic structure at internal oxidation front (d) Growth front of internal oxidation zone along grain boundary

Figure 117: Oxide morphology after coiling at X-45°C

X-45°C HRC Figure 117 shows the samples taken from a B32 coil, coiled at a temperature 45°C below that of the previous sample. The internal oxide was significantly thinner than the previous sample indicating that coiling temperature does play a crucial role in the depth of oxidation.

A distinct difference in oxidation was noted between the edge of the strip and the middle region. The edge depth of oxidation was considerably lower than towards the middle region. Additionally the internal oxide was denser and more compacted towards the middle of the strip. The difference in thickness of the internal oxide was due to geometry effects with the edges cooling rapidly preventing growth of the internal oxide front.

The morphology of the strip tended towards a globular morphology at the interface but then transitioned into a lamella structure as the oxide penetrated deeper into the substrate. The globular structure varied in thickness, but reached a maximum depth of 3µm. The globular precipitates can be seen joining together creating areas of weakness within the structure. The coarsened internal oxide zone contained a multitude of cracks and was less adherent than the lamella structure found further into the substrate.

Figure 117d shows the oxide front of the IOZ. The oxide front grew along the grain boundaries and then slowly consumed the remainder of the steel grain.

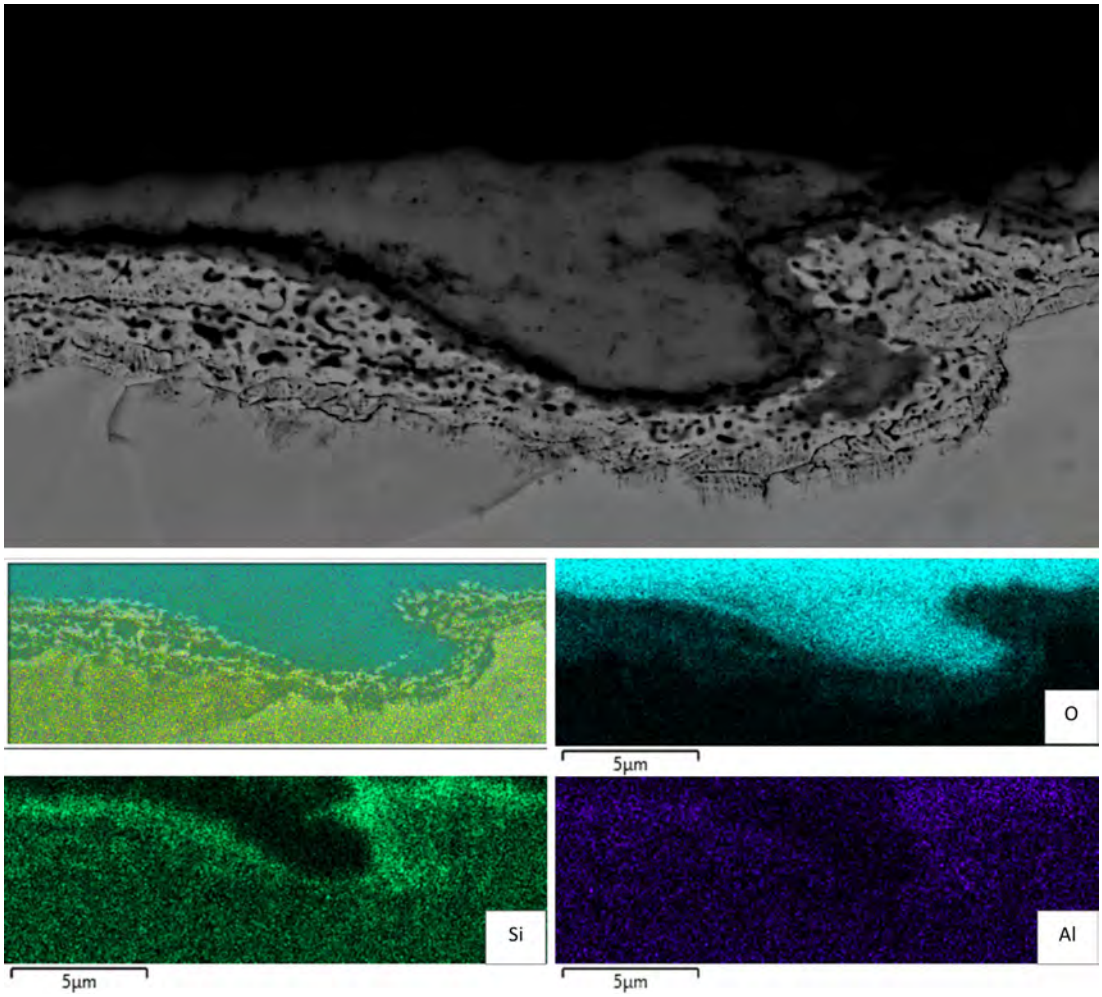

Figure 118: EDS conducted on edge of coil after coiling at X-45°C

The EDS shown in figure 118 was performed on a sample taken from the edge of the coil. An increase of Al was detected towards the interface of the external oxide and the substrate. High levels of Si were detected within the globular regions of the oxide. The globular zone contained both SiO2 and fayalite. The external oxide appears as if it has been rolled into the underlying substrate with the internal oxide growing around the indent.

X-45°C HBA After sandblasting and pickling X-45°C produced a clean surface, free of oxides. Moderate sub-surface damage was observed, with lateral cracking detected through the top 10µm of the sample. Cracking was assumed to be due to excess force during sandblasting. The BSE shows the surrounding deformation.

(a) Surface roughness after HBA

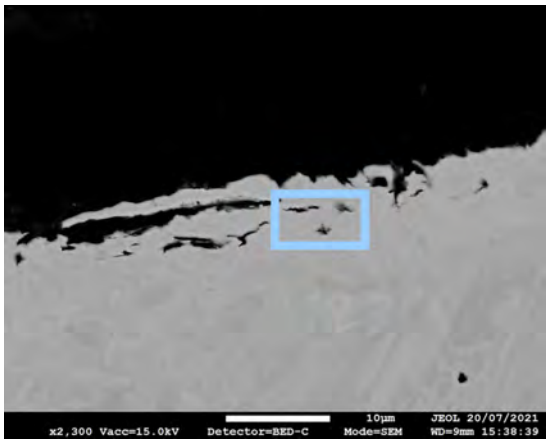

(b) Surface roughness after HBA

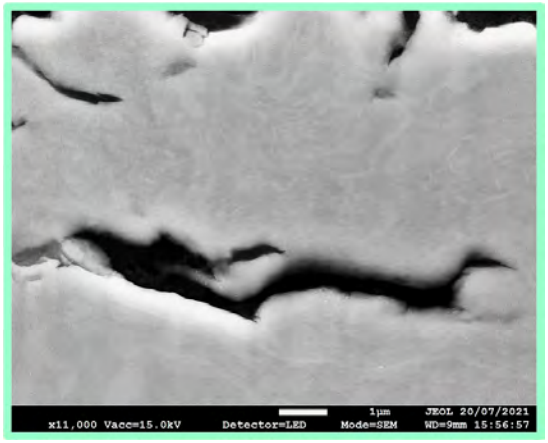

(c) Highlight of subsurface cracking

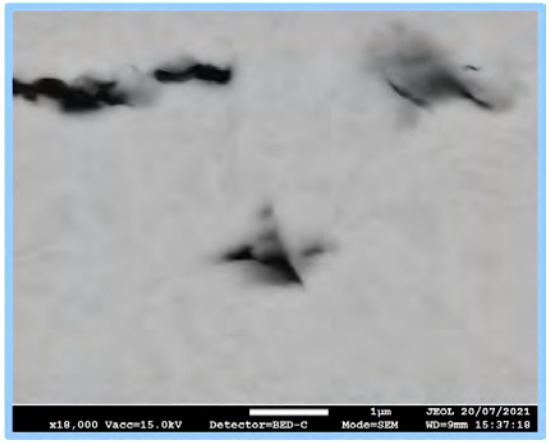

(d) Highlight of subsurface cracking

Figure 119: Surface state of X-45°C after sand blasting and pickling

X-50°C Trial 2

X-50°C The oxide produced coiling at X-50°C was highly similar to that observed on X-45°C. Secondary and tertiary dendrites were present at the internal oxidation front. The internal oxide penetrated the furthest into the substrate along the grain boundaries. Oxidation was preferential along grain boundaries due to the ease of diffusion.
Figure 120c shows very fine and evolving nuclei. At higher coiling temperatures such as X°C fewer nuclei were observed. Its presupposed that the majority of the nuclei at higher temperatures would have sufficiently grown and developed into an interlocking dendritic structure, producing the dense internal oxidation zone commonly observed.
The surface after hot-band annealing was free of oxide and optimal for further processing in the cold rolling mill.

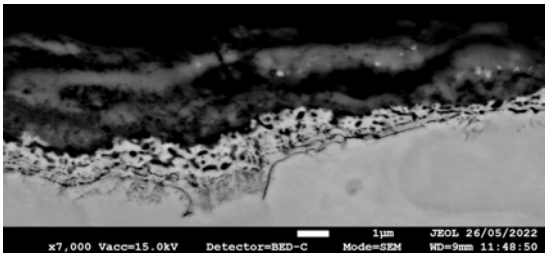

(a) Oxide morphology overview

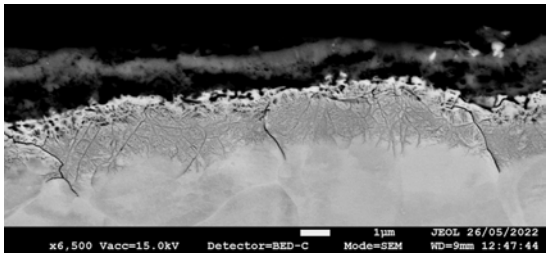

(b) Internal oxidation displaying a preference for direction of growth depending on the underlying grain

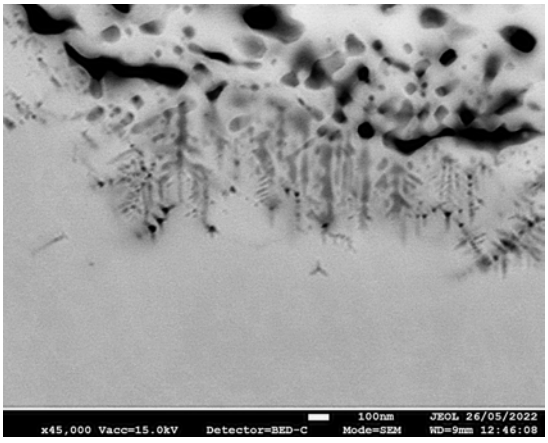

(c) Extremely fine interface displaying a transition from spherical to dendritic growth

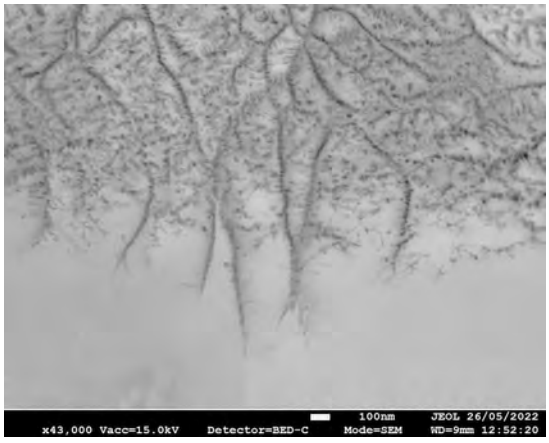

(d) Growth front for fine dendritic particles of silica interacting with the underlying substrate

Figure 120: Morphology of internal oxidation after coiling at X-50°C

X-75°C Trial 1 and 2

X-75°C Coiling at X-75°C produced a substantially thinner oxide compared to previous coiling temperatures. Once again affirming that a lower coiling temperature will reduced oxide growth. The internal oxide morphology shifted between globular and dendritic. Figure 121 shows a clear shift from globular morphology to dendritic. Its possible that this was an orientation effect however further work needs to be conducted in order to understand the phenomena fully.
The surface after hot-band annealing was free of oxide and optimal for further processing in the cold rolling mill.

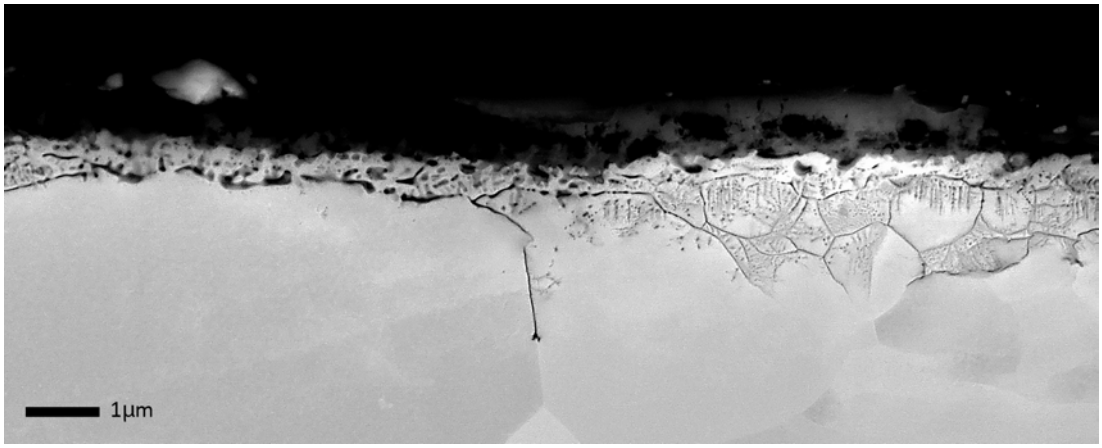

Figure 121: Morphology of internal oxidation after coiling at X-75°C

X-100°C Trial 2

X-100°C HRC Figure 122b shows the HRC surface state of a strip coiled at X-100°C. The internal oxidation varied in thickness but was substantially reduced compared to earlier samples. The morphology was primarily dendritic with fine spheres of silica located at the oxide-scale interface.
The dendrites were primarily secondary and tertiary dendrite arms were interlocking in areas however the oxide was very sparse appearing relatively premature in growth. The oxide front travelled along both the grain boundaries and sub grain boundaries. The ease of diffusion along grain boundaries and sub grain boundaries was due to the misalignment along the grain boundaries creating an area of high energy allowing for easy diffusion. The external oxide was very adherent and remained intact through handling.

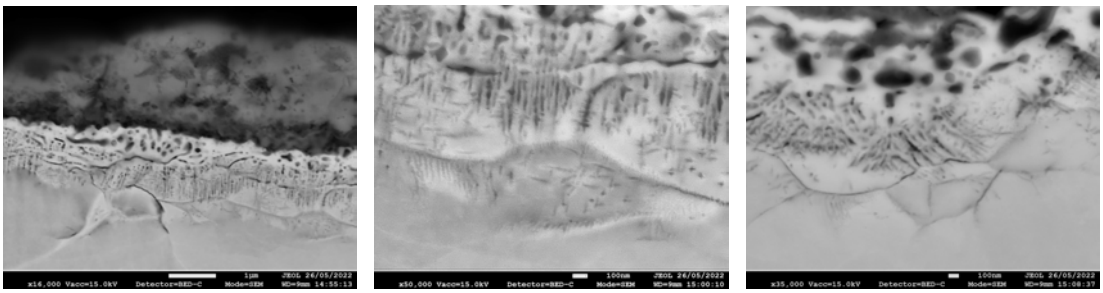

(a) Morphology overview of internal and external oxide at X-100°C (b) Dendritic particles of silica (c) Highlight of fine growth along subgrain boundaries

Figure 122: Morphology of internal oxidation region after coiling at X-100°C

X-100°C HBA Figure 123 shows the strip surface of X-100°C after sand blasting and pickling. Regions of detrimental coarsened internal oxide were present throughout the sample but the quantity of coarse internal oxides was substantially lower than that of X°C. It was conjectured that the internal oxides on the HRC were too fine and thus did not coarsen appropriately through process and hence could not be easily or evenly removed during sandblasting and pickling.

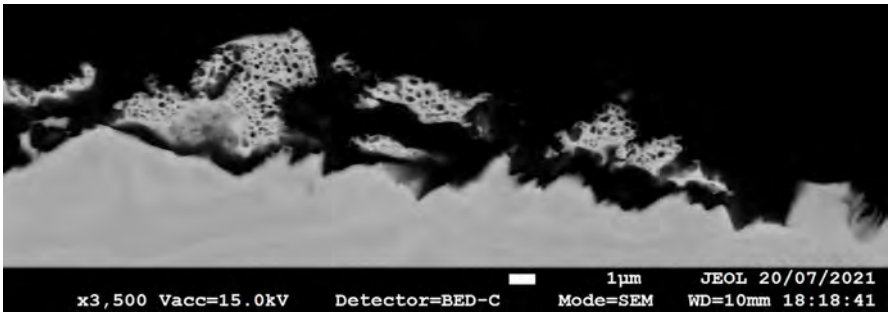

(a) Poor surface quality after sand blasting and pickling at 100°C

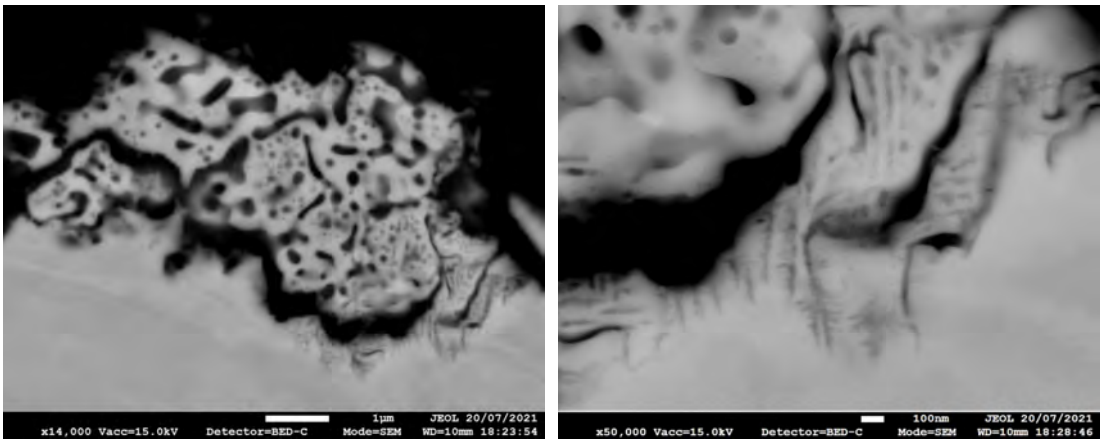

(b) Mildly coarsened internal oxide (c) Highlight of fine dendritic structure evident of lack of coarsening through process

Figure 123: Persisting internal oxidation on HBA strip after sand blasting and pickling at X-100°C

X-115°C Trial 1

X-115°C The surface state of the HRC produced at X-115°C was displayed in figure 124. The oxide was highly similar in thickness and morphology to X-100°C. Fine nuclei had a greater presence towards the middle of the coil and were observed forming in a pattern similar to that of a dendritic structure. Submicron globules of silica and fayalite were located towards the edge of the coil and appeared to act as nucleation sites for dendritic growth.
Regions of coarsened internal oxide were observed after sand blasting and pickling

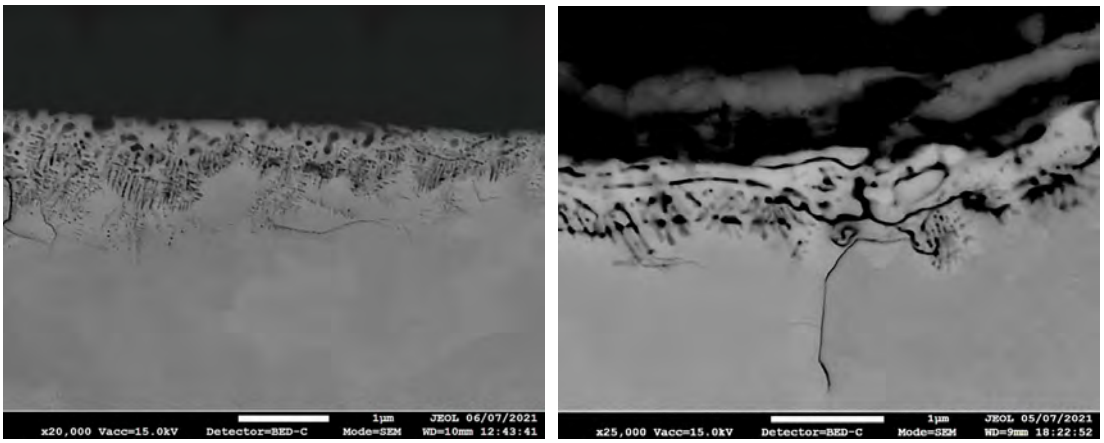

(a) Center of coil (b) Edge of coil

Figure 124: Morphology of internal oxidation region at X-115°C

8.3.1 Summary

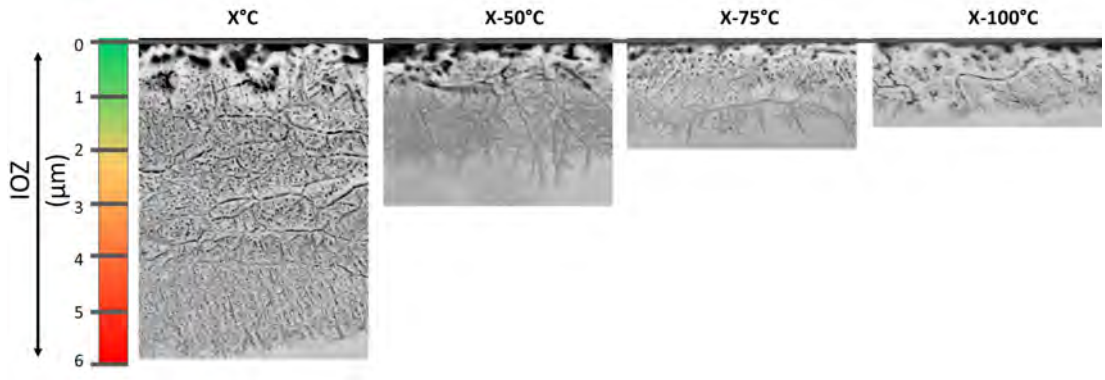

Figure 125: Thickness of internal oxidation region versus coiling temperature

HRC The effect of coiling temperature on internal oxide growth has proven to be significant. Figure 125 shows that the depth of the internal oxidation decreases linearly with a decrease in coiling temperature. The morphology and phase composition did not vary substantially with changes in temperature.

All samples contained globules of silica and fayalite close towards the interface and dendritic silica particles further into the substrate. Silica particles will form first due to selective oxidaiton with the dendritic structure forming afterwards. Dendritic particles of silica are commonly observed in steels with high Si contents [76]. At X°C entire grains of the substrate were consumed by the dendritic structure. The internal oxidation grew firstly along the grain boundaries and then inwards consuming the grain. Large scale internal oxidation of this type was not observed at lower temperatures.

From X°C to X-50°C a dramatic decrease in internal oxidation was observed. The internal oxidation region was more than halved in thickness from 6µm to approximately 2.5µm. Nonetheless the decrease in depth of oxidation was not as dramatic at the following lower temperatures at 2µm and 1.5µm respectively.

The external oxide was not measured for this work, however upon reflection only a slight decrease in thickness was observed for the tertiary scale. The morphology of the external scale was affected to a far greater extent. At lower temperatures, closer to the eutectoid transition temperature, the morphology was predominantly magnetite, however at higher temperatures, such as X°C, the morphology was magnetite with large islands of reduced α-iron throughout.

The proposed formation mechanism of coiling oxidation was as follows - A thin layer of tertiary scale was present after processing and persists during coiling. The tertiary scale then acts as an oxygen reservoir allowing for the oxidation of the substrate. As the scale cools, wustite will decompose and oxygen will then diffuse down into the steel substrate due to thermodynamics of reaction. The formation and growth of these internal oxides will reduce the exterior scale forming larger islands of α-iron in the exterior scale. This was observed at X°C, which was significantly above the eutectoid transition temperature and contained large particles of α-iron throughout the exterior

scale. At lower coiling temperatures, closer to the eutectoid transition temperature, the oxygen would not have the kinetics to diffuse down into the substrate [130].
It was assumed that a thin layer of internal oxidation was present prior to coiling but the thickness was nominal and presumably similar or less than that of X-100°C at 1.5µm.

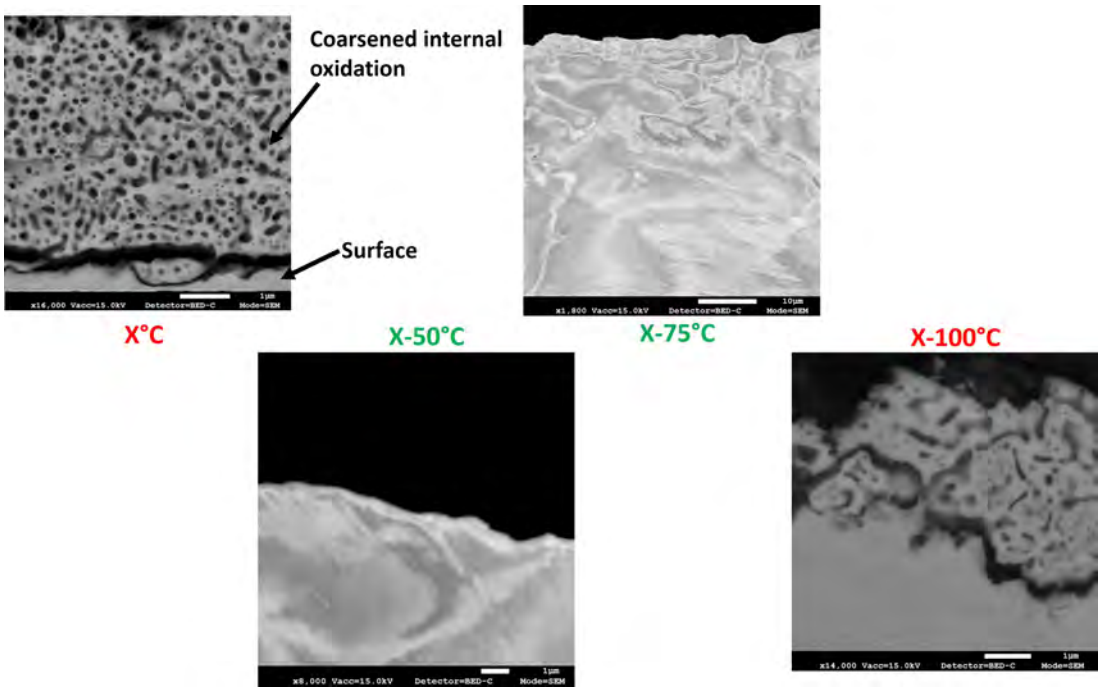

Figure 126: Surface appearance after sand blasting and pickling through process for each temperature trial

HBA Figure 126 illustrates the HRC samples after sand blasting and pickling through an intermediate annealing. It was immediately apparent that not all of the samples have produced the clean and desired surface required for cold rolling. At X°C a thick coarsened region of internal oxidation persisted throughout the entire width of the sample.
It was surmised that the oxide coarsened through the annealing process due to Ostwald ripening, producing large spheres of silica and fayalite. Smaller precipitates have a higher solubility than that of larger precipitates due to curvature of radius. The coarsened precipitates observed are a result of diffusion controlled ripening [46]. The coarsened internal oxide was far less adherent than the dendritic silica particles however the oxide was too large to remove wholly during sand blasting and pickling.
X-50°C and X-75°C have produced the optimum surface. Both appear smooth with minimal damage to the surface. It was conjectured that the internal oxides coarsened during processing forming a thin continuous band of precipitates. Upon sand blasting and pickling the coarsened oxide has then fractured at the interface with the substrate and been removed entirely. X-75°C was deemed the best coiling temperature due to the lower quantity of energy used.
At lower temperatures internal oxide was still intermittently persistent across the strip. Small segments of dendritic silica were present and the oxide did not appear entirely coarsened. It was conjectured that the internal oxide did not grow to the optimum

thickness and thus did not form a continuous coarsened layer of oxidation that could easily be removed as a whole.

8.4 Conclusions

Internal oxidation on a high silicon steel (Si 3.2wt%) was investigated after processing through plant. Plant trials were conducted with differing coiling temperatures after hot rolling in order to determine the effect on cleanliness after hot-band annealing.

- Coiling temperature was found to have a significant impact on the depth of internal oxidation after hot rolling with a strong negative correlation associated between temperature and depth of the IOZ.
- A dramatic decrease in internal oxidation was observed from X°C to X-50°C. The IOZ more than halved in thickness from 6µm to approximately 2.5µm. Further decreases in thickness of the IOZ were observed at lower temperatures; at 2µm and 1.5µm for X-75°C and X-100°C respectively.
- Coiling temperature was not found to significantly impact the morphology of the IOZ, however at higher temperatures a greater quantity of dendritic silica particles was observed. Samples had a globular morphology of silica and fayalite towards the oxide/ steel interface with dendritic silica particles present at the growth front.
- Internal oxide precipitates were coarsened during annealing; producing large spheres of silica and fayalite. Coarsened internal oxide was found to be far less adherent than the dendritic silica particles.
- At X°C the IOZ grew astronomically during coiling and a layer of coarsened internal oxide persisted after hot-band annealing.
- At X-100°C internal oxidation was intermittently persistent across the strip as the oxide did not correctly coarsen and was not fully removed.
- Both X-50°C and X-75°C produced the optimum surface for further processing with no coarsened internal oxidation present on the surface.

The recommend coiling temperature from this work was X-75°C due to the premium surface produced after HBA.

9 Conclusions

The effect of chemical composition, temperature and elapsed time on scale formation was investigated in this thesis. TGA testing, advanced characterisation and large scale plant trials were utilised to conduct systematic research. The results are outlined as follows:

Chapter 5 - Oxidation of Rapid Alloy Prototyping Samples
RAP was successfully used to investigate the formation of oxides associated with Mn, Si and Mo in isolation. The oxide thickness was shown to vary significantly depending on the alloying additions. The addition of Si produced a complex and intricate oxide composed of many regions; however, a minimum fundamental addition of 1wt.% was requisite. Below 1wt.% it was found that an incomplete passivation layer was produced and oxidation was accelerated. 2Mn-1Mo produced the best oxide scale morphology from an industrial standpoint of the 11 compositions examined. The oxide was non-adherent and light, resulting in low yield loss, with a critical temperature of oxidation above 700°C.

Chapter 6 - Oxidation of Industrial Steels
A thermodynamic study of industrially pertinent steel grades was conducted. Selective surface oxidation of Si and Al limited the mass gain for B32 and DP800 at temperatures below 1100°C. The vast majority of internal oxide precipitates formed within the first 10s of heating in DP800. It was found that a high Si content will stop providing oxidation resistance at higher temperatures and will then begin to expeditiously accelerate oxidation due to a liquid fayalite phase.

Chapter 7 - External Oxidation Blistering
A number of new and previously unidentified blister formation mechanisms were discovered. Blister upon cooling was discovered for steel grade 3812 during air cooling and observed on a number of samples. Unique and new phenomena such as blister crown splitting and secondary blister were identified on DP800 due to the presence of a conglomerated spinel phase and hematite in the outer oxide. High Si steels were only found to form blister at high temperatures with the aid of a liquid fayalite phase to promote growth.

Chapter 8 - Industrial Optimisation of Internal Oxidation
Plant trials found that coiling temperature had a significant impact on the depth of internal oxidation after hot rolling, with a strong negative correlation associated between temperature and depth of the internal oxidation zone. The suggested coiling temperature, X-75°C, eliminated issues surrounding surface cleanliness after hot-band annealing.

10 Future Works

- Further RAP work should be undertaken to understand the additional effects of Al. Further alloying combinations such as Al and Si should be combined to see the influence of the rate of reaction. A combination of Al and Si should be used to determine at what wt% a passivation layer was produced.
- Thermodynamic studies should be undertaken on the DP800 steel to discern why a shift in internal oxide morphology was observed from inter-granular to intra-granular.
- Further heat treatments on DP800 samples should be conducted in order to identify the volume fraction of blister, the blister regime nose and the transition temperature between mode 1 and 2.
- HRC temperature trial samples should be heat treated under reducing atmosphere in order to discern the rate of coarsening. Experiments should then be conducted on the samples to ascertain de-scalability.

References

[1] Theyssier MCC. Manufacturing of advanced high-strength steels (AHSS). Elsevier Ltd; 2015.

[2] Hirsch J. Aluminium sheet fabrication and processing. Fundamentals of Aluminium Metallurgy. 2011:719-46.

[3] Serizawa Y. Heat Transfer Technology for Steel Rolling Process. 2016;(111).

[4] Saunders SRJJ, Monteiro M, Rizzo F. The oxidation behaviour of metals and alloys at high temperatures in atmospheres containing water vapour: A review. Progress in Materials Science. 2008;53(5):775-837.

[5] Fukumoto M, Maeda S, Hayashi S. Effect of Water Vapor on the Oxidation Behavior of Fe – 1 . 5Si in Air at 1073 and 1273 K. 2001;55:401-22.

[6] Birosca S. The microstructural development of oxide scales on low carbon steels; 2006.

[7] Callister WD. Materials Science and Engineering: An Introduction. 5th ed.; 2015.

[8] Bhadeshia H, Honeycombe R. Steels: Microstructure and Properties; 2006.

[9] Ashby MF, Jones D. Alloy Steels. In: Steels 2; 2013. p. 221-36.

[10] Bain E. Effects of Alloying elements in forming austenite. In: The alloying elements of steel; 2004. .

[11] Canale LCF, Albano L, Totten GE, Meekisho L. Hardenability of Steel. vol. 12. Elsevier; 2014.

[12] Aghaei Lashgari V, Lashgari V, Aghaei Lashgari V, Lashgari V. Internal and External Oxidation of Manganese in Advanced High Strength Steels. september; 2014.

[13] Fushiwaki Y, Nagataki Y, Nagano H, Tanimoto W, Sugimoto Y. Influence of Fe Oxidation on Selective Oxidation Behavior of Si and Mn Added in High Strength Sheet Steel. 2014;54(3):664-70.

[14] Hawezy D. The influence of silicon content on physical properties of non-oriented silicon steel. Materials Science and Technology (United Kingdom). 2017;33(14):1560-9.

[15] Steiner Petrovič D. Non-Oriented Electrical Steel Sheets. Materials and technology. 2010;44(6):317-25.

[16] Gong J, Ma J, Sun M. Recent Development of Grain Oriented Electrical Steel in Shougang. 6th International Conference on ThermoMechanical Processing, TMP 2022 - Proceedings. 2016;21(21):29-34.

[17] Waide P, Brunner CU. Energy-Efficiency Policy Opportunities for Electric Motor-Driven Systems. Internationale energy agency. 2011;na(na):132.

[18] Smallman RE. Modern Physical Metallurgy and Materials Engineering; 2016.

[19] Birks N, Heier G. Introduction to the high temperature oxidation of metals;.

[20] Prostakova V, Shishin D, Shevchenko M, Jak E. Thermodynamic optimization of the Al2O3–FeO–Fe2O3–SiO2 oxide system. Calphad: Computer Coupling of Phase Diagrams and Thermochemistry. 2019;67(October).

[21] Jung S, Park J, Bin S. Rapid quantitative analysis of fayalite and silica formed during decarburization of electrical steel. 2012;(February 2011):270-5.

[22] Huo SH, Qian M, Schaffer GB, Crossin E. Aluminium powder metallurgy. In: Lumley RBTFoAM, editor. Woodhead Publishing Series in Metals and Surface Engineering. Woodhead Publishing; 2011. p. 655-701. Available from: http://www.sciencedirect.com/science/article/pii/B9781845696542500213.

[23] Price K, Price K. Effect of minor alloying elements on the formation of oxides during decarburisation of of grain oriented electrical steels; 2018.

[24] Khanna AS. High-temperature oxidation. Handbook of Environmental Degradation Of Materials: Third Edition. 2018;2:117-32.

[25] Oono NH, Ukai S, Tominaga K, Ebisawa N, Tomura K. Precipitation of various oxides in ODS ferritic steels. Journal of Materials Science. 2019;54(11):8786-99.

[26] Husain SW, Ahmed MS, Qamar I. Dendritic morphology observed in the solid-state precipitation in binary alloys. Metallurgical and Materials Transactions A: Physical Metallurgy and Materials Science. 1999;30(6):1529-34.

[27] Adeleke OA, Latiff AAA, Saphira MR, Daud Z, Ismail N, Ahsan A, et al. Principles and Mechanism of Adsorption for the Effective Treatment of Palm Oil Mill Effluent for Water Reuse. Elsevier Inc.; 2018.

[28] Kim Bk. High Temperature Oxidation of Low Carbon Steel. 2003;(June).

[29] Wagner JB, Pettit FSS. Transition from the Linear to the Parabolic Rate Law During the Oxidation of Iron to Wustite in CO – CO2 Mixtures. 1964.

[30] Abuluwefa HT, Engineering M. Characterization of Oxides (Scale) Growth of Low Carbon Steel during Reheating; 1996.

[31] Uda S. Stoichiometry of Oxide Crystals. vol. 1. Second edi ed. Elsevier B.V.; 2015.

[32] Dalton J. A New System of Chemical Philosphy. 1808;3:30.

[33] Pieraggi B. Defects and transport in oxides and oxide scales. Shreir's Corrosion. 2010:101-31.

[34] ALONSO JAA, MARCH NHH. Physical Metallurgy. In: Electrons in Metals and Alloys. 4th ed.; 1989. p. 129-203.

[35] Kofstad P. High Temperature Corrosion; 1988.

[36] Raw B, SEl L, Bt HaU Japan C, Porter D, Easterling K. Phase Transformations in Metals and Alloys; 1995.

[37] Liu S, bin Wu H, Li X, tao Jiang H, Tang D. Characterizing the structure evolution of tertiary scale during simulated coiling by EBSD. Journal of Iron and Steel Research International. 2014;21(2):215-21.

[38] Müller J, Schierling M, Zimmermann E, Neuschütz D. Chemical vapor deposition of smooth α-Al2O3 films on nickel base superalloys as diffusion barriers. Surface and Coatings Technology. 1999;120-121:16-21.

[39] Tartaj J, Messing GL. Anisotropic grain growth in α-Fe2O3-doped alumina. Journal of the European Ceramic Society. 1997;17(5):719-25.

[40] Badini C, Laurella F. Oxidation of FeCrAl alloy: Influence of temperature and atmosphere on scale growth rate and mechanism. Surface and Coatings Technology. 2001;135(2-3):291-8.

[41] Mohamed HE, Philosophy DOF, Engineering M, Engineering FOF. Oxidation Behavior of Some Cr Ferritic Steels for High Temperature Fuel Cells. 2012.

[42] Voss DA, Butler EP, Mitchell TE. The Growth of Hematite Blades during the High Temperature Oxidation of Iron. Metallurgical Transactions A. 1982;13(5):929-35.

[43] Mrowec S, Stokłosa A. Oxidation of copper at high temperatures. Oxidation of Metals. 1971;3(3):291-311.

[44] Krupp U, Christ HJ. Internal corrosion of engineering alloys: Experiment and computer simulation. Journal of Phase Equilibria and Diffusion. 2005;26(5):487-93.

[45] Tadros T. Ostwald Ripening. In: Encyclopedia of Colloid and Interface Science. Heidelberg: Springer, Berlin; 2013. p. 820-0.

[46] Schmitt V, Arditty S, Leal-Calderon F. Stability of concentrated emulsions. In: Petsev DNBTIS, Technology, editors. Emulsions: Structure Stability and Interactions. vol. 4. Elsevier; 2004. p. 607-39.

[47] Mao W. Oxidation Phenomena in advanced high strength steels. June; 2015.

[48] Bergholz W, Binns MJ, Booker GR, Hutchison JC, Kinder SH, Messoloras S, et al. A study of oxygen precipitation in silicon using high-resolution transmission electron microscopy, small-angle neutron scattering and infrared absorption. Philosophical Magazine B: Physics of Condensed Matter; Statistical Mechanics, Electronic, Optical and Magnetic Properties. 1989;59(5):499-522.

[49] Falster R, Voronkov VVV, Resnik VYY, Milvidskii MGG. Thresholds for Effective Internal Gettering in Silicon Wafers. Society. 2002;638:2002-2.

[50] Murphy JD, Al-Amin M, Bothe K, Olmo M, Voronkov VV, Falster RJ. The effect of oxide precipitates on minority carrier lifetime in n -type silicon. Journal of Applied Physics. 2015;118(21).

[51] Chen Nw, Readey DW, Moore JJ. OXIDE WHISKER GROWTHa Ning-Wei Chen, Dennis W. Readey, and John. 1994.

[52] Krzyzanowski M, Beynon JH, Farrugia DCJ. Scale Growth and Formation of Subsurface Layers; 2010.

[53] Chen RY, Yuen WYDD. Review of the high-temperature oxidation of iron and carbon steels in air or oxygen. Oxidation of Metals. 2003;59(5-6):433-68.

[54] Geiger AL. Effects of internal oxidation and nitridation on the magnetic properties of non-oriented electrical steels. Journal of Applied Physics. 1979;50(B3):2366-8.

[55] Dunning JS, Alman DE, Rawers JC. THE EFFECT OF SILICON AND ALUMINUM ADDITIONS ON THE OXIDATION RESISTANCE OF LEAN CHROMIUM STAINLESS STEELS;(11).

[56] Kucera J, Hajduga M, Glowacki J, Broz P. Decarburisation and Hardness Changes of Fe-C-Cr-Mn-Si Steels Caused by High Temperature Oxidation in Ambient Air. International Journal of Materials Research. 1999.

[57] Soedel W. Stress Corrosion Cracking; 2010.

[58] Matsuno F. Blistering and Hydraulic Removal of Scale Films of Rimmed Steel At High Temperature. Transactions of the Iron and Steel Institute of Japan. 1980;20(6):413-21.

[59] Da Costa E Silva ALV. Non-metallic inclusions in steels - Origin and control. Journal of Materials Research and Technology. 2018;7(3):283-99.

[60] Zhang JS, editor. 21 - Creep Damage Physics. Woodhead Publishing; 2010.

[61] Kondo Y, Tanei H, Suzuki N, Ushioda K, Maeda M. Blistering behavior during oxide scale formation on steel surface. ISIJ International. 2011;51(10):1696-702.

[62] Basabe V. BLISTERING FORMATION IN THREE STEELS WITH DIFFERENT CARBON AND ALLOY ADDITIONS.

[63] Hildal K, Perepezko JH. Chapter 19 - Metals and Alloys. vol. 6 of Handbook of Thermal Analysis and Calorimetry. Vyazovkin S, Koga N, Schick C, editors. Elsevier Science B.V.; 2018.

[64] Fabrikant II, Eden S, Mason NJ, Fedor J. Chapter Nine - Recent Progress in Dissociative Electron Attachment: From Diatomics to Biomolecules. vol. 66 of Advances In Atomic, Molecular, and Optical Physics. Arimondo E, Lin CC, Yelin SF, editors. Academic Press; 2017.

[65] Inkson BJ. 2 - Scanning electron microscopy (SEM) and transmission electron microscopy (TEM) for materials characterization. Hübschen G, Altpeter I, Tschuncky R, Herrmann HG, editors. Woodhead Publishing; 2016.

[66] Ingle NJC. 2 - Inelastic scattering techniques for in situ characterization of thin film growth: backscatter Kikuchi diffraction. Koster G, Rijnders G, editors. Woodhead Publishing Series in Electronic and Optical Materials. Woodhead Publishing; 2011.

[67] Dingley DJ, Randle V. Microtexture determination by electron back-scatter diffraction. Journal of Materials Science. 1992;27(17):4545-66.

[68] Lewis BJ, Thompson WT, Iglesias FC. 2.20 - Fission Product Chemistry in Oxide Fuels. 2012:515-46.

[69] Wang H, Chu PK. Chapter 4 - Surface Characterization of Biomaterials. Bandyopadhyay A, Bose S, editors. Oxford: Academic Press; 2013.

[70] Springer H, Raabe D. Rapid alloy prototyping: Compositional and thermo-mechanical high throughput bulk combinatorial design of structural materials based on the example of 30Mn-1.2C-xAl triplex steels. Acta Materialia. 2012;60(12):4950-9.

[71] Zhang L, Harrison W, Yar MA, Brown SGR, Lavery NP. The development of miniature tensile specimens with non-standard aspect and slimness ratios for rapid alloy prototyping processes. Journal of Materials Research and Technology. 2021;15:1830-43.

[72] Lavery NP, Mehraban S, Pleydell-Pearce C, Brown SGRR, Jarvis DJ, Voice W, et al. Combinatorial development and high throughput materials characterisation of steels. Ironmaking and Steelmaking. 2015;42(10):727-33.

[73] JEOL Ltd . JSM-7800F Schottky Field Emission Scanning Electron Microscope;.

[74] Farrugia D, Brown S, Lavery NP, Pleydell-Pearce C, Davis C. Rapid Alloy Prototyping for a range of strip related advanced steel grades. Procedia Manufacturing. 2020;50(2019):784-90.

[75] Beckley P, House CF, Hill B. Steels , Silicon Iron-Based : Magnetic Properties. 2016;(September 2015):1-7.

[76] Zhang X, Corrêa C, Liu C, Prabhakar M, Rohwerder M. Selective oxidation of ternary Fe-Mn-Si alloys during annealing process. Corros Sci. 2020;174(July):108859.

[77] Roth WL. Magnetic Structures of MnO, FeO, CoO, and NiO. Phys Rev. 1958 Jun;110:1333-41.

[78] Juricic C, Pinto H, Cardinali D, Klaus M, Genzel C, Pyzalla AR. Evolution of microstructure and internal stresses in multi-phase oxide scales grown on (110) surfaces of iron single crystals at 650 °c. Oxid Met. 2010;73(1-2):115-38.

[79] Jin X, Chen S, Rong L. Effects of Mn on the mechanical properties and high temperature oxidation of 9Cr2WVTa steel. J Nucl Mater. 2017.

[80] Lashgari VA, Kwakernaak C, Sloof WG. Transition from internal to external oxidation of Mn steel alloys. Oxid Met. 2014;81(3-4):435-51.

[81] Zhu Y. Effect of internal oxidation in bendability of UHSS;.

[82] Story M. Microstructural Effects on High-Temperature Selective Oxidation of CMnSi Advanced High-Strength Steels. Canegie Mellon University; 2018.

[83] CHEN RY, YUEN WYD. Examination of Oxide Scales of Hot Rolled Steel Products. ISIJ International. 2006;45(1):52-9.

[84] Auinger M, Praig VG, Linder B, Danninger H. Grain boundary oxidation in iron-based alloys, investigated by 18O enriched water vapour - The effect of mixed oxides in binary and ternary Fe-{Al, Cr, Mn, Si} systems. Corros Sci. 2015;96:133-43.

[85] Olives J. Surface thermodynamics, surface stress, equations at surfaces and triple lines for deformable bodies. J Phys Condens Matter. 2010;22(8):1-22.

[86] Diawara B, Beh YA, Marcus P. Nucleation and growth of oxide layers on stainless steels (FeCr) using a virtual oxide layer model. J Phys Chem C. 2010;114(45):19299-307.

[87] Sachs K, Jay F. A magnetite seam at the scale/metal interface on mild steel. Iron Steel Inst. 1960;195:180.

[88] Takeda M, Onishi T, Nakakubo S, Fujimoto S. Physical Properties of Iron-Oxide Scales on Si-Containing Steels at High Temperature Physical Properties of Iron-Oxide Scales on Si-Containing Steels at High Temperature. 2015;(January):6-11.

[89] Agusu L, Alimin, Ahmad LO, Firihu MZ, Mitsudo S, Kikuchi H. Crystal and microstructure of MnFe2O4 synthesized by ceramic method using manganese ore and iron sand as raw materials. J Phys Conf Ser. 2019;1153(1):2-9.

[90] Tei S, Hirotoshi M, Tatsuya S. Oxygen Plasma Interactions with Molybdenum :. Oxid Met. 2001.

[91] Yun DW, Seo HS, Jun JH, Lee JM, Kim KY. Molybdenum effect on oxidation resistance and electric conduction of ferritic stainless steel for SOFC interconnect. Int J Hydrogen Energy. 2012;37(13):10328-36.

[92] Nitta H, Yamamoto T, Kanno R, Takasawa K, Iida T, Yamazaki Y, et al. Diffusion of molybdenum in α-iron. Acta Mater. 2002;50(16):4117-25.

[93] Gesmundo F, Viani F. The formation of multilayer scales in the parabolic oxidation of pure metals-II. Temperature and pressure dependence of the different rate constants. Corrosion Science. 1978;18(3):231-43.

[94] Gesmundo F, Viani F, Young DJ. The transition from single to double oxide growth during the high temperature corrosion of a pure metal by a single oxidant. Oxidation of Metals. 1992;38:309-22.

[95] Yoshihara M, Taniguchi S, Fujita K. The effect of nitrogen ion implantation on the oxidation behavior of TiAl. Nippon Kinzoku Gakkaishi/Journal Japan Inst Met. 2004;68(7):468-74.

[96] Mège-Revil A, Steyer P, Cardinal S, Thollet G, Esnouf C, Jacquot P, et al. Correlation between thermal fatigue and thermomechanical properties during the oxidation of multilayered TiSiN nanocomposite coatings synthesized by a hybrid physical/chemical vapour deposition process. Thin Solid Films. 2010;518(21):5932-7.

[97] Picque B. Experimental study and numerical simulation of iron oxide scales mechanical behavior in hot rolling; 2004.

[98] XU J. Kinetics of Wüstite Formation and Reduction of Manganese alloyed Steel. 2013:50.

[99] Mikkelsen L. High Temperature Oxidation of Iron-Chromium Alloys; 2003.

[100] Wagner C. Passivity and inhibition during the oxidation of metals at elevated temperatures. Corrosion Science. 1965;5(11):751-64.

[101] Rapp RA. Kinetics, Microsctructure and Mechnism of Internal Oxidation. Its Effect and Prevention in High Temperature Alloy Oxidation. Nucl Phys. 1959;13(1):104-16.

[102] Yu X, Jiang Z, Yang D, Wei D, Yang Q. Precipitation behavior of magnetite in oxide scale during cooling of microalloyed low carbon steel. Advanced Materials Research. 2012;572:249-54.

[103] Shewmon PG. Surface Self Diffusion at High Temperatures. 1966:111-2.

[104] Alaoui Mouayd A, Koltsov A, Sutter E, Tribollet B. Effect of silicon content in steel and oxidation temperature on scale growth and morphology. Materials Chemistry and Physics. 2014;143(3):996-1004.

[105] Singh R, Singh R. Classification of Steels. Applied Welding Engineering. 2016:57-64.

[106] Sauerhammer B, Spiegel M, Senk D, Schmidt E, Sridhar S, Safi M. Effect of liquid phase on scale formation during high-temperature oxidation of AlSi-transformation-induced plasticity steel surfaces. Metallurgical and Materials Transactions B. 2005;36(August):503-12.

[107] Okada H, Steel N, Metal S. Mechanism of Red Scale Defect Formation in Si-added Hot-rolled Steel of Red Scale Defect Formation Mechanism Si-added Hot-rolled. 1994;(November).

[108] Kondo Y, Tanei H, Ushioda K, Maeda M, Abe Y. Effect of nitrogen on blister growth process of blistering during high temperature oxidation of steel. Tetsu-To-Hagane/Journal of the Iron and Steel Institute of Japan. 2013;99(9):559-63.

[109] Kondo Y, Tanei H, Ushioda K, Maeda M. Role of hematite formation on blister generation during high temperature oxidation of steel. Tetsu-To-Hagane/Journal of the Iron and Steel Institute of Japan. 2014;100(3):352-8.

[110] Kim DJ, Lee JS, Koo YM. Influences of carbon and silicon on blister formation in scale surface during high temperature oxidation of carbon steels. Metals and Materials International. 2017;23(4):715-9.

[111] Pilling NB, Bedworth RE. The Oxidation of Metals at High Temperatures. Jinst. 1923;29:529-91.

[112] Xu C, Gao W. Pilling-bedworth ratio for oxidation of alloys. Materials Research Innovations. 2000;3(4):231-5.

[113] Panashchenko L. Tin Whisker Growth on Sn77.2-In20-Ag2.8 Solder; 2018. .

[114] Brusse JN. Tin Whiskers. In: Capacitor and Resistor Technology Symposium 2002; 2002. .

[115] Khaleel MA, Stephens EV, Stevenson J. Interfacial stresses and degredation of oxide scale and substrate interface at high temperature. In: TMS Middle East- Mediterranean Materials Congress on Energy and Infrastructure Systems (MEMA 2015). vol. 0; 2015. p. 351-2.

[116] Goursatt AG, Smeltzert WW. Kinetics and Morphological Development of the Oxide Scale on Iron at High Temperatures in Oxygen at Low Pressure *. 1973;6:101-16.

[117] Baud J, Ferrier A, Manenct J. Study of Magnetite Film Formation at Metal-Scale Interface During Cooling of Steel Products *. 1978;12(4).

[118] Pilania G, Thijsse BJ, Hoagland RG, LaziÄ I, Valone SM, Liu XY. Revisiting the Al/Al 2 O 3 interface: Coherent interfaces and misfit accommodation. Scientific Reports. 2014;4:1-9.

[119] Uberuaga BP, Dholabhai PP, Pilania G, Chen A. Semicoherent oxide heterointerfaces: Structure, properties, and implications. APL Materials. 2019;7(10).

[120] Cogswell DA, Bazant MZ. Coherency strain and the kinetics of phase separation in LiFePO 4 nanoparticles. ACS Nano. 2012;6(3):2215-25.

[121] Schwenk W, Rahmel A. Theoretical considerations on phase boundary reactions and mass transfer during the oxidation of iron. Oxidation of Metals. 1986;25(5-6):293-303.

[122] Wagner C. Theoretical Analysis of the Diffusion Processes Determining the Oxidation Rate of Alloys. Journal of The Electrochemical Society. 1952 oct;99(10):369.

[123] De Oliveira FB, Da Silvab GA, Gracaa LM. Defining the hematite topotaxial crystal growth in magnetite-hematite phase transformation. Journal of Applied Crystallography. 2020;53:896-903.

[124] Suárez L, Rodríguez-calvillo P, Houbaert Y, Colás R. Oxidation of ultra low carbon and silicon bearing steels. Corrosion Science. 2010;52(6):2044-9.

[125] Höfler T, Linder B, Angeli G, Gierl-Mayer C, Danninger H, Auinger M, et al. Internal oxidation and formation of Si/Al-enriched oxide bands in the scale of electrical steel grades. Corrosion Science. 2021;187(October 2020):109502.

[126] He B, Xu G, Zhou M, Yuan Q. Effect of Oxidation Temperature on the Oxidation Process of Silicon-Containing Steel. 2016.

[127] Garza-montes-de oca NF, Adolfo L, Lezama L, Mercado-solis RD. Oxidation of silicon and silicon copper bearing steels OXIDATION OF SILICON AND SILICON AND COPPER BEARING. 2011;(October).

[128] Burke DP, Higginson RL. Characterization of multicomponent scales by electron back scattered diffraction (EBSD). Scripta Materialia. 2000;42(3):277-81.

[129] Chen RY, Yuen WYD. A Study of the Scale Structure of Hot-Rolled Steel Strip by Simulated Coiling and Cooling. 2000;53:539-60.

[130] Yu X, Wang X. Effect of coiling temperature on oxide scale of hot- rolled strip. 2012;417:853-8.

[131] Melfo W, Paulussen G. Surface Dents and Attached Build-Ups Surface Defect on Non- Grain-Oriented Electrical Steel Reference Source number. Hot-Spot Research Development, Ijmuiden Technology Center. 2014;31.

11 Appendix

11.1 Oxidation of RAP

	Fe	C	Mn	Si
Target wt%	99.4000	0.1000	0.5000	0.0000
Target mass (g)	19.8800	0.0200	0.1000	0.0000
Measured mass (g)	19.8801	0.0203	0.1000	0.0000
Measured wt%	99.3985	0.1015	0.5000	0.0000
Error percentage	0.0005	1.5000	0.0000	0.0000

Table 18: Appendix: Composition 1: 0.5Mn

	Fe	C	Mn	Si
Target wt%	97.9000	0.1000	2.0000	0.0000
Target mass (g)	19.5800	0.0200	0.4000	0.0000
Measured mass (g)	19.5840	0.0205	0.4002	0.0000
Measured wt%	97.8970	0.1025	2.0005	0.0000
Error percentage	0.0204	2.5000	0.0500	0.0000

Table 19: Appendix: Composition 2: 2Mn

	Fe	C	Mn	Si
Target wt%	97.4000	0.1000	2.0000	0.5000
Target mass (g)	19.4800	0.0200	0.4000	0.1000
Measured mass (g)	19.4797	0.0204	0.4000	0.1004
Measured wt%	97.3961	0.1020	2.0000	0.5020
Error percentage	0.0015	2.0000	0.0000	0.4000

Table 20: Appendix: Composition 3: 2Mn-0.5Si

	Fe	C	Mn	Si
Target wt%	96.9000	0.1000	2.0000	1.0000
Target mass (g)	19.3800	0.0200	0.4000	0.2000
Measured mass (g)	19.3802	0.0205	0.4010	0.2000
Measured wt%	96.8928	0.1025	2.0048	0.9999
Error percentage	0.0010	2.5000	0.2500	0.0000

Table 21: Appendix: Composition 4: 2Mn-1Si

	Fe	C	Mn	Si
Target wt%	95.9000	0.1000	2.0000	2.0000
Target mass (g)	19.1800	0.0200	0.4000	0.4000
Measured mass (g)	19.1801	0.0204	0.4001	0.4001
Measured wt%	95.8971	0.1020	2.0004	2.0004
Error percentage	0.0005	2.0000	0.0250	0.0250

Table 22: Appendix: Composition 5: 2Mn-2Si

	Fe	C	Mn	Si	Mo
Target wt%	98.9000	0.1000	0.5000	0.0000	0.5000
Target mass (g)	19.7800	0.0200	0.1000	0.0000	0.1000
Measured mass (g)	19.7810	0.0202	0.1039	0.0000	0.1037
Measured wt%	98.8615	0.1010	0.5193	0.0000	0.5183
Error percentage	0.0051	1.0000	3.9000	0.0000	3.7000

Table 23: Appendix: Composition 6: 0.5Mn-0.5Mo

	Fe	C	Mn	Si	Mo
Target wt%	97.6500	0.1000	2.0000	0.0000	0.2500
Target mass (g)	19.5300	0.0200	0.4000	0.0000	0.0500
Measured mass (g)	19.5311	0.0201	0.4042	0.0000	0.0506
Measured wt%	97.6262	0.1005	2.0204	0.0000	0.2529
Error percentage	0.0056	0.5000	1.0500	0.0000	1.2000

Table 24: Appendix: Composition 7: 2Mn-0.25Mo

	Fe	C	Mn	Si	Mo
Target wt%	97.4000	0.1000	2.0000	0.0000	0.5000
Target mass (g)	19.4800	0.0200	0.4000	0.0000	0.1000
Measured mass (g)	19.4792	0.0202	0.4030	0.0000	0.1002
Measured wt%	97.3833	0.1010	2.0147	0.0000	0.5009
Error percentage	0.0041	1.0000	0.7500	0.0000	0.2000

Table 25: Appendix: Composition 8: 2Mn-0.5Mo

	Fe	C	Mn	Si	Mo
Target wt%	97.1500	0.1000	2.0000	0.0000	0.7500
Target mass (g)	19.4300	0.0200	0.4000	0.0000	0.1500
Measured mass (g)	19.4306	0.0201	0.4020	0.0000	0.1508
Measured wt%	97.1360	0.1005	2.0096	0.0000	0.7539
Error percentage	0.0031	0.5000	0.5000	0.0000	0.5333

Table 26: Appendix: Composition 9: 2Mn-0.75Mo

	Fe	C	Mn	Si	Mo
Target wt%	96.9000	0.1000	2.0000	0.0000	1.0000
Target mass (g)	19.3800	0.0200	0.4000	0.0000	0.2000
Measured mass (g)	19.4014	0.0201	0.4014	0.0000	0.2005
Measured wt%	96.8936	0.1004	2.0047	0.0000	1.0013
Error percentage	0.1104	0.5000	0.3500	0.0000	0.2500

Table 27: Appendix: Composition 10: 2Mn-1Mo

	Fe	C	Mn	Si	Mo
Target wt%	96.6500	0.1000	2.0000	1.0000	0.2500
Target mass (g)	19.5300	0.0200	0.4000	0.2000	0.0500
Measured mass (g)	19.5312	0.0198	0.4024	0.2005	0.0505
Measured wt%	96.6681	0.0980	1.9916	0.9924	0.2499
Error percentage	0.0061	1.0000	0.6000	0.2500	1.0000

Table 28: Appendix: Composition 11: 2Mn-1Si-0.25Mo

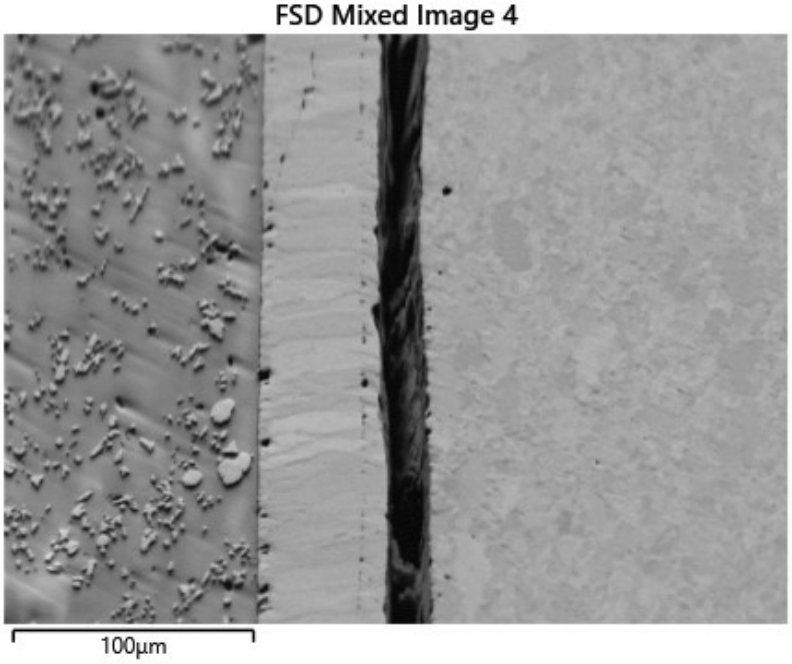

Figure 127: Appendix: 2Mn- EBSD forward scatter image

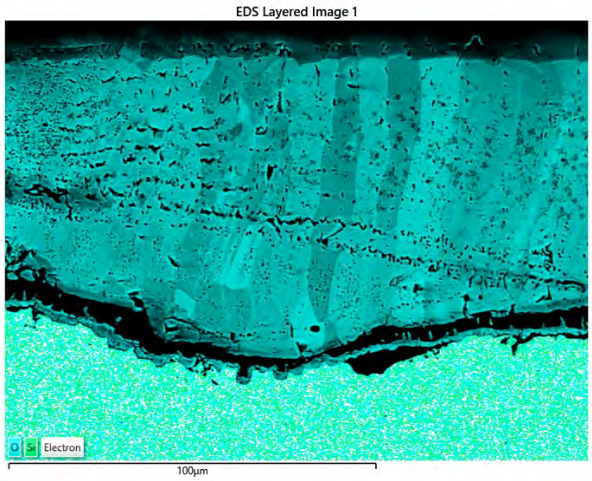

(a) EDS mixed image

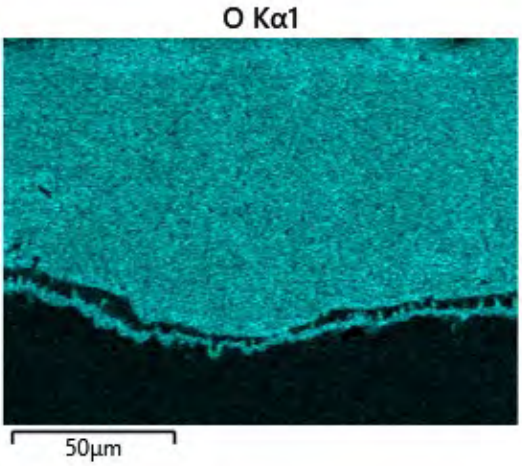

(b) O elemental map

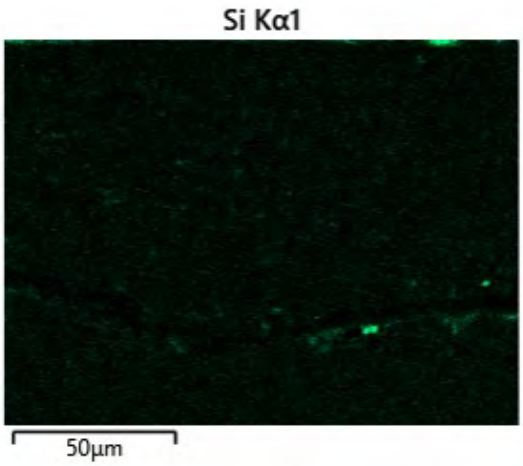

(c) Si elemental map

Figure 128: Appendix: 2Mn-0.5Si EDS

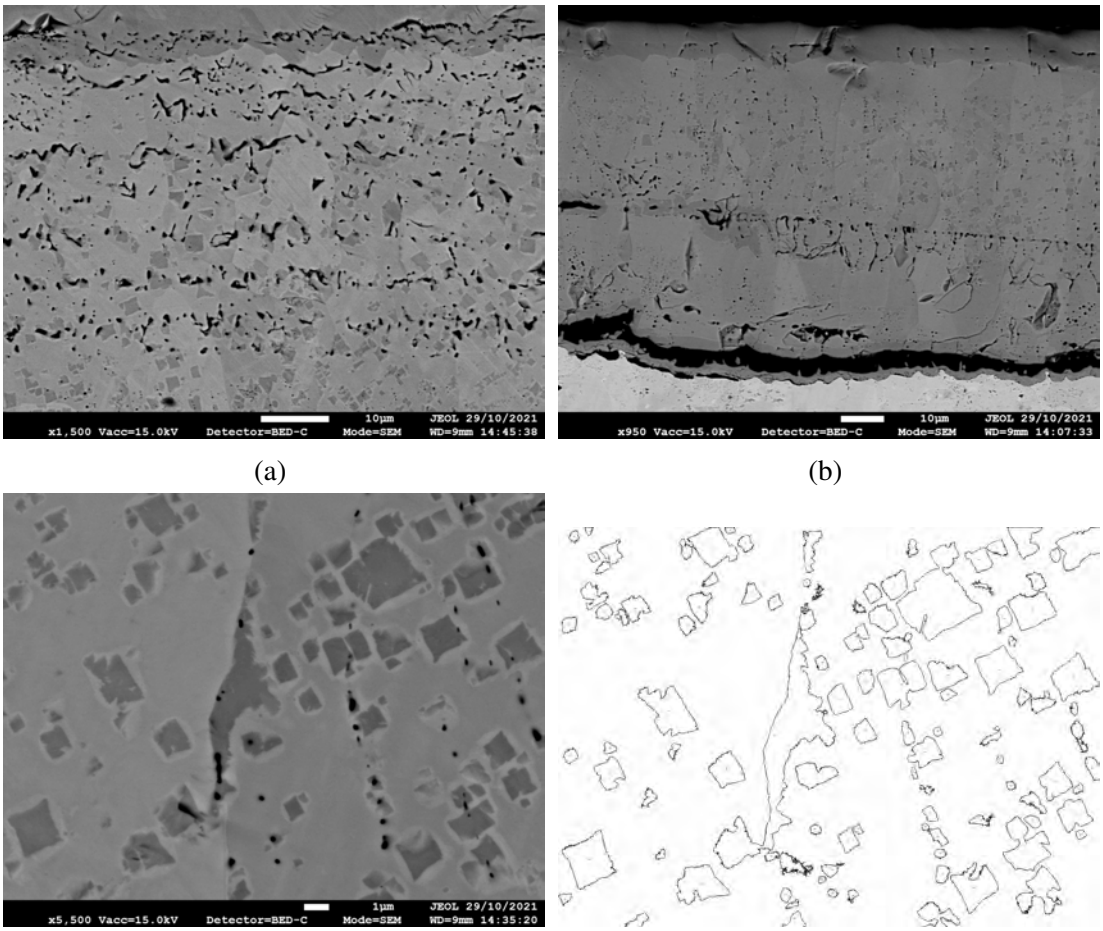

(a) (b)

(c) Image J reference image (d) Image J precipitate analysis

Figure 129: Appendix: 2Mn-0.5Si oxide morphology

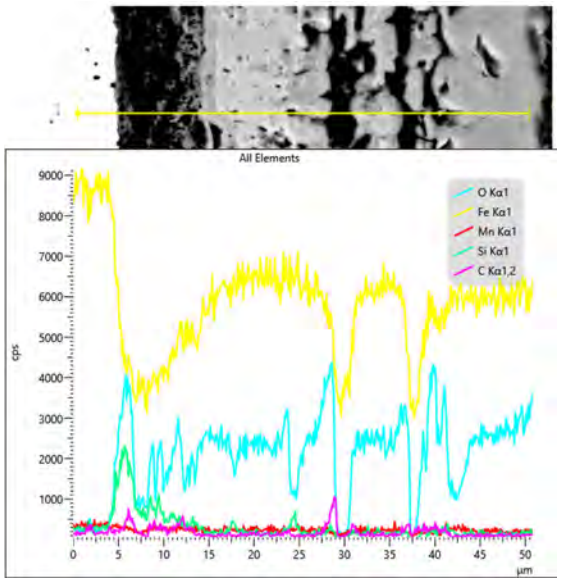

Figure 130: Appendix: 2Mn-1Si EDS line scan

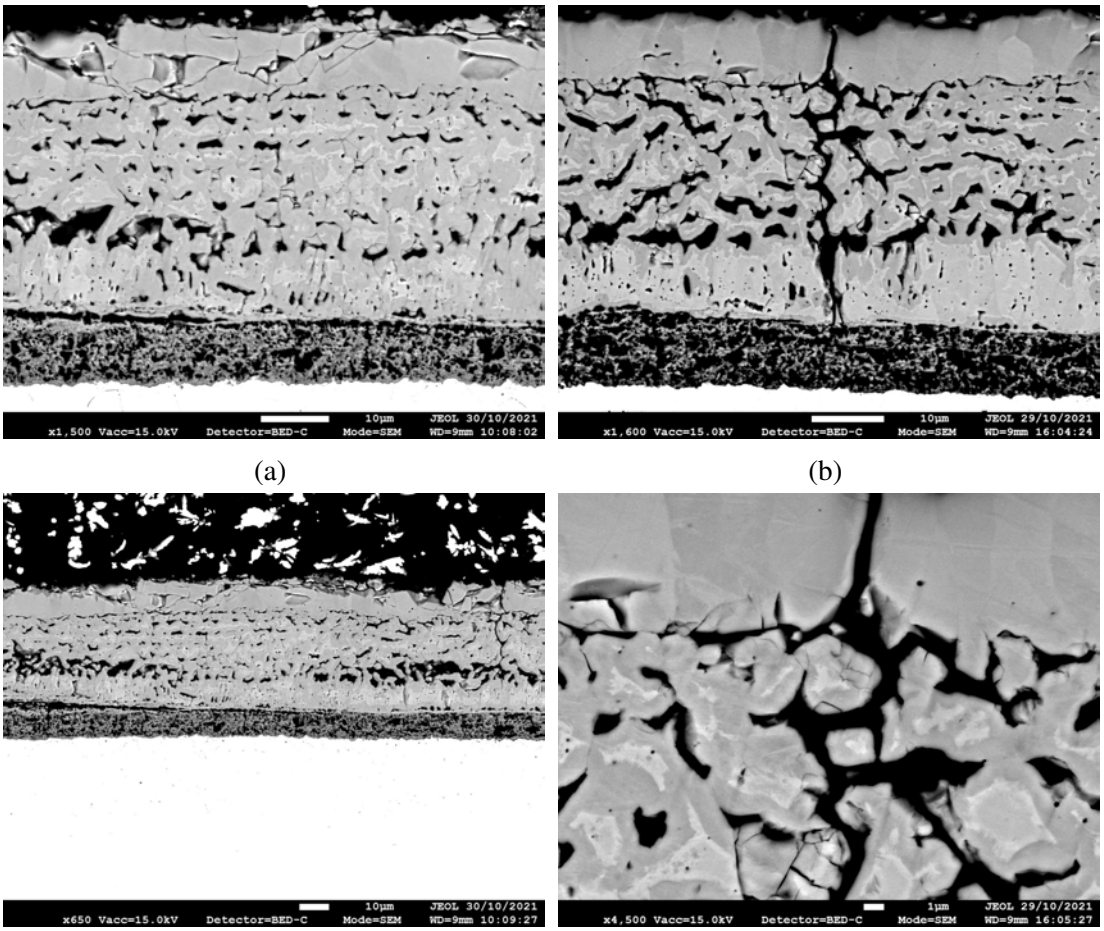

(a) (b)

(c) (d)

Figure 131: Appendix: 2Mn-1Si oxide morphology

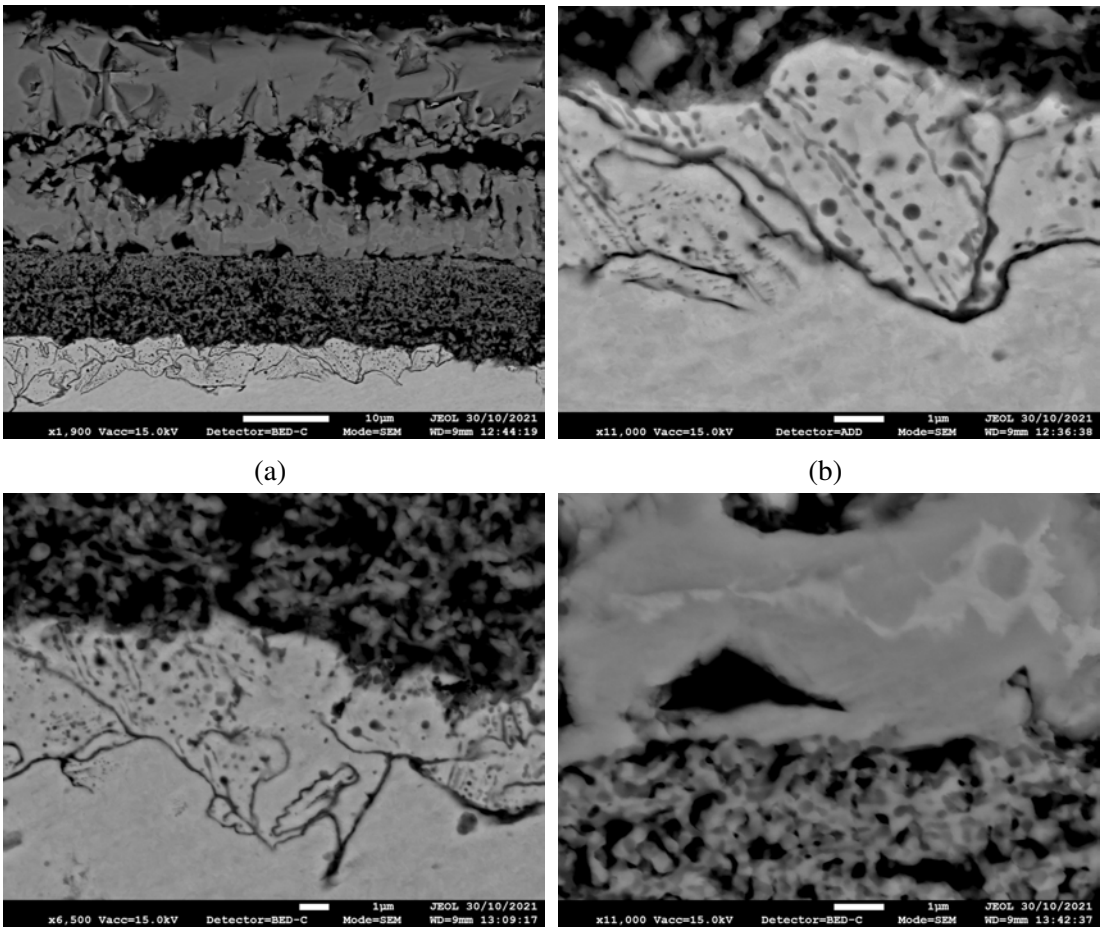

(a) (b)

(c) (d)

Figure 132: Appendix: 2Mn-2Si oxide morphology

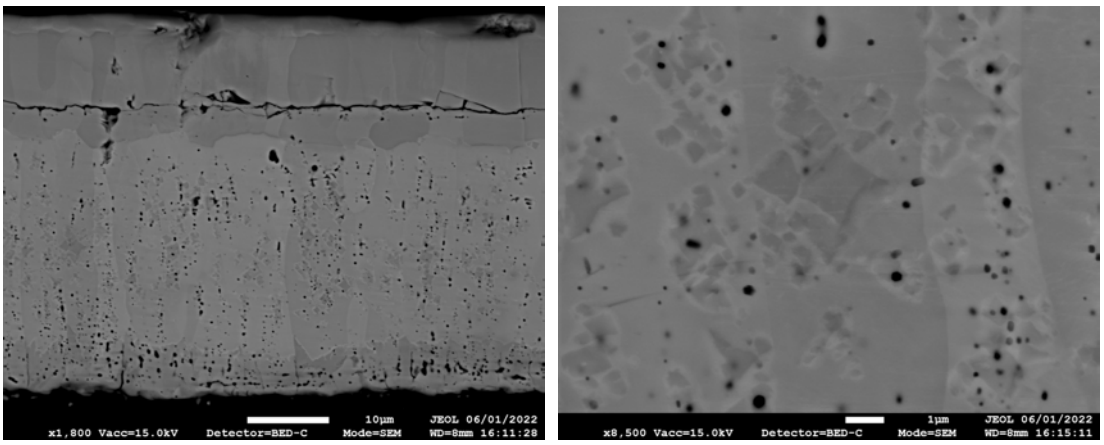

(a) (b)

Figure 133: Appendix: 0.5Mn-0.5Mo oxide morphology

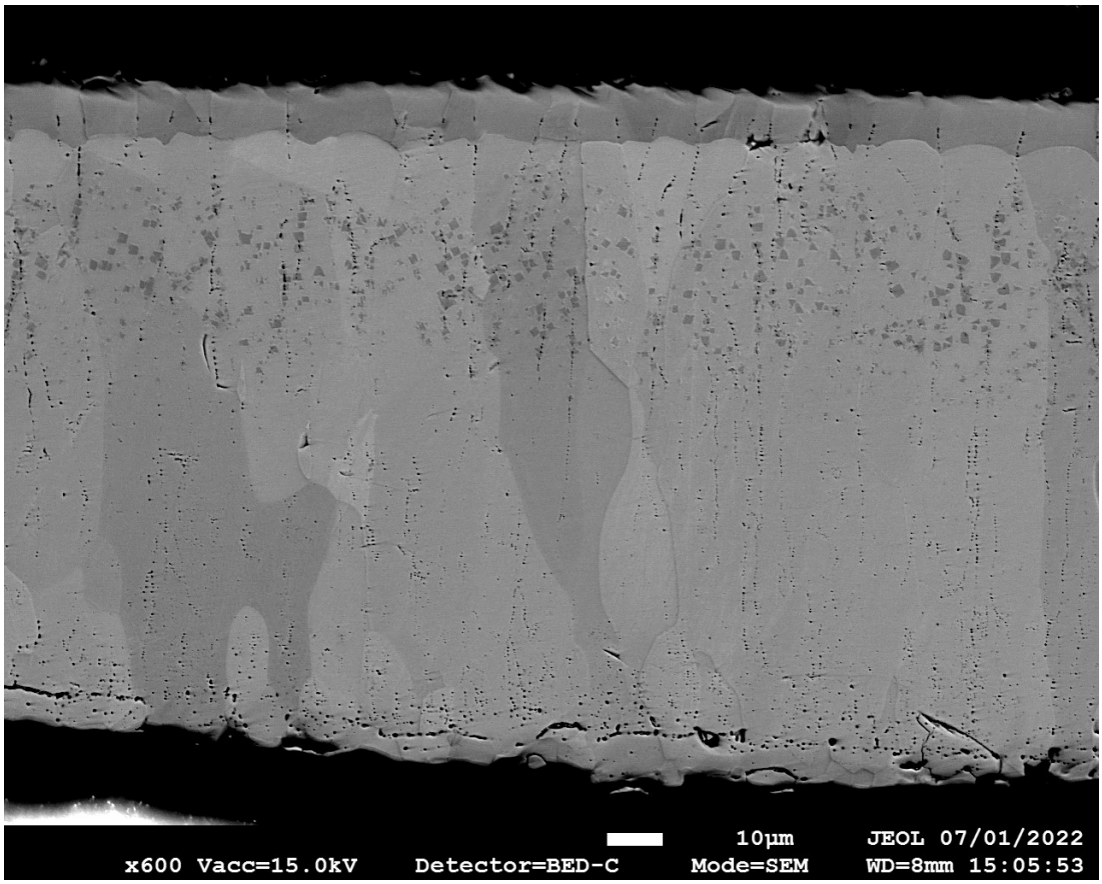

Figure 134: Appendix: 2Mn-0.25Mo Oxide morphology

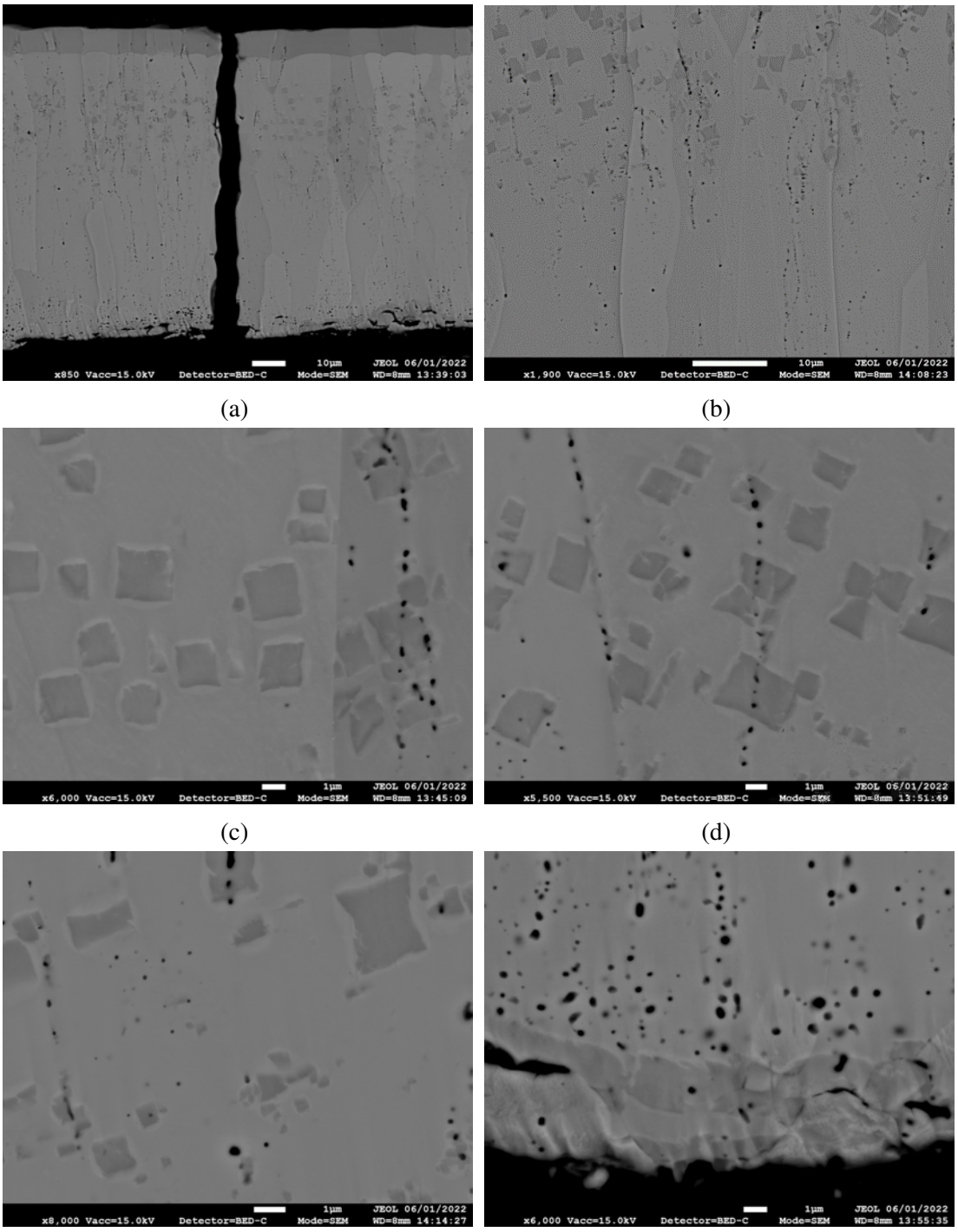

(a) (b)

(c) (d)

(e) (f)

Figure 135: Appendix: 2Mn-0.5Mo oxide morphology

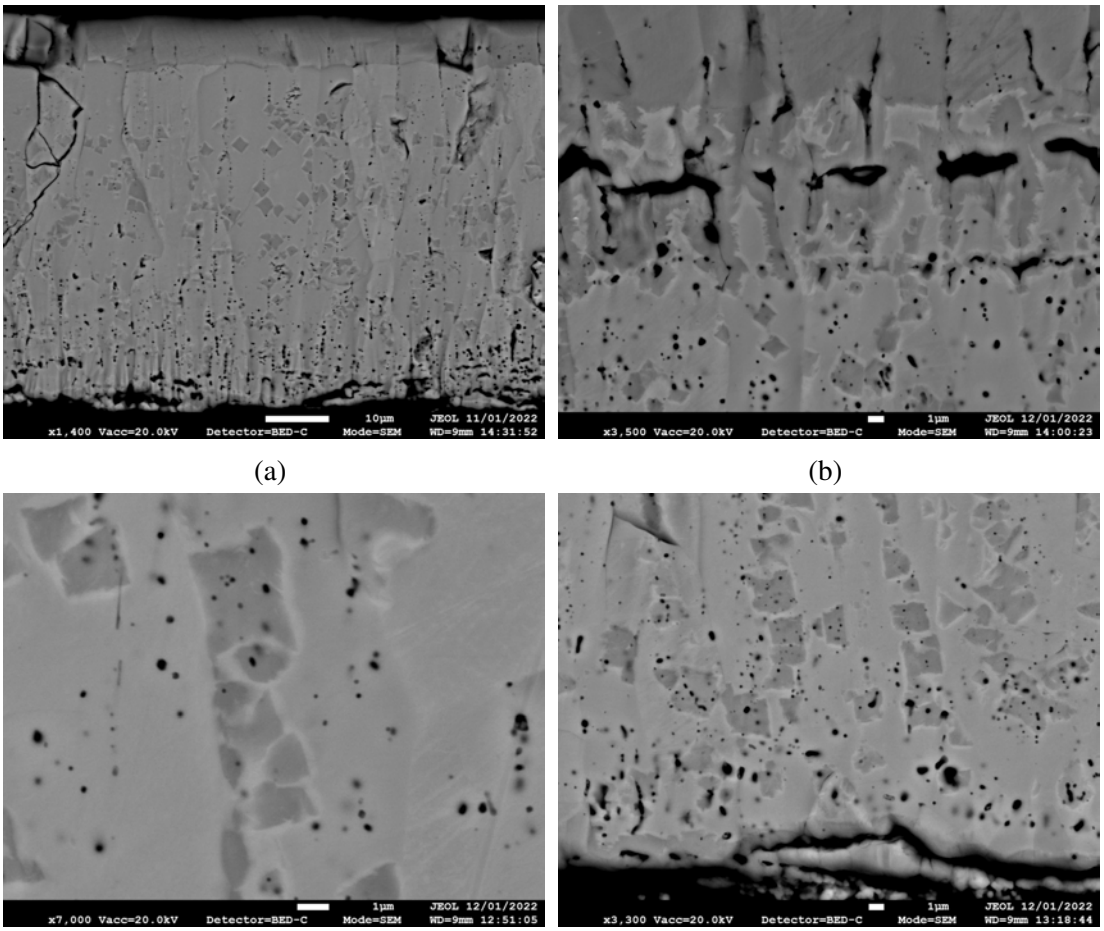

(a) (b)

(c) (d)

Figure 136: Appendix: 2Mn-0.75Mo oxide morphology

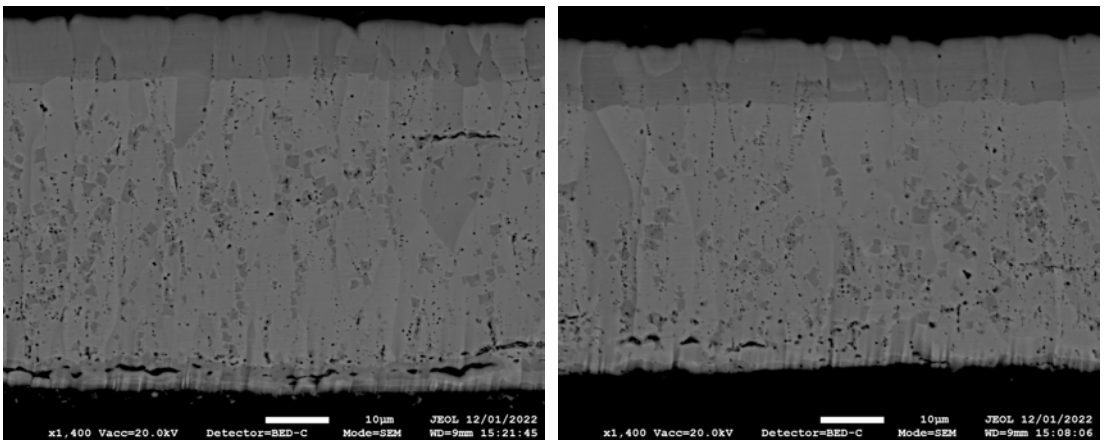

(a) (b)

Figure 137: Appendix: 2Mn-1Mo oxide morphology

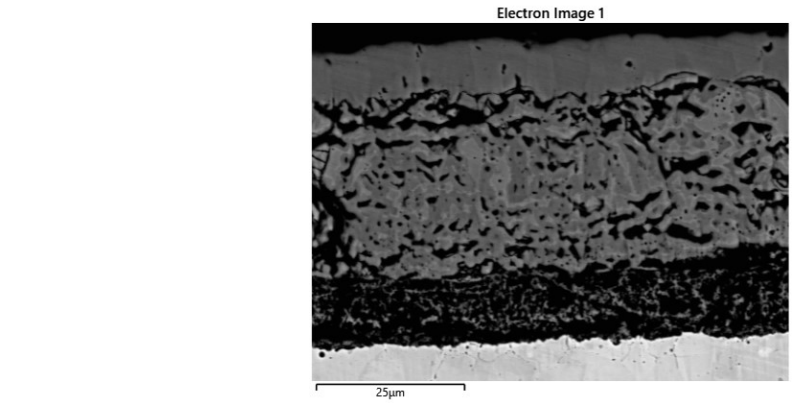

(a)

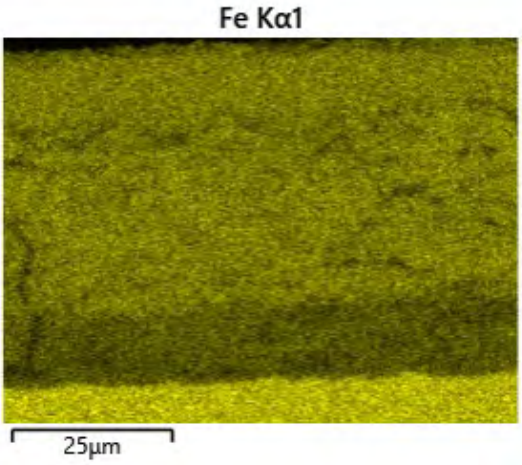

(b)

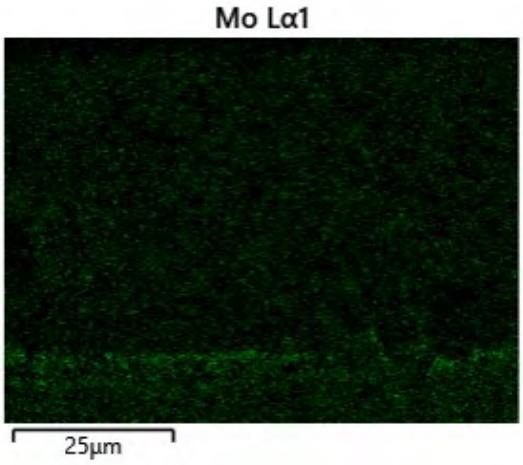

(c)

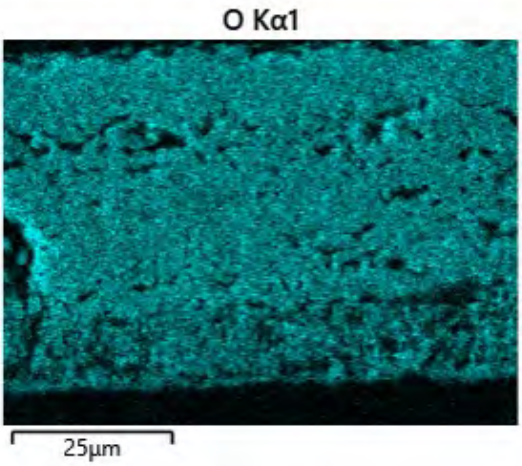

(d)

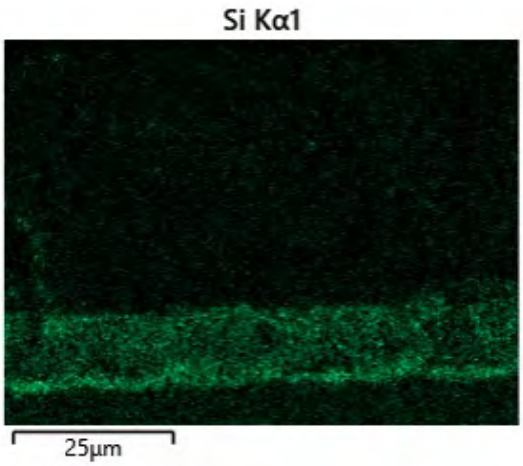

(e)

Figure 138: Appendix: 2Mn-1Si-0.25Mo EDS

11.2 Oxidation of ISG

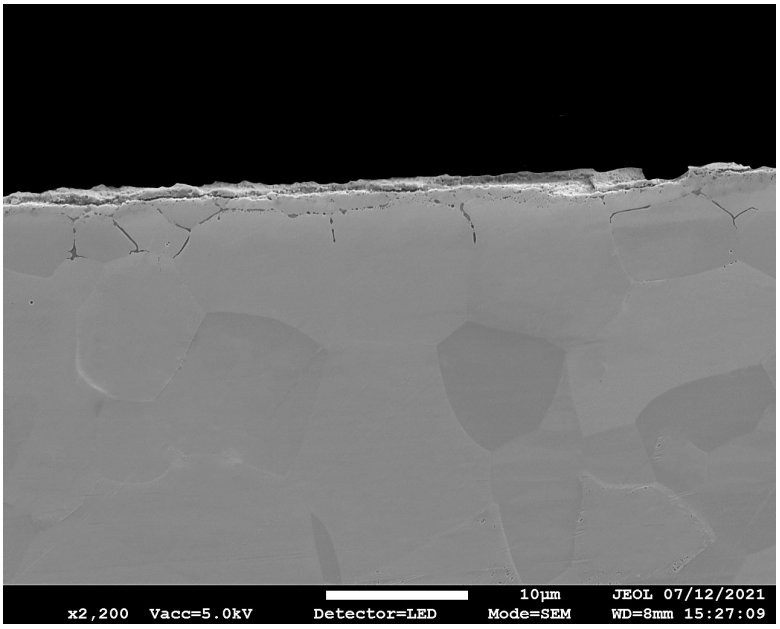

(a)

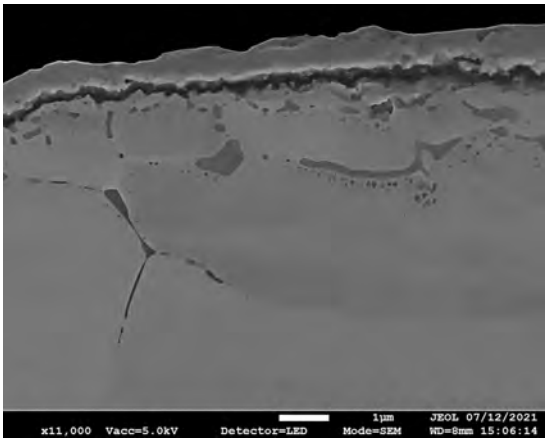

(b)

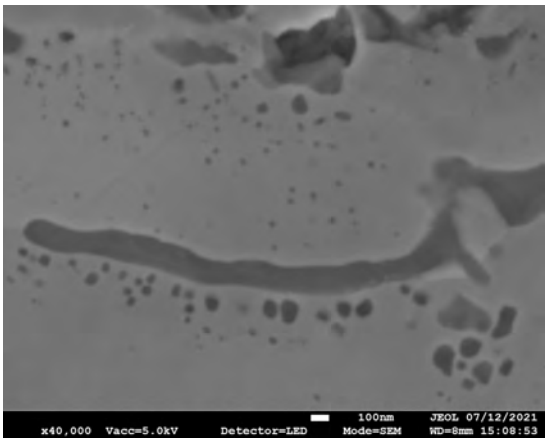

(c)

Figure 139: Appendix: DP800 800°C for 10s oxide morphology

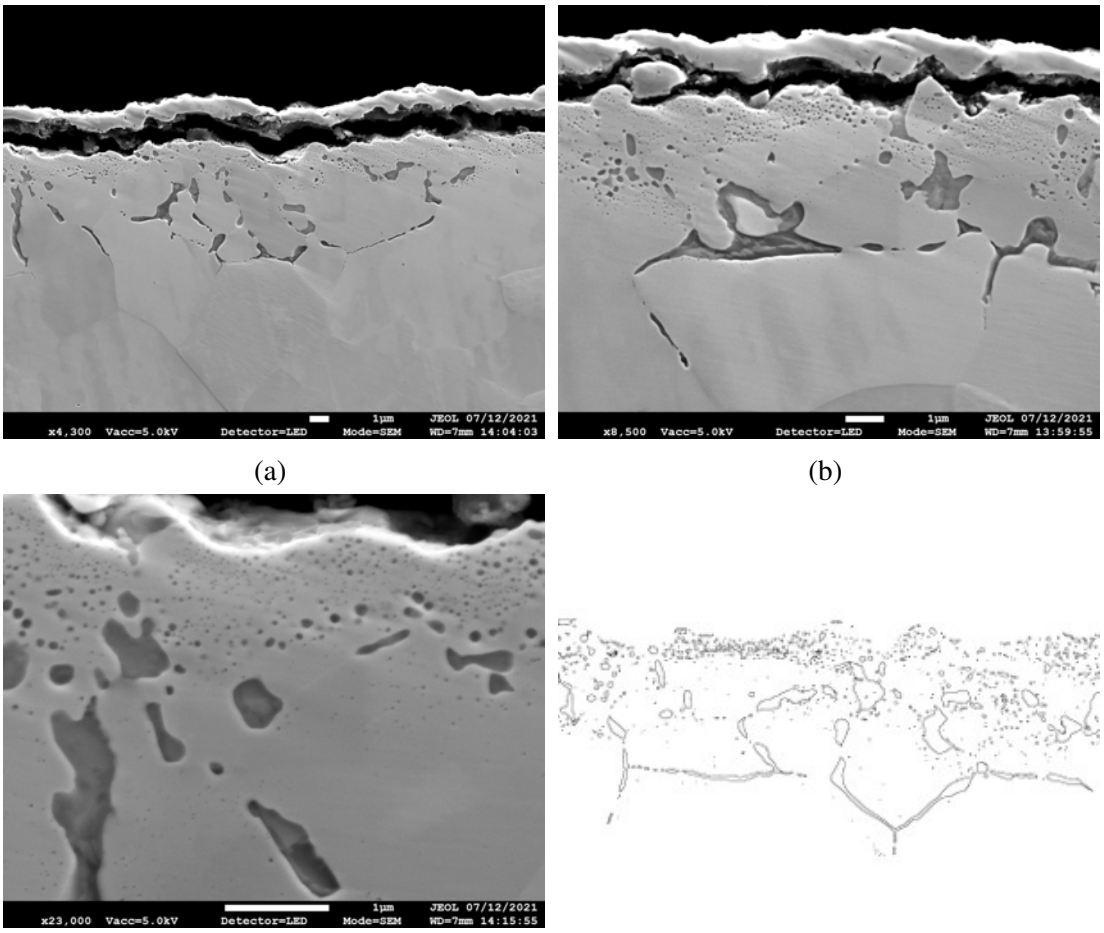

(a) (b)

(c) (d) Image J analysis of precipitates

Figure 140: Appendix: DP800 850°C for 10s oxide morphology

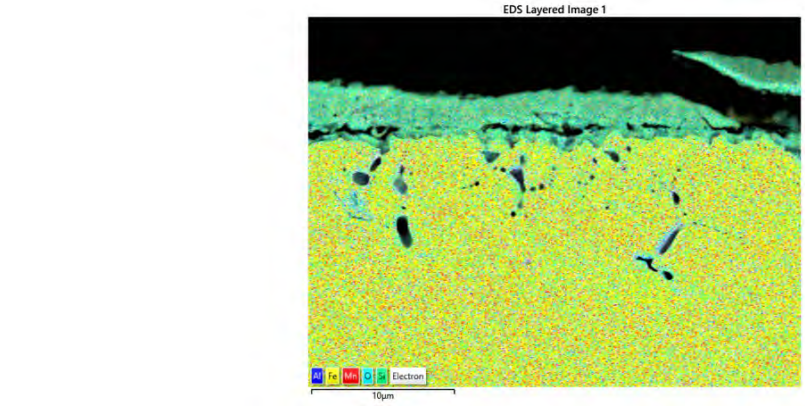

(a)

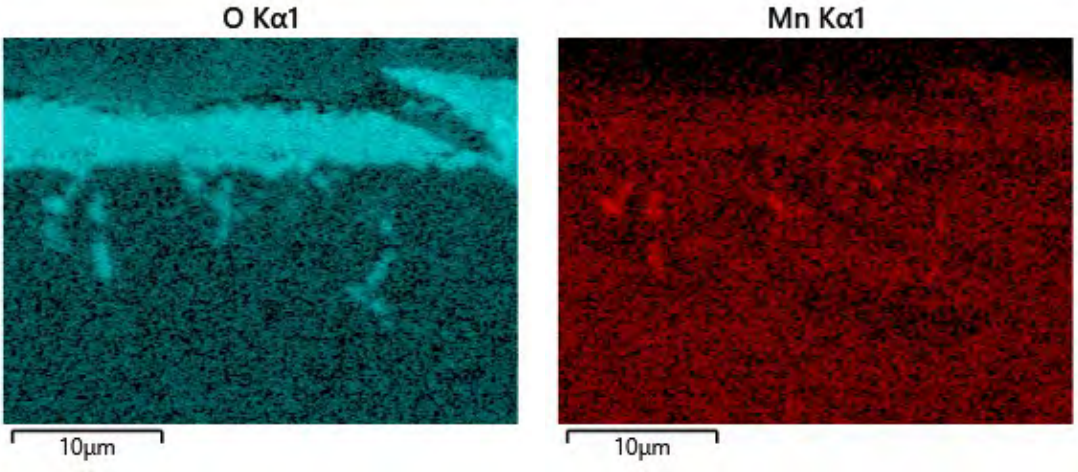

(b)

(c)

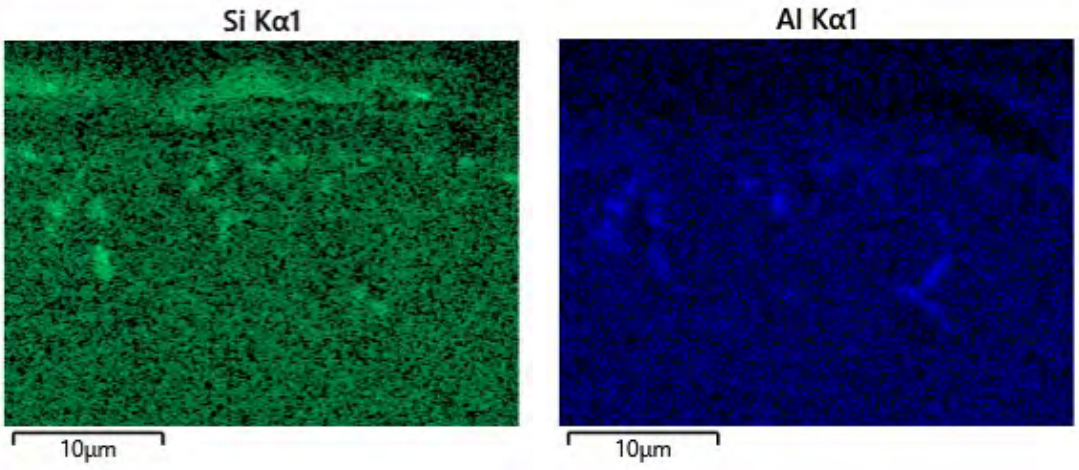

(d)

(e)

Figure 141: Appendix: DP800 950°C for 10s oxide morphology

11.3 External Oxidation Blister

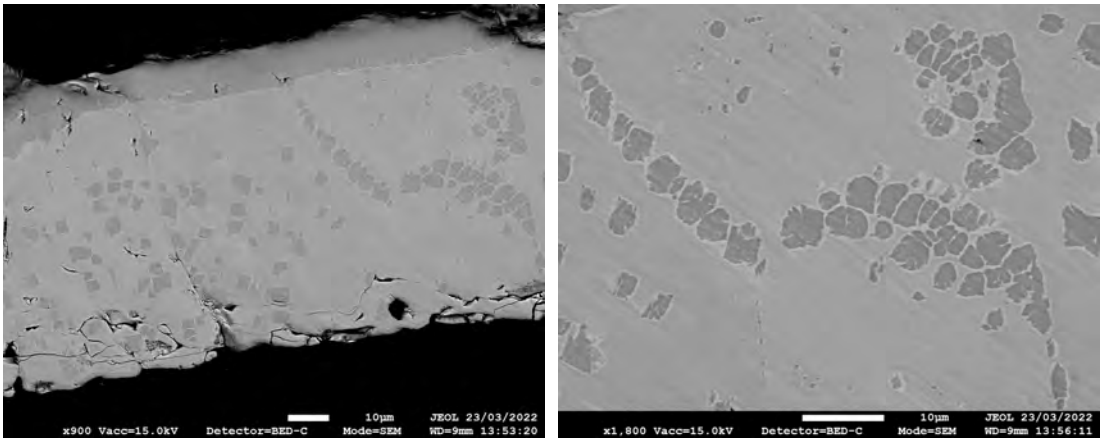

(a) (b)

Figure 142: Appendix: Blister 1200°C 30s

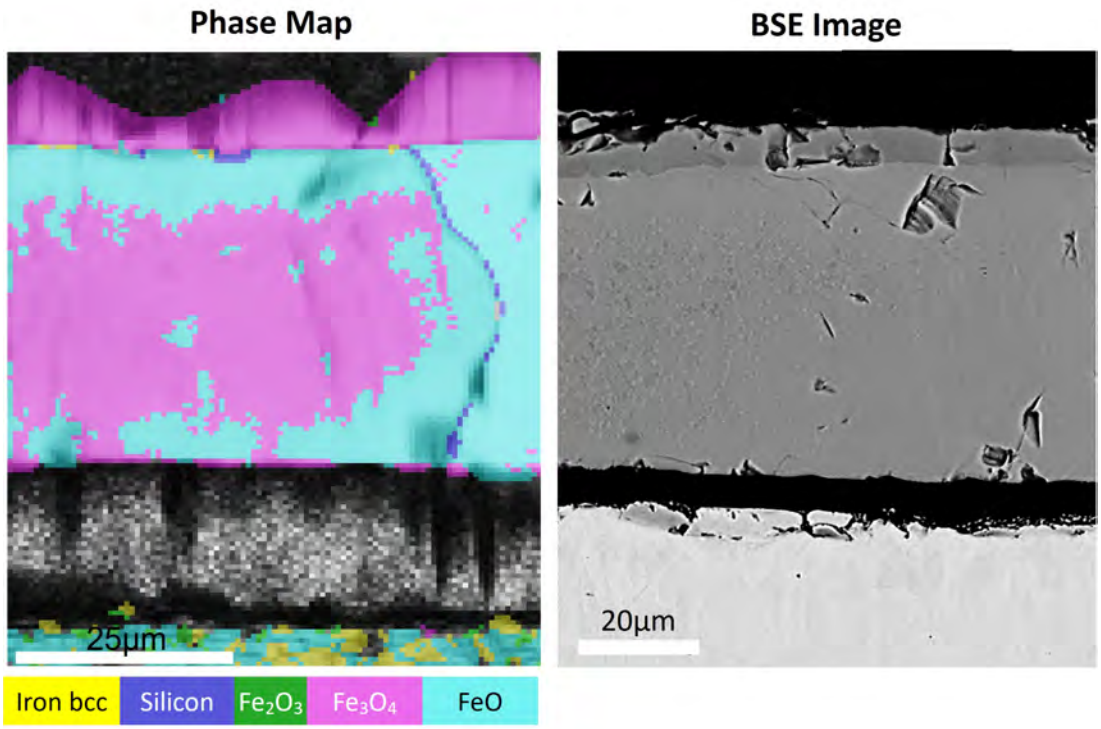

Figure 143: Appendix: EBSD Blister 1200 30s

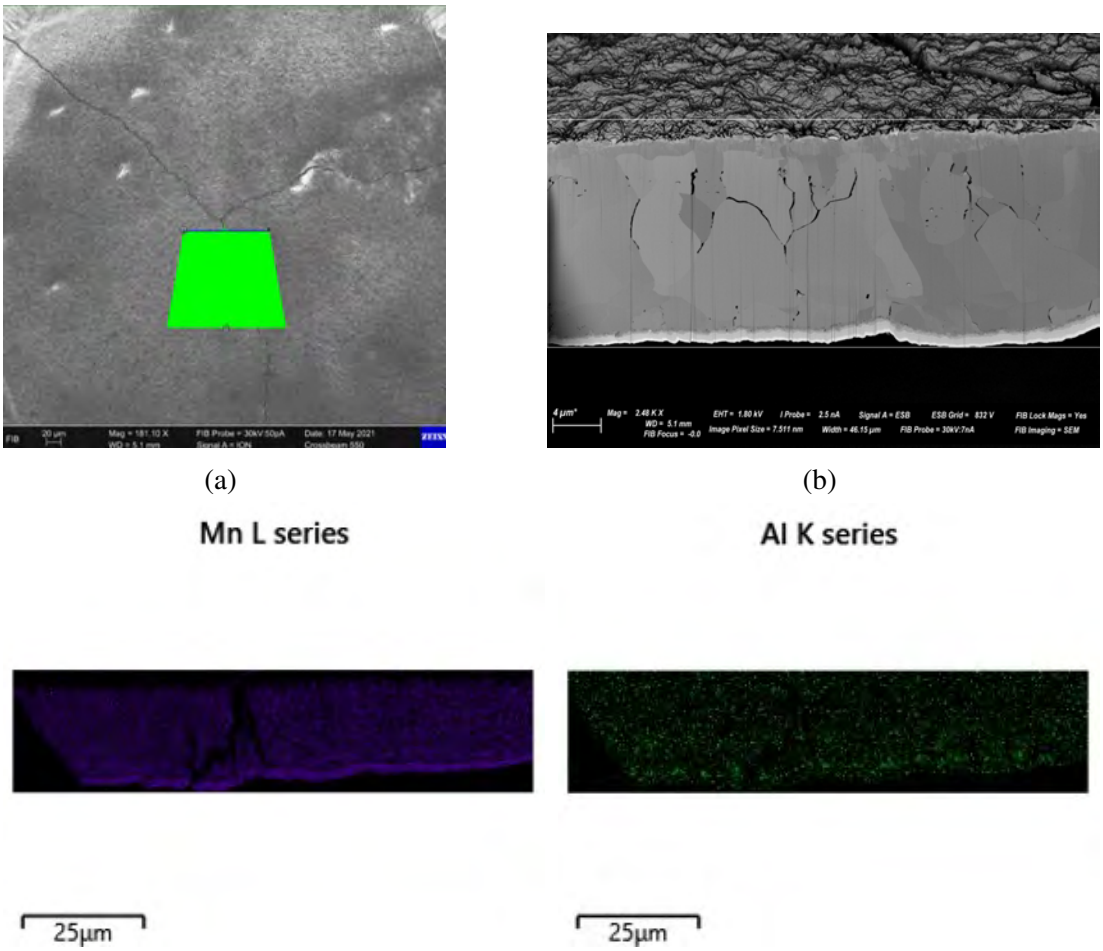

Figure 144: Appendix: Blister FIB 900°C 60s

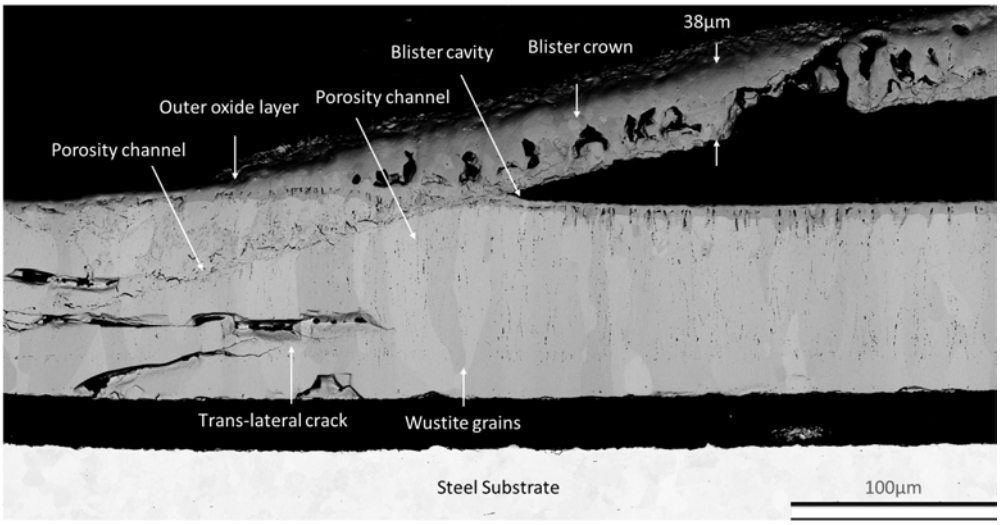

Figure 145: Appendix: Blister 900°C 600s with labels

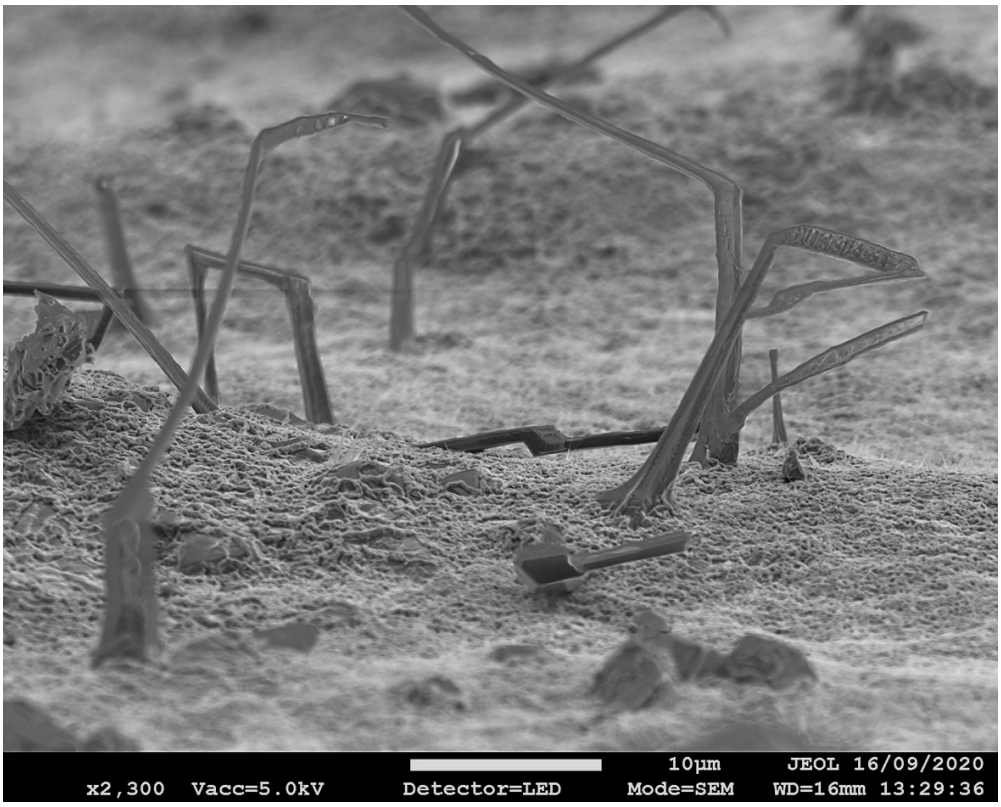

(a)

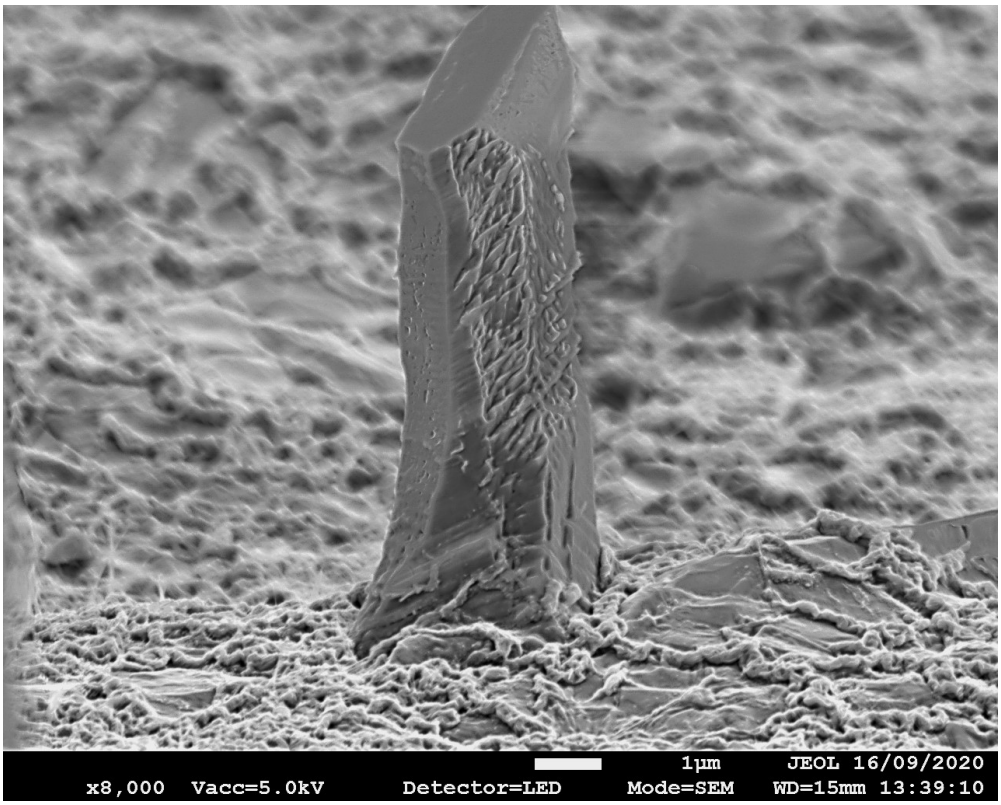

(b)

Figure 146: Appendix: Whiskers

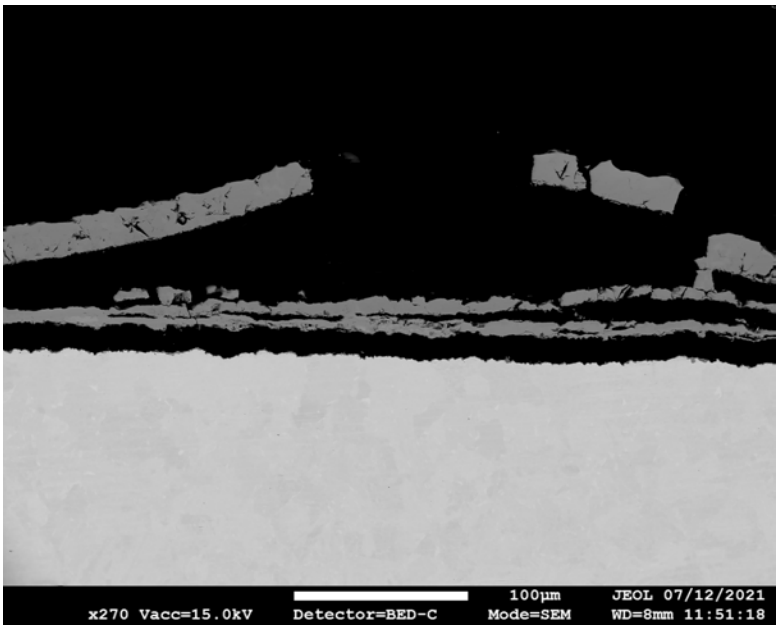

(a)

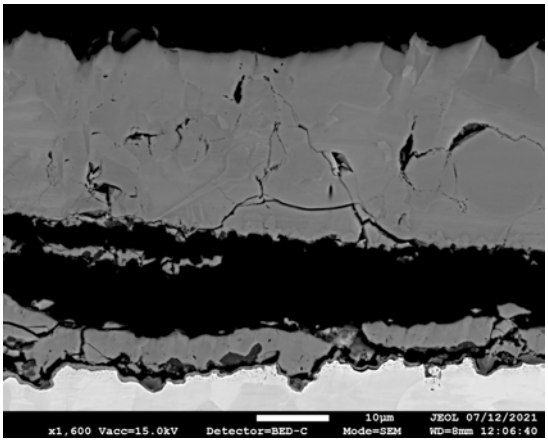

(b)

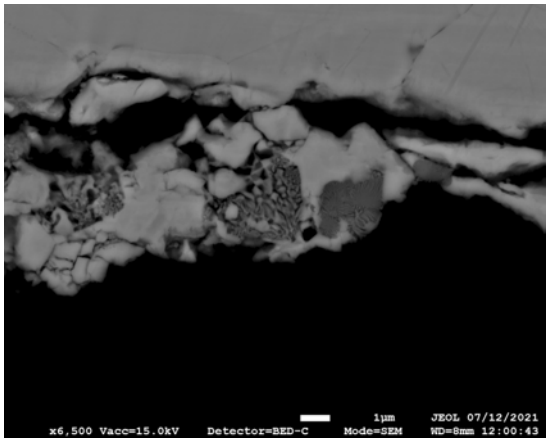

(c)

Figure 147: Appendix: Blister produced DP800 1000°C 10s

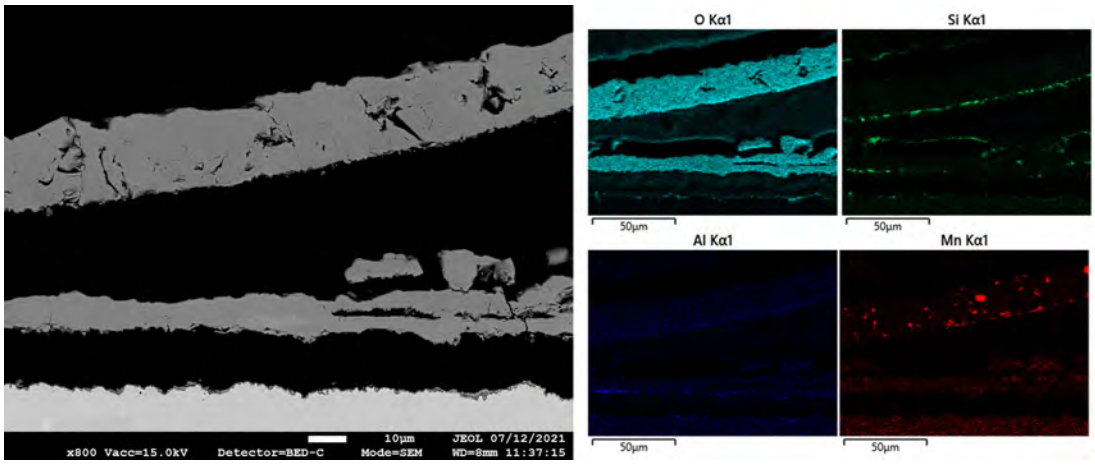

Figure 148: Appendix: EDS conducted on DP800 blister at 1000°C 10s

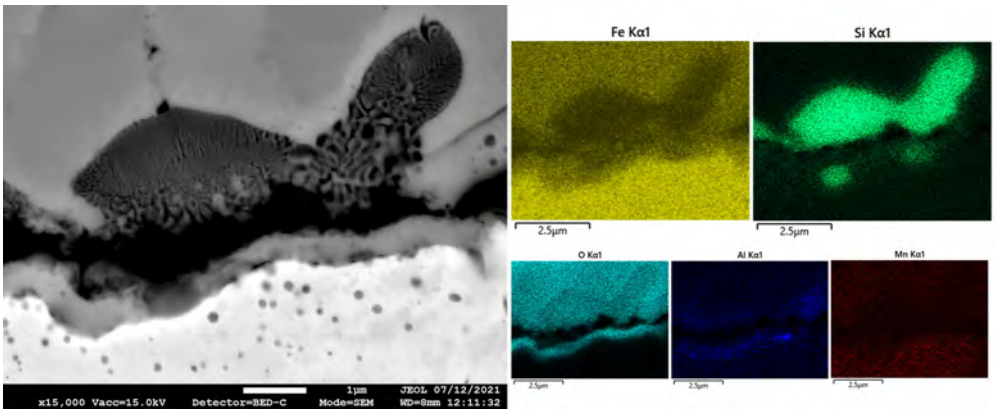

Figure 149: Appendix: EDS conducted on interface of oxide and underlying substrate

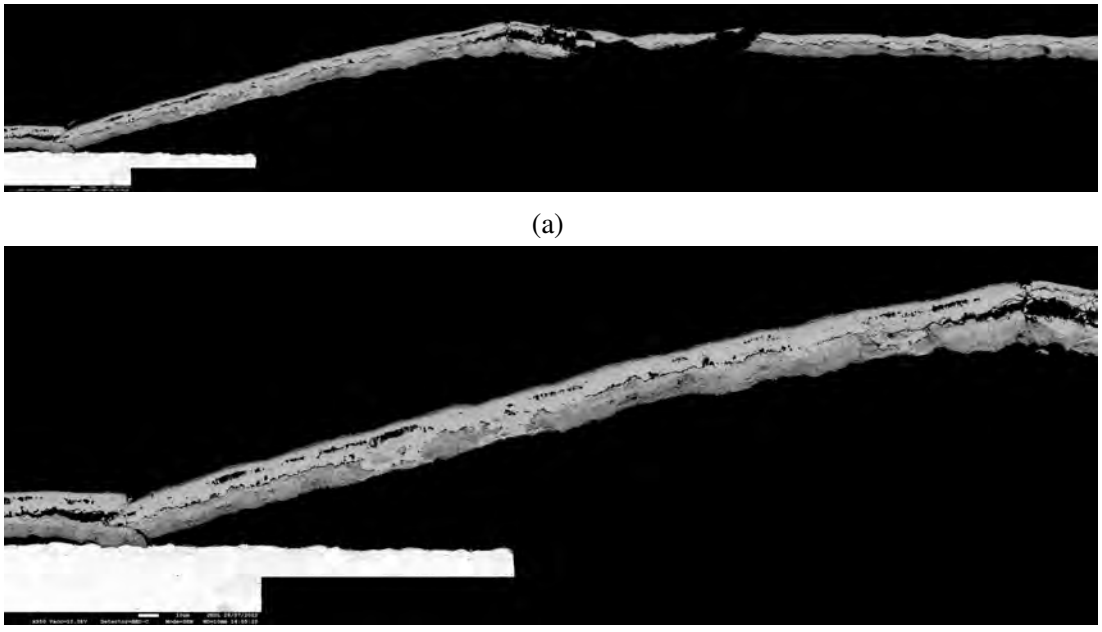

(a)

(b)

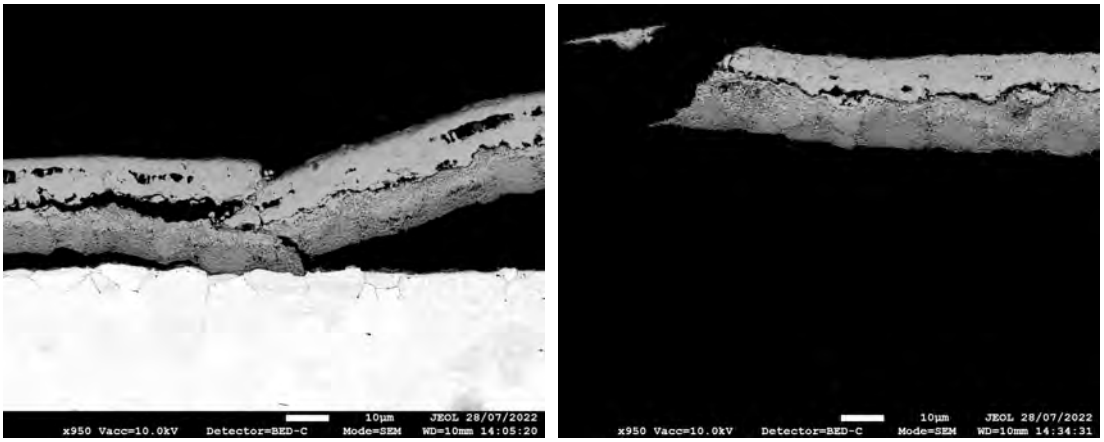

(c) (d)

Figure 150: Appendix: DP800 Blister at 800°C after 2hrs of heating

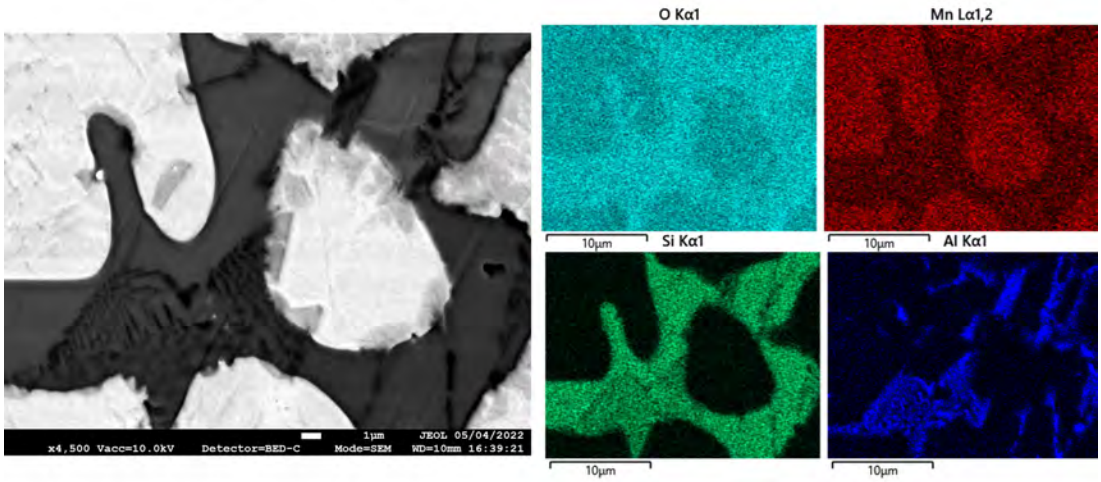

Figure 151: Appendix: B32 Blister EDS on precipitate

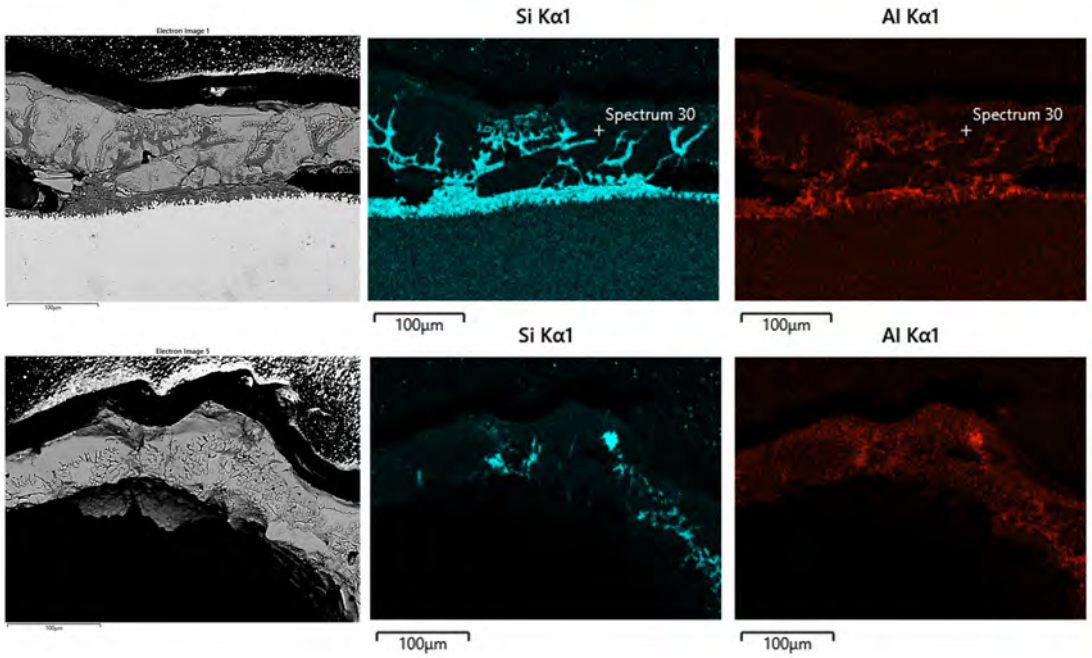

Figure 152: Appendix: EDS conducted on B32 blister